Progress in Materials Science 116 (2021) 100703

Contents lists available at ScienceDirect

Progress in Materials Science

journal homepage: www.elsevier.com/locate/pmatsci

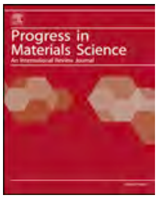

# Mechanistic models for additive manufacturing of metallic components

H.L. Wei[a,*], T. Mukherjee[b], W. Zhang[c], J.S. Zuback[b], G.L. Knapp[b], A. De[d], T. DebRoy[b,*]

[a] *School of Mechanical Engineering, Nanjing University of Science and Technology, Nanjing, China*
[b] *Department of Materials Science and Engineering, The Pennsylvania State University, University Park, PA, USA*
[c] *Department of Materials Science and Engineering, Ohio State University, Columbus, OH, USA*
[d] *Department of Mechanical Engineering, IIT Bombay, Mumbai, India*

ARTICLE INFO

*Keywords:*
Additive manufacturing
3D printing
Modeling
Heat transfer and fluid flow
Microstructure
Defects

ABSTRACT

Additive manufacturing (AM), also known as 3D printing, is gaining wide acceptance in diverse industries for the manufacturing of metallic components. The microstructure and properties of the components vary widely depending on printing process and process parameters, and prediction of causative variables that affect structure, properties and defects is helpful for their control. Since models are most useful when they can correctly predict experimental observations, we focus on the available mechanistic models of AM that have been adequately validated. Specifically, the applications of transport phenomena models in the studies of solidification, residual stresses, distortion, formation of defects and the evolution of microstructure and properties are critically reviewed. The functionality of AM models in understanding of the printability of commonly used AM alloys and the fabrication of functionally graded alloys are also assessed. Opportunities for future research are identified considering the gaps in knowledge in modeling. The uniqueness of this review includes substantive discussions of the rapid certification of the AM components aided by scale models, bidirectional models, cloud based big data, machine learning and digital twins of AM hardware.

## 1. Introduction

The growing adaptation of commercial additive manufacturing (AM) machines in various industry sectors is intensifying the need to produce high quality parts that can be standardized and certified rapidly. Defect free, structurally sound and reliable parts are now produced and certified by trial and error for each individual component, material and AM process variant [1]. This is a time consuming and expensive undertaking because of the need to determine the effects of a large number of AM process variables. Largely, the attributes of the parts are controlled by causative factors, such as the type of heat source, scanning pattern, hatch spacing, powder properties, and the resultant transient temperature fields, solidification conditions and cooling rates. The main difficulty is that currently there is no generally available standard tool for engineers to control the important AM variables that affect the product quality such as the geometry, microstructure, properties, residual stresses, distortion and defects prior to conducting experiments. In the last two decades, efforts have started to quantitatively understand the role of these parameters using phenomenological models of the transport processes in AM. These models seek to gain improved understanding of heat transfer, liquid metal flow, and mass

---

[*] Corresponding authors.
*E-mail addresses:* hlwei@njust.edu.cn (H.L. Wei), debroy@psu.edu (T. DebRoy).

https://doi.org/10.1016/j.pmatsci.2020.100703
Received 1 July 2019; Received in revised form 21 May 2020; Accepted 3 June 2020
Available online 19 June 2020
0079-6425/ © 2020 The Author(s). Published by Elsevier Ltd.

## Nomenclature

| | |
|---|---|
| $a$ | Coefficient in 1-D heat conduction equation |
| $\acute{a}$ and $A$ | Alloy dependent constant |
| $a_1$ to $a_4$ | Constant |
| $a_A$ | Side length of austenite |
| $a_i$ | Constant for element i |
| $A_s$ | Surface area |
| $b$ | Coefficient in 1-D heat conduction equation |
| $\overrightarrow{B}$ | Magnetic flux vector |
| $B_N$ | Constant in momentum equation |
| $C$ | Constant or weighing factor |
| $C_4$ | Constant |
| $CA$ | Cross-sectional area |
| $CE$ | Carbon equivalent |
| $C_i^b$ | Concentration of i in bulk gas |
| $C_i$ | Concentration of alloying element i |
| $C_p$ | Specific heat |
| $Cp_e$ | Effective specific heat of powder bed |
| $Cp_g$ | Specific heat of shielding gas |
| $Cp_s$ | Specific heat of solid |
| $D$ | Thermal diffusivity |
| $d$ | Plate thickness |
| $d_0$ | Initial diameter of gamma prime particle |
| $d_L$ | Layer thickness |
| $d_P$ | Pool depth |
| $d_t$ | Diameter of gamma prime particle at time t |
| $E$ | Young's modulus |
| $E_V$ | Volumetric energy density |
| $eq$(suffix) | Equilibrium |
| $f$ | Power distribution factor |
| $F^b$ | Buoyancy force |
| $F^{emf}$ | Electromagnetic force |
| $F^n$ | Normal force |
| $Fo$ | Fourier number |
| $F_R$ | Vapor recoil force |
| $F_S$ | Surface tension force |
| $F^s$ | Shear force |
| $f_e$ | Extent of transformation |
| $f_L$ | Liquid fraction |
| $f_l^V$ | Volume fraction of liquid in the mushy zone |
| $G$ | Temperature gradient |
| $G_L$ | Lengthening rate of Widmanstatten ferrite |
| $g$ | Acceleration due to gravity |
| $gb$(suffix) | Grain boundary |
| $H$ | Linear heat input |
| $h$ | Enthalpy |
| $h_c$ | Convective heat transfer coefficient |
| $H_d$ | Droplet heat content |
| $h_e$ | Effective height of the cylindrical heat source |
| $I$ | Moment of inertia of the substrate |
| $i$ | Direction index, element index |
| $j$ | Direction index, element index |
| $\overrightarrow{j}$ | Current density vector |
| $J_i$ | Vaporization flux of element i |
| $J_P$ | Vaporization flux from the pool surface |
| $k$ | Thermal conductivity |
| $K_0$ | Modified Bessel function |
| $k_e$ | Effective thermal conductivity of powder bed |
| $k_g$ | Thermal conductivity of shielding gas |
| $K_{g,i}$ | Mass transfer coefficient of vapor |
| $k_i$ | Coefficient for regression analysis |
| $K_P$ | Permeability constant |
| $k_s$ | Thermal conductivity of gas |
| $L$ | Ratio of a constant and powder particle diameter |
| $L_C$ | Length of the graded joint |
| $l$ | Pool length |
| $L_F$ | Lack of fusion index |
| $M$ | Mach number |
| $MP$ | Empirical quantity |
| $MF_i$ | Mole fraction of element i |
| $M_i$ | Molecular weight of element i |
| $M_v$ | Molecular weight of vapor |
| $\dot{m}$ | Powder mass flow rate |
| $N$ | Coordination number |
| $N_0$ | Number of nucleation sites |
| $N_d$ | Nucleation density |
| $n$ and $\acute{n}$ | Alloy specific constant |
| $\overrightarrow{n}$ | Normal direction to the surface |
| $P$ | Heat source power |
| $P_a$ | Arc pressure |
| $P_d$ | Absorbed power |
| $P_i$ | Partial pressure of element i |
| $P_{pure}$ | Property of pure solvent |
| $P_L$ | Laser power |
| $P_S$ | Heat absorbed by surface |
| $PR$ | Property of graded component |
| $PR_{eff}$ | Effective property of graded component |
| $PR_1$ and $PR_2$ | Properties of terminal alloys in graded component |
| $p_i^0$ | Partial pressure of i over pure liquid |
| $p_1$ | Pressure in the front of the wave-front in Knudsen layer |
| $p_2$ | Pressure in the behind of the wave-front in Knudsen layer |
| $p_g$ | Gas pressure |
| $p_i^0$ | Vapor pressure of element i on the molten pool surface |
| $p_L$ | Pressure on liquid metal surface |
| $p_o$ | Surrounding pressure |
| $p_R$ | Pressure exerted by the recoil force |
| $p_v$ | Pressure of vapor in Knudsen layer |
| $Q$ | Activation energy |
| $q$ | Absorbed power from the heat source |
| $q_c$ | Convective heat loss |
| $q_r$ | Radiative heat loss |
| $q_v$ | Heat loss due to vaporization |
| $q_{VA}$ | Magnitude of volumetric heat source |
| $q_{VL}$ | Volumetric heat flux |
| $R$ | Solidification growth rate |
| $R_a$ | Surface roughness |
| $R_e$ | Residual |
| $R_g$ | Gas constant |
| $R_i$ | Vaporization rate of element i |
| $R_v$ | Vapor constant |
| $RC$ | Rate constant |
| $RC_0$ | Pre-exponent constant |
| $r$ | Radial distance |
| $r_b$ | Heat source radius |
| $r_e$ | Effective height of the cylindrical heat source |

| | |
|---|---|
| $r_m$ | Minimum particle radius |
| $r_p$ | Powder particle radius |
| $r_1$ and $r_2$ | Particle radius |
| $r_{s1}$ and $r_{s2}$ | Surface curvature components |
| $r_w$ | Wire radius |
| $S$ | Speed of sound |
| $\overrightarrow{s}$ | Surface tangential direction |
| $S_h$ | Source term in energy equation |
| $S_{uj}$ | Momentum equation source term |
| $S_V$ | Volumetric heat source energy |
| $T$ | Temperature |
| $T_a$ | Ambient temperature |
| $T_d$ | Droplet temperature |
| $T_g$ | Temperature of gas |
| $T_L$ | Temperature at liquid surface in Knudsen layer |
| $T_0$ | Initial temperature |
| $T_{ref}$ | Reference temperature |
| $T_v$ | Vapor temperature |
| $t$ | Time |
| $t_{SL}$ | Thickness of the isolated solid–liquid interface |
| $U$ | Characteristic velocity |
| $u$ | Velocity along x-direction |
| $u_i$ | Velocity component along i-direction |
| $u_j$ | Velocity component along j-direction |
| $u_k$ | Vertical component of velocity |
| $u_s$ | Surface velocity |
| $u_v$ | Velocity of vapor in Knudsen layer |
| $u^n$ | Normal displacement |
| $u^s$ | Shear displacement |
| $V$ | Scanning speed |
| $v$ | Velocity along y-direction |
| $V_0$ | Volume fraction including martensite |
| $V_1$ and $V_2$ | Volume fractions of terminal alloys in graded component |
| $V_a$ | Volume fraction of allotriomorphic layer |
| $V_m$ | Volume of molten metal |
| $V_w$ | Volume fraction of Widmanstatten ferrite |
| $w$ | Velocity along z-direction |
| $w$(suffix) | Widmanstatten |
| $w_P$ | Pool width |
| $w_f$ | Wire feed rate |
| $X$ | Distance between two successive nodes |
| $X_p$ | Volume fraction of the phase '$p$' |
| $x_i$ | Distance along i-direction |
| $x$ | Co-ordinate |
| $y$ | Co-ordinate |
| $z$ | Co-ordinate |
| $z_0$ | z-location of top surface |
| $\alpha_1$ | 1D parabolic constant |
| $\alpha_m$(suffix) | Martensite |
| $\beta$ | Condensation factor |
| $\beta$(suffix) | Phase |
| $\beta_L$ | Thermal expansion coefficient |
| $\gamma$ | Coefficient of surface tension |
| $\gamma_g$ | Ratio of specific heats of gas |
| $\gamma_{gb}$ | Grain boundary energy |
| $\gamma_M$ | Surface tension at the melting point |
| $\gamma_{SL}$ | Solid/liquid interfacial energy |
| $\gamma_v$ | Ratio of specific heats of vapor |
| $\Delta G_{max}$ | Maximum driving force for nucleation |
| $\Delta H$ | Latent heat of fusion |
| $\Delta H_i$ | Enthalpy of vaporization of element $i$ |
| $\Delta H_v$ | Enthalpy of metal vapor |
| $\Delta P$ | Pressure difference |
| $\Delta Q$ | Net change in heat flow |
| $\Delta S_f$ | Fusion entropy |
| $\Delta T$ | Temperature difference |
| $\Delta T_c$ | Critical undercooling |
| $\Delta T_n$ | Undercooling |
| $\Delta T_\sigma$ | Standard deviation at critical undercooling |
| $\Delta t$ | Time increment |
| $\Delta t_{max}$ | Maximum time increment |
| $\Delta x$ | Grid spacing |
| $\Delta \Gamma_b$ | Difference in energy |
| $\delta$ | Hatch spacing |
| $\epsilon$ | Absorptivity |
| $\varepsilon$ | Emissivity |
| $\varepsilon^*$ | Thermal strain parameter |
| $\eta$ | Packing efficiency of powder bed |
| $\eta_l$ | Fraction of power absorbed by the deposited layer |
| $\eta_m$ | Interference factor to account for shielding |
| $\eta_p$ | Fraction of power absorbed by the powder |
| $\eta_s$ | Fraction of available power absorbed by the solid particles |
| $\theta$ | Build angle |
| $\lambda_2$ | Secondary dendrite arm spacing |
| $\mu$ | Viscosity |
| $\nu$ | Poisson's ratio |
| $\xi$ | Constant in Langmuir equation |
| $\rho$ | Density |
| $\rho_e$ | Effective density of powder bed |
| $\rho_g$ | Density of gas |
| $\rho_L$ | Density of the liquid |
| $\rho_l$ | Saturated vapor density at liquid temperature |
| $\rho_p$ | Density of the powder particle |
| $\rho_s$ | Density of solid |
| $\rho_v$ | Density of vapor |
| $\sigma$ | Stefan-Boltzmann constant |
| $\tau$ | Time of flight of the powder |
| $\tau_i$ | Incubation time |
| $\tau_x$ | Marangoni stress along x-direction |
| $\tau_y$ | Marangoni stress along y-direction |
| $\tau_z$ | Marangoni stress along z-direction |
| $\phi$ | Surface profile parameter |
| $\phi^v$ | Volume fraction of equiaxed grains |
| $\phi_s$ | Solidified surface profile |
| $\chi$ | Integer in CALPHAD |
| $\Omega_{ij}^v$ | Binary interaction parameter |

transfer to calculate the important metallurgical variables that affect the microstructure and properties of components. The simulated results are then rigorously validated with experiments. This combined theoretical and experimental approach is critical for improved understanding of cooling rates, solidification parameters, microstructures, lack of fusion defects, residual stresses and distortion of the components all of which define the product quality [2]. Increasing interest in the modeling of AM is apparent from the expanding volume of publications in recent years as shown in Fig. 1.1. Modeling of various AM process variants and physical processes has been

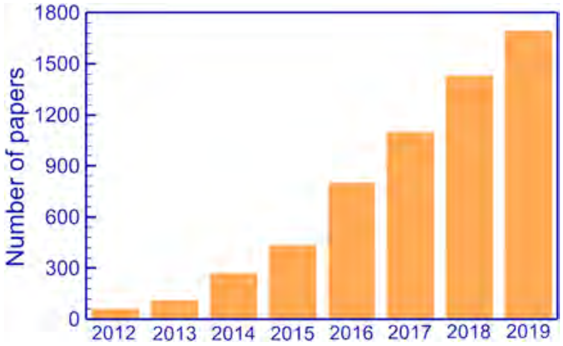

**Fig. 1.1.** Number of peer-reviewed papers on the modeling of additive manufacturing in the Web of Science (core collection) as on 23rd April 2020. Search was done using keywords “additive manufacturing” OR “3D printing” AND “model”.

reviewed before [3–16]. Because this is a rapidly evolving field, a periodic critical review of the models is important.

Repeated heating, melting, cooling and solidification of different regions of a build resulting from its interaction with a moving heat source, results in multiple thermal cycles at any monitoring location [17–19]. The small size of the molten pool, strong recirculating motion of the liquid alloy driven mainly by Marangoni convection [20], the movement of the heat source and the rapid temperature changes make the accurate measurement of transient temperature and other important variables challenging. In addition, experimental measurements of temperatures and other variables are only practical on surfaces that are easily accessible and not on interior locations. Models of heat transfer, fluid flow and mass transfer, are essential to calculate the temperature fields, fusion zone size and other parameters needed for the predictions of residual stresses, distortion, defects, grain structure and texture. Fig. 1.2 shows the important role of heat transfer, fluid flow and mass transfer calculations in the overall understanding of the physical processes in AM. The capabilities and the scope of the phenomenological models of AM vary depending on their content and the length scale of their applicability. Models that focus on smaller scale can reveal detailed information about the role of powders and the manner of interaction of different powder particles during melting and solidification processes [21]. These multi-scale models [21,22] capable of resolving powder particles are good choices when the focus is on a small region. However, AM involves conversion of feedstock to components by a multi-layer and multi-hatch operation where the structure and properties of the entire components

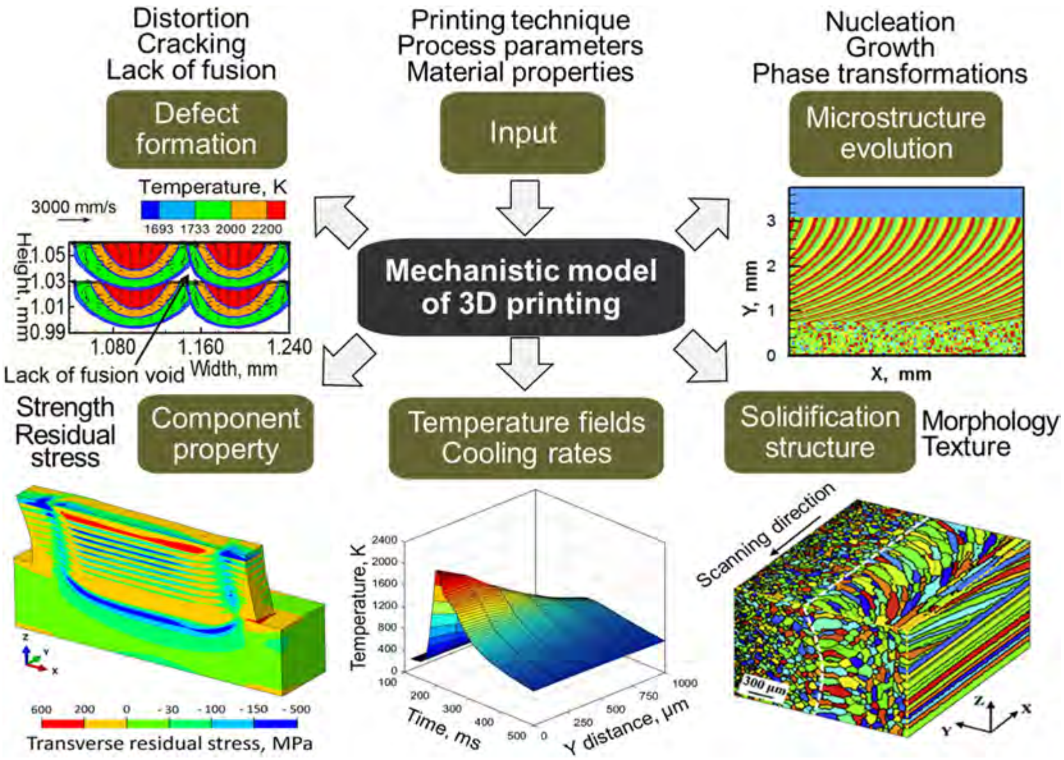

**Fig. 1.2.** The centrality of heat and mass transfer and fluid flow for understanding both the AM process and the manufactured metallic components [23].

beyond just a small area or volume are important. Consideration of multiple layers and hatches is critical to understand the structure and properties of the entire build and continuum models are more suitable for that purpose [19,22].

Calculations of heat transfer in AM starts with a quantitative description of the heat source based largely on the experimental measurements. Various simplifications are commonly made to describe both the geometry of the heat source and the power density distribution. These include idealization of the energy source in the form of a point, line, area, or a volume. An assessment of the roles of these different types of heat source is important to understand the simulated results that provide insights to the thermal cycles, solidification phenomena and the evolution of microstructure and properties of the components made by AM. Characterization of microstructure and properties experimentally without any concomitant modeling of the transient temperature field cannot uncover the origins of the spatial variation of microstructure and properties [23]. In contrast, when characterization studies are augmented with modeling of transient temperature fields, thermal cycles and solidification parameters, such studies uncover not just how the microstructure and properties vary with location but why [24].

Not all alloys are equally printable just like not all alloys are equally weldable [25]. While the concept of weldability is well established in the welding literature, the concept of printability is still developing. Printability is the ability of an alloy feedstock, powder or wire, to be converted to a component with acceptable metallurgical, mechanical and functional requirements for a specific application. It depends on both the nature of the alloy and the AM process variables. Some alloys are particularly susceptible to distortion [26–28] as well as other defects such as lack of fusion defects and the loss of volatile alloying elements [25]. Modeling of heat transfer and fluid flow can provide an idea of the relative susceptibilities of different alloys to common AM defects and thus, help in building a theoretical basis for understanding printability of different alloys [25].

Ongoing research on the numerical modeling of heat transfer, fluid flow and mass transfer in AM generates a large volume of data that show the effects of alloy feedstock and process variables on the structure, properties and serviceability of the builds. In the shop floors, a large volume of digitized data is obtained every time a component is built. These include all the process parameters, the data from sensing and control, post processing, inspection and quality control as well as technical papers, theses and reports [29]. The volume of such big data is estimated to be on the order of millions of gigabytes, and is expected to reach exabytes (one billion gigabytes) within a decade [23]. The resulting colossal data on the interrelation between the materials, process parameters, test results and serviceability need to be connected in such a manner that allows access, classification and interrogation of the data in a meaningful way. With the advancement of computational hardware and software and development of innovative algorithms, it is now possible to integrate mechanistic models with classifiable big data into a useful framework of digital twins of the AM processes [30,31]. Construction of these digital twins of AM is just beginning. When adequately tested for specific applications, digital twins would shrink the parameter space for trial and error testing, reduce development cost and shorten the lead-time between design and certification.

By exploring the methods and results of the various mechanistic models, this review focuses on the applicability and merits of the available mechanistic models, examines the recent progress made and identifies the gaps in the modeling. In addition, the applications of the numerical models of heat transfer, fluid flow and mass transfer in the studies of various types of defects, residual stresses, distortion and the evolution of microstructure and properties are discussed. Moreover, this review critically examines the application of the numerical models to understand the printability of commonly used AM alloys. The role of modeling heat transfer, fluid flow and mass transfer in developing digital twins of AM is examined and the interrelation between the cloud based big data for AM and numerical modeling of transport processes is critically assessed. It is hoped that this review will be helpful to understand the current state of the modeling of transport phenomena in AM, the gaps in the published literature and the research needs for improved quantitative understanding of AM of metallic materials.

## 2. Transport phenomena models for AM of metallic materials

Two types of AM processes, i.e., powder bed fusion (PBF) and directed energy deposition (DED), are primarily used for metallic materials [32]. These AM processes can be distinguished further based on the primary heat source used such as laser beam (L), electron beam (EB), gas tungsten arc (GTA), plasma arc (PA), and gas metal arc (GMA). Accordingly, nomenclatures as PBF-L, PBF-EB, DED-L, DED-EB, DED-GTA, DED-PA, and DED-GMA will be followed throughout this paper. During PBF, a focused energy beam is used to selectively melt or sinter the powder particles in a powder bed and form the build layerwise. In the DED process, a high energy beam is used to generate a molten pool that fuses the added feedstock material with a substrate and previously deposited material to form the part. Only powder feedstock materials are used in PBF, whereas both powders and filler wires are used as feedstocks in DED processes.

A series of physical processes take place as fine powder particles or filler wires are melted by the heat source to build a multi-track, multi-layer AM part. These processes include the energy absorption by feedstock and substrate materials, different modes of heat transfer, formation of the molten pool, liquid metal flow within the molten pool, vaporization of alloying elements from the pool surface, solidification, and solid-state phase transformations. Modeling of physical processes based on transport phenomena is critical for the understanding of the process, structure and properties of the metallic components.

### 2.1. Mathematical representation of heat sources

A quantitative description of the energy distribution of the heat source is needed for an accurate calculation of heat transfer, solidification, deposit's geometry and its structure and properties. Their mathematical descriptions vary, and they can be broadly classified as point source, line source, power distributed over an area (i.e., surface heat flux), and power distributed over a volume (i.e., volumetric or body heat flux). The first two are exclusively used in the analytical solution of the heat conduction equation, whereas the latter two have been widely used in the numerical modeling of heat transfer and fluid flow in AM. The salient features of these heat sources and their mathematical descriptions are discussed below.

### 2.1.1. Point heat sources

Lasers, electron beams and electric arcs, commonly used as the heat source in AM, are focused on small spots. The diameter of the focused laser/electron beam and arc is of the order of 100 μm and 5 mm, respectively. However, the size can differ significantly from these values depending on the application. Zeng et al. discussed the point heat source when reviewing thermal analysis methods in selective laser melting [33]. They indicated that the solution of the heat conduction equation assuming a point heat source has been useful in laser-based manufacturing. Yang and Ayas showed that the use of a point heat source results in a higher peak temperature for the building of a 2 mm × 2 mm × 2 mm cube of Ti-6Al-4V than a surface or a volumetric heat source [34]. However, the point heat source was considerably more time efficient than the other models of heat source. Li et al. solved the heat conduction equation assuming a point heat source to model temperature field during DED-L of Ti-6Al-4V [35]. They compared measured temperatures at several locations of the substrate with the computed temperatures and showed the errors ranged from 12% to 27%.

The assumption of a point heat source has been often used for the solution of the following heat conduction equation in AM [36,37]:

$$\rho C_p V\frac{\partial T}{\partial x} = \nabla(k(T)\nabla \mathrm{T}) \tag{2.1}$$

where ρ is density, $C_p$ is the specific heat, $V$ is scanning speed, $T$ is temperature, and $k$ is thermal conductivity. The simplification of a point heat source reduces the complexity to account for the distribution of energy and allows a closed-form analytical solution to estimate the temperature field in three-dimensions. For example, one such analytical solution of the heat conduction equation with the moving point heat source is given as [36,37]:

$$T = T_0 + \frac{q(x)}{4\pi k\sqrt{x^2+y^2}}e^{\frac{-V\sqrt{x^2+y^2}+x}{2D}} \tag{2.2}$$

where $D$ is the thermal diffusivity, which is equal to $k/(\rho\ C_p)$. The heat source is located at $x = 0$ and $y = 0$ and at this point, the temperature is infinite because the distance from the heat source appears in the denominator of the above expression. The small focal area of the heat source that motivates the use of a point source also results in unrealistically high values of temperature close to the point source [38] and erroneous values of temperature gradients and other parameters computed from the temperature field.

Eq. (2.2) which is sometimes referred to as the Rosenthal solution is widely used because of its simplicity. However, the errors in calculations using equations similar to Eq. (2.2) do not originate only from the erroneous dimensions of the heat source. The governing equation of heat transfer, Eq. (2.1), considers heat conduction as the only mechanism of heat transfer and ignores convective heat transfer which is the dominant mechanism of heat transfer in the molten pool. There are many examples of the ill effects of heat conduction equation in the literature. For example, Svensson et al. [39] indicated that the "…the heat conduction equation has been found to be inadequate in representing experimental cooling curves" and recommended use of empirical equations instead of using the Rosenthal solution. Since the heat conduction equation does not allow mixing of hot and cold fluids in the molten pool, it predicts unrealistically high temperature gradients and cooling rates. Furthermore, the shape and size of the molten pool are known to be significantly affected by the presence of surface-active elements such as sulfur, oxygen, selenium and tellurium, because these elements alter the flow pattern of liquid metal and the resulting transport of heat within the molten pool [40,41]. The role of such surface-active elements in alloys cannot be calculated by heat conduction models because the flow of liquid metal is ignored. Heat conduction calculations are useful for back of the envelope calculations of relative values of parameters for qualitative assessment as long as the deficiencies are fully appreciated.

### 2.1.2. Line heat sources

The application of the point heat source can be further extended to a line heat source in cases where the nature of heat transfer is predominantly two-dimensional and perpendicular to the source. Such a situation often prevails with heat sources of high power density that leads to instant melting and pronounced vaporization under the heat source forming a deep and narrow vapor cavity known as the keyhole [42].

In some cases, this type of interaction between the heat source and material has been investigated by a solution of the heat conduction equation with a line heat source. The quasi-steady state temperature distribution is given by the following equation [43]:

$$T - T_0 = \frac{q}{2\pi kd}e^{\frac{-Vx}{2D}}K_0\left[\frac{-Vr}{2D}\right] \tag{2.3}$$

where $T$ is the temperature, $T_O$ is the initial temperature, $q$ is the absorbed power, $k$ is the thermal conductivity, $D$ is the thermal diffusivity, $d$ is the plate thickness, $K_O$ is the modified Bessel function of second kind and zeroth order, $V$ is the scanning speed, $x$ is the distance from the moving line source along the scanning direction and $r$ is the distance from the heat source to the location where the temperature is calculated.

When a keyhole forms, calculations considering a line heat source are more appropriate than the point source [42,44]. This is demonstrated in electron beam [45] and laser beam [46,47] partial-penetration and full-penetration welds in low-carbon steel [45], aluminum alloys [45], 304 SS [45,46] and a nickel-based superalloy [47]. Line heat sources of variable lengths were used to simulate step-wise filling of a J-groove in multi-pass welding to quickly compute temperature field for a subsequent residual stress analysis [48]. The analytical heat conduction model with a line heat source is also used in simulating PBF-EB to estimate solidification parameters such as temperature gradient and cooling rates [49]. However, as has been discussed in the previous section, heat conduction calculations ignore mixing of hot and cold liquids and provide inaccurate temperatures, temperature gradients and other parameters derived from the temperature field. They also cannot elucidate the role of surface-active elements such as sulfur and oxygen in steels on the molten pool shape and size.

### 2.1.3. *Surface heat sources*

For many heat sources, the power intensity varies as a function of radius from the beam axis. This radial variation cannot be defined in point or line heat sources. For the conduction mode AM, the heat input can be described by a Gaussian distribution as a function of distance from its center. Such surface heat flux distributions have been measured for lasers, electron beams and electric arcs and commonly found to follow the following axisymmetric Gaussian profiles [50]:

$$P_d = \frac{f \in P}{\pi r_b^2} exp\left(-f\frac{r^2}{r_b^2}\right) \tag{2.4}$$

where $f$ is the power distribution factor, $\in$ is the energy absorptivity, $P$ is the gross power of the heat source, $r_b$ is the radius of the heat source, and $r$ is the radial distance of a surface point to the heat source axis. The typical value of the distribution factor varies from 1 to 3; a higher value indicates a more focused power density near the beam axis and, as a result, a higher peak temperature underneath the beam. Fig. 2.1 compares the power density distributions for a 500 W heat source with a 1 mm radius using distribution factors of 1, 2, and 3. Depending on the nature of the heat source (e.g., laser beam), the power density distribution can also be nearly uniform which is commonly called a top hat power distribution [50].

### 2.1.4. *Volumetric heat sources*

In a powder bed, the absorption of a focused laser or electron beam is not limited to its surface because of the multiple reflections of the beam within the bed. In powder feeding systems such as DED-L, the powders are preheated as they travel through the beam and the preheat of the powders needs to be considered for an accurate thermal simulation. Mechanistic modeling of the heat source requires consideration of the important physical processes that are specific to the individual AM processes, which is presented in the text to follow.

*2.1.4.1. Heat sources for powder bed fusion.* In PBF-L processes, the absorption of laser energy is markedly enhanced due to the multiple times of reflection and absorption between particles on the powder bed [51]. On the other hand, in PBF-EB, electrons dissipate their kinetic energy into thermal energy over a small volume, the depth of which depends on the density and atomic number of the alloying elements [52]. Moreover, both beams are energy-intensive, forming a deep keyhole in many cases. With the presence of a keyhole, the heat input can be approximated as a volumetric heat source which is axisymmetric about the beam axis. Such a heat source was shown to accurately simulate the most important metallurgical variables in a PBF-L system [52]. The power density distribution of the heat source can be expressed by the following equation which considers the laser power ($P_L$), laser beam radius ($r_b$)

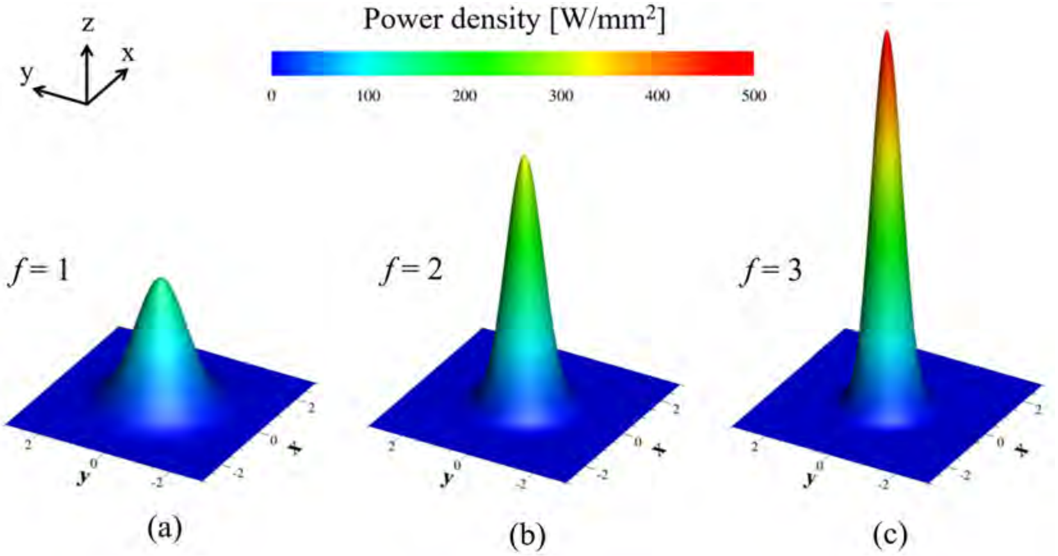

**Fig. 2.1.** Comparison between power density distributions for a 500 W heat source with a 1 mm radius using distribution factors of (a) $f = 1$, (b) $f = 2$, and (c) $f = 3$.

and power distribution factor ($f$):

$$S_v = \frac{f \in P}{\pi r_b^2 d_L} exp\left(-f\frac{(x^2+y^2)}{r_b^2}\right) \tag{2.5}$$

where $x$ and $y$ are the distances to the axis of the laser beam, and $d_L$ is the powder layer thickness. The symbols $\in$ and $f$ are the same as those defined in Eq. (2.4). The distribution of the laser power is practically uniform along the depth of the powder layer which is typically between 30 and 200 μm [1]. For PBF-L, the laser absorptivity is high inside the powder layer due to the multiple reflections of the laser beam prior to melting. However, as the powder melts the absorptivity drops to the Fresnel absorptivity [50].

Eq. (2.5) may also be used for an electron beam heat source by replacing the laser power with the power of the electron beam which is equal to the product of the current and the accelerating voltage. Typically a Gaussian distribution about the beam axis is used for EB power distribution [52,53], meaning that in Eq. (2.5) $f$ is equal to 2 and $r_b$ is the electron beam waist, i.e., the beam radius that contains 86.5% of the total power. A more sophisticated numerical approach for calculating electron collisions and the resulting power distribution has also been used [54]. Notably, this numerical approach shows similar results for the volumetric distribution of the heat source compared to existing empirical or analytical results, even when considering the effect of individual powder particles in PBF-EB.

Some recent work showed that a significantly depressed region of the molten metal may be present underneath the laser beam during PBF-L, as shown in Fig. 2.2 [22]. This depression may not be strictly defined as a keyhole. Rather, it is an intermediate state between keyhole mode melting and conduction mode melting. In such a case, a volumetric heat source is preferable to a point, line or surface heat source. Experimental observation of the transverse cross sections of the fusion zone provides a clear indication of the conduction mode and the keyhole mode of AM as shown in Fig. 2.3(a) and Fig. 2.3(b), respectively. Surface and line heat sources have been used for the simulation of these modes of AM. However, for situations intermediate between the keyhole and conduction modes of AM shown in Fig. 2.2, appropriate volumetric heat sources can provide the correct geometry of the fusion zone.

*2.1.4.2. Heat sources for directed energy deposition.* In the powder feeding DED, the metal particles are heated during flight prior to their impingement to the depositing surface. The extent of heating of the particles depends on the residence time of the particles, particle size, gas velocity, material properties and laser power density [17,18]. The temperature rise of the particles during their flight can be estimated from the approximate heat balance [17,18]:

$$\Delta T = \frac{\eta_m\ \eta_s\ \frac{\mathrm{P}}{\pi \mathrm{r}_\mathrm{b}^2}\ (2\pi r_p^2)\tau}{(\frac{4}{3}\pi \mathrm{r}_\mathrm{p}^3)\ C_P\ \rho_p} \tag{2.6}$$

where $\Delta T$ is the average in-flight temperature rise of the powder particles, $P$ is the laser power, $r_b$ and $r_p$ are the laser beam radius and the average radius of the particles, respectively, $C_P$ is the specific heat, $\eta_m$ is an interference factor to account for shielding of some particles from the laser beam by other particles, $\eta_s$ is the fraction of available laser power absorbed by the solid particles, $\tau$ is the time of flight, and $\rho_P$ is the density of the particles. The expression is based on the assumption that the absorption of the laser beam occurs on one half of the total surface area $2\pi r_p^2$ which is exposed to the heat source during flight. The calculation of the energy absorbed by the powders should further consider the latent heat of fusion if the heated powder particles are melted during flight.

A significant portion of the heat source energy, which remains after heating the powder particles, irradiates directly on the deposit. The extent of energy absorbed by the deposit surface depends on beam characteristics, the nature of the deposit and the shielding gas [1,17,18]. The total amount of heat absorbed by the depositing surface, $P_s$, is given by [17,18]:

$$P_s = \eta_l(1 - \eta_P)P \tag{2.7}$$

where $\eta_p$ and $\eta_l$ are the fractions of the laser power absorbed by the powder and the growing layer, respectively. The value of $\eta_l$ depends on both time and local temperature of the deposit. The energy absorbed by the powder and the depositing layer is considered as a spatially dependent volumetric heat flux as follows [17,18]:

$$q_{VL} = \frac{fP}{\pi r_b^2 d_L}[\eta_P + \eta_l(1 - \eta_P)]\ exp\left(-f\frac{r^2}{r_b^2}\right) \tag{2.8}$$

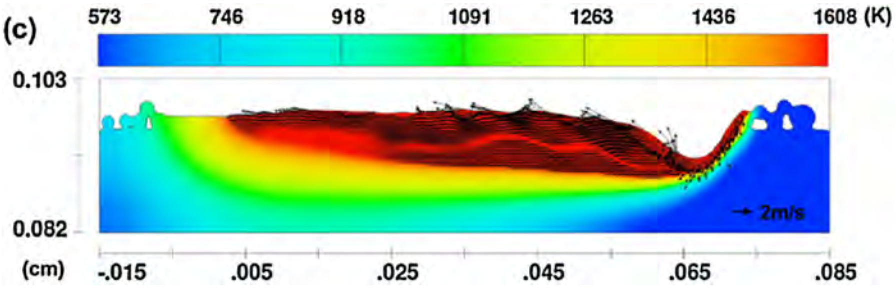

**Fig. 2.2.** Temperature and velocity fields with a depression at the front of the molten pool in the longitudinal section during PBF-L [22].

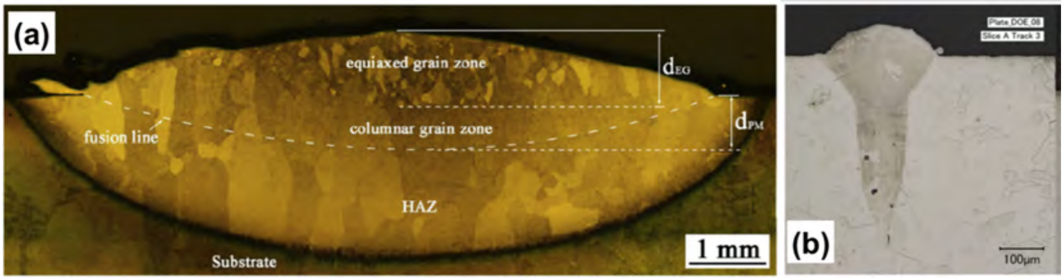

**Fig. 2.3.** (a) Conduction mode melting by DED-L of titanium alloy TC11 [73], (b) Keyhole mode melting by PBF-L of SS316L [76].

where $\eta_p$ is the fraction of laser energy absorbed by the powder during flight, $P$ is the laser power, $f$ is the laser energy distribution factor, $d_L$ is the layer thickness, and $r$ is the radial distance from laser beam axis. The two terms within the square brackets represent the fraction of laser energy transferred to the particles during their flight and the direct heating by the beam on the deposit surface, respectively. The exponential term represents the spatial variation of heat source energy as a function of distance from the axis of the beam.

In the DED-GMA process, the filler wire absorbs heat in a manner similar to that for a consumable electrode in fusion welding processes. The wire is sometimes preheated by resistive or inductive heating or using a secondary heat source to enhance heat input and increase melting rate. A volumetric heat source is typically used to model the DED-GMA process [55]. In DED-GMA, the energy from the hot metal droplets is distributed inside the fusion zone. This energy from the droplets can be assumed to uniformly distribute in a small cylindrical region (cavity) underneath the melting filler wire [56]. The magnitude of the volumetric heat source, $q_{VA}$, is calculated from the following equation [56]:

$$q_{VA} = \frac{H_d}{\pi h_e r_e^2} \tag{2.9}$$

where $H_d$ is the heat content of the droplets, and $h_e$ and $r_e$ are the effective height and radius of the cylindrical cavity, respectively. The heat content of the droplets is calculated from the average temperature of the droplet [57].

$$H_d = \rho\, \pi\, r_w^2\, w_f\, [C_P\, (T_d - T_a) + \Delta H] \tag{2.10}$$

where ρ is the density of the liquid droplets, $r_w$ is the wire radius, $w_f$ is the wire feed rate, $C_P$ is the specific heat, $T_d$ is the droplet temperature, $T_a$ is the ambient temperature, and $\Delta H$ is the latent heat. The dimensions of the cylindrical cavity are estimated by equating the total work done in creating the cavity and the kinetic energy of the droplets. Both the work done against the hydrostatic pressure and that in increasing the surface area are considered for the estimation of the total work done [58].

*2.1.4.3. Double ellipsoidal models.* The mathematical representations of heat sources are often simplified to make complex calculations tractable. For example, models for the calculation of residual stresses and distortion often require days of calculations in a fast computer using crude calculations of temperature field based on a simple heat conduction model. Although advanced calculations of residual stresses and distortion considering convective heat transfer are emerging [26–28], they are rare exceptions rather than the norm for the simulations of AM and welding.

The double ellipsoidal asymmetric distribution of power density of the heat source [58], proposed in early 1980s to model the heat flow in welding, has been used by many researchers in welding and AM. The fusion zone of welds and AM commonly exhibits a tear drop shape because of the motion of the heat source and the flow of liquid metal within the molten pool. The computed temperature fields need to be consistent with the experimentally determined fusion zone shapes and sizes for various heat inputs. The specified power distribution significantly affects the computed temperature distribution and the fusion zone shape and size. The measured power density distribution of all commonly used heat sources such as an electric arc or a laser beam is axisymmetric about the beam axis when the heat sources impinge on a flat surface and do not conform to the asymmetric double ellipsoidal power distribution. Why then is the double ellipsoidal heat source distribution widely used? When a realistic axisymmetric distribution of power density is used in heat conduction calculations, the computed results do not agree with the experimental fusion zone shape and size. The difficulties arise because the convective heat transfer which is the main mechanism of heat transfer, within the fusion zone is ignored in these calculations. To address the mismatch, heat is artificially distributed along the length, depth and width directions of the source to partially correct the erroneous pool shape obtained from heat conduction calculations.

The empirical double ellipsoidal power density distribution does save computational time but does not in any way compensate for the failure to consider heat transfer by convection. In summary, the use of empirical heat sources for heat conduction calculations results in three types of serious errors. First, a diversity of fusion zone shapes for various process parameters that have been reported in the literature cannot be predicted by the heat conduction models. Second, the pronounced role of surface-active elements such as sulfur and oxygen in steels cannot be calculated by heat conduction models. Finally, failure to consider mixing of hot and cold fluids results in erroneous temperature gradients, cooling rates, solidification parameters and all other variables that are affected by the temperature field.

### *2.2. Modeling heat absorption*

In AM, the laser, electron beam, and electric arc are the three common sources of energy. The mechanism of heat absorption depends on the type of feedstock, liquid metal in the molten pool and solid part. In addition, various feedstocks such as powder and wire absorb heat differently. Therefore, an understanding of absorption of heat from the three main heat sources are critical for successful modeling of AM processes. This section provides a discussion of the modeling of heat absorption of these heat sources for different AM process and feedstock combinations.

#### *2.2.1. Laser heat source*

In powder feeding DED processes, the powder particles absorb heat in two stages. First, heat is absorbed by the powder during their flight from the nozzle to the substrate. This in-flight heating of the particles depends on the type, shape, size and speed of the powders, beam characteristics, and the shielding gas, and it is incorporated in the modeling of volumetric heat source as described in Section 2.1.4. The published literature reports significant loss of beam energy due to attenuation and in-flight pre-heating of powder particles in DED-L of various alloys [59,60]. Combining the energy reflected by the in-flight powder particles and the energy loss due to heated powder particles not being captured into the molten pool, 15–20% of the supplied laser power was lost [59]. Second, after the flight, the heated powder particles on the substrate absorb heat and melt to form the molten pool. This absorbed heat depends on the absorptivity of the powder particles and is incorporated in the surface or volumetric heat source for modeling the laser beam [59,60].

The absorptivity depends on the laser wavelength, nature of the material surface, local temperature of the material, and nature and size of the plasma present above the molten pool [59]. The dependence of the absorptivity of different metallic materials on the laser wavelength is shown in Fig. 2.4 [61]. It shows that the laser energy absorptivity varies significantly for metals and alloys. For example, the energy absorption rate of the Nd:YAG laser with 1060 μm wavelength for aluminum is around 5%, which indicates that 95% of the energy is lost and not actually used to heat the material [61]. In contrast, the fiber laser absorptivity for steels is significantly higher than that for aluminum, copper and precious metals such as silver and gold. However, depending on the surface roughness and impurities, the laser absorptivity of aluminum could be as large as ~35%, which is significantly higher than the value indicated in Fig. 2.4 [62]. The absorptivity of Ti was reported as 0.39 for laser wavelength of 1 μm and 0.45 for laser wavelength of 0.45 μm [63].

In powder bed processes, the absorption of heat depends on inter-reflection of the laser beam among the powder particles. Both direct measurement and numerical modelling were used to assess the real-time laser absorptivity [4,63]. Since the net amount of laser energy absorbed increases with each reflection and subsequent absorption, depending on the packing efficiency of the powder bed, the absorptivity can be significantly higher than that of a flat surface or just a single powder particle. This effect of inter-reflection of laser beam on heat absorption is modeled using ray-tracing simulations [5,51,64–67] where absorptivity is calculated based on the incident angle of the laser beam, powder particle size, packing efficiency of the powder bed, and optical properties of the laser beam. It has been shown that depending on the packing efficiency the absorptivity of the powder bed can be greater than the absorptivity of a flat surface of the same material. For example, the powder bed absorptivity has been shown to be 6 times greater for silver and gold, and around twice for stainless steel and titanium than the flat surface [4]. However, for simplicity, in many models [4,68] the effect of inter-reflection is considered just by enhancing the absorptivity values in the volumetric heat source for the laser beam as described in Section 2.1.4. Note that the real-time monitoring of laser energy absorptivity using approaches such as calorimetric measurements is also important, considering the complex shape, surface condition, and refractive index of the alloys that cannot be completely incorporated in the numerical models [4,69].

For wire based DED processes, the filler wire is irradiated by the laser beam and the wire tip is fed into the molten pool [70–72]. However, there is no quantitative study of the laser energy absorptivity by the filler wire considering the characteristics such as the wire feeding angle and rate.

The heat absorption rate changes drastically as soon as the feed-stock melts and forms a molten pool. The absorptivity of the laser beam by the molten pool is generally considered as the Fresnel absorptivity. The absorption of heat inside the molten pool has a

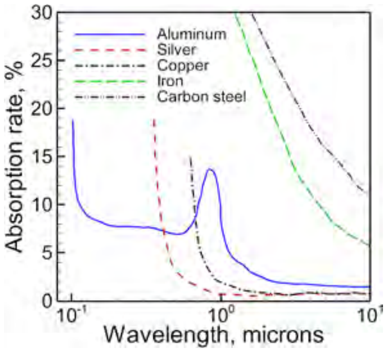

**Fig. 2.4.** Absorptivity of laser energy for various materials, plotted based on the data available in [61].

significant effect on the shape of the molten pool. Fig. 2.5 shows that laser processing can take place in the conduction, keyhole or mixed modes depending on the laser power intensity [73,74]. Generally, for DED processes, the power intensity is less because of the large spot size of laser beam used. That results in the conduction mode with a low depth to width ratio of the molten pool as shown in Fig. 2.3(a). The laser beam is absorbed only once and the remaining energy is reflected from the pool surface. Consequently, the laser energy is mainly transported from the surface into the interior of material through heat conduction and melt convection. However, in PBF processes, often due to very small laser spot size, vaporization of alloying elements takes place on the pool surface. The resulting recoil force severely depresses the liquid metal, forming a deep cavity, or keyhole [75,76], which is full of volatile vaporized alloying elements. The mechanism of heat absorption in the keyhole mode involves bouncing of the beam within the keyhole surfaces in multiple locations. In each location a portion of the beam is absorbed and the remaining portion is reflected. Because of the deep geometry of the keyhole and multiple reflections of the beam, a high value of the overall absorptivity often exceeding 80% is achieved [77,78]. The molten pool in the keyhole mode has a very high depth to width ratio as shown in Fig. 2.3(b). However, laser based PBF processes in conduction mode are common and widely reported in the literature [68,78].

The laser absorptivity in both PBF and DED processes are significantly affected by various factors including the characteristics of the energy sources and the materials. Although a few calorimetric measurements of the laser absorptivity values are now available in the published literature [4], real-time experimental measurements of these values as a function of the above-referenced factors remain critically needed for AM processes.

### 2.2.2. Electron beam heat source

In electron beam AM processes, electrons are generated in a gun accelerated by an electric potential up to approximately 100 kV [79]. Electromagnetic lens focuses the electron beam to achieve high energy densities used to melt the metal feedstock. Compared to the mechanically driven mirrors used in laser-based systems, electromagnetic lens enables faster scanning speeds, on the order of 10 m/s [80]. Since the electron beam based AM is performed in vacuum ($\sim 10^{-4}$–$10^{-5}$ Torr), vaporization of elements and keyhole formation are very common [81]. However, depending on the scanning speed, the conduction mode PBF-EB can also be possible [82].

In the PBF-EB process, the packing of a powder layer is followed by an immediate pre-sintering step during which a defocused beam is used to scan rapidly over the powder bed to sinter the particles together. This increases mechanical, thermal and electrical connections between the powder particles, which is necessary to prevent the electrostatic repulsion of powder particles from the bed due to the negative electrical charge buildup in individual particles, a phenomenon commonly referred to as “smoking” [24]. This pre-sintering step is unnecessary in DED-EB due to the use of a wire feedstock [83].

Once the electrons impact the atomic nuclei of the feedstock material, the kinetic energy of the electrons largely transforms into thermal energy over a distance on the order of several micrometers [80]. The energy dissipation of the incident electrons is a function of the power, the atomic number of the material, and the incident angle of the beam [80]. Some of the initial energy is lost through backscattered electrons, which emits back out of the material into the surroundings. Electron beam welding literature estimates that up to 40% of the input power can be lost to those electrons [52] for metals typically found in AM alloys. However, the lost energy due to backscattered radiation will be less for cases where a keyhole forms due to metal vaporization, because backscattered electrons emitted from the keyhole wall will be largely reabsorbed by the material [53].

### 2.2.3. Arc heat source

The feedstock materials are melted through the arc energy during arc based DED processes. Depending on the type of the arc, there are three major variants of arc-based DED (DED-A) which are DED-GTA, DED-PA, and DED-GMA, respectively [1]. The electrode is non-consumable in DED-GTA and DED-PA, and thus an external filler wire is needed and fed separately as the feedstock material. In contrast, the consumable electrode is the filler wire itself in DED-GMA, which can be fed coaxially with the arc through the torch [71]. The absorption of heat by the wire feed stock depends on the alloy, arc temperature, surface finish of the wire and metal transfer mode.

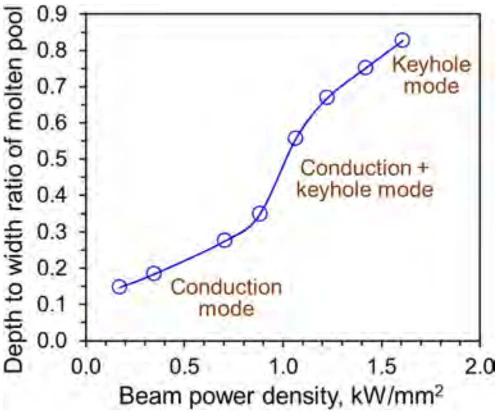

**Fig. 2.5.** Identification of the three modes in laser welding. Adapted from Buvanashekaran et al. [74].

An electric arc is established between the electrode and the substrate during DED-A, which serves as the heat source. The arc can be divided into three regions, i.e. the anode, the cathode and the arc column [84]. Depending on the different variants of DED-A, the electrode and the substrate serve as the anode and the cathode, respectively, or vice versa. The arc column is electrically neutral on macroscopic scales and is composed of neutral atoms, electrons and positive ions. Electrons are emitted from the cathode, traveling through the arc column, and condensed at the anode. Ions travel along a reversed path, i.e. from the anode to the cathode through the arc column [84]. Significant amount of energy is released from the arc due to the agitated activities of the particles. Both the filler wire and the substrate or solidified deposit are heated and melted by the arc.

The characteristics of the arc are determined by major variables including the polarity of the electrode, the arc voltage and current, arc length as well as other external factors such as shielding gas composition and wire diameter [85]. Tungsten is commonly used as the non-consumable electrode during GTA, and oxides such as thoria can be added to have better electron emissivity, current-carrying capacity, and contamination resistance. The absorption rate of the arc energy is usually among 60%~80% for GTA processes [86]. The consumable filler wire is melted during GMA, with three common modes of metal transfer, i.e. globular, spray, and short-circuiting, depending on the interactions between the arc and the tip of the filler wire [86]. Because of the considerable amount of heat transported by the liquid metal from the filler wire to the molten pool, the energy efficiency is typically over 80% during the GMA process [86]. The arc heat absorption by the molten pool is similar to that for laser and electron beam based processes. Conduction mode melting is generally observed in arc based DED processes using GTA and GMA due to the large size and thus low power intensity of the arc source [87]. However, DED-PA can operate in keyhole mode due to the highly concentrated arc energy [88].

### 2.3. *Heat transfer and fluid flow*

Despite of the large varieties of the heat sources and feedstock materials, the transport processes of heat, mass, and momentum of different AM techniques share significant similarities. Solution of the equations of conservation of mass, momentum and energy for PBF and DED based AM processes is essential to examine the quantitative relations between process parameters and important metallurgical variables such as the cooling rates, temperature gradients and fusion zone geometry that affect the microstructure and properties of the fusion zone.

The liquid metal undergoes a considerable recirculating motion driven mainly by the spatial gradient of surface tension and this convection is a major mechanism of heat transfer within the fusion zone. Additionally, in wire based DED, fluid flow is affected by the momentum of mass transferred from the molten wire typically in the form of droplets. Lorentz forces [86] from electric heat sources such as an arc can also drive fluid flow. As a result, solution of the velocity field in the fusion zone is a prerequisite for an accurate calculation of heat transfer in AM.

#### 2.3.1. *Governing equations*

The heat transfer and fluid flow analysis in the molten pool and its surroundings commonly follows the conservation equations of mass, momentum and energy in transient form in Cartesian coordinate as [1,17]:

$$\frac{\partial(\rho u_i)}{\partial x_i} = 0 \tag{2.11}$$

$$\frac{\partial(\rho u_j)}{\partial t} + \frac{\partial(\rho u_j u_i)}{\partial x_i} = \frac{\partial}{\partial x_i}\left(\mu \frac{\partial u_j}{\partial x_i}\right) + S_{uj} - K_P \frac{(1-f_L)^2}{f_L^3 + B_N} u_j \tag{2.12}$$

$$\rho\frac{\partial h}{\partial t} + \frac{\partial(\rho u_i h)}{\partial x_i} = \frac{\partial}{\partial x_i}\left(\frac{k}{C_p}\frac{\partial h}{\partial x_i}\right) - \rho\frac{\partial \Delta H}{\partial t} - \rho\frac{\partial(u_i \Delta H)}{\partial x_i} + S_h \tag{2.13}$$

where ρ is the density, $u_i$ and $u_j$ are the velocity components along the $i$ and $j$ directions, respectively, $x_i$ is the distance along the $i$ direction, $t$ is the time, $\mu$ is the viscosity, $S_{uj}$ is the source term for the momentum equation that includes the driving forces for fluid motion described later in Section 2.3.2, $h$ is the sensible heat, $C_p$ is the specific heat, $k$ is the thermal conductivity, $\Delta H$ is the latent heat content, and $S_h$ is the source term for the energy transfer that includes the volumetric heat sources. Detailed explanations on Eqs. (2.11)–(2.13) are documented in published literature [1,17]. The molten material is considered incompressible and Newtonian, and a laminar flow is commonly assumed in the molten pool.

The variables in Eq. (2.13) depict the total enthalpy that is the sum of the sensible heat ($h$) and the latent heat content ($\Delta H$). The temperature values are calculated from this enthalpy by using the specific heat of the alloy. The last term on the right-hand side of Eq. (2.12) is obtained from the Carman-Kozeny equation that accounts for the frictional dissipation of flow velocity in the mushy region [17]. The term $f_L$ refers to the liquid fraction, $K_P$ is a permeability coefficient, and $B_N$ is a small numerical constant introduced to avoid division by zero when $f_L = 0$. The liquid fraction is assigned following the computed local temperature ($T$). For instance, $f_L = 1$ when $T \geq T_L$, and $f_L = 0$ when $T \leq T_S$, and, $f_L$ varies linearly from 0 to 1 as $T$ increases from $T_S$ to $T_L$ [89]. This enthalpy-porosity formulation has the advantage that it does not require an explicit tracking of the location of liquid/solid interface nor does it require imposing any boundary condition at such interface.

#### 2.3.2. *Driving forces for fluid motion*

In the momentum conservation Eq. (2.12), $S_{uj}$ is used to account for the forces that drive the motion of liquid metal in the fusion zone. In general, the most important force for the fluid motion is the Marangoni force which arises because of the spatial variation of interfacial tension on the surface of the fusion zone. Additionally, when an electric arc is used as the heat source, momentum from the droplet transfer becomes an important driver of the fluid flow. The interaction between the arc current and the magnetic fields induced by the current results in the electromagnetic force that also contributes to convection of the liquid metal. The spatial variation of temperature and density also results in a gravitational force which can be neglected in most cases because it is much weaker than the other forces [20].

*2.3.2.1. Marangoni force.* In most heat transfer fluid flow models, the Marangoni shear stress is imposed on the top surface of the molten pool as a boundary condition for the momentum conservation equation (also refer Section 2.3.4):

$$\frac{d\gamma}{dT}\cdot\frac{dT}{d\vec{s}} = \mu\frac{\partial u_s}{\partial \vec{n}} \tag{2.14}$$

where $\frac{d\gamma}{dT}$ is the temperature coefficient of surface tension ($\gamma$), $\frac{dT}{d\vec{s}}$ is the temperature gradient along a surface tangential direction $\vec{s}$, $\mu$ is the viscosity, $u_s$ is the surface velocity along $\vec{s}$, and $\vec{n}$ is the surface normal direction. The right-hand side in Eq. (2.14) is the viscous shear stress for a Newtonian fluid. An accompanying boundary condition for such a steady-state or quasi-steady surface profile is $u_n = 0$, i.e., the velocity normal to the surface is equal to zero.

Apart from the models where the Marangoni force is applied as a boundary condition on the flat or curved top surface of the molten pool, there are models that explicitly track the transient evolution of molten pool surface using methods such as volume of fluid (VOF). In such models, the implementation of the above boundary conditions requires special methods. For example, the surface force can be converted to a body force and included in the source term ($S_{uj}$) in the momentum equation Eq. (2.12). One such method is the continuum surface force (CSF) model developed by Brackbill et al. [90].

Surface tension is temperature-dependent and therefore varies spatially on the surface of the fusion zone. This variation of surface tension drives the fluid flow tangential to the pool surface, commonly known as the Marangoni flow. For pure metals, increasing temperature leads to a decrease in surface tension, and this trend holds for most alloys [91]. The region of the molten pool directly under the heat source will have the highest temperature, typically causing liquid to be pulled to the sides of the pool which has a lower temperature and consequently higher surface tension. However, some alloying elements in steels and nickel alloys, particularly sulfur, selenium, nitrogen and oxygen, can affect how the surface tension changes with both temperature and the concentration of these elements [22]. The manner in which the surface tension varies with temperature can significantly affect the direction of fluid flow within the fusion zone and its geometry [41].

*2.3.2.2. Lorentz or electromagnetic force.* Another body force that can be included as a source term in momentum conservation equation is the Lorentz (or electromagnetic) force that arises when an electric current is used, such as in the case of PBF-EB, DED-EB and DED-A. This force is given as:

$$F^{emf} = \vec{j} \times \vec{B} \tag{2.15}$$

where $F^{emf}$ is the electromagnetic force, $\vec{j}$ is the current density vector, and $\vec{B}$ is the magnetic flux vector. A widely employed method to calculate $F^{emf}$ in the welding literature is the analytical expression derived by Kou and Sun by solving Maxwell's equations in an axisymmetric coordinate system with Magneto-hydrodynamics (MHD) approximation [92]. It can also be estimated by solving Maxwell's equations numerically [93].

*2.3.2.3. Droplet and powder impact force.* For DED processes such as DED-L and DED-A, where a feedstock material is actively deposited into the molten pool, there is a force generated by liquid droplets or powder particles impacting the molten pool. Such impact can be modeled considering the transient evolution of the pool surface (such as by the VOF method) if the droplet size, temperature and impact velocity can be specified. For GMA-based processes, this can be done by direct calculation of the droplet [94] or by approximation of the droplet impact as a force on the molten pool surface [95]. A similar approach of calculating individual droplet impact force has been used for modeling the powder based DED-L process [96], by considering the impact force of the droplets. However, the impact force of the powder particles is typically ignored [97] due to the smaller size of the metal powder compared to the metal droplets formed in DED-GMA.

*2.3.2.4. Buoyancy force.* The buoyancy force is commonly treated using the following Boussinesq approximation [98]:

$$F^b = \rho_L\, g\, \beta_L\, (T - T_{ref}) \tag{2.16}$$

where $F^b$ is the buoyancy force, $\rho_L$ is the liquid metal density at the reference temperature $T_{ref}$, $g$ is the gravitational acceleration, $\beta_L$ is the linear thermal expansion coefficient, and $T$ is the liquid metal temperature. The effect of buoyancy force on convection is much weaker compared to other driving forces (e.g., the surface tension force) [20].

*2.3.2.5. Recoil force.* Because of the high temperature during AM, a significant vaporization of alloying elements takes place. The vaporization results in a downward force acting upon the molten pool surface, known as the recoil force [99,100]. This recoil force causes a depression near the axis of the heat source, where the power intensity, temperatures, and vapor pressures are the highest. Depending on the magnitude of the force, the local deformation of the liquid surface may be significant. When the pressure imposed on the molten pool by the recoil force is sufficiently large, a keyhole forms and alters the interaction between the heat source and the deposit or substrate material. Moreover, if the recoil force is greater than the surface tension force, then ejection of material from the molten pool can occur and both mass and energy are lost from the pool. The pressure exerted by the recoil force can be calculated using the following analytical equation [22,101]:

$$p_R = 0.54\ p_0\ exp\left(\frac{\Delta H_v (T - T_v)}{R_g T T_v}\right) \tag{2.17}$$

where $p_0$ is the atmospheric pressure, $\Delta H_v$ is the enthalpy of metal vapor, $T$ is the surface temperature of the molten pool, $T_v$ is the boiling temperature, and $R_g$ is the universal gas constant. The main influential factors for the recoil pressure include the local energy density, the thermal conductivity of the material, and the equilibrium vapor pressure of the alloying elements.

### 2.3.3. Geometry of the free surface

For modeling the molten pool fluid flow, the profile of the pool surface is not known *a priori* and varies with time. The molten pool surface must be determined explicitly to apply appropriate boundary conditions. This problem, commonly referred to as fluid dynamics with moving boundaries [102], can be solved by two groups of numerical methods. The first group is the interface capturing method such as the boundary fitted grid where a set of grids moves with and exactly fits the interface [103]. While it allows an accurate application of boundary conditions at the interface, it is difficult to consider the breakup and coalescence of fluids by this method, making it impractical to simulate the molten pool in AM (for instance, fusing of multiple particles into the pool). The second group is the interface tracking methods used with a set of fixed grids, among which the most widely used one is perhaps the VOF method [104]. In this method, the following conservation equation of fluid fraction is solved:

$$\frac{\partial f_l^v}{\partial t} + \frac{\partial (u_i f_l^v)}{\partial x_i} = 0 \tag{2.18}$$

where $f_l^v$ is the fluid volume fraction ($0 \leqslant f_l^v \leqslant 1$) and not to be confused with the liquid fraction $f_L$ defined previously. The term $f_l^v$ defines the volume fraction of a cell occupied by fluid (either liquid or solid). Specifically, $f_l^v = 0$ indicates a void cell where no fluid is present, $f_l^v = 1$ depicts a liquid cell completely occupied by the fluid, and $0 < f_l^v < 1$ refers to an interface cell containing the molten pool interface. The VOF equation is solved concurrently together with the conservation Eqs. (2.11)–(2.13) to obtain the fluid volume fraction distribution. Next, the fluid fraction of neighboring cells is used to construct the interface position using algorithms such as the piecewise linear interface calculation (PLIC) [105]. The boundary conditions such as surface heat flux and surface tension force can then be updated based on the new interface position and orientation.

A nuance in using VOF is the choice of single fluid versus two fluids. For PBF-L where an inert shielding gas is used, it may be tempting to choose two fluids: one for the molten metal and the other for the shielding gas. However, in many implementations of VOF, there is only one set of velocities in a grid cell shared by both liquid and gas. In other words, the liquid and gas have the same velocities in the grid cell. This implementation is prone to numerical error when there is a large difference in density and viscosity between liquid and gas. Hence, for simulating molten pool dynamics in AM, the single fluid option may be more desirable for improved numerical robustness.

The level-set method is another interface tracking approach, using a level-set function to compute the levels of the interface region [106]. The zero-level set represents the actual position of the free surface, with other level sets distributed at various distances from the interface [107]. The motion of the interface depends on the local forces acting on it. The molten metal flow was considered to determine the velocity of the interface during AM, incorporating the influences of driving forces including the Marangoni stress and surface tension [108–110]. During DED-L, the additional influence of the powder addition on the motion of the gas metal interface was incorporated through solving the coupled force and level-set functions [111]. Note that level-set method does not inherently conserve the total volume, and thus constrictions need to be developed in the model to ensure mass conservation [111,112].

The surface profile of the fusion zone can also be estimated by minimizing the total energy on the top surface of the molten pool. The total energy includes the surface energy due to the change in the pool surface area, the potential energy and the recoil force and the work performed by the arc pressure displacing the pool surface. This method assumes a continuous interface along the molten pool surface. Therefore, there is a limitation of easily calculating the breakup and the coalescence of the fluid. Detailed procedure for the calculation is available in the literature [103], and only important features are presented here.

The arc pressure ($P_a$) depends on the total arc force exerted on the top surface of the molten pool [113]. The average droplet impact force on the top surface of the molten pool depends on the droplet mass, velocity and transfer frequency [103]. The pressure due to the droplet impact ($P_d$) is essentially the impact force per unit area and is assumed to have Gaussian distribution on the top surface of the molten pool [103]. The following two equations are solved to obtain the fusion zone surface profile [103]:

$$\gamma\left\{\frac{(1+\varphi_y^2)\varphi_{xx} - 2\varphi_x\varphi_y\varphi_{xy} + (1+\varphi_x^2)\varphi_{yy}}{(1+\varphi_x^2+\varphi_y^2)^{3/2}}\right\} = \rho g\varphi + P_a + \lambda \tag{2.19}$$

$$\int (\varphi_s - z_0)dy - \frac{\pi r_w^2 w_f}{U_w} = 0 \tag{2.20}$$

Subscripts x and y in Eq. (2.19) represent partial derivative with respect to x and y, respectively, γ is the surface tension, and λ is the Lagrange multiplier. In Eq. (2.20), $r_w$, $w_f$ and $V$ are the wire radius, wire feed rate and the welding speed, respectively, and $\phi_s$ is

**Table 2.1**
Thermophysical properties of commonly used alloys in additive manufacturing. ‘T’ denotes the temperature in K which varies between room temperature to solidus temperature [1,19,115]. Density values are given at room temperature. Viscosity, surface tension and $d\gamma/dT$ are given at the liquidus temperature of alloys.

| Properties | SS316 | Ti-6Al-4V | IN718 | H13 | 800H | AlSi10Mg |
|---|---|---|---|---|---|---|
| Liquidus temperature (K) | 1733 | 1928 | 1609 | 1725 | 1675 | 867 |
| Solidus temperature (K) | 1693 | 1878 | 1533 | 1585 | 1608 | 831 |
| Thermal conductivity (W/m K) | $11.82 + 0.0106\ T$ | $1.57 + 1.6 \times 10^{-2}\ T - 1 \times 10^{-6}\ T^2$ | $0.56 + 2.9 \times 10^{-2}\ T - 7 \times 10^{-6}\ T^2$ | $18.29 + 7.5 \times 10^{-3}\ T$ | $0.51 + 2.0 \times 10^{-2}\ T - 6 \times 10^{-6}\ T^2$ | $113 + 1.06 \times 10^{-5}\ T$ |
| Specific heat (J/kg K) | $330.9 + 0.563T - 4.015 \times 10^{-4}\ T^2 + 9.465 \times 10^{-8}\ T^3$ | $492.4 + 0.025T - 4.18 \times 10^{-6}\ T^2$ | $360.4 + 0.026\ T - 4 \times 10^{-6}\ T^2$ | $341.9 + 0.601T - 4.04 \times 10^{-4}\ T^2$ | $352.3 + 0.028\ T - 3.7 \times 10^{-6}\ T^2$ | $536.2 + 0.035\ T$ |
| Density (kg/m$^3$) | 7800 | 4430 | 8100 | 7900 | 7270 | 2670 |
| Viscosity (kg/m s) | $7 \times 10^{-3}$ | $4 \times 10^{-3}$ | $5 \times 10^{-3}$ | $7 \times 10^{-3}$ | $7.5 \times 10^{-3}$ | $1.3 \times 10^{-3}$ |
| Surface tension (N/m) | 1.50 | 1.52 | 1.82 | 1.90 | 1.82 | 0.82 |
| $d\gamma/dT$ (N/m K) | $-0.40 \times 10^{-3}$ | $-0.26 \times 10^{-3}$ | $-0.37 \times 10^{-3}$ | $-0.43 \times 10^{-3}$ | $-0.40 \times 10^{-3}$ | $-0.35 \times 10^{-3}$ |

the solidified surface profile, $z_0$ is the z location of the specimen top surface. Eq. (2.19) represents the static force balance at the fusion zone surface, while Eq. (2.20) defines a constraint condition that the deposited area, $A_{FW}$, at a solidified cross section of the fusion zone is equal to the amount of feedstock per unit length. To obtain the free surface profile, both equations need to be solved. Eq. (2.20) is discretized using the finite difference method. It is then solved using the Gauss-Seidel point-by-point method for an assumed $\lambda$ with appropriate boundary conditions. The resulting free surface profile is applied to the constraint equation, and the residual (defined as the left-hand side of Eq. (2.19)) is evaluated. The value of $\lambda$ is determined iteratively using the bisection method until both Eqs. (2.19) and (2.20) are satisfied.

### 2.3.4. Boundary conditions

The surface heat flux and the heat loss can be implemented as boundary conditions of the energy conservation Eq. (2.13) as:

$$k\frac{\partial T}{\partial \vec{n}} = q - q_c - q_r - q_v \tag{2.21}$$

where $k$ is the thermal conductivity, $\frac{\partial T}{\partial \vec{n}}$ is the temperature gradient along the surface normal direction ($\vec{n}$), $q$ is the heat input from the heat source, and $q_c$, $q_r$ and $q_v$ are the heat loss by convection, radiation and vaporization, respectively. The heat loss due to radiation is given as [1,22]:

$$q_r = \sigma\varepsilon(T^4 - T_a^4) \tag{2.22}$$

where $\sigma$ is the Stefan-Boltzmann constant ($5.67 \times 10^{-8}$ W m$^{-2}$ K$^{-4}$), $\varepsilon$ is the emissivity, $T_a$ is the ambient temperature. The heat loss to the surrounding due to shielding gas flow is given as [1,22]:

$$q_c = h_c(T - T_a) \tag{2.23}$$

where $h_c$ is the convective heat transfer coefficient. The heat loss due to vaporization is given as [114]:

$$q_v = \sum_{i=1}^{n} J_i \Delta H_i \tag{2.24}$$

where $n$ is the number of the alloying elements, $J_i$ is the vaporization flux of element $i$, $\Delta H_i$ is the enthalpy of vaporization of the element $i$. The volumetric heat flux, such as that in Eqs. (2.5) and (2.9), are directly added to the source term $S_h$ in Eq. (2.13). Volumetric heating due to viscous friction of liquid metal flow and Joule heating due to electric current flow in DED-GMA are typically much smaller than the heat input from heat source and are thus ignored.

The spatial variation in pool surface temperature creates a surface tension gradient that drives the convective flow of molten metal inside the pool. The application of Marangoni stress developed due to surface tension gradient as boundary conditions has been explained in Section 2.3.2. However, for deposits with curved surface typically observed in DED processes the boundary conditions depend on the temperature gradient on the 3D curved surface along the x-, y-, and z-directions ($G_x$, $G_y$, $G_z$, respectively) [31]. The Marangoni stress at any point on the curved surface along the x-, y-, and z-directions, respectively, is,

$$\tau_x = \mu\frac{du}{dz} = \frac{d\gamma}{dT}G_x \tag{2.25}$$

$$\tau_y = \mu\frac{dv}{dz} = \frac{d\gamma}{dT}G_y \tag{2.26}$$

$$\tau_z = \mu\frac{dw}{dr} = \frac{d\gamma}{dT}G_z \tag{2.27}$$

where $T$ is the temperature, $\gamma$ is the surface tension, $\mu$ is the viscosity of the liquid metal, $r$ is the radial distance from the central axis of the heat source, and $u$, $v$, and $w$ are the velocities of the liquid metal along the x-, y-, and z-directions, respectively. Appropriate

**Table 2.2**
Thermophysical properties of common shielding gases, Argon [119], Nitrogen [118,119] and air [120]. Here 'T' represents temperature in K.

| Properties | Argon | Nitrogen | Air |
|---|---|---|---|
| Density (kg/m$^3$) at ambient temperature | 0.974 | 1.25 | 1.20 |
| Specific heat (J/kg K) | 519.16 at ambient temperature | 1040.00 at ambient temperature | $1034.09 - 0.285\,T + 0.782 \times 10^{-3}\,T^2 - 0.497 \times 10^{-6}\,T^3$ |
| Thermal conductivity (W/m K) | $\frac{-0.1125}{\sqrt{T}} + 1.35 \times 10^{-3}\sqrt{T} + 1.453 \times 10^{-7}\,T^{1.5}$ | $\frac{-0.0924}{\sqrt{T}} + 1.65 \times 10^{-3}\sqrt{T} + 5.255 \times 10^{-7}\,T^{1.5}$ | $-2.276 + 0.126\,T - 1.481 \times 10^{-4}\,T^2 + 1.735 \times 10^{-7}\,T^3$ |
| Range of temperature 'T' (K) | 300–4500 | 300–2200 | 300–1050 |

values of convective and radiative heat transfer coefficients as well as Marangoni stresses are required for an accurate calculation of the temperature field.

### 2.4. Thermophysical properties of materials

Calculations of heat, mass, and momentum transfer during AM processes require thermophysical properties of alloys such as thermal conductivity, specific heat, density, latent heat, viscosity and liquidus and solidus temperatures [114]. Properties responsible for the heat transport such as thermal conductivity and specific heat vary significantly with temperature. Therefore, an assumption of constant values of these properties may result in errors in the calculated results. In AM, the most commonly used alloys are stainless and tool steels, titanium alloys, nickel based super alloys and aluminum alloys [1]. Table 2.1 summarizes temperature dependent thermophysical properties [1,19,115] of these commonly used alloys in AM.

Special care is needed for the assignment of the thermophysical properties for each variant of the AM processes [1,17]. For example, in the PBF processes, the effective thermophysical properties of the packed powder bed depend on the shielding gas entrapped among the powder particles and the packing efficiency of the powder bed [116,117]. Table 2.2 provides the thermophysical properties [118–120] of shielding gases commonly used in AM processes. The effective density ($\rho_e$) and specific heat ($Cp_e$) of the powder bed are written as [19,121]:

$$\rho_e = \rho_s\eta + \rho_g(1-\eta) \tag{2.28}$$

$$Cp_e = \frac{\rho_s\eta Cp_s + \rho_g(1-\eta)Cp_g}{\rho_s\eta + \rho_g(1-\eta)} \tag{2.29}$$

where $\eta$ is the powder packing density of the powder bed, $\rho_s$ and $\rho_g$ are the density of the solid and gas, respectively, and $Cp_s$ and $Cp_g$ are the specific heat of the solid and the gas, respectively. The effective density of the powder bed is not strongly affected by the nature of the gas, since the density of the solid is significantly higher than the density of the gas. Therefore, for a given powder bed, the effective density is proportional to the powder packing density. However, the effective thermal conductivity of the powder bed depends significantly on the thermal conductivity of the shielding gas.

Several models have been proposed to represent the effective thermal conductivity of the powder bed ($k_e$). It is often represented as a packing density dependent weighted average [122,123] of thermal conductivities of alloy powder and shielding gas:

$$k_e = k_s\eta + k_g(1-\eta) \tag{2.30}$$

where $k_s$ and $k_g$ are the thermal conductivity of the solid and the gas, respectively. However, the contact area between two adjacent powder particles is very small. Therefore, effective heat conduction from one powder particle to another is almost negligible [19,116]. It has been found that the effective thermal conductivity of the powder bed depends largely on the thermal conductivity of shielding gas but not on the thermal conductivity of the powder [116]. Therefore, the following simplified formula for the effective thermal conductivity [116] has been suggested:

$$k_e = \frac{k_g}{(1-\eta)^2} \tag{2.31}$$

Although this formula is simple, it does not consider the effects of powder particle shape and size and inter-particle distance. Rombouts et al. [116] proposed the following correlation that considers these two factors.

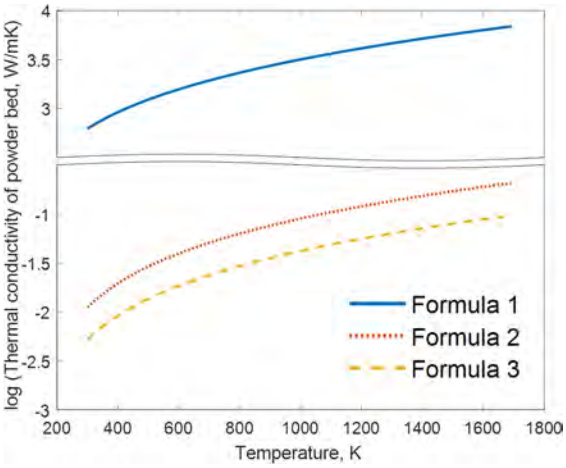

**Fig. 2.6.** Effective thermal conductivity of powder bed (SS316 powder + Ar gas) calculated using different formulae. Formulae 1, 2 and 3 correspond to the Eqs. (2.30), (2.31) and (2.32), respectively.

$$k_e = k_g \frac{\eta N}{2}\left[0.5\ln(1+L) + \ln(1+\sqrt{L}) + \frac{1}{1+\sqrt{L}} - 1\right] \tag{2.32}$$

where $k_g$ is the thermal conductivity of the gas, $N$ is the coordination number and $L$ is a product of a constant and powder particle diameter. The value of the constant depends on the shielding gas type [116] and for Ar its value is $5.4 \times 10^{-4}\ \mathrm{m}^{-1}$. The computed values of the thermal conductivity agree well with the experimental data. When the distance between two powder particles is smaller than the gas free mean path, inter-particle radiation can affect the effective thermal conductivity of the powder bed [124]. Inter-particle radiation depends on temperature of the powder bed, mean free path of the gas, and the Stefan-Boltzmann constant and it can be calculated using Zehner-Schlunder model [125]. However, for most PBF processes, the values of inter-particle radiation are small [124] and can be neglected.

Fig. 2.6 represents the temperature dependent effective thermal conductivity of powder bed consisting of SS316 powder and Ar gas. The effective thermal conductivity is calculated using all three formulae mentioned above. A log scale is used to plot all values of thermal conductivity in the same graph. Since thermal conductivities of both the powder particles and Ar gas increase with temperature, the effective thermal conductivity of the powder bed also follows the same trend. The effective thermal conductivity calculated using Eq. (2.30) is about 100 times higher than that calculated using Eqs. (2.31) or (2.32). Eq. (2.32) provides the values of effective thermal conductivity that agree with the experiments, whereas Eq. (2.30) significantly overestimates its values [116]. Therefore, Eq. (2.32) is recommended to use. For a higher packing density, it becomes easier to transfer heat from one particle to another due to increased area of contact. Therefore, the effective thermal conductivity of powder bed calculated using Eq. (2.32) increases with packing efficiency as shown in Fig. 2.7. These implementations of the effective thermophysical properties are required for the molten pool models where individual powder particles are not considered. In contrast, in the powder-scale models where interactions among the individual powder particles are modeled, effective thermophysical properties for the powder bed are not required.

Unlike the PBF processes where feedstock materials are supplied as packed powders, in DED, the assignment of properties of the feedstock depends on the type of the materials such as wire in DED-GMA and powder in DED-L and DED-EB [1,17,55]. Generally, the properties of the wire feedstock are the same as the alloy as provided in Table 2.1. For the cold wire supplied in DED-GMA [55,87], the properties of the wire feedstock are assigned at the room temperature [87]. However, in the DED-GMA processes with preheating of the wire [126], the properties are updated based on the preheating temperature as expressed in Table 2.1. However, in the powder based DED processes, the powder feedstock has a high surface to volume ratio and different heat transfer and heat absorption characteristics compared to the solid alloy [1].

Assignment of the thermophysical properties to the substrate, deposited track and molten pool are identical for all AM processes. At the beginning of the process, the substrate is assigned with the properties at room temperature or at a specified preheat temperature. During the process, the properties of the substrate and already deposited tracks are updated based on the temperature field [17,127] as provided in Table 2.1. Inside the molten pool where the temperature is higher than the liquidus temperature of the alloy, properties of the liquid alloy are assigned. Inside the solid-liquid two phase region where the temperature is between the solidus and liquidus temperatures of the alloy, the thermophysical properties are updated based on both the temperature and the liquid fraction [17]. Properties at every grid point are updated when new values of temperatures are obtained by iteration.

For efficient numerical calculations, explicit functional relations between properties and temperature are desirable, instead of tabulated values at discrete temperatures. Examples of such relations are available in recent reviews [1]. Exact values of high temperature thermophysical data are not always available and estimations are often made. However, with the increasing availability of computational resources and thermodynamic data bases, thermophysical data can be calculated for many commercial alloys based on pertinent theories where experimental data are scarce.

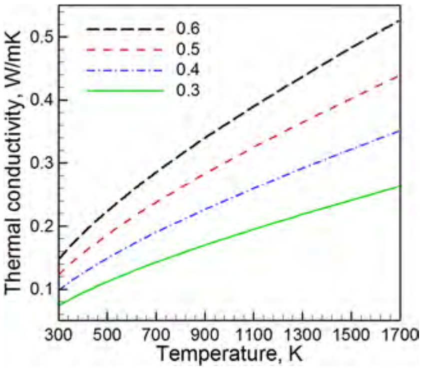

**Fig. 2.7.** Temperature dependent effective thermal conductivity of powder bed (SS316 powder + Ar gas) calculated using Eq. (2.32) for different powder packing efficiency [19].

### 2.5. Modeling of functionally graded alloys

Mechanistic models are important for the understanding of microstructures, mechanical properties and residual stresses and distortion of functionally graded alloys as they provide a detailed insight about the shape and size of the molten pool, peak temperature, and solidification parameters. Different from multi-material structures with discrete interfaces [128–132], the chemical composition, microstructure and properties change gradually in functionally graded materials [28,133], which can be advantageous for overcoming challenges associated with the abrupt changes in properties of dissimilar joints. DED is the most commonly used AM process to fabricate the graded alloys [133], although PBF [134] and an AM process combining wire and powder [135] have also been successfully implemented to produce these graded alloys. Since the microstructure and properties of graded alloys vary spatially depending on the local composition, modeling can provide an important tool for their control. In addition, measurements of thermo-mechanical responses such as residual stresses and strains are hindered by the limited availability of the strain free lattice spacing and other data of these graded alloys [28].

There are three main challenges in the modeling of AM of functionally graded alloys. First, temperature dependent thermo-physical and mechanical properties data for different compositions of these graded alloys required for the calculations are not readily available. Second, the local composition changes continuously with the fabrication process because of the dilution effect due to the mixing of different alloy compositions during the remelting of the substrate or the previously deposited layers. Finally, continuously varying thermo-physical and mechanical properties due to the addition of new layers with different alloy compositions affect the convergence of the numerical models.

#### 2.5.1. Thermo-physical and mechanical properties of graded alloys

Thermo-physical and mechanical properties depend on the local composition of functionally graded alloys. There are several methods to predict these properties based on how they vary with composition. If the property data are available for multiple compositions in a functionally graded material, they can be fitted into a polynomial for use in mechanistic models. If data is not available, effective alloy properties ($PR_{eff}$) at a particular location can be approximated using a rule of mixtures relationship [136],

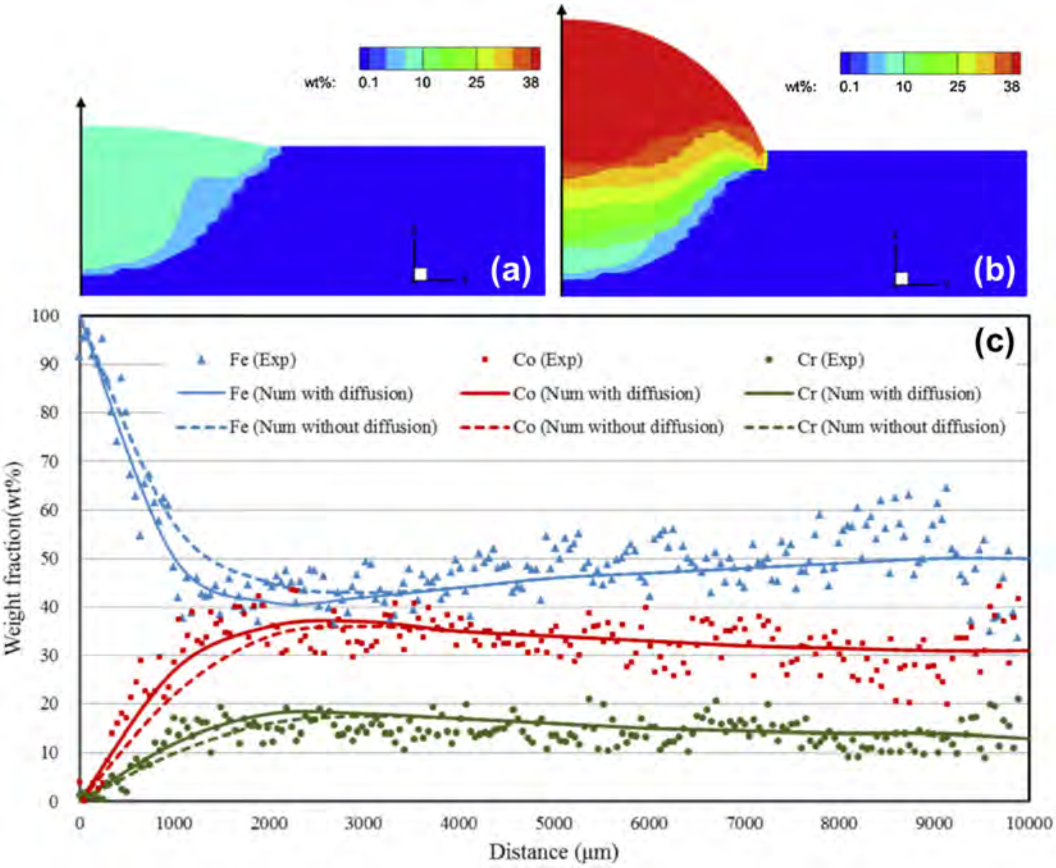

**Fig. 2.8.** Calculated composition profile of Ni in the cross-section of the deposit by DED-L of Ni-Co–Cr alloy powder over the graphite cast iron substrate: (a) One layer, and (b) Six layers [97]. (c) Weight fraction of Fe, Co, and Cr along a single track during DED-L of Co–Cr–W alloy powder over the 38MnVS medium carbon steel substrate [138].

$$PR_{eff} = PR_1 \; V_1 + PR_2 \; V_2 \tag{2.33}$$

where $PR_1$ and $PR_2$ are the terminal alloy properties, and $V_1$ and $V_2$ are the corresponding volume fractions. However, more complex relations have also been used in the literature [137] to incorporate the compositional dependence of properties. These relationships take the form,

$$PR_{eff} = P_{pure} + \sum k_i C_i \tag{2.34}$$

where $P_{pure}$ is the property of the pure solvent, $k_i$ is the coefficient for element $i$ determined from regression analyses, and $C_i$ is the concentration of element $i$ in a particular region of the functionally graded alloy. In multi-phase microstructures, the relationship in Eq. (2.34) can be used for each individual phase and the total effective property can be estimated using the rule of mixtures in Eq. (2.33).

In some instances, the local compositional variation cannot be specified a-priori and numerical modeling is necessary to determine the properties. For example, spatial variations of temperature and composition occur within the molten pool and they affect properties. These variations are computed by solving the equations of conservation of mass, momentum and energy. For example, the prediction of the composition profile of Ni during DED-L for Ni-Co–Cr alloy powder over the substrate of graphite cast iron is shown in Fig. 2.8(a) and (b) [97]. Fig. 2.8(c) shows the weight fraction of Fe, Co, and Cr along a single track during DED-L of Co–Cr–W alloy powder over the substrate of 38MnVS medium carbon steel [138]. These two cases demonstrate the capability of numerical models to quantitatively predict the variation of the alloying element concentrations with the continuous building process [97,138].

Thermodynamic programs designed for materials processing applications can also model important alloy properties such as equilibrium phases, phase transformations and thermo-physical properties [139]. The CALculation of PHAse Diagrams (CALPHAD) method [140] is commonly used to determine phase fractions and compositions for a given alloy concentration and temperature or temperature range. The prediction of thermo-physical properties using CALPHAD involves the following steps. First, the equilibrium fractions of phases are determined by minimizing the total Gibbs energy using thermodynamic excess functions. The property, $PR$, for a particular phase is expressed as [141],

$$PR = \sum_i MF_i \; PR_i + \sum_i \sum_{j>1} MF_i MF_j \sum_\chi \Omega_{ij}^{v} \; (MF_i - MF_j)^\chi \tag{2.35}$$

where $PR_i$ is the property of the phase in the pure element, $\Omega_{ij}^{v}$ is a binary interaction parameter between elements $i$ and $j$. $MF_i$ and $MF_j$ are the mole fractions of $i$ and $j$ in the phase, respectively. Both $PR_i$ and $\Omega_{ij}^{v}$ are temperature-dependent. The total property of the graded alloy is then determined from the mass fractions and properties of each phase using the rule of mixtures discussed previously [142]. This method has been successfully used to calculate phase equilibria for graded alloys between titanium alloys, nickel base alloys and steels [143,144]. Bobbio et al. [144] used this method to calculate phase fractions in a functionally graded alloy between a titanium alloy (Ti-6Al-4V) and a nickel alloy (Invar 36). The computed phase diagram was calculated by approximating the system as a Ti-Fe-Ni ternary system and is shown in Fig. 2.9(a). The diagram shows that depending on the amount of these main constituting elements several primary and secondary phases can form and play a significant role in determining the properties of the graded alloys. For example, Fig. 2.9(b) shows that both liquidus and solidus temperatures of the graded alloys change significantly with the volume fraction of Invar 36 and the variations across the entire composition gradient are not linear. The figure also shows that the temperature difference between the liquidus and solidus temperatures changes for different compositions of the graded alloy. It may result in a different dimension of the mushy region, temperature field, cooling rates and solidification parameters for different compositions of the graded alloys. The changes in these metallurgical variables based on local alloy compositions can be captured using transport phenomena-based models.

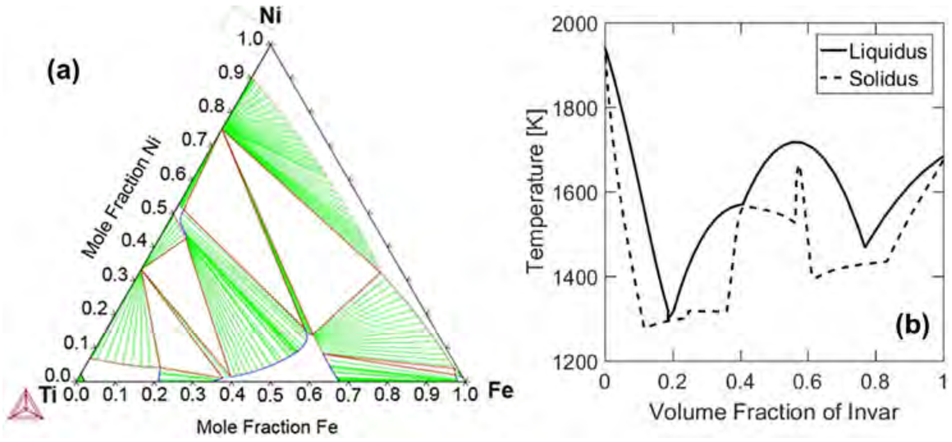

**Fig. 2.9.** (a) Ternary phase diagram of Fe-Ti-Ni system calculated using CALPHAD method [144]. (b) Variations in liquidus and solidus temperatures with the volume fraction of Invar in the graded alloy between Ti-6Al-4V and Invar [144].

It is noted that similar to their use in functionally graded alloys, elemental powder blends have been used to create “bulk” alloys in-situ during PBF-L. Examples include the creation of Mg-*x*Al-Zn alloys from mixtures of Al and Mg-Zn powders [145], Al-*x*Cu alloys from mixtures of Al-4.5Cu and Cu powders [146], an Al-Cu12 alloy from blends of pure elemental Al and Cu powders [147], a Ti-35Nb alloy from elemental mixed powder [148], and Ti-Mo-TiC metal matrix composites from a powder mixture of commercial pure Ti, 6.5 wt% Mo and 3.5 wt% $Mo_2C$ [149]. To date, transport phenomena models for PBF-L of elemental powder blends are limited. It is expected that the existing models without the powder packing simulations (see later in Section 2.8.1) can be readily extended to PBF-L of element powder blends by using the thermophysical properties of the final alloys. On the other hand, many complexities arise for the models with the powder packing simulations due to the need to track powder particles of different materials in both powder packing and molten pool calculations.

## 2.6. Computational methodologies

### 2.6.1. Overview of numerical methods

Unlike conventional melting and solidification processes of alloys, AM requires the treatment of transport phenomena over a wide range of time and length scales. In particular, the length scale can be at the powder-scale (50–100 μm) where the heat absorption and melting of a single powder particle is of interest, as well as at the part-scale (~1 cm) where millions of particles are melted and solidified forming a continuous track. The diversity is compounded further as melting and solidification of the alloy powders will involve a mushy region over which both the solid and liquid will coexist, thereby requiring special treatment of the governing equations.

*2.6.1.1. Spatial discretization.* The finite difference method (FDM), finite volume method (FVM), and finite element method (FEM) are the three traditional numerical methods that are used to solve the governing equations (Eqs. (2.11), (2.12), (2.13) and (2.18)) along with appropriate boundary conditions. The formulation of these numerical methods is well documented in the literature and thus not repeated here. While these traditional methods can consider a wide range of length scales, the computational burden increases exponentially for finer spatial resolution and thus an increase in total number of cells or elements.

FDM is normally formulated with a structured mesh and as a result it is easy to implement into a computer code and the calculation is computationally efficient. The reliance on structured mesh, however, limits FDM to computational domains that can be represented by rectangular grids. However, the interface tracking methods (e.g., VOF) can be used in FDM to track complex geometries inside the simple rectangular domain. The mesh has to be very fine in order to accurately track the position and orientation of the geometry.

FVM and FEM work with a computational domain comprising unstructured mesh to capture the complex geometry. The common element shapes for unstructured mesh include hexahedral and tetrahedral. It is noted when the VOF method is used to track complex geometries (such as melting of individual powder particles), there is no advantage of FVM or FEM over FDM since the computational domain is a simple rectangular prism (e.g., see Ref. [150] versus Ref. [22]).

The Lattice Boltzmann method (LBM) has been used to simulate the selective beam melting process [151,152]. In this method, two sets of distribution functions were defined at each lattice site: one for mass and momentum transport, and the other for movement of the internal energy. Equations of collision and displacement were formulated for the two distribution functions and numerically solved in a D2Q9 scheme (2-dimensional, cubic grid; each node point with 8 neighboring nodes). The free surface (liquid/gas interface) was tracked using a VOF-type method, and the solid phase was assumed to be immobile (i.e., same treatment as the enthalpy-porosity formulation). LBM has shown an ability to treat the transport process in powder-scale in a manner that is found easier for parallel computation. Another special group of numerical methods includes the meshless or mesh-free algorithms based on discrete element method [153] and smoothed particle hydrodynamics (SPH) method [154]. These specialized methods are still evolving and not widely used for modeling of transport phenomena in AM [124].

For FDM, FVM and FEM, the heat transfer and fluid flow model is commonly solved in structured or unstructured fixed (Eulerian) grids. On the other hand, the mechanical stress-displacement model solved by FEM often uses a deformable (Lagrangian) mesh which follows the material deformation. The use of fixed grids in solving fluid flow problems by FDM, FVM and FEM is necessitated by the large movement of material. For problems involving only heat conduction, fixed grids are appropriate since the material does not move in this case.

*2.6.1.2. Time marching.* To solve the transient form of governing equations, the time marching approach is used. Specifically, in increment 1, the initial conditions at time $t = 0$, where all the degrees of freedom (DOFs) (e.g., temperature and flow velocities) are given, are used to calculate the values of DOFs at the next time $t = \Delta t$, where $\Delta t$ is the time increment size. Due to the high non-linearity of governing equations, the numerical algorithm may require multiple iterations to reach a converged solution within the current time increment. In increment 2, the values of DOFs at $t = \Delta t$ are used to calculate the new values at $t = 2\Delta t$. Such time marching continues until the entire time is marched.

For time marching, explicit and implicit time integrations are two common schemes [155]. The explicit integration scheme tends to be more stable as it requires fewer iterations to converge in a time increment than the implicit scheme. Moreover, the small time increments needed for the explicit scheme make them suitable for solving the evolution of free surfaces. On the other hand, implicit models are accurate and have been used to model multi-layer DED-L [17].

### *2.6.2. Accuracy and stability*

There are two levels of accuracy for a numerical model of AM: physical accuracy and numerical accuracy. The physical accuracy, a measure of how well the model prediction is consistent with the experimental result, is the one that end users of the model would pay the most attention to. Fundamentally, it is affected by how well the model describes the important physical phenomena in AM. For instance, a heat conduction only model will likely have a low accuracy in predicting the melt track shape. This is because the important physical phenomena for melt shape include fluid flow which is not considered in the heat conduction model. In addition, uncertainties in materials properties (such as laser absorptivity) and process parameters (such as beam radius) and assumptions used in the model can have a deleterious effect on the physical accuracy. It is noted that the smart calibration of numerical model utilizing multivariable optimization algorithms [156] can markedly improve the physical accuracy of the model over a wide range of processing parameters and materials.

The numerical accuracy is crucial to numerical analysts as it measures the soundness of numerical solution to the governing equations. The first type of numerical accuracy is the temporal and spatial discretization accuracy. For example, the transient term in energy conservation equation is usually discretized as $\frac{\partial T}{\partial t} = \frac{T^t - T^{t-\Delta t}}{\Delta t}$, where $\Delta t$ is the time increment size, and $T^t$ and $T^{t-\Delta t}$ are the

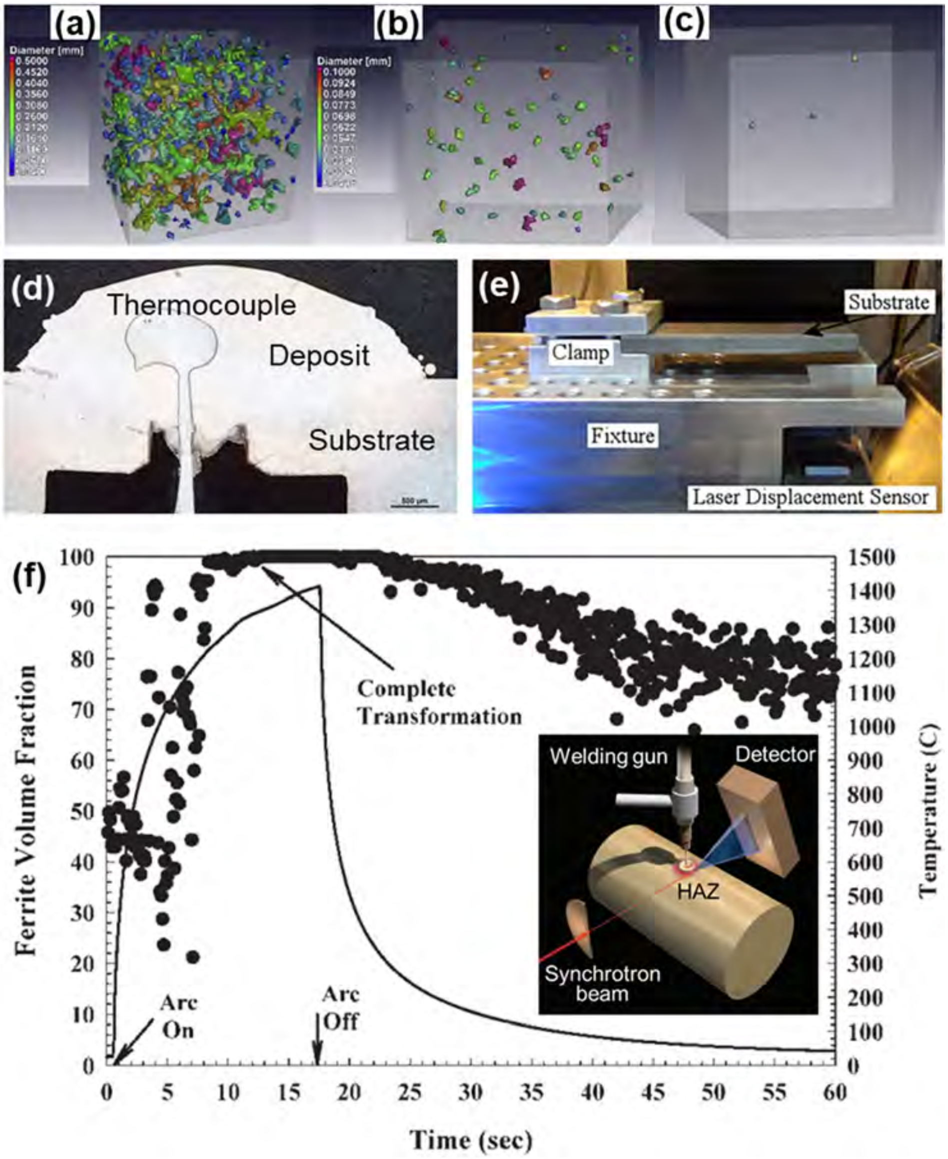

**Fig. 2.10.** Void distribution measured using X-ray CT in a PBF-L Ti-6Al-4V component [160] using (a) 160 W, (b) 185 W, and (c) 210 W of laser power. (d) Measurement of temperature inside the deposit using a thermocouple [161]. (e) Use of laser displacement sensor to measure in-situ distortion in AM [165]. (f) Measured ferrite volume fraction (black dots) using synchrotron and calculated temperature (black line) variations with time during welding of 304 stainless steel [166]. Inset: Schematic of the experimental set up.

temperature at the end of current and previous time increments, respectively. This is the first-order accurate temporal discretization for which the truncation error is proportional to $\Delta t$. In another example, the central difference approximation of the spatial temperature gradient is given as $\frac{\partial T}{\partial x} = \frac{T_{i+1} - T_{i-1}}{2\Delta x}$, where $\Delta x$ is the mesh grid spacing, and $T_{i+1}$ and $T_{i-1}$ are the temperature of two adjacent cells, respectively. The central difference approximation is said to have the second-order accuracy as the truncation error is proportional to $\Delta x^2$. The higher order accurate discretization is available. For FDM and FVM, it involves neighboring cells in addition to the immediately adjacent cells. For FEM, it is done through the addition of mid-side nodes within an element.

The actual temporal and spatial discretization accuracy realized in a particular model depends on the time increment size and mesh spacing. For a high accuracy, it may be intuitive to use the smallest values of Δt and Δx. However, that may lead to excessive CPU time without improving the accuracy significantly. Hence, it may be helpful to start a simulation with relatively coarse mesh spacing and large time increment, and perform subsequent runs with reduced mesh spacing and time increment until results independent of the selected values are obtained.

Another type of numerical accuracy is related to the residuals that represent the errors during iterative solution of the discretized equations. For example, the general form of a discretized 1-D heat conduction equation has the form of $|a_i T_i = a_{i-1} T_{i-1} + a_{i+1} T_{i+1} + b|$, where the subscript (e.g., $i + 1$) indicates the cell number, and $a$ and $b$ are coefficients [155]. Due to the highly non-linearity of the governing transport equations, the solution of the discretized equation is not exact. A residual, defined as, $R_e = |a_{i-1} T_{i-1} + a_{i+1} T_{i+1} + b - a_i T|$ is used to monitor the solution accuracy. Multiple iterations within a time increment are typically needed to reduce the residual to an acceptably low value.

Numerical instability occurs when the solution algorithm fails to decrease the residuals; in such a case, the simulation is said to be not converged or diverged. AM models can be especially susceptible to numerical divergence issue due to the highly non-linear equations solved. In some cases, the divergence can be caused by ill-posed boundary conditions or material properties that change too abruptly. In other cases, it results from the numerical algorithm itself. For example, the free surface simulation using VOF is prone to divergence, especially when both liquid and gas are considered due to the sharp change in material properties across the liquid/gas interface. If a simulation diverges, decreasing the time increment size and mesh spacing used in the model may help. If available, switching the time integration from implicit to explicit scheme may help to improve the convergence. Continued improvements of the robustness of numerical algorithms for solving highly non-linear problems common to AM are still urgently needed.

### 2.7. Model validations

Since almost all mechanistic models are approximate and developed based on several assumptions, they should be verified and validated to the degree needed for the intended application [157,158]. Mechanistic models of AM are generally validated by comparing the model outputs with the corresponding experimental results at different processing conditions [158]. It is important to decide which experiments need to be performed to validate a model. For example, if the model calculates the volume fraction of porosity in a component (Section 4.2.3), the computed tomography (CT) experiments performed using sophisticated and expensive equipment can be replaced by estimations based on the Archimedes method [159]. However, experimental results such as X-ray CT based characterizations are needed to validate the distribution of voids in three dimensions [160] as shown in Fig. 2.10(a)–(c).

In some cases, it may be difficult to obtain the experimental data for model validation. For example, temperatures inside the molten pool are difficult to measure accurately, so calculated temperature fields are often validated by measuring temperatures in the substrate away from the molten pool [55]. From these types of measurements, it is difficult to accurately validate a model because of the difficulties in the measurement of temperatures in a small moving liquid pool. High melting point thermocouples have been inserted through the substrate (Fig. 2.10(d)) to measure temperatures inside the pool [161], which provide a more direct method of validation for molten pool temperatures. However, the temperature varies throughout the molten pool, so spatial variations in temperature, repeatability of measurements and measurement errors are important.

Infrared (IR) thermography using IR cameras and pyrometers is a well-established technique for surface temperature measurement. Its recent applications to AM include in-situ monitoring of surface temperatures during PBF-EB of Ti-6Al-4V [162] and in-situ defect detection during PBF-L of AlSi10Mg when IR thermal signature was combined with a thermal model and ex-situ SEM characterization [163]. However, an accurate temperature measurement of the melt pool region remains challenging. The main challenge is the difficulty in converting IR intensities into temperatures due to factors such as the temperature-dependent emissivity and the interference of plasma plume. Cameras and pyrometers using two wavelength technique can obtain surface temperatures without considering the emissivity although the validity of such temperatures needs more rigorous examinations for different processing conditions and materials. Additionally, existing commercial IR cameras typically have a maximum frame rate of ~100 frames per second (fps) and specialized ones have ~1000 fps. Even at 1000 fps, there can be a significant amount of motion blur for a fast traveling heat source (e.g., laser speed of ~1 m/s in PBF-L). Pyrometers can operate at very high framerates although the measurement is limited to single spatial points. Lastly, unlike thermocouples that could measure interior temperature profiles, IR thermography is limited to temperature measurement on exposed surfaces.

In addition to temperature fields, heat transfer and fluid flow models calculate the distribution of velocity inside the molten pool. However, for a highly transient process like AM, it is very difficult to directly measure velocities of the liquid metal. Calculations of transient residual stresses (Section 4.5) and microstructural evolution (Section 4.1) are other cases where an indirect model validation is necessary. Numerical models are used to investigate the evolution of stresses based on the transient temperature field during both the deposition and cooling. However, it is difficult to measure the stresses during fabrication, so residual stresses measured after the fabrication are used to validate models [164]. This issue is partially resolved by measuring the in-situ distortion of the substrate

[165] during the process, as shown in Fig. 2.10(e). Similar to residual stresses, the final microstructural features predicted by models can be validated using microscopy. In situ x-ray diffraction can provide the phase fraction information during processing that can be used for the validation of microstructural evolution, though it is difficult to implement in most laboratory settings. In one example of this technique, a synchrotron beamline was used to measure the evolution of ferrite volume fraction in 304 stainless steel during welding [166] (Fig. 2.10(f)). More recently, applications of high-speed synchrotron X-ray imaging and diffraction have enabled the observation of molten pool dynamics and keyhole morphology [75,167] and phase transformation in Ti-6Al-4V [168,169] in PBF-L, respectively.

Validation of different mechanistic models requires experimental datasets containing essential input and output variables for different processing conditions and alloys. The National Institute of Standards and Technology (NIST) in the United States has developed methods and datasets so that models for laser welding can be validated against standardized datasets [170]. Similar datasets are also required for validating models for metal printing, and NIST also has some available datasets through their Additive Manufacturing Benchmarks test series [171]. Since the literature data do not always report all essential input and output variables for a given process, publicly available and complete datasets are crucial for having standardized AM model validation methods in the future.

### 2.8. Progresses in transport phenomena models

This section critically examines the progress made in developing verifiable mechanistic models of AM. Both models of the main component physical processes as well as the overall models for each variant of the AM processes are examined. The models for the component physical processes focus on finer details of a selected portion of the process, often at shorter length and time scales. In contrast, the integrated models of AM processes seek to simulate the overall process in part scale and typically involves larger length and time scales.

#### 2.8.1. Powder bed fusion

Features of two types of models for the PBF processes are critically examined here. The first type, i.e., powder packing models, is for the calculation of the motion and the eventual positions of the particles. The second type, molten pool models, focuses on the calculation of heat transfer and liquid metal flow in the substrate, deposit and the powder. Molten pool models can be used with or without the powder packing simulations.

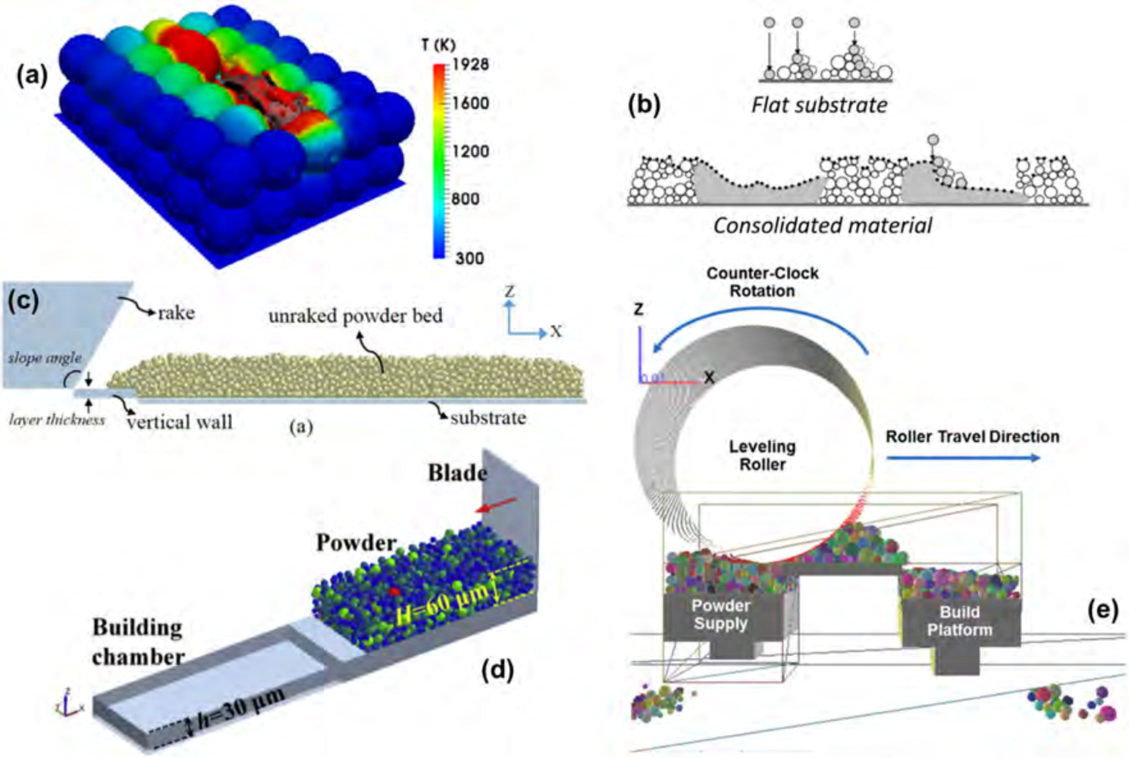

**Fig. 2.11.** Comparison of different approaches used to calculate powder particle positions on the powder bed. (a) Simplistic cubic arrangement [150], (b) Raindrop of particles onto flat substrate surface, and non-flat surface of consolidated material represented by virtual particles [152], (c) DEM simulation of rake-particle interactions on powder bed [177], (d) DEM simulation of interactions between WC/IN718 composite powders and the blade [176], and (e) DEM simulation of roller-particle interactions [175].

*2.8.1.1. Powder packing models.* There are three groups of powder packing models as shown in Fig. 2.11. The simplest approach is to assign a pre-defined stacking pattern such as cubic arrangement to particles which was used by Qiu et al. [150] for the simulation of PBF-L of Ti-6Al-4V as shown in Fig. 2.11(a). These models do not consider the stochastic nature of powder packing and can significantly overestimate the packing density.

The next approach is the sequential addition algorithm, also referred to as the raindrop model. It starts with spheres that are randomly distributed in an open space. These spheres are then dropped sequentially one by one into a box below, as shown in Fig. 2.11(b) [151]. The final stable position of a sphere is determined by it either hitting the floor or having contacts with three pre-deposited spheres. This algorithm does not consider the particle-particle mechanical interactions. Examples include the works of Zhou et al. that applied this method to simulate 2D multilayer melting by placing virtual particles on the consolidated surface of the previous layer as boundary conditions [172].

The third approach is a dynamic algorithm that simulates a transient packing process considering mechanical interactions of individual particles. In particular, Discrete Element Method (DEM) was used by Kovaleva et al. [173], Mindt et al. [174], Lee et al. [22,175], Gu et al. [176] and Yan et al. [177] for spherical metallic powders as shown in Fig. 2.11(c) and (d). The method was also used by Parteli [178] and Haeri et al. [179] for AM of cylindrical polymeric powders. DEM models consider the contact forces among a large number of discrete particles [180,181]. Considering two elastic spheres, the normal force is calculated as a function of normal displacement between the two particles as shown by the following equation [180,181]:

$$F^n = 2E\frac{r_1 r_2}{r_1 + r_2}u^n \tag{2.36}$$

where $F^n$ is the normal force of contact, $E$ is the Young's modulus, $r_1$ and $r_2$ are the radii of two particles in contact, and $u^n$ is the normal displacement. Similarly, the shear (or tangential) force is calculated as [180,181]:

$$F^s = 2E\nu\frac{r_1 r_2}{r_1 + r_2}u^s \tag{2.37}$$

where $F^s$ is the shear force of contact, $\nu$ is the Poisson's ratio, and $u^s$ is the shear displacement. Particle size distribution can be directly input into the DEM model. Recent advances in DEM have considered non-spherical particles such as rod-shaped particles approximated by combining spherical particles of different sizes in the multi-sphere method [178,179]. Being an explicit time integration algorithm, a practical challenge in modeling powder dynamics using DEM is the need for extremely small time increment given by [180,181]:

$$\Delta t_{max} = \frac{\pi\ r_m}{0.163\ \nu + 0.877}\sqrt{\frac{\rho}{E}} \tag{2.38}$$

where $\Delta t_{max}$ is the maximum time increment limit, $r_m$ is the minimal radius of particles, and $\rho$ is the density. Eq. (2.38) shows that the maximum time increment is proportional to particle size and smaller particles require finer time increments. The techniques used to make these calculations tractable are examined below.

**Table 2.3**
Examples of molten pool models and their features for powder bed simulation considering powder packing.

| Process | Material | Models | Features | Refs |
|---|---|---|---|---|
| PBF-L | IN718 | Flow-3D | ● Mesh size: 4–8 µm<br>● Computational domain: 1000 µm × 400 µm × 210 µm<br>● Number of cells: 1.25 million<br>● Single layer and two tracks<br>● Computational time: 24 h | [22] |
| | SS316L | ALE3D | ● Mesh size: 3 µm<br>● Time step: 1 ns<br>● Computational domain: 1000 µm × 300 µm × 50 µm<br>● Single layer, single track<br>● Calculation time 100,000 CPU hours | [21,67] |
| | Ti–6Al–4V | OpenFOAM | ● Mesh size: 5 µm<br>● Computational domain 1000 µm × 250 µm × 250 µm<br>● Total elements: 0.5 million<br>● Single layer, single track | [194] |
| | IN718 | Fluent | ● Single layer and multiple tracks<br>● Computational domain:<br>400 µm × 300 µm × 60 µm | [191] |
| PBF-EB | Ti-6Al-4V, TiAl alloy | Lattice-Boltzman Method | ● 2D model<br>● computational domain: 1.25 mm × 1.0 mm; 5.0 mm × 0.75 mm<br>● Mesh size 3 µm, 5 µm<br>● Time step: 50 ns, 220 ns. | [99,151] |
| | Ti-6Al-4V | Flow-3D | ● Mesh size: 5 µm<br>● Number of cells: 5 million<br>● Physical time: 4 ms<br>● Computation time: 140 h | [189] |

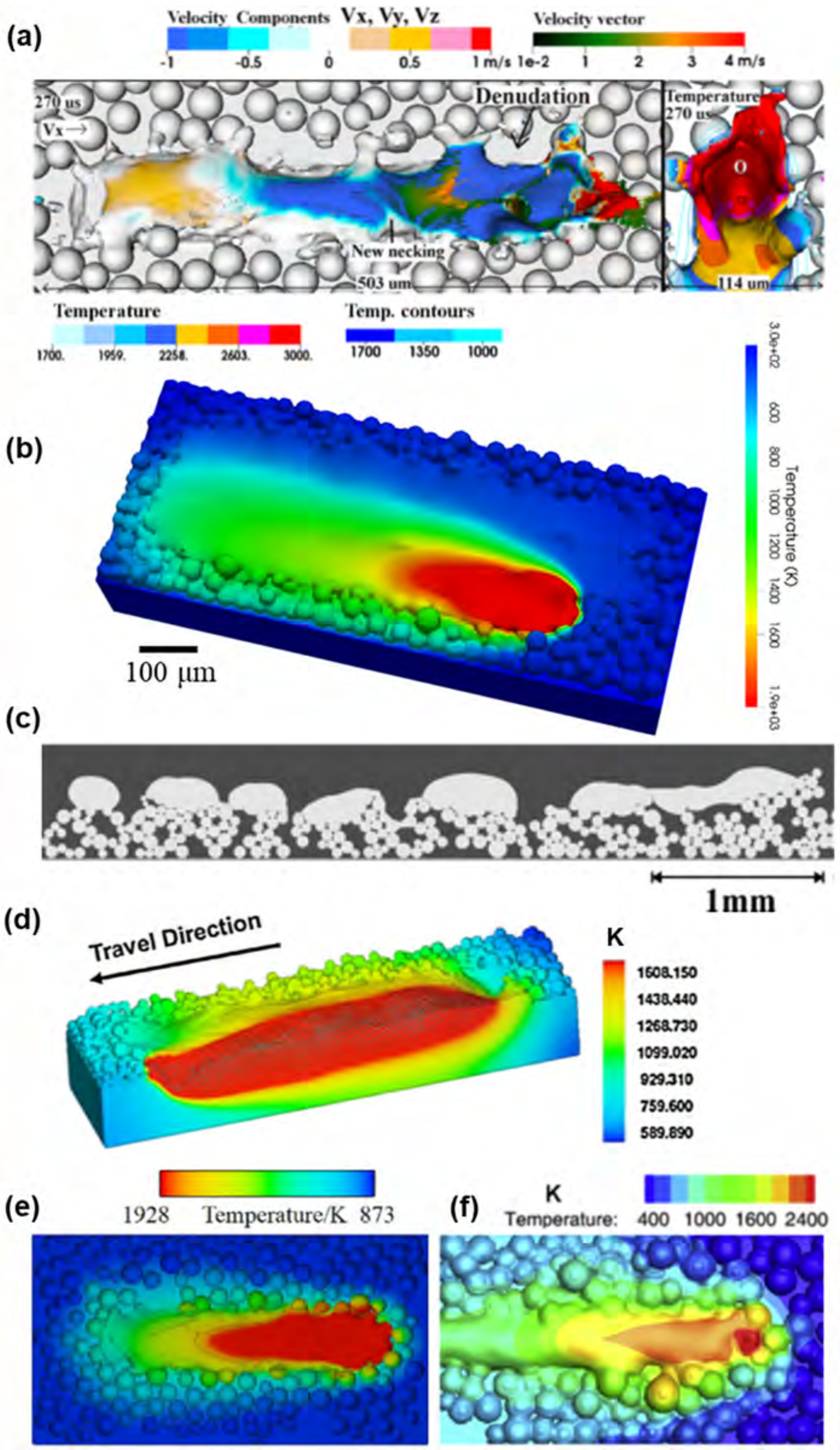

**Fig. 2.12.** Molten pool and powder particles simulated using various powder-scale PBF models: (a) PBF-L by ALE3D [67], (b) PBF-L by OpenFOAM [186], (c) PBF-EB by LBM [151], (d) PBF-L by Flow-3D [22], (e) PBF-EB by Flow-3D [189], (f) PBF-L by Fluent [176].

Since the ratio of density to elastic modulus ($\rho/E$) is very small for metallic powders, the maximum time limit is of the order of 1 ns for a metallic particle with diameter of 10 μm. To ensure a tractable time-step size, Yan et al. excluded particles with diameter below 30 μm [177]. Parteli and Pöschel addressed the time step issue by arbitrarily reducing the Young's modulus by 100 times [178]. Lee et al. employed the mass-scaling method, commonly used by explicit finite element methods, where the density was arbitrarily enhanced [22]. They systematically studied the extent of mass-scaling on the calculated packing density. Despite the various ways for speed-up, the current DEM models are still limited to simulating powder spreading using miniature rake/roller onto miniature powder bed (dimension about 1 mm). Nevertheless, statistically important quantities such as packing density have been validated against the existing experimental data [22]. The DEM based powder spreading model has been used for both PBF-L [22] and PBF-EB [151]. It is noted that the powder particles are partially sintered prior to electron beam melting in PBF-EB. Such sintering step has not been considered by the existing models [151].

The aforementioned discussions indicate the progress made in the development of powder packing models. The scale of the calculation domain and the computational efficiency vary among different models. The reliability of the computed results depends on the assumptions made in developing these models. However, the size of the computational domain and the speed of computations often affect the usage of a particular model.

*2.8.1.2. Molten pool models.* There are two types of numerical molten pool models, with and without integration with the powder packing model as described below.

(a) Molten pool models with powder packing simulation

Molten pool models with powder packing simulation are capable of resolving transport phenomena in powder-scale, often referred as powder-scale models. Currently available powder-scale models include multi-physics code ALE3D [7,67,182], Open source Field Operation And Manipulation (OpenFOAM) [150,183–186], the Lattice-Boltzmann method (LBM) [187,188], and commercial computational fluid dynamics (CFD) software such as Flow-3D [22,177,189,190] and Fluent [191,192]. Table 2.3 provides a summary of these powder-scale PBF models. Typical simulation results of the powder-scale models are presented in Fig. 2.12. The features of these models are briefly discussed below.

For multilayer calculations, the solidified surface profile calculated by the molten pool model can be exported out as a stereolithography (STL) file, which is a representation of surface topology using 3D triangular facets or shell elements. The STL file was used by Yan et al. for PBF-EB [177]. Another method, used by Körner et al. [151] in their 2D model, is the placement of virtual particles generated on the surface of the consolidated material. The surface topology can then be imported to the powder packing model to calculate powder spreading over non-flat surface for the next layer. The above sequential coupling continues for multilayer calculations.

ALE3D is a multi-physics massively parallel numerical simulation software tool utilizing arbitrary Lagrangian-Eulerian techniques [21]. The code generates randomly distributed particles for powder-scale modeling of the PBF-L process. ALE3D considers the metal particles randomly overlaid on a uniform Cartesian background mesh [21]. A hybrid finite element and finite volume formulation on an unstructured grid is used. An example of the simulated molten pool and powder particles is shown in Fig. 2.12(a) [67]. The formation of denudation, spattering, pore defects, and the strong dynamic flow of the molten metal were simulated considering the recoil pressure and Marangoni convection [21,67,182,193].

OpenFOAM is an open source toolbox that is capable of considering both powder packing and molten pool modeling based on programming language C++. The physical processes of PBF-L of Ti-6Al-4V were simulated considering the surface tension, Marangoni flow, recoil pressure, drag force due to solid/liquid transition [150,186,194]. Powder particles were packed on the substrate before laser scanning [150,186]. A probability density function with Gaussian fit was used to simulate the size distribution of powder particles. Subsequently, a powder dropping model was used to calculate the random positions and arrangements of the powder particles in the powder bed [194]. An example of the simulated molten pool and powder particles using OpenFOAM is shown in Fig. 2.12(b) [186]. The evolution of the liquid/gas interface of the molten pool was simulated through the coupling of the Navier-Stokes equation, energy conservation, continuity equation and volume-of-fluid equation [150,186,194].

PBF processes simulated by LBM compute the temporal evolution of the particle distribution functions [151]. LBM considers free surface boundary conditions [5]. The local powder melting and re-solidification processes, and the formation of defects such as lack of fusion, porosity and balling were explored considering physical mechanisms like wetting or capillary forces as well as the influence of the stochastic powder bed [99,151,195]. The LBM models developed for transport phenomena during PBF are mostly 2D. An example of the simulated molten pool and powder particles is shown in Fig. 2.12(c) [151]. The LBM model allows for large-scale parallel computations and has been used to simulate 3D PBF-EB. However, a simulation of a domain of 0.98 mm × 0.98 mm × 0.48 mm for about three milliseconds took 20,000 time steps [151]. Thus 3D LBM models are computationally intensive for the simulation of most real components.

Commercially available software such as Flow-3D and Fluent have been used to simulate transport phenomena during PBF [22,189,191]. Flow-3D was used to calculate the interaction between laser beam and individual powder particles, the evolution of the free surface of the molten pool and the solidification parameters during PBF-L of IN718 [22]. An example of the simulated molten pool and powder particles using Flow-3D is shown in Fig. 2.12(d) [22]. The powder packing conditions were simulated using an open source DEM code considering the dropping of particles, vibration of the container, and spreading of the powder layer. Defects including the balling effect, single track non-uniformity and inter-track or inter-layer voids were simulated for PBF-EB of Ti-6Al-4V [177,189]. An example of the simulated molten pool and powder particles during PBF-EB using Flow-3D is shown in Fig. 2.12(e)

[189]. The generation of the powder layer was simulated using a DEM based model [177,189]. The porosity and surface morphology of IN718 made by PBF-L were simulated using Fluent [176,191,196,197]. A simulated result of molten pool and powder particles is shown in Fig. 2.12(f) [172]. The figure shows that depending on the local temperature field, the particles can be completely melted or sintered in the deposited track. These models can provide complex part attributes such as porosity and surface roughness in addition to temperature and velocity fields.

Powder-scale models consider small length scales and short processing times. Moreover, the time increment used for explicit integration has to be correspondingly reduced due to the fine meshes used in the numerical model. In view of the computationally intensive nature of the powder scale models, there are opportunities to develop more efficient computational algorithms.

(b) Molten pool models without powder packing simulation

These molten pool models enable simulation of build profiles and the transient temperature fields over the entire component without explicitly considering the motion and packing behaviors of the powder particles. Initial attempts to realize the underlying phenomena in PBF based AM processes were restricted to analytical heat conduction models to examine the melt pool dimensions in PBF [198–202]. These models included several simplifications such as temperature independent material properties and provided a qualitative understanding of the effects of beam power, scanning speed, and initial porosity of the packed bed (i.e., packing density) on the peak temperature and pool dimensions in a single layer PBF process [198–202]. Besides the analytical models, numerical models have also been developed to compute the transport of heat, mass, and momentum during PBF.

Current models without powder packing simulation for PBF include in-house programs such as the heat transfer and fluid flow code developed at Penn State University [19], the open source code Truchas developed at Los Alamos National Laboratory [203–205], commercially codes such as Fluent [206,207], COMSOL Multiphysics [208–210], MSC Marc [211], Ansys [212,213], and Abaqus [214]. Typical results using different computational tools are presented in Fig. 2.13 [205,211,214–216]. The results show that reasonable agreement with experimental data can be attained in these simulations although they do not explicitly model powder melting.

The 3D model for PBF process considering multiple layers and hatches developed at Penn State [19,211] solves the equations of conservation of mass, momentum, and energy in a transient form. The temperature dependent thermophysical properties of the powder bed are considered. The temperature and velocity fields and solidification parameters are computed for various laser powers, scanning speeds, powder layer thicknesses, packing efficiencies and hatch spacings for the deposition of SS316, Ti-6Al-4V, IN718 and AlSi10Mg [19]. The model uses non-uniform traveling grids to reduce computational time. Adaptive meshing techniques are easier to

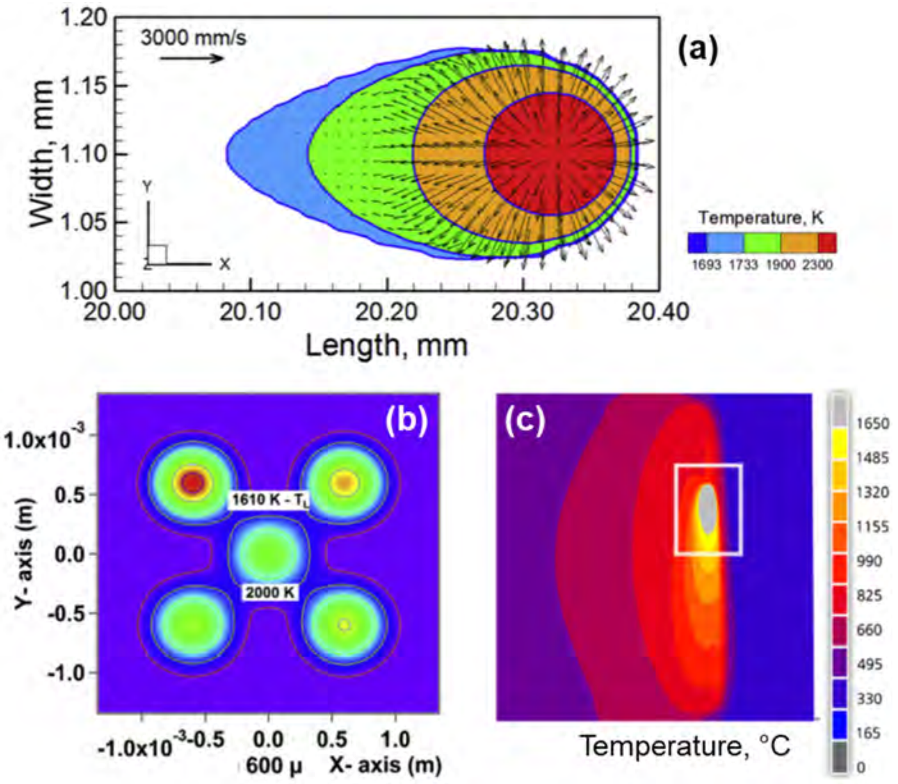

**Fig. 2.13.** Temperature and velocity fields and molten pool for multi-track multi-layer PBF simulated using part-scale models: (a) PBF-L by the heat transfer and fluid code developed at Penn State University [215], (b) PBF-EB by the Truchas code [205], (c) PBF-L by MSC Marc [211].

apply in these models without losing resolution due to the simplified geometries of the domain and larger mesh sizes which can be greater than individual powder particles [19]. This is desirable, because reducing the number of active nodes or control volumes decreases the computational cost significantly.

The Truchas code was used to simulate the physics of heat transfer of a point heat source scan strategy in PBF-EB of IN718 [204,205]. Truchas considers non-isothermal phase change in the mushy zone during solidification. The effects of various beam parameters on the molten pool dynamics were studied. The spatial and temporal variations of temperature gradient and growth rate at the liquid-solid interface of the molten pool were calculated.

COMSOL Multiphysics, MSC Marc, Ansys, and Abaqus are FEM based platforms for the computation of heat conduction processes during PBF [208–214]. The convection of liquid metal in the molten pool during PBF is often neglected in these models. Several types of elements can be used such as tetrahedral, cuboid, and octahedral to support the simulation of parts with complex geometries [208–214]. In contrast, Fluent is a FVM based software often used to calculate the temperature and velocity fields in the PBF parts [206,207].

Note that the physical behaviors of the powder particles such as the heating, melting, solidification, cooling, and motion processes are not explicitly simulated in order to reduce the computational cost. However, the computation processes take hours of time even using the molten pool models without powder packing simulations. Thus, reducing the computational costs still remains a significant challenge and more computationally efficient models are needed.

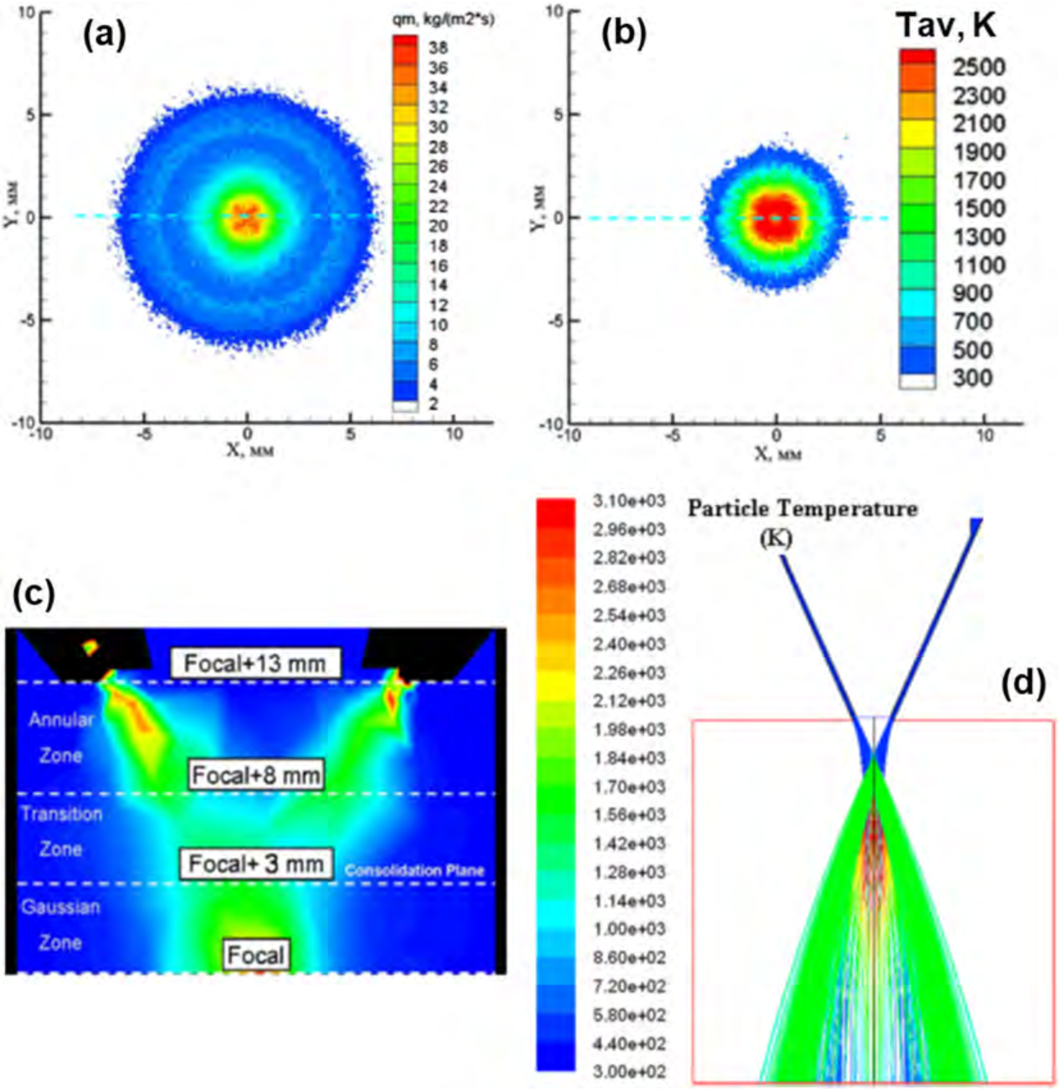

**Fig. 2.14.** Transport phenomena during powder feeding DED computed through numerical models: (a) and (b) Distributions of the particle mass flow and mean-mass temperature on the substrate surface formed by a triple coaxial nozzle system, respectively [223]. (c) Evolution of powder concentration distribution along the outlet nozzle [224]. (d) Powder jet temperature profile in a coaxial head with four radially symmetrical powder flow nozzles and optics [218].

### *2.8.2. Directed energy deposition with powder feedstock*

In the powder feeding DED process, the powder particles are introduced into the molten pool through powder injection from the feeding nozzles [111]. The models consider the powder feeding process, the interactions between the powder particles and the laser beam, the impingement of the powder particles on the molten pool, and the transport phenomena in the molten pool.

There are two types of models for DED processes with powder feed stock. The first powder feeding model considers the interaction of the powder particles with the heat source and the shielding gas during their flight from the nozzle to the fusion zone. The second model addresses the heat transfer and fluid flow in the substrate and the deposited tracks with or without consideration of powder feeding mechanisms.

*2.8.2.1. Powder feeding models.* A major focus of the powder feeding models is the determination of the catchment efficiency during DED-L [96] which is the ratio of the amount of materials deposited to the amount of powders delivered in a given time period [217]. The catchment efficiency depends on various factors such as the velocities of the powder, flow of shielding gas, diameter and standoff distance of the nozzle, powder size and size of the molten pool [3,96,111,218].

The catchment efficiency was calculated using a numerical model based on Fluent considering the trajectories and velocities of the feeding particles [96]. Through analytical modeling and high speed imaging, particle self-shielding was found to impose unavoidable upper limits on the catchment efficiency for DED-L process [219]. Particles often impact and float on the molten pool surface for several hundreds of microseconds before melting into it, which causes rebounding of the subsequent incoming particles by these floating particles [219]. The gas flow and the powder particle flow between the powder nozzle and the molten pool surface was simulated using a model based on COMSOL considering the powder particle distribution and the attenuation of the laser beam by the powder particles. [220]. The sizes and the trajectories of the powder particles are important factors for their heating [218,221].Various numerical models have been reported for the simulation of the powder feeding processes through coaxial or multi-nozzle deposition heads during DED-L, with several examples shown in Fig. 2.14 [96,218,222–224]. The computed results show that the important variables for the heating of the particles include nozzle angle, type and velocity of the shielding gas, powder characteristics and mass flow rate and power distribution profile of the heat source. Heating of the powder particles in the gas phase affects the accuracy of the calculations of temperature field in the fusion zone.

The optimum position of the molten pool relative to the powder streams depends on the spatial distribution of the powder mass flux and thus the powder motion trajectories [225,226]. The path of the powder stream is influenced by the powder particle size, carrier gas flow, powder feeding rate and nozzle angle [221,227]. Thus, the modeling of the flow behavior of the powder particles requires tracking of the individual powder particles travelling through the shielding gas [228]. Numerical models based on Fluent have been used for coaxial powder flow during DED-L [228,229]. Fig. 2.14(a) and (b) show the density and temperature distributions of the particle on the flat substrate surface with a coaxial feeding nozzle [223]. The standoff distance with the maximum mass deposition did not necessarily coincide with the beam focal plane [230]. The computed results show that the maximum powder concentration located above the averaged powder focal point [96]. Convergence of the powders from the four nozzles occurred at the point where the powder concentration reached a localized maximum near the powder focal point [96]. The powder flux distribution varies significantly during the flight of powders from the nozzle to the substrate as shown in Fig. 2.14(c) [224].

The simulations of particle transport in the gas stream show that particles may be significantly overheated during flight depending on their trajectories, size, and time of retention in the laser-radiation region [223]. The peak temperature of the particles reached 2500 K, nearly 1000 K above the solidus temperature of the cobalt alloy powder as shown in Fig. 2.14(b) [223]. Fig. 2.14(d) shows that in a quadruple nozzle DED-L system, the particles experienced a sharp increase of the temperature to around 1000 K or even higher when they passed through the laser irradiation zone [218]. The temperature of the powder particles irradiated by the laser beam can exceed the liquidus temperature or even the boiling point of the feedstock materials according to Katinas et al. [231] and Kovalev et al. [232]. Therefore, a significant amount of energy is carried by the particles and subsequently transferred to the deposit during powder feeding DED processes. The temperature, speed, and trajectory of the powders [233] affect the absorption of heat and mass into the molten pool and the shape of the deposit [222]. Powder absorption has been modeled by considering individual powder particles [222] and their interaction with the heat source [234], as well as by empirical models [31,235–237]. The computed results of the powder feeding models such as the catchment efficiency, the temperature and velocity fields, and the concentration distribution of the powder particles can be integrated to the molten pool models for the DED processes.

In summary, the powder feeding models have focused on the heating of the powder particles and their assimilation into the molten pool considering the important interactions among the flowing gas, powder and the heat source. These models often consider streamline flow of powders and gases to make the calculations tractable. In addition, since the grid size should be smaller than the size of the powder particles, most of these models are in 2D to achieve computational efficiency. The effects of metal vapors from the fusion zone in altering the characteristics of shielding gas are often neglected in these models. Opportunities exist for the rigorous assessment of the impact of these simplifications on the powder heating and development of unified powder models that are accurate and tractable.

*2.8.2.2. Molten pool models.* There are two types of molten pool models: (1) molten pool models considering powder feeding, and (2) molten pool models without powder feeding simulations. The progresses made in these two types of models are critically examined here.

(a) Molten pool models with powder feeding

The sequentially coupled simulation consists of two steps: The concentration, temperature and velocity fields of the powder particles are computed using the powder feeding model. The results are then used in the molten pool model to compute the geometrical and thermal features of the molten pool. Fig. 2.15 shows several examples of the molten pool and powder particles during DED-L simulated using various models considering powder feeding [223,231,238–240].

Fig. 2.15(a) shows the molten pool and powder particles simulated using VOF for DED-L [241]. Fig. 2.15(b) and (c) show the molten pool and feeding powders for a single track deposition with coaxial nozzle computed by commercial code CFD-ACE+ [239]. The energy and mass transferred from the powder to the molten pool, temperature-dependent material properties, and buoyancy and Marangoni forces were considered for the molten pool calculations [239]. It was found that the powders were not homogeneously distributed on the surface. This indicates that the catchment efficiency of the powders is dependent on the trajectories of individual particles. Han et al. showed that the powder injection had a significant effect on molten pool flow pattern and penetration. Laser power attenuation due to the presence of the powder cloud affected the molten pool shape and size [242].

Fig. 2.15(d) illustrates the results of the bead growth with insignificant substrate fusion computed from a DED-L model considering the dynamics of the nozzle, the carrier and shielding gases, the heating of the powder particles by the laser, the transportation and thermal processes of the powders in the bead and substrate. However, the fluid convection in the molten pool was not considered [223]. The track geometry and temperature fields of the DED-L process for single track were predicted. The catchment efficiency was obtained based on the available local energy and powder feed profiles without a priori knowledge of the deposition [231].

Wen et al. simulated the transient temperature of individual particles as they were carried by a turbulent gas flow through the laser beam while absorbing laser energy [228]. The calculated mass flux was exported to a sequentially coupled model to calculate geometries and sizes of the molten pool using the level-set method. They also developed a 3D model to simulate a three-layer single track DED-L of a metal matrix composite [243]. A 3D transient model was used to simulate the two-track and three-layer DED-L process, with the deposition profile and temperature distribution computed considering the laser-powder interaction, laser-substrate interaction, and melting and solidification processes [240].

Comprehensive models for multiple tracks and layers approaching part scale simulation are scarce due to their computationally

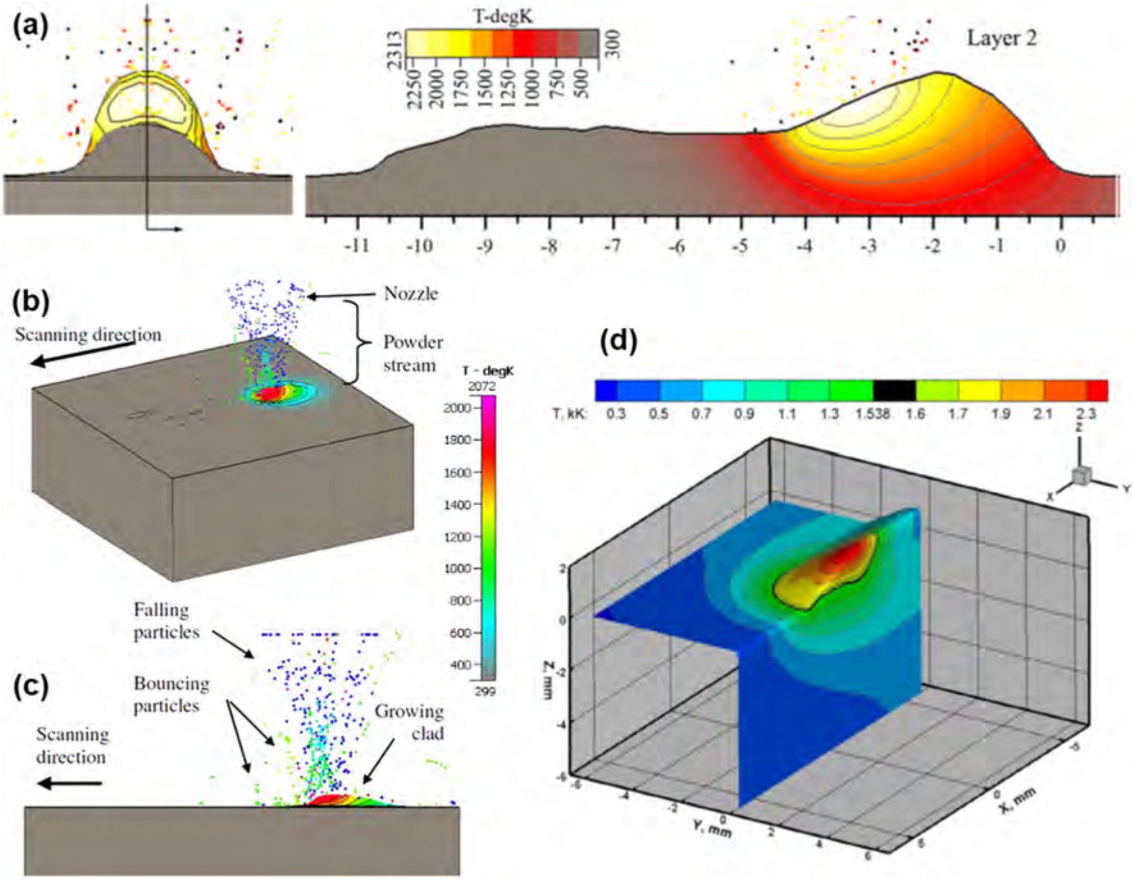

**Fig. 2.15.** Molten pool and powder particles during DED-L simulated using various molten pool models with powder feeding simulation: (a) Temperature field with an annular nozzle using VOF [241]. (b) Isometric and (c) lateral views of the molten pool and feeding powders with coaxial nozzle computed by commercial code CFD-ACE+ [239]. (d) 3D temperature field on the surface and inside the bead with coaxial nozzle [223].

intensive nature. Thus, models with significantly higher efficiency are needed.

(b) Molten pool models without powder feeding

Molten pool models without powder feeding simulation often use analytical equations to describe the powder flow behavior, the catchment efficiency, the laser energy attenuation and absorption of the powder particles [236,237,244,245]. Thus, both mass and heat flux can be defined as boundary conditions on the surface of fusion zone for heat transfer and fluid flow calculations [17,18,31,236,246]. Several typical examples of the temperature and velocity fields calculated using such molten pool models are shown in Fig. 2.16 [18,31,220,247–249]. The geometrical and thermal features related to the molten pool are the main focus of these models.

The modeling approaches used to add mass into the molten pool during DED-L can be divided into two main categories: (a) calculations with pre-defined track thickness and (b) calculation of deposit geometry and free surface morphology.

The first approach uses a predefined shape for the bead surface, such that the mesh geometry is known before calculations are started. Manvatkar et al. developed a transient heat transfer and fluid flow model for laser DED of SS316 [17,18]. They calculated fusion zone geometry from the computed temperature fields. Wei et al. reported the temperature fields in multi-layer deposition of IN718. Their models achieved a high level of computational efficiency by considering the material deposition from molten particles via pre-placed mesh blocks, as shown in Fig. 2.16(a). Knapp et al. used experimental data to specify the surface geometry and

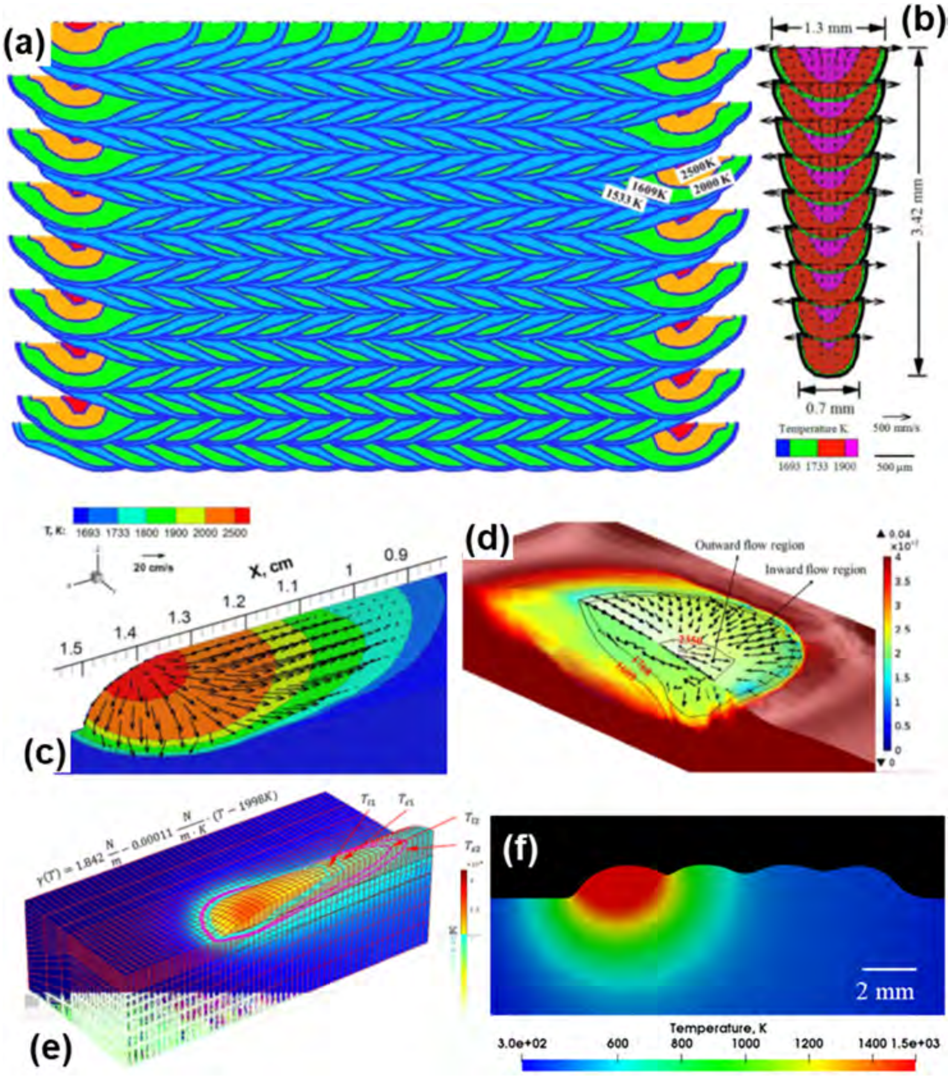

**Fig. 2.16.** Temperature and velocity fields calculated using molten pool models without powder feeding simulation for powder-based DED-L: (a) Model reported by Wei et al. [248], (b) Model reported by Manvatkar et al. [18], (c) Model reported by Knapp et al. [31], (d) Model reported by Gan et al. [247], (e) Model based on COMSOL Multiphysics reported by Wirth el al. [220], (f) Model reported by Wei et al.[249].

determined fusion zone shape and size from the solution of three dimensional Navier Stokes equation and energy equation. Their results shown in Fig. 2.16(c) demonstrate that an excellent computational efficiency can be attained by using experimental data on the shape of the free surface [31]. Commercially available software AutoDesk Netfabb® [250] and GeonX Virfac® [251] also calculate temperature fields from predefined track dimensions for simulating the DED process.

The second approach is to calculate the shape and free surface geometry of the molten pool by using VOF [249,252], level-set [109,253,254] or surface pressure balancing methods [97]. Lee and Farson developed a transient model based on VOF method to predict molten pool shape for multiple layers in laser DED [252]. The mass of feedstock particles was considered as a boundary condition of mass flux. The approach of using a constant mass flux is also used in the surface pressure balancing technique, as demonstrated in Fig. 2.16(d) for a DED process [247]. Notably, these two approaches do not explicitly consider the interaction of heat source and the powders.

Various additional molten pool models have been developed to compute the transport phenomena during DED without powder feeding simulations. For example, Fig. 2.16(e) shows the results of a transient heat transfer and fluid flow calculation using COMSOL [220]. A multilayered DED-L process was simulated with the dynamic shape of the free surface explicitly tracked using an ALE moving mesh [255]. It was found that the clad height at the two end-points of the multi-layered wall was greater, which was attributed to thermal phenomenon due to edge effect and the Marangoni effect due to liquid metal flow. A 3D thermal model using VOF method was used to investigate the transport phenomena in multi-track DED-L and to generate the thermal history of the entire process, as shown in Fig. 2.16(f) [249]. Thermal, metallurgical and mechanical aspects were computed using finite element method and element re-activation such as Abaqus or Ansys software [244]. However, liquid metal flow within the molten pool are often not considered in these FEM models.

For large-scale parts, heat transfer and fluid flow models without the powder feeding simulations are computationally efficient and tractable. However, the effects of powder heating during their flight from the nozzle to the fusion zone in these models are simplified based on several assumptions. Their impact on the accuracies of the calculated temperature and velocity fields remains to be rigorously evaluated.

### 2.8.3. Directed energy deposition with wire feeding

Wire-based DED processes are receiving increasing attention due to their high deposition rate in comparison with the powder feeding DED processes. The simulation of wire based DED has much similarity with the modeling of gas-metal-arc welding [256]. In both these processes, the heat and mass additions owing to the supply of feed stock wire need to be considered. In addition, for DED-GMA, a significant depression of the fusion zone directly under the arc is observed due to arc pressure. Significant progresses have been made for the calculation of temperature and velocity fields, fusion zone geometry and the solidification parameters as described below.

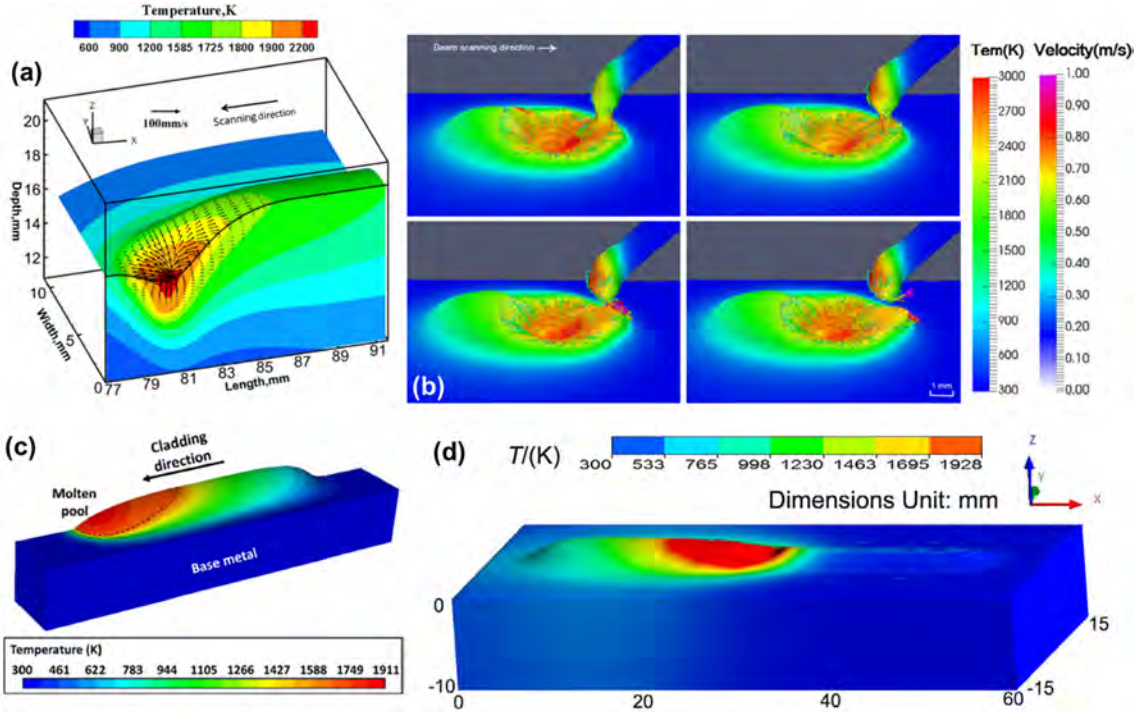

**Fig. 2.17.** Temperature and velocity fields and molten pool for wire-based DED: (a) DED-GMA [55], (b) DED-EB [83], (C) DED-L [257], (d) DED-PA [88].

Fig. 2.17 shows the temperature and velocity fields and molten pool for wire-based DED using various heat sources [55,83,88,257]. The surface morphology of the molten pool was computed using VOF or energy minimization algorithm in the modeling of wire feeding DED. For example, Ou et al. [55] used an energy minimization technique for DED-GMA, as shown in Fig. 2.17(a). Gas-metal arc welding models have simulated the transfer of metal droplets from the wire to the molten pool [258,259]. Ding et al. simulated DED-A heat transfer using Abaqus from the specified width and height of each layer [260]. They also proposed expressions for multi-layer and multi-hatch deposit geometry based on single-bead geometries [261]. The mass and energy transfer from the filler wire and the molten pool dynamics during DED-EB were numerically simulated by Hu and Tang et al [83,262]. The simulated metal transfer dynamics from the filler wire to the molten pool are shown in Fig. 2.17(b) [83]. The interface between the filler wire and the molten pool was simulated using the VOF method. The adaptive mesh refinement method was used to enhance computational efficiency.

Fluent was used to compute the transport phenomena during the wire feeding DED [257,263]. A comprehensive model was developed to compute the heat transfer and convective metal flow of the hot-wire DED-L process for single-track deposition of a maraging steel [257]. A coupled level-set and VOF method was used to capture the free surface between the gas and metal phases, with an example of the molten pool shown in Fig. 2.17(c) [257]. A three-dimensional transient model based on Fluent software was developed to compute the temperature and liquid metal flow during multi-layer DED-PA, with an example of the second layer deposition shown in Fig. 2.17(d) [88]. A model based on Fluent was developed to compute the arc, molten pool dynamic and droplet impingement during DED-GMA. The arc model was used to calculate the electromagnetic force, arc pressure, plasma shear stress and heat flux. The data were then transferred to the molten pool model [264]. Other commercial codes such as MSC Marc [265] and Abaqus [260,266] were also used to model the wire feeding DED process without considering the liquid metal convection within the molten pool.

Hybrid manufacturing processes by coupling a PBF or DED based additive technique with a conventional subtractive (or machining) process such as milling are emerging as practical routes to control the dimensional consistency of parts with complex geometry [267–270]. The mechanistic models for most of the subtractive/machining processes are well-established since these processes have been matured over a long period. In contrast, the AM processes are new and comprehensive mechanistic models for AM processes are going through initial development and validation stages, which is the main focus of the present review. Coupled

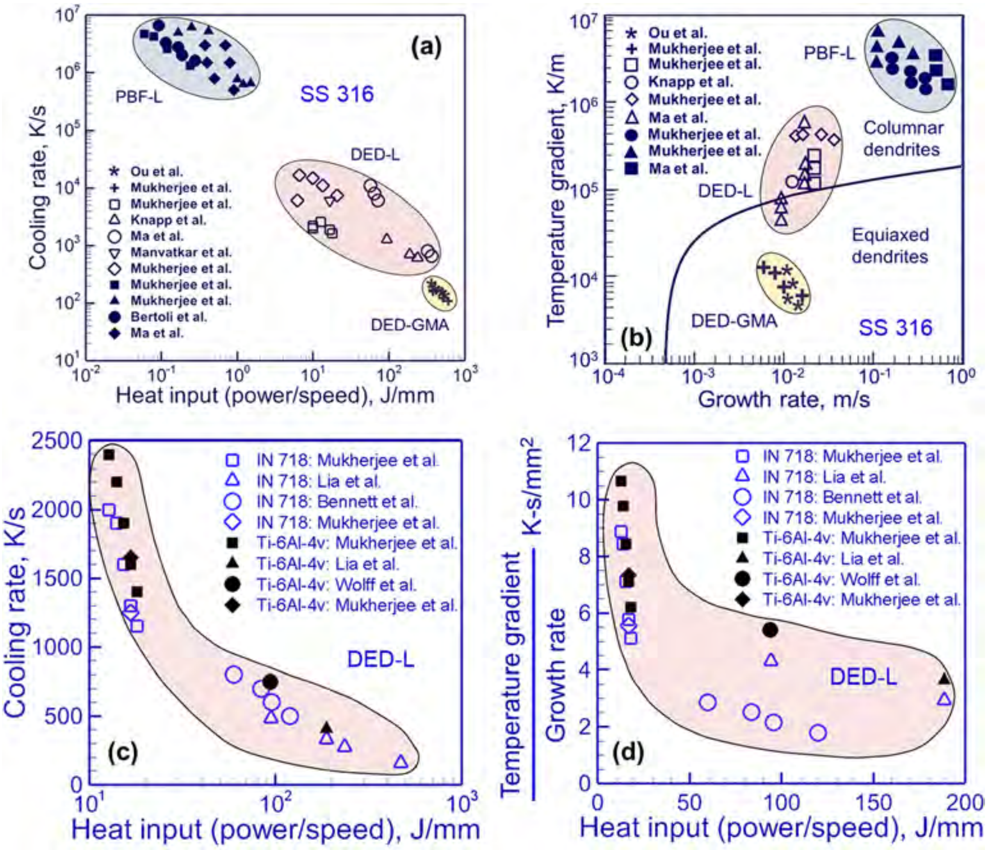

**Fig. 3.1.** (a) Variation of cooling rates during solidification calculated on the top of a SS316 build with respect to linear heat input for DED-GMA [55], DED-L [18,31,271,272], and PBF-L [19,208,271]. (b) Comparison of temperature gradient and growth rate on the solidification map [273] for DED-GMA [55], DED-L [31,271,272], and PBF-L [19,208]. Variations of (c) cooling rates during solidification [27,161,272,274,275] and (d) temperature gradient to solidification growth rate ratio [27,161,272,274,275] with heat input in DED-L of Ti-6Al-4V and IN718.

mechanistic models to analyze the sequential additive and subtractive processes, track-by-track and layer-by-layer, are critically needed but currently do not appear to be viable.

In summary, significant progresses have been made in developing both the sub-models for the component physical processes as well as comprehensive models for the widely used AM variants. Opportunities exist for developing models on each variant of the PBF and DED process based on consideration of the most important physical processes that attain accurate predictions and high efficiency

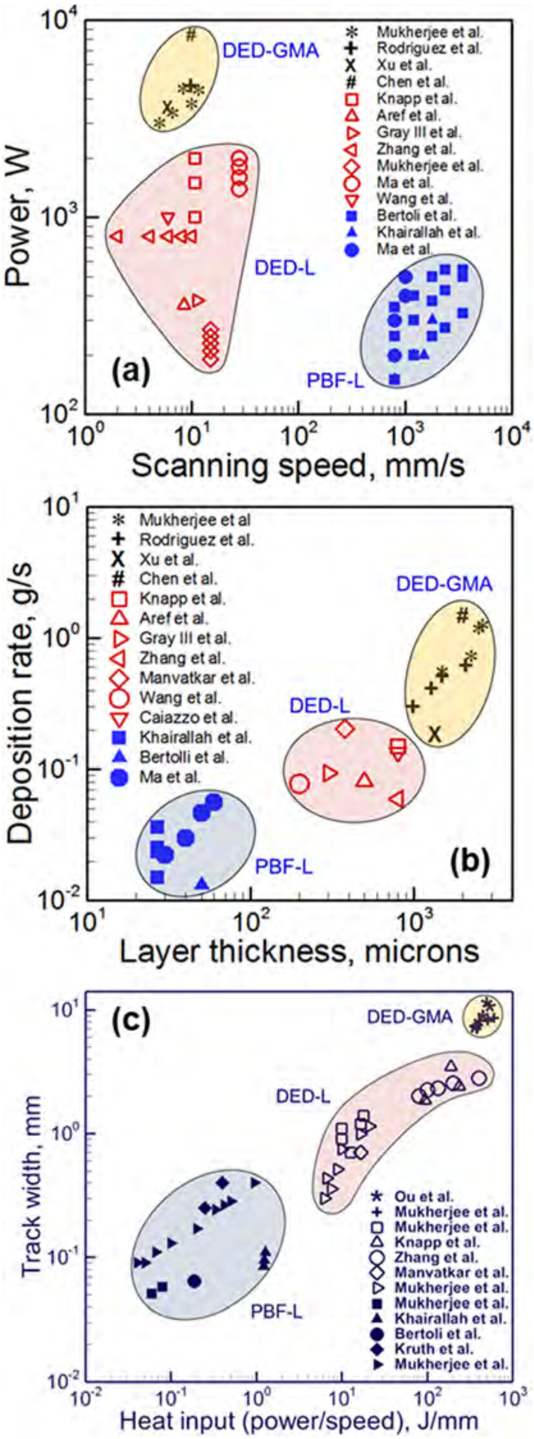

**Fig. 3.2.** Variations [18,19,23,31,55,67,72,208,271–273,276–282] in (a) heat source power and scanning speed, (b) mass deposition rate and layer thickness for PBF-L, DED-L and DED-GMA processes for SS316L, (c) The relationship of track width with heat input for DED-GMA [55], DED-L [18,31,272], and PBF-L [19,67,208,279] for SS316L.

of computations.

### 2.9. Research needs

The preceding discussion shows that significant progresses have been made in developing both the mechanistic sub-models for the component physical processes as well as comprehensive models for the widely used AM variants. The sub-models such as the heating of the powder are relatively simpler and computationally efficient. In contrast, the complexity of the physical processes in the various PBF and DED variants makes the development and testing of the comprehensive phenomenological models challenging. There are two main areas of AM modeling where future development efforts are important. First, numerical models of AM are computationally intensive for the simulation of multiple layers and hatches for the printing of real components. There is a need to quantitatively evaluate the impact of various component physical processes on the simulation results. Such evaluation would allow building more efficient models that can provide realistic simulations considering the most important physical processes. Second, the validation work of various sub-models has started but more work is needed to include well tested sub-models in large comprehensive transport phenomena-based models for all variants of AM processes.

## 3. Primary modeling results

Structure, properties and susceptibility to defect formation in AM components depend on important parameters such as transient temperature and velocity fields, molten pool shape and size, cooling rates and solidification parameters [1]. Quantitative assessments of these variables are useful to print defect free components with desired properties. In addition to single alloy components, the role

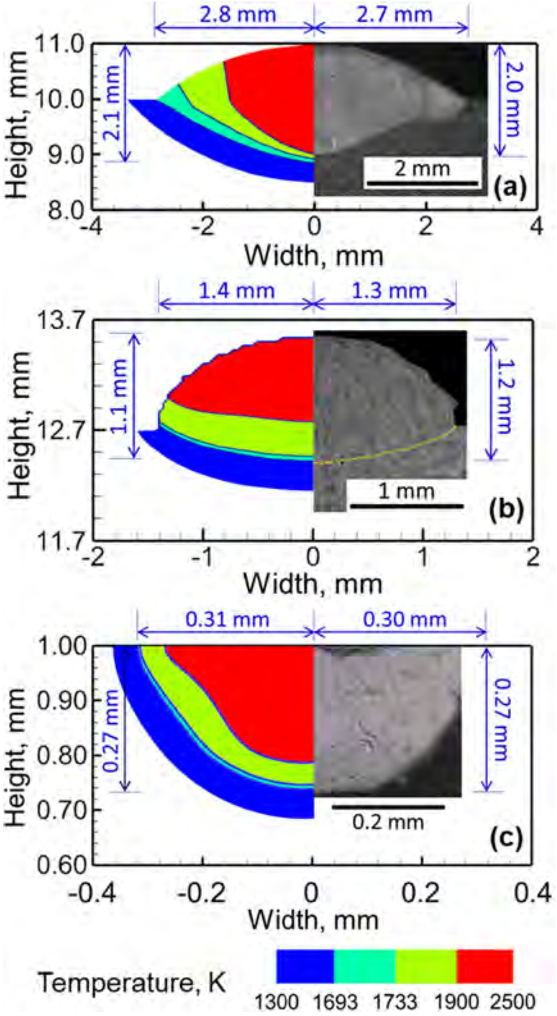

**Fig. 3.3.** Comparison between calculated transverse sections of the deposit with the corresponding experimental results for (a) DED-GMA, (b) DED-L, and (c) PBF-L. The width and depth of the deposits are provided to clearly indicate the size differences. The figure is for SS316L and is adapted from Mukherjee et al. [283].

of the mechanistic models in examining these variables for printing functionally graded alloys is also reviewed in this section. With rigorous experimental validation, the mechanistic model serves as a powerful tool for the printing of both single alloy and graded alloy components.

### *3.1. Temperatures, deposit geometries and solidification parameters*

For a particular alloy, the temperature fields, deposit geometries and solidification parameters vary widely depending on the wide range of processing conditions for different metal printing techniques [23]. For example, Fig. 3.1(a) [18,19,23,31,55,208,271,272] shows that the cooling rate during solidification is in the order of $10^6$ K/s in PBF-L, which is around 1000 times higher than that in DED-L and 10,000 times higher than that in DED-GMA. Such a high cooling rate often leads to fine microstructure in PBF-L components. In addition, both the temperature gradient and solidification growth rate that determine the solidification morphology vary widely for PBF-L, DED-L, and DED-GMA [19,31,55,208,271–273] as shown in Fig. 3.1(b). Columnar dendrites often form during PBF-L for high values of the ratio of temperature gradient over solidification rate. However, for the same printing process, different alloys exhibit various magnitudes of these variables due to their differences in thermo-physical properties. For example, Fig. 3.1(c) and (d) show that for DED-L cooling rate, temperature gradient and solidification growth rate [27,161,272,274,275] vary significantly depending on the alloy system used. Transport phenomena-based models can provide information about the extent of these variations

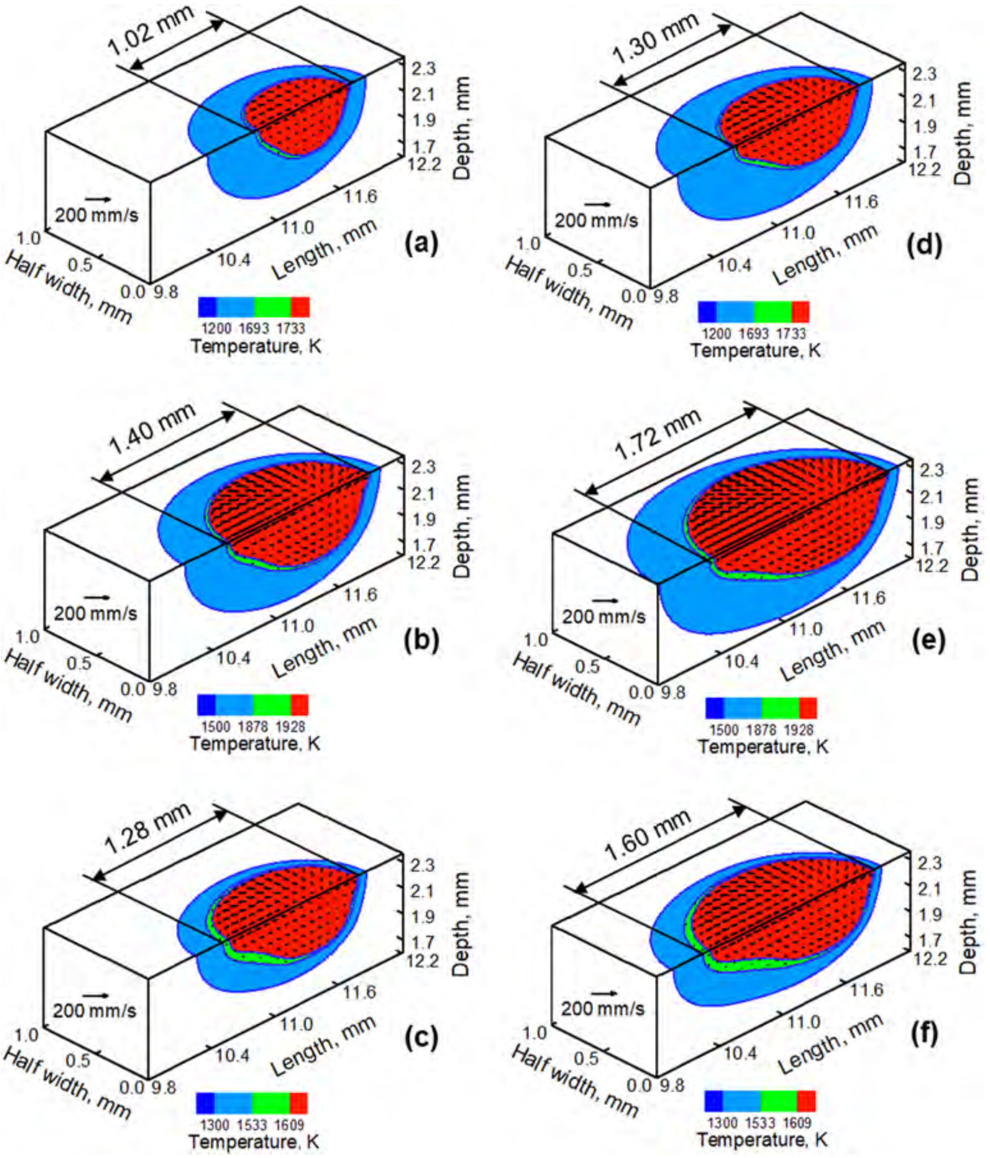

**Fig. 3.4.** Temperature and velocity fields and molten pool geometry for laser power of 190 W for (a) SS316 (b) Ti-6Al-4V (c) IN718 and of 230 W for (d) SS316 (e) Ti-6Al-4V (f) IN718. All data are for 15 mm/s scanning speed of DED-L [272].

for different AM processes and alloys.

### 3.1.1. Variations for different processes

For a particular alloy, metallurgical variables vary primarily due to the differences in process conditions and amount of material melted and deposited during different printing processes. The power and the scanning speed of the heat source for DED-GMA, DED-L, and PBF-L can vary widely as shown in Fig. 3.2(a) [18,19,23,31,55,67,72,208,271–273,276–281]. The scanning speed in PBF-L is on the order of $10^3$ mm/s, which is around 100 times higher than those in DED-L and DED-GMA. The heat source power in DED-GMA is on the order of several kW, which is around 10 times higher than those in DED-L and PBF-L. Fast scanning speed and low heat input of the heat source in PBF-L is responsible for very high cooling rates as shown in Fig. 3.1(a). Similarly, Fig. 3.2(b) [18,19,23,31,55,67,72,208,271–273,276–282] shows that the high deposition rate in DED-GMA facilitates the process to build the component using layer thickness that is 2 to 3 times higher than that in DED-L. The PBF-L components are printed with thin layers that are 10–50 times thinner than those used in DED-L and DED-GMA. Fig. 3.2(c) [18,19,23,31,55,67,208,271–273,276–279] shows the correlation of the width of the deposited track with the linear heat input which is the ratio of power to scanning speed for

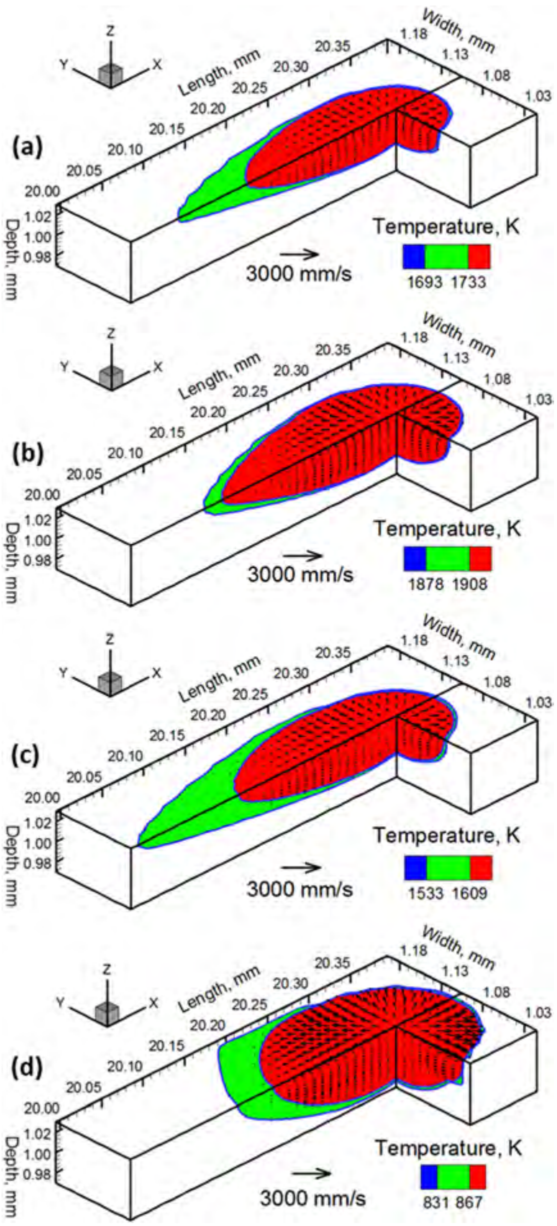

**Fig. 3.5.** Three-dimensional temperature and velocity distributions in the 1st layer 1st hatch of a 20 mm long PBF-L build of (a) SS316, (b) Ti-6Al-4V, (c) IN718, and (d) AlSi10Mg using 1000 mm/s scanning speed. Scanning direction of the laser beam is along the positive x-axis [19].

different approaches. The width of the track produced by PBF-L is on the order of 100 µm, which is close to the diameter of the laser spot used. The track widths in DED-L and DED-GMA are larger due to correspondingly higher heat inputs.

Effects of these aforementioned variations of process conditions for different printing processes are captured by heat transfer and fluid flow models where temperature field and deposit geometry are calculated for SS316 for PBF-L, DED-L, and DED-GMA [283]. Fig. 3.3 [283] compares the calculated shape and size of the transverse section of single track SS316 builds printed using the three different processes. The molten pool is bounded by the solidus (1693 K) isotherm. The linear heat input (power/speed) in PBF-L is on the order of 0.1 J/mm, Fig. 3.2(a), which results in very small pool with dimensions in micrometers. However, linear heat inputs in DED-L and DED-GMA are in the order of 10 J/mm and 100 J/mm, respectively. Therefore, the molten pool width in DED-GMA is the largest followed by that in DED-L. Fig. 3.3 shows that the pool dimensions in PBF-L are around 10% and 30% of those for DED-GMA and DED-L respectively. Smaller molten pool cools rapidly and therefore, PBF-L components experience fast cooling rate during solidification as pointed out in Fig. 3.1(a). In addition, small molten pools have large temperature gradient that increases the temperature gradient to solidification growth rate ratio. Therefore, PBF-L exhibits a high temperature gradient to growth rate ratio that results in columnar grain as pointed out in Fig. 3.1(b).

### 3.1.2. Variations for different alloys

For a particular AM technique with a specified set of processing conditions, various alloys exhibit remarkably different metallurgical variables due to the differences in their thermophysical and mechanical properties (as shown in Table 2.1). Fig. 3.4 shows that the molten pool size exhibited by three common AM alloys, namely SS316, Ti-6Al-4V and IN718, differs in both shape and size when deposited using the same processing conditions during DED-L [272]. In these figures, the red and green bands indicate the liquid and two phase solid-liquid regions, respectively. The larger pool volume for Ti-6Al-4V is attributed to its lower density and thermal diffusivity than those of SS316 and IN718. In addition, higher power results in larger pools (Fig. 3.4(d)–(f)) for each of the alloys as compared to that for lower powers (Fig. 3.4(a)–(c)). Similar observations can also be made during PBF-L [19], as shown in Fig. 3.5. For a given processing condition, AlSi10Mg exhibits the largest molten pool due to its low density and liquidus temperature. The build with IN718 alloy powder exhibits the largest mushy zone due to the maximum difference between the liquidus and solidus temperatures.

The different thermophysical properties of various alloys result in remarkable differences in temperature field, cooling rates and

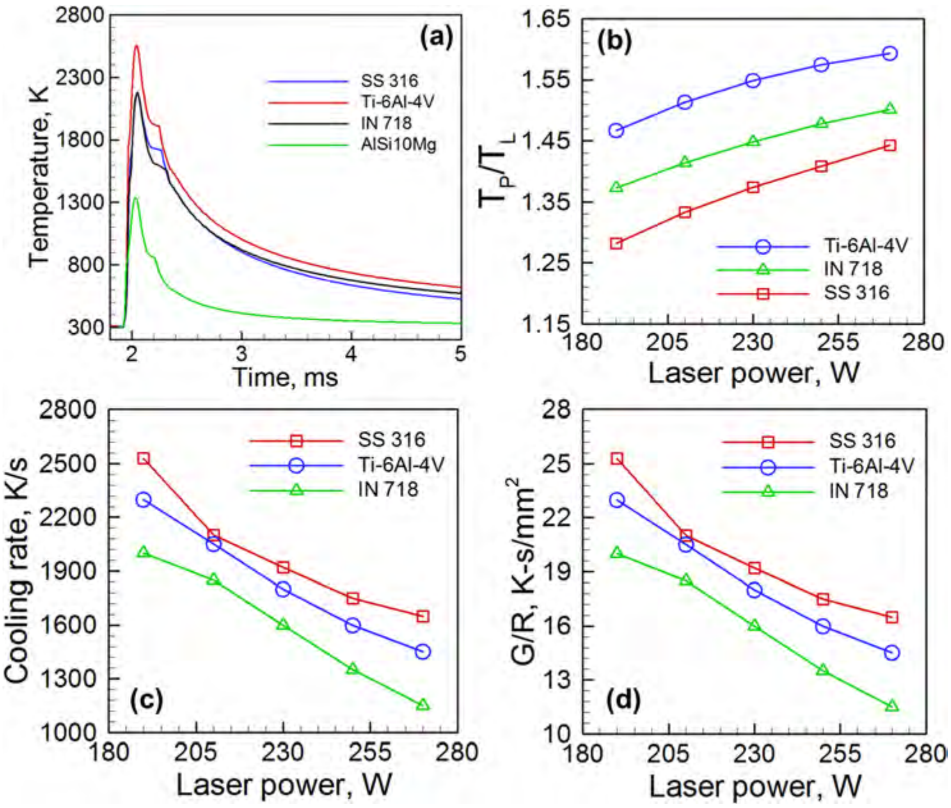

**Fig. 3.6.** (a) Temperature variation with time for a location on the top surface and at the mid length of first layer, first hatch of the PBF-L build of four different alloys using 1000 mm/s scanning speed [19]. (b) Effects of the laser power for three alloys during DED-L on the ratio of peak temperature ($T_P$) to liquidus temperature ($T_L$). (c) Cooling rate during solidification. (d) Ratio of temperature gradient (G) to solidification growth rate (R) [272].

solidification parameters, such as, ratio of temperature gradient (G) to solidification growth rate (R) [23]. For example, Fig. 3.6(a) compares the variations in temperature with time for a particular location of PBF-L builds of four alloy powders processed with the same laser power and scanning speed [19]. All four alloy builds exhibit the similar thermal cycle that is the unique characteristic of the AM process. The results show that the heating rate is very high and the alloy feedstock exceeds the liquidus temperature within a few microseconds after the heat source energy is applied. However, the rate at which the built part cools is slower than the rate of heating. The rate of cooling primarily depends on the thermal diffusivity of the alloy and the ambient conditions. For all four alloys, during the cooling, the thermal cycle exhibits a 'knee' like shape due to the liquid-solid phase change during the solidification. For the same heat input, the peak temperatures for different alloys differ primarily due to the thermo-physical properties such as density, specific heat and thermal conductivity. A specified heat input per unit volume of the feed stock material results in high peak temperature for low density alloys. Therefore, the highest peak temperature for the Ti-6Al-4V build is attributed primarily to its lowest density among the four alloys. The AlSi10Mg build exhibits the lowest peak temperature because of its highest thermal diffusivity among all four alloys which facilitates rapid heat transfer from the molten pool and reduces the peak temperature.

Similar trends in the peak temperature are also observed during DED-L [272] as shown in Fig. 3.6(b). The ratio of the peak temperature, $T_P$, to the liquidus temperature, $T_L$, for the three alloys examined increases with laser power. The reductions in both cooling rate during solidification and G/R with laser power are attributed to slower cooling of larger molten pools for high laser power [272], as shown in Fig. 3.6(c) and (d), respectively. The lowest density of Ti-6Al-4V also contributes to the formation of a large molten pool for this alloy. The slower cooling rate of IN718 than SS316 deposits can be attributed to its larger difference between the liquidus and solidus temperatures. The temperature gradient in the DED-L molten pool is the smallest for IN718 deposits followed by that in Ti-6Al-4V and SS316 alloy deposits. As a result, the SS316 deposits exhibit the highest G/R followed by that of Ti-6Al-4V and IN718 alloy deposits.

From the aforementioned results it is evident that the important variables such as the cooling rate, solidification growth rate and temperature gradient can vary widely depending on the printing process, process parameters and alloys system used. These variables largely depend on molten pool geometry and heat and mass transport inside the molten pool. Since, convective flow of liquid metal often dominates the heat transfer mechanism inside the molten pool, it is worthwhile to review the effects of molten metal convection on these variables. In addition, it is also important to examine when the effects of convection can be neglected. This is important because heat conduction calculations that do not consider convection can significantly improve computational speed.

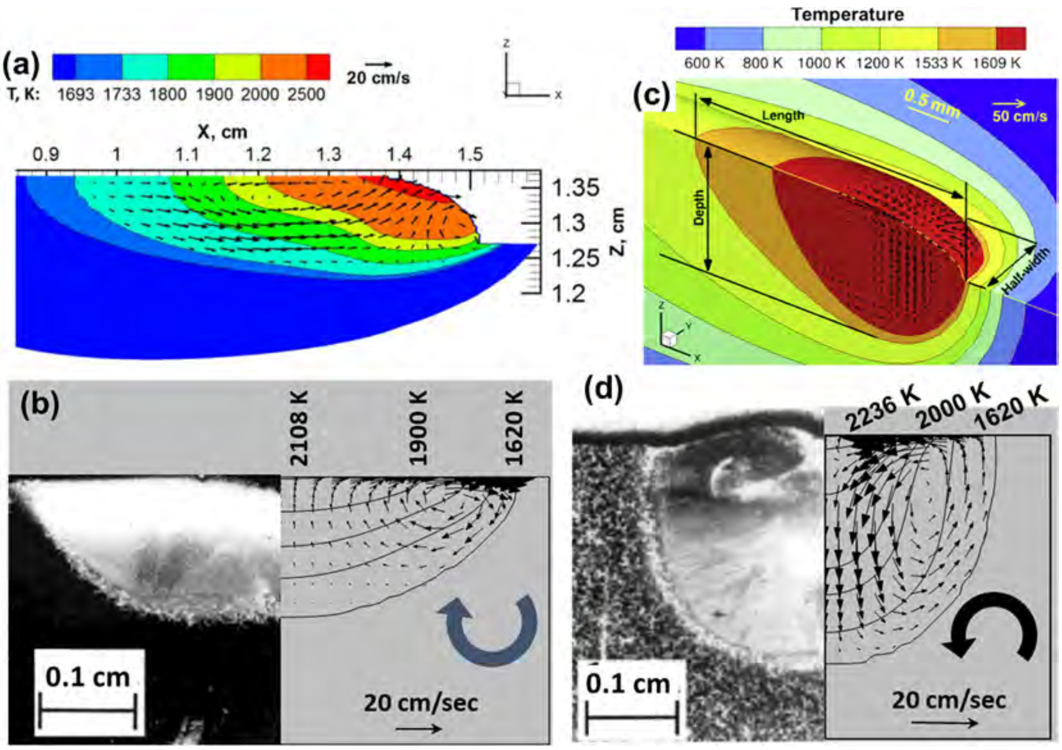

**Fig. 3.7.** Convective flow of liquid metal in the molten pool under laser irradiation. (a) and (b) Outward flow from the center to the periphery of the molten pool [31,41]. (c) and (d) Inward flow from the periphery to the center of the molten pool [41,284]. Figures (a) and (c) are for DED-L of SS316L and IN718 respectively. Figures (b) and (d) are for laser welding of stainless steel.

## 3.2. Effects of molten metal convection

### 3.2.1. Fluid flow in DED and PBF processes

Convective flow of liquid metal inside the molten pool is primarily caused by the combined effects of the Marangoni, electromagnetic, buoyancy forces, and momentum from mass transfer as explained in Section 2.3.1. Both the Marangoni and buoyancy forces are considered for calculations in all AM processes [1], whereas the electromagnetic and droplet impingement forces are generally important only for the DED-GMA and DED-PA processes [55]. Though electromagnetic forces are present in PBF-EB they can generally be neglected, because the typical electric current that governs the magnitude of the Lorentz force is very low ($\sim 10^{-2}$ A) compared to DED-GMA ($\sim 10^{2}$ A) [55,80]. In laser and electron beam AM, the buoyancy force is significantly lower than that of Marangoni force [55,82] and can often be neglected in the calculations. The mixing of hot and cold liquids due to convective flow reduces the temperature gradient inside the molten pool and affects the peak temperature, cooling rate, temperature gradient and the solidification growth rate [17]. Therefore, accurate calculations of heat transfer during AM need to consider the effects of the convective flow of molten metal in the fusion zone.

The liquid metal commonly flows from the center outward to the edge on the top surface of the molten pool, as shown in Fig. 3.7(a) and (b) [31,41]. However, the flow direction may reverse with the presence of surface-active element such as sulfur or oxygen, i.e., from the periphery inward to the center of the molten pool, as shown in Fig. 3.7(c) and (d) [41,284]. The penetration depth of the molten pool is significantly larger in the case of inward flow due to the heat transported to the bottom of the fusion zone, which results in a greater depth-to-width ratio. Heat conduction calculations that ignore convective flow cannot simulate the role of surface-active elements on the changes in the shape and size of the fusion zone, cooling rates and solidification parameters.

The liquid metal convection is primarily driven by the spatial gradient of surface tension which is a function of the local temperature gradient and the temperature coefficient of surface tension, $d\gamma/dt$ [20]. Fig. 3.8 shows the variations in surface tension, $\gamma$, and the temperature coefficient of surface tension, $d\gamma/dt$, with temperature and the concentrations of oxygen and sulfur [285]. It can be seen from Fig. 3.8(b) that for low oxygen concentration such as 1 ppm, $d\gamma/dt$ is negative over a wide temperature range. Negative values of $d\gamma/dt$ means higher surface tension at lower temperatures and vice versa. In this case, the liquid metal on the surface of the fusion zone flows from the middle to the periphery. In contrast, $d\gamma/dt$ is positive over the entire range of temperature on the molten pool surface at sufficiently high concentrations of the surface-active elements such as the cases shown in Fig. 3.7(c) and (d). The sign of $d\gamma/dt$ may also change from negative to positive at certain temperature and concentration of the surface-active elements, e.g.,

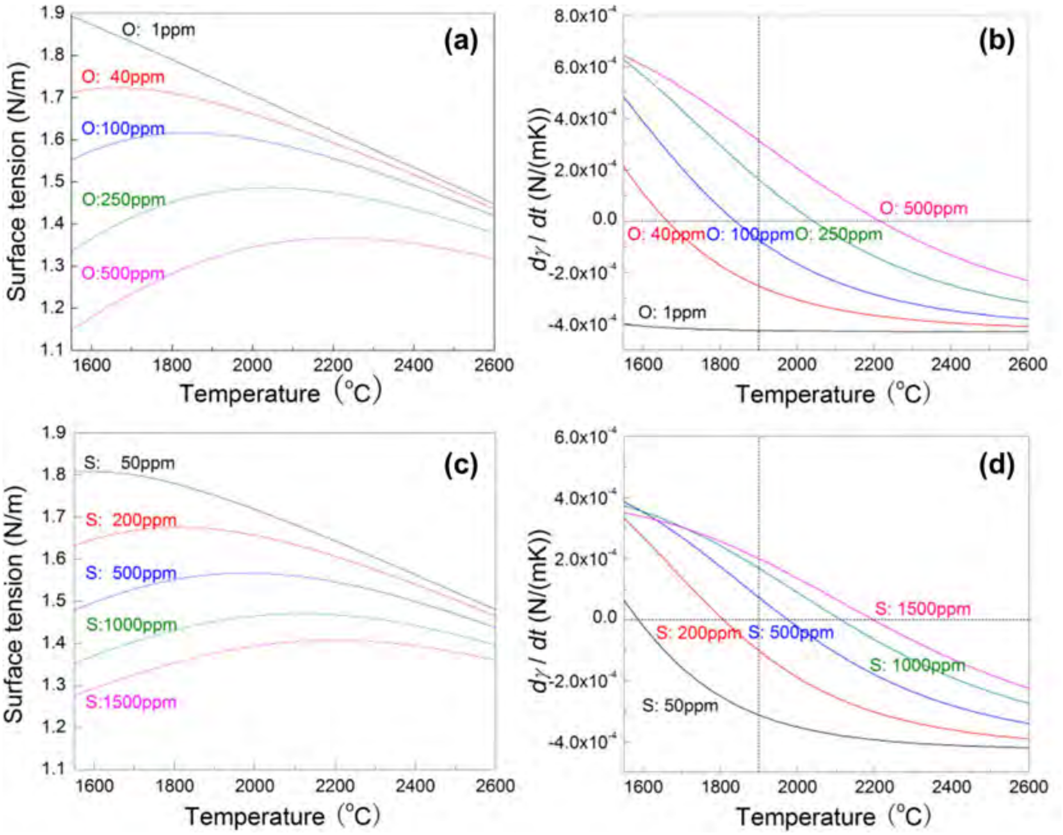

**Fig. 3.8.** (a) and (b) Surface tension and temperature coefficient for Fe–O system as function of temperature [285]. (c) and (d) Surface tension and temperature coefficient for Fe–S system as function of temperature [285].

500 ppm of sulfur as shown in Fig. 3.8(d). Thus, the direction of the liquid velocity may change direction and appear at an intermediate temperature between the solidus and the peak temperatures of the molten pool [285,286].

The aforementioned variations in $d\gamma/dt$ result in different shapes of the molten pool as shown in Fig. 3.9. The fluid flow in the molten pool and the resultant changes in fusion zone shape and size during DED-L are significantly affected by the sulfur concentration [252]. The shape and size of the molten pool in multilayer DED-L depend on the interaction of surface tension, gravity effect associated with interaction time between deposit layers, and fluid convection [252]. The manipulation of the thermocapillary gradient of the molten pool can be used to tune the nonuniformity and surface finish of the deposit sidewall during DED. The molten pool shown in Fig. 3.9(a) and (b) demonstrate a net movement of the liquid metal from 303 SS with high sulfur to 304L SS with low sulfur [287], which originates from the Marangoni convection. The rotational asymmetry of the molten pool shown in Fig. 3.9(c) results from the interaction between the velocity field in the molten pool and its linear motion with the scanning of the laser beam [287]. The variable shapes of the molten pool shown in Fig. 3.9(d)–(f) are attributed to the heat input parameters and the thermophysical properties of the materials. The wavy boundary shown in Fig. 3.9(f) originates from the interaction of counter-rotating liquid metal loops at high Marangoni forces [288]. Fig. 3.9(g)–(k) show the variation of the sulfur concentration profile in the longitudinal section [247]. The sulfur content in the molten pool experienced a transition from the maximum at the beginning of the track due to the concentration of sulfur in the substrate to the end of the track due to the addition of the sulfur-free powder feedstock. Thus, the liquid metal flow correspondingly experienced the inward, mixture, and outward patterns along the deposition path of the track.

The velocity of liquid metal flow is on the order of 1 m/s during AM depending on the value of the temperature coefficient of

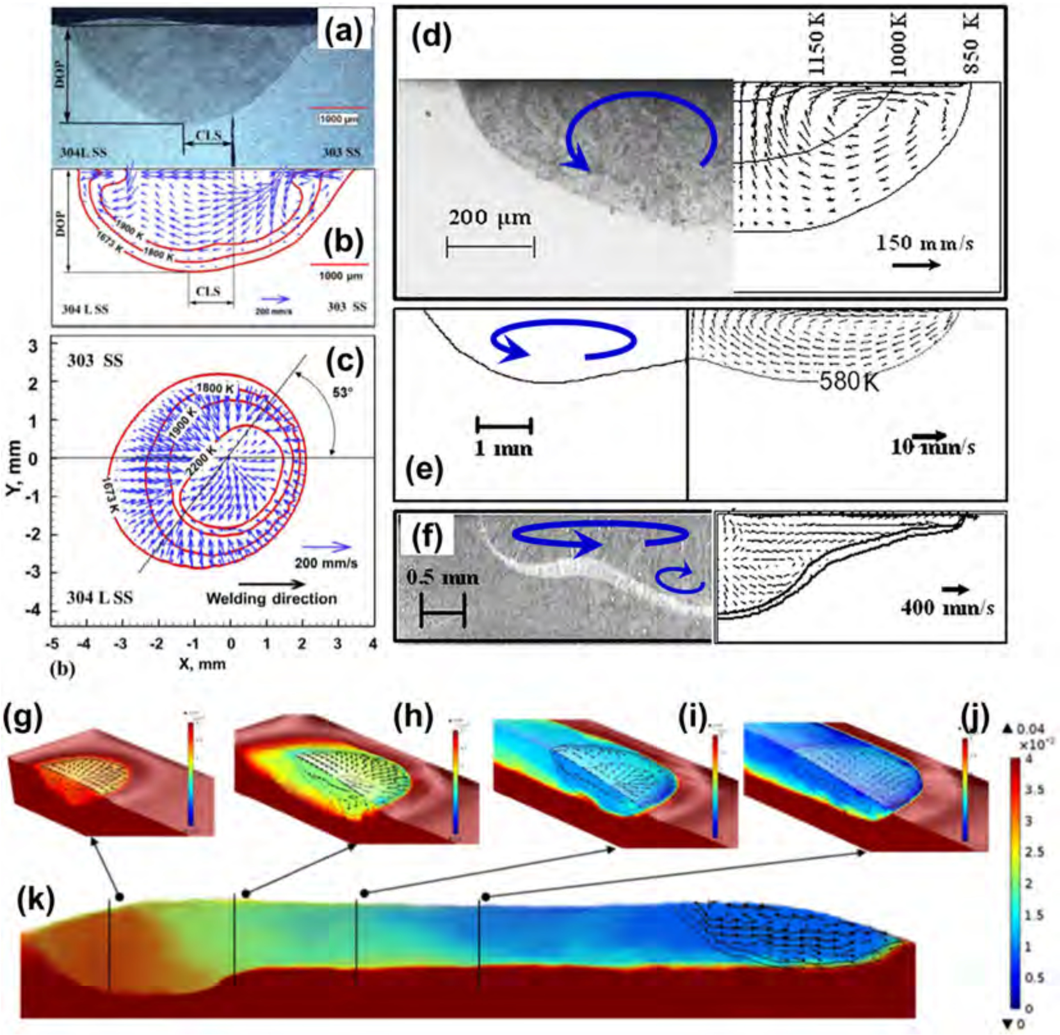

**Fig. 3.9.** Various molten pool shapes with different flow patterns of the liquid metal. (a)–(c) The center line shift, rotational and translational asymmetry of the molten pool during welding of two stainless steels with different sulfur concentrations [287]. (d)–(f) Molten pool geometries of Al alloy 5182, NaNO3, and steel, respectively [288]. (g)–(k) Variation of the sulfur concentration and fluid flow pattern in different longitudinal sections of a DED-L sample [247].

surface tension, $d\gamma/dt$ and local temperature gradient [19,22,167,289]. This flow of molten metal influences the pool geometry (as explained in Fig. 3.9), heat transfer mechanism inside the pool and thus the metallurgical variables. Therefore, calculations of these variables using heat conduction models that ignore the effects of molten metal convection are often unrealistic. For example, Fig. 3.10(a) shows that the heat conduction calculation significantly overestimates the transient temperature distribution during DED-L [290]. Similarly, the peak temperature in PBF-L estimated by heat conduction model is overestimated by approximately 400 K [290], as shown in Fig. 3.10(b). Since molten metal convection mixes hot and cold liquid and reduces the peak temperature, the temperature values predicted by heat conduction models are overestimated. In the absence of surface-active elements like sulfur and oxygen [19,127], liquid metal flows from the center to the periphery of the molten pool, resulting in a wide and shallow deposit. In contrast, heat conduction calculations, where convective flow is neglected, predict narrower and deeper molten pool geometries that often do not agree well with the experimental measurements [55,216], as shown in Fig. 3.10(c). Convective flow reduces temperature gradients in the liquid metal, allowing the molten pool to cool and solidify faster than the cooling rates predicted by conduction calculations. As a consequence, calculated cooling rates during solidification by neglecting the molten metal convection are higher and often do not agree with experimental data [17,55], as shown in Fig. 3.10(d) and (e) for DED-GMA and DED-L, respectively. It has been shown in the literature [17] that simple mechanical properties such as micro-hardness can be estimated from the calculated cooling rate during solidification for SS316. Fig. 3.10(f) shows the variations in micro-hardness values for SS316 components [17]

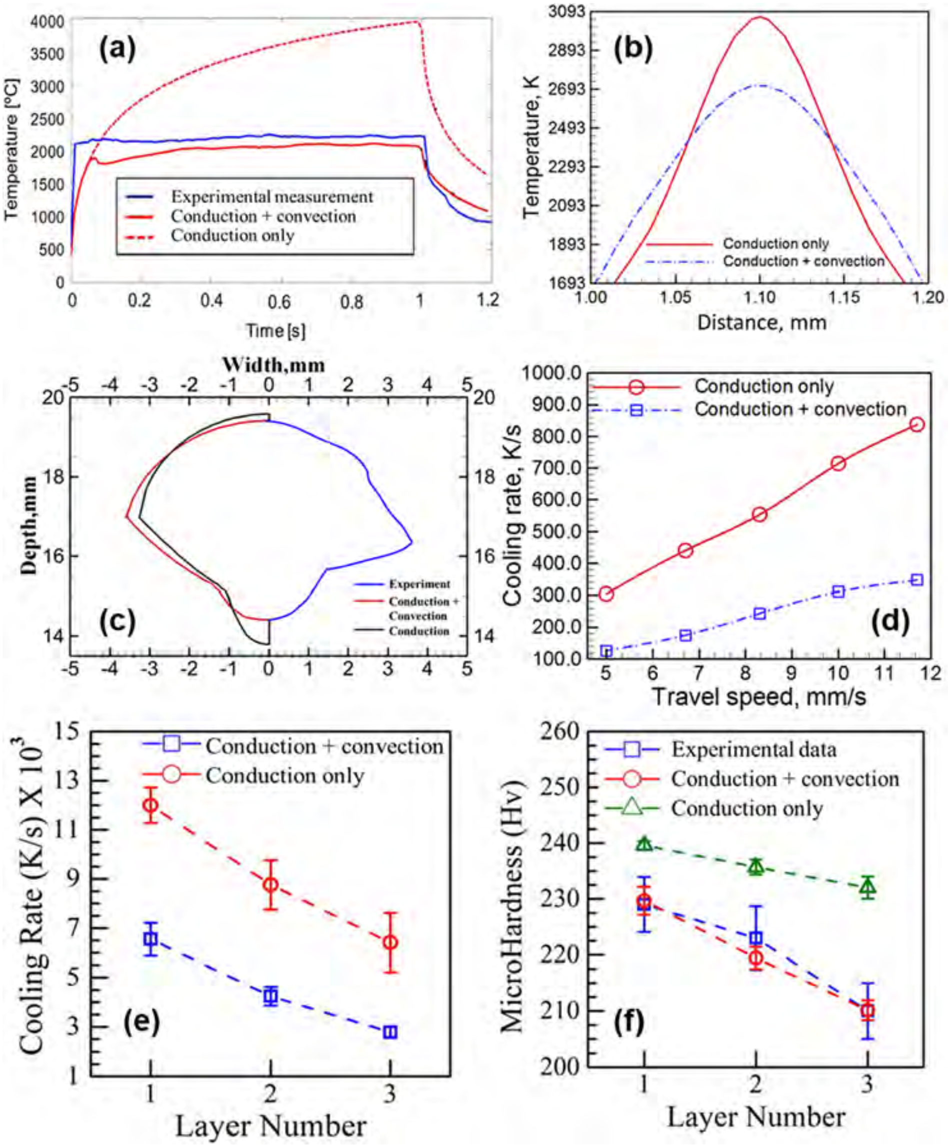

**Fig. 3.10.** Comparisons between conduction only and conduction + convection calculations of (a) Temperature variation with time during DED-L [290], (b) Spatial distribution of temperature field in PBF-L [290], (c) Build geometry for DED-GMA [55], (d) Cooling rates during solidification in DED-GMA [55], (e) Cooling rates during solidification in DED-L [17], and (f) Micro-hardness of SS316 DED-L component [17].

fabricated by DED-L calculated based on the cooling rates. The micro-hardness values calculated using the cooling rates estimated using heat conduction models are also overestimated and do not agree with the experimental measurements [17]. In the heat conduction models, often the effects of convective flow are incorporated by artificially increasing the thermal conductivity of liquid metal. However, this method is unable to capture the effects of surface-active elements on the shape and size of the molten pool.

### 3.2.2. When can molten metal convection be neglected?

From the aforementioned results it is clear that the calculated metallurgical variables neglecting the effects of molten metal convection often do not agree with the experimental observations. However, incorporation of molten metal flow makes the model computationally expensive. Arrizubieta et al. [290] noted that computational time can be reduced by ten times by neglecting the effect of molten metal convection. Therefore, before any model is developed, it is important to determine whether it is necessary to include the effects of molten metal convection. Traditionally, the Peclet number (see Section 5.1.1) indicates the relative importance of convective heat transfer over heat transfer by conduction [20], and is used to evaluate the importance of molten metal convection. Effects of molten metal convection are considered to be significant if the Peclet number is much greater than unity [1]. More recently, scanning speed in AM has been found to be a significant factor that determines the importance of molten metal convection. Fig. 3.11(a) shows that the heat conduction model overestimates the deposit geometry for DED-L by 31% at a scanning speed of 500 mm/min [290]. However, in Fig. 3.11(b), the deposit geometries calculated both considering and neglecting molten metal convection are similar at a scanning speed of 1000 mm/min [290]. Similarly, Fig. 3.12 shows that the effects of molten metal convection on peak temperature and pool width during PBF-L become less significant at high scanning speeds [19,290]. At higher scanning speed, the molten pool solidifies rapidly even before the convective flow can mix the hot and cold liquids. Therefore, inclusions of molten metal convection in the modeling for very high speed AM processes often provides limited advantage. Arrizubieta et al. [290] proposed an empirical quantity ($MP$) to quickly evaluate the significance of molten metal convection in DED-L. Effects of molten metal convection are significant when the value of $MP$ is greater than unity.

$$MP = C\ t\left(\frac{P}{\pi\ r_b^2\ V}\right)^2/(1+\dot{m}) \tag{3.1}$$

where $P$, $r_b$, $V$, $\dot{m}$ and $t$ represent heat source power, beam radius, scanning speed, powder mass flow rate and average time for which molten pool remains liquid estimated based on pool length and scanning speed, respectively. $C$ is a constant whose value is in the order of $10^{-4}$ for the AISI 304 steel used for this investigation. However, it is not known how the value of this constant can be calculated for different alloys depending on their thermo-physical properties.

These methods for evaluating the importance of molten metal convection either depend on empirical relations that are useful only for a certain set of process conditions and alloy system or largely depend on the simulation results. Therefore, most of these methods cannot be used to judge whether to include the effect of molten metal convection before developing the model. Therefore, currently, techniques to evaluate the importance of molten metal convection for all processes and alloy systems are scarce and thus need further research. However, conditions for which the effects of molten metal convection are significant, heat conduction models result in unrealistic results.

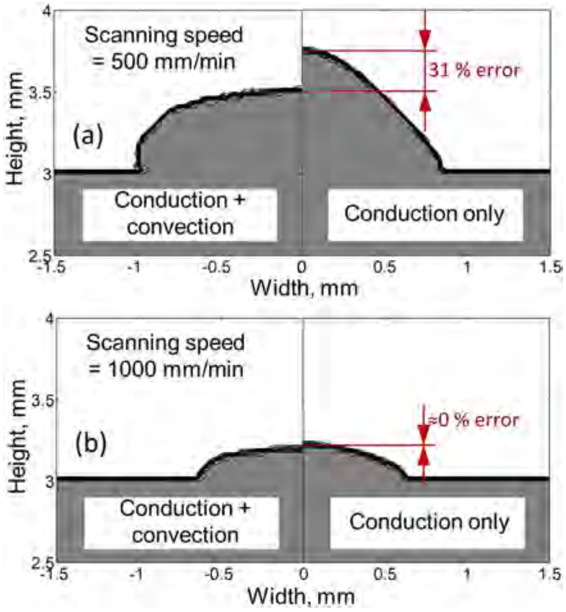

**Fig. 3.11.** Comparison of deposit geometries during DED-L calculated both considering and neglecting the effects of molten metal convection at scanning speeds of (a) 500 mm/min and (b) 1000 mm/min [290].

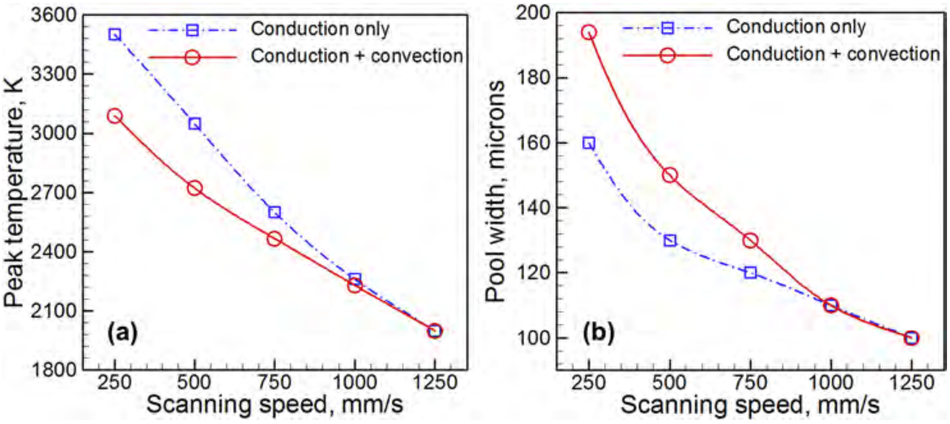

**Fig. 3.12.** Comparison of (a) peak temperature and (b) pool width at different scanning speeds during PBF-L calculated both considering and neglecting the effects of molten metal convection. (Calculated results based on the model proposed by Mukherjee et al. [19].)

### 3.3. *Computed results for AM of functionally graded alloys*

As mentioned earlier, the transient temperature and velocity fields, molten pool shape and size, cooling rates, and solidification parameters are essential metallurgical variables for understanding the microstructure and properties of the as-built part. While the precise relationships between these variables and the as-built microstructure will be explored in Section 4.1, this section focuses on the unique challenges associated with understanding the impact of these variables for functionally graded alloys.

While a standard part will typically be manufactured using a single set of processing parameters, a functionally graded part will require a spatial variation of processing parameters to successfully incorporate the compositional or microstructural gradients. For compositionally graded parts, this requires an understanding of the thermo-physical properties of all alloys involved and the metallurgical variables that result from processing. Significantly varying thermo-physical properties throughout the graded region can result in build failures if no precautions are taken, such as in a grading between Invar and Ti-6Al-4V that failed due to a low melting point composition around 20 vol% Invar [144]. In microstructurally graded parts, the reaction of a single material to changes in processing parameters must be well understood in order to spatially vary process variables in an appropriate manner. Sufficient sensitivity of the columnar-to-equiaxed transition of IN718 alloy to changes in processing parameters during PBF-EB has been shown by the successful spatial control over equiaxed or columnar grain formation [49]. Subsequent modeling efforts enabled calculation of the essential metallurgical variables during processing, providing further understanding of the process [82,205,291].

The basis of understanding sensitivity of metallurgical features to process parameters for single alloys is the focus of many experiments and modeling efforts. For example, the power of the heat source or scanning speed is often varied to observe changes in pool size [236] or microstructure [292]. These results create an initial understanding for building compositionally graded alloys, however, mixing of different alloys in the molten pool due to remelting of previous tracks and heterogeneous thermo-physical properties throughout can cause further complications. Differences in thermal diffusivity and melting range of compositionally graded alloys can cause differences in the rate of heat accumulation and molten pool volume within different areas of the part. Fig. 3.13 shows the results of this effect through the modeling of temperature and velocity fields in graded joints of Alloy 800H with Ti-6Al-4V and 2.25Cr-1Mo steel [28]. A total of 10 layers were deposited, starting with Ti-6Al-4V alloy or 2.25Cr-1Mo and varying composition to increase the amount of Alloy 800H by 10 wt% in each layer. Since most of the heat is transferred downwards through the substrate, heat transfer from the molten pool is dependent on the thermal diffusivity of previous layers. Due to the lower thermal diffusivity of Ti-6Al-4V compared to of 2.25Cr-1Mo steel, more heat build-up in the part occurs and a larger molten pool forms in the tenth layer when grading from Ti-6Al-4V, Fig. 3.13(f) than when grading from 2.25Cr-1Mo steel, Fig. 3.13(c). Because the processing parameters and composition used for the tenth layer were the same in both simulations, this case highlights the difficulty in extrapolating existing knowledge for the sensitivity of metallurgical variables to processing parameters in single alloys to compositionally graded alloys. However, it also highlights the utility of numerical modeling in understanding and designing processing paths for manufacturing graded parts.

Spatially varying thermo-physical properties in compositionally graded joints also affect cooling rates and solidification parameters inside the molten pool [97,138]. Fig. 3.14 shows that both cooling rate and the solidification parameter G/R change during the deposition of subsequent layers during simulation of a cast iron to Ni-base alloy graded part [97]. Depending on the differences in thermo-physical properties that govern heat transfer between the two alloys, these differences may be exaggerated or diminished. Sensitivity of microstructural variation of different alloys can also vary widely. For example, the columnar to equiaxed transition (CET) region of the graded alloy between Ti-6Al-4V and a nickel alloy Rene 88 shifts depending on the composition, as shown in Fig. 3.15 [293]. The sensitivity of microstructure the solidification parameters is even more important in microstructurally graded parts, because it directly determines the ability of microstructural grading in the material. While the CET of IN718 alloy parts made by PBF-EB can be controlled [49], not all material and process combinations may demonstrate a similar microstructural response to process parameter changes. Mechanistic models can be helpful in addressing these issues.

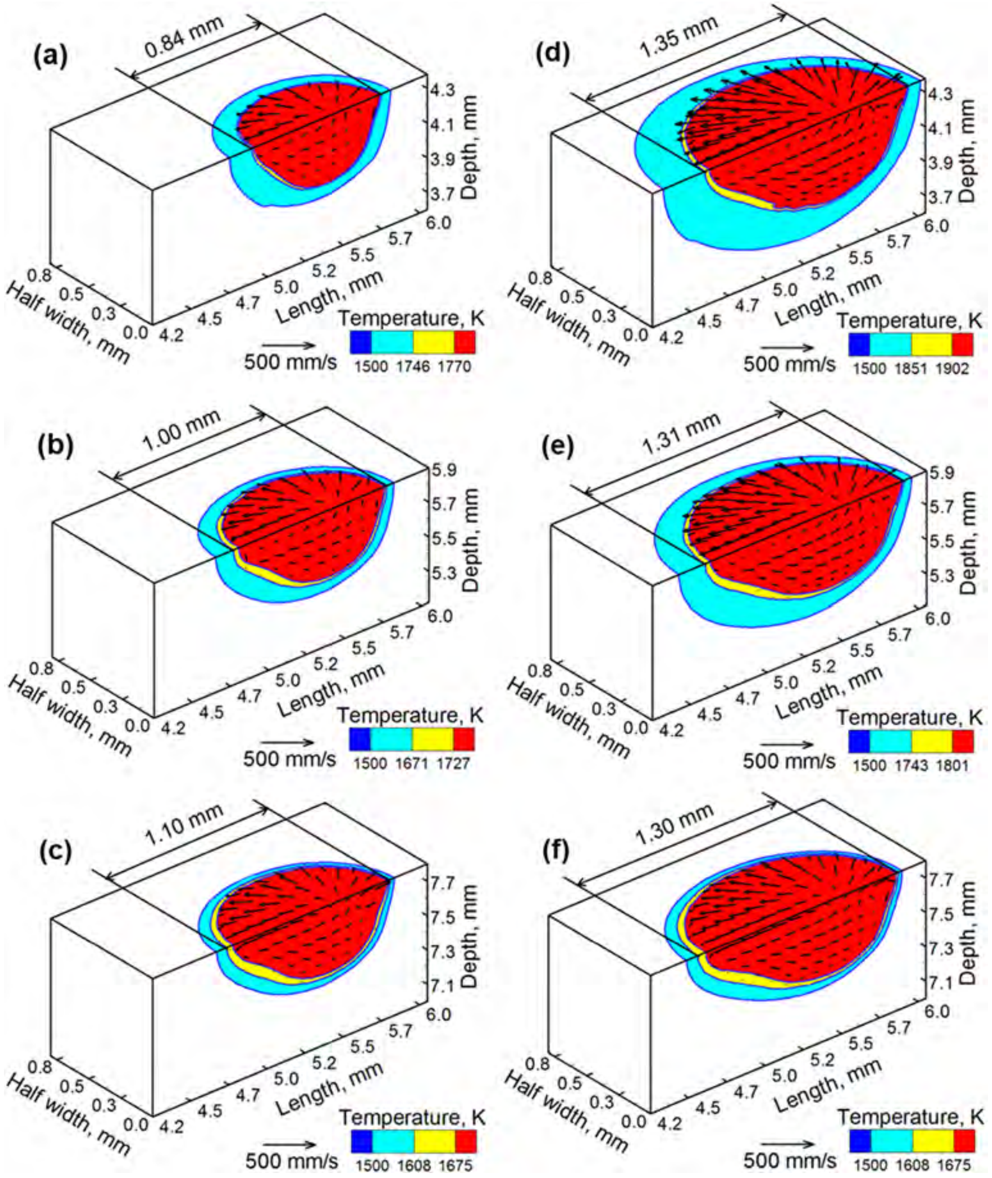

**Fig. 3.13.** Temperature and velocity distributions [28] for 2.25Cr-1Mo steel to 800H joint during the deposition of (a) 1st (b) 5th and (c) 10th layer and for Ti-6Al-4V to 800H joint during the deposition of (d) 1st (e) 5th and (f) 10th layer.

During the fabrication of parts with compositional grading, detrimental phases may sometimes form. Due to the combination of two alloys in the gradient region, brittle intermetallic compounds may form that lead to cracking [294,295]. Undesired intermetallic phases can be suppressed through careful selection of the compositional gradient based on phase diagrams generated using a thermodynamic model [294–296]. For common alloy systems with a small number of alloying elements, the available experimental data may be helpful to avoid these problems. However, for uncommon alloys or alloys with a large number of alloying elements, the ability of thermodynamic models to accurately predict phases is limited by the available thermodynamic databases and thus requires further research.

## *3.4. Research needs*

The computed results from transport phenomena-based models presented in this chapter show their utility for the understanding of the geometry, composition and structure of the metallic components. The computed results reveal the origins of the diversity of heat input, cooling rates and solidification parameters in the widely used variants of AM. Transport phenomena-based models are helpful to identify the appropriate combination of printing process, process conditions and alloy system that can produce defect free components. There is clearly a compelling need for the greater use of the transport phenomena-based models. Such usage will enable

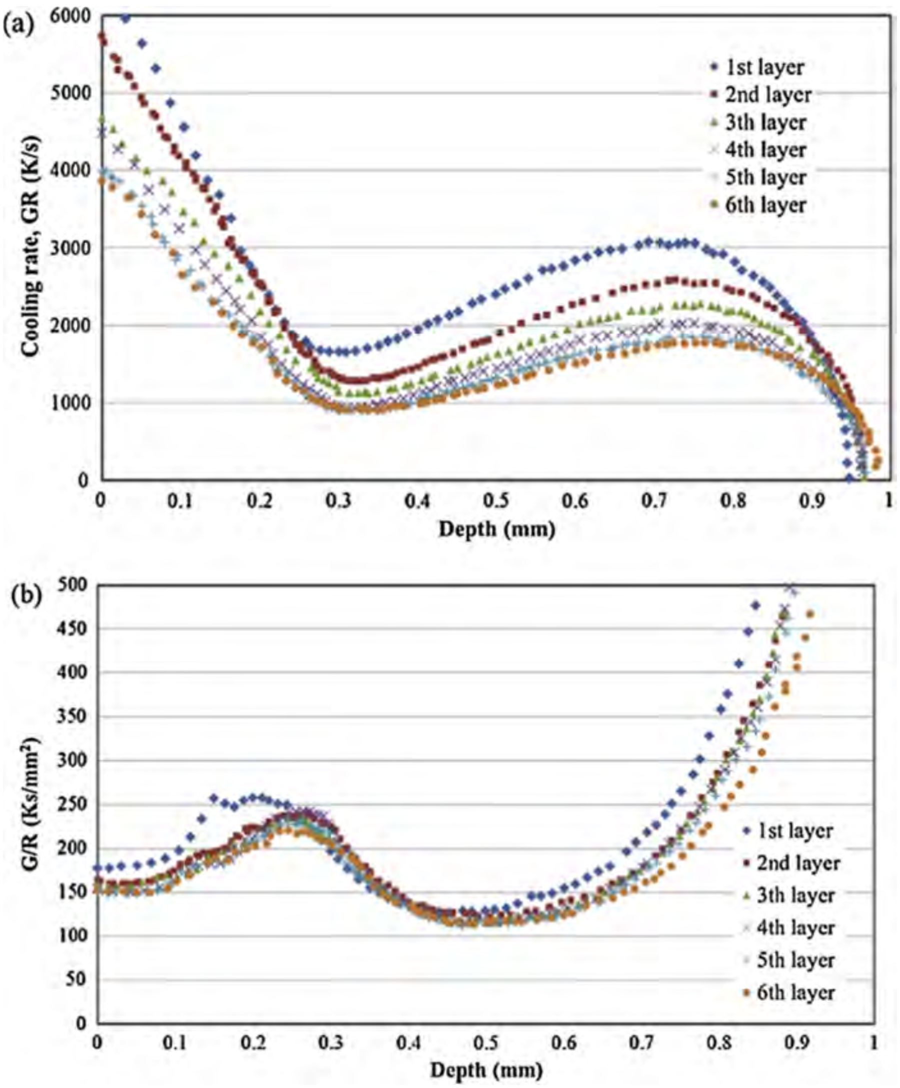

**Fig. 3.14.** Variation of solidification parameters with depth from the top-surface of the deposit from a simulation of a graded deposition of Ni-based alloy on cast iron. Reproduced from [97].

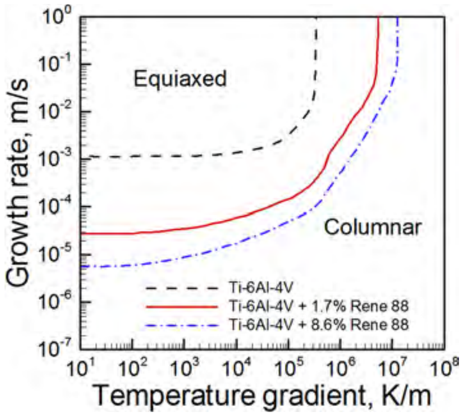

**Fig. 3.15.** The solidification map of Ti-6Al-4V and its graded alloy with Rene 88 showing the columnar to equiaxed transition at different compositions [293].

significant reduction of the wide parameter space for the printing of sound components with significantly reduced expensive trials. An important application of numerical models is the printing of components with graded properties. For example, materials with very different melting points such as tungsten and copper [297], can have difficulty in printing, resulting in a heterogeneous microstructure. Also, the mixing of materials in the molten pools of functionally graded alloys due to convective and diffusional processes can be difficult to study experimentally. Numerical simulations can provide a good starting point for the printing of graded materials, without a large number of trial-and-error testing. In addition to those research needs discussed in Section 2.9, another main difficulty is the greater access of these models. Therefore, open source, rigorously tested numerical models are needed.

## 4. Modeling of microstructure, defects and printability

The properties and performance of components produced by AM depend largely on the microstructure and defects that are affected by factors such as the fusion zone geometry, chemical composition and properties, time–temperature history, temperature gradient and solidification growth rate for a given alloy. Understanding these factors solely by physical experiments is difficult, and mechanistic modeling was shown to be a useful way to determine the role of those variables [23]. This section will critically examine the current status and future opportunities of applying mechanistic models to understand and control the microstructure, defects and printability of AM components.

### *4.1. Microstructure*

The microstructure of AM components has distinctive features due to the layer-by-layer deposition process and relatively high cooling rates and temperature gradients compared to traditional manufacturing processes like casting. Without proper understanding and control of the AM processing conditions, microstructural differences can lead to different mechanical properties than comparable wrought products. These differences can arise through simple Hall-Petch relationships between grain size and strength, or through more complex phenomena due to solid-state phase transformations and the resulting microstructures. Therefore, effective control of the microstructure relies on quantitative understanding of the process conditions, particularly the time-temperature history.

Key metallurgical parameters, such as the temperature gradient and solidification rate at the liquid/solid boundary, largely determine the solidification structure. However, they are difficult to measure due to the high temperatures and short time scales involved in molten pool dynamics. Also, the deposition and melting of the new metal layer heats the previously deposited material, which acts as *in situ* repetitious heat treatment of the build. By overcoming the challenges presented by directly measuring the thermal histories and solidification parameters, mechanistic models can serve as powerful tools to obtain these variables. Therefore, the prediction and understanding of the microstructure of AM components are important applications of transport phenomena based models [254,298–301].

The Johnson-Mehl-Avrami-Kohnogorov (JMAK) models are used to calculate phase transformations during heating and cooling based on the kinetics of specific alloys [302]. The computational efficiency is high but with the limitation of not being able to provide the morphological information of the phases. Phase field models can compute the phase morphologies during solid-state phase transformations [303]. Moreover, phase field simulations can resolve the microstructural features for both grain and sub-grain structure during solidification [304]. However, the phase field models are computationally intensive, and thus the applications are limited to small temporal and spatial ranges. Cellular automata can simulate the growth of grain and sub-grain structure during solidification with medium accuracy and computational efficiency [305]. Monte Carlo simulation, which is a probabilistic approach computing changes of grain boundary energies, can simulate the grain growth process with a high computational efficiency [284]. Monte Carlo approach can simulate solid-state grain growth and can provide information of the spatiotemporal variations and topological distributions of the grain structure [306,307].

#### *4.1.1. Solidification morphologies*

The capability of obtaining a target solidification structure, i.e., columnar or equiaxed grains of a particular size, often determines the properties and serviceability of a component produced by AM [308]. For typical PBF of metallic materials, elongated columnar grains often dominate in the microstructure. For example, PBF-L of Al 7075 resulted in significant degradation of tensile strength due to the dominant columnar grain structure and the resulting cracks due to hot tearing [308]. However, in some processing conditions equiaxed grains dominated the microstructure and the component showed significantly better tensile properties [308,309].

Prediction of solidification structure requires quantitative understanding of the nucleation and growth during the cooling process. A relationship has been derived by Gäumann et al. between the temperature gradient $G$ at the solidification front, the solidification rate $R$, the volume fraction of equiaxed grains $\phi^V$, the nucleation undercooling $\Delta T_n$, the number of nucleation sites $N_0$, and the dendrite tip undercooling $\Delta T$ as [310]:

$$G = \frac{1}{n+1}\sqrt[3]{\frac{-4\pi N_0}{3\,\ln\,(1-\phi^V)}}\left(1-\frac{\Delta T_n^{n+1}}{(aR)^{(n+1)/n}}\right)(aR)^{1/n} \tag{4.1}$$

The alloy parameters, $a$ and $n$, correspond with the amount of undercooling needed to achieve columnar to equiaxed transition (CET) and the sensitivity of the CET to $G$ and $R$ on the CET, respectively. Under high temperature gradients, the nuclei density $N_0$ dominates whereas the nucleation undercooling $\Delta T_n$ can be neglected and set to zero. Thus, Eq. (4.1) can be rewritten as:

$$\frac{G^n}{R} = a\left[\sqrt[3]{\frac{-4\pi N_0}{3\ ln(1-\phi^V)}}\ \frac{1}{n+1}\right]^n \tag{4.2}$$

Eq. (4.2) indicates that the $G$, $R$, and $N_0$ are three major causative factors that determine the CET for any given material. The variables

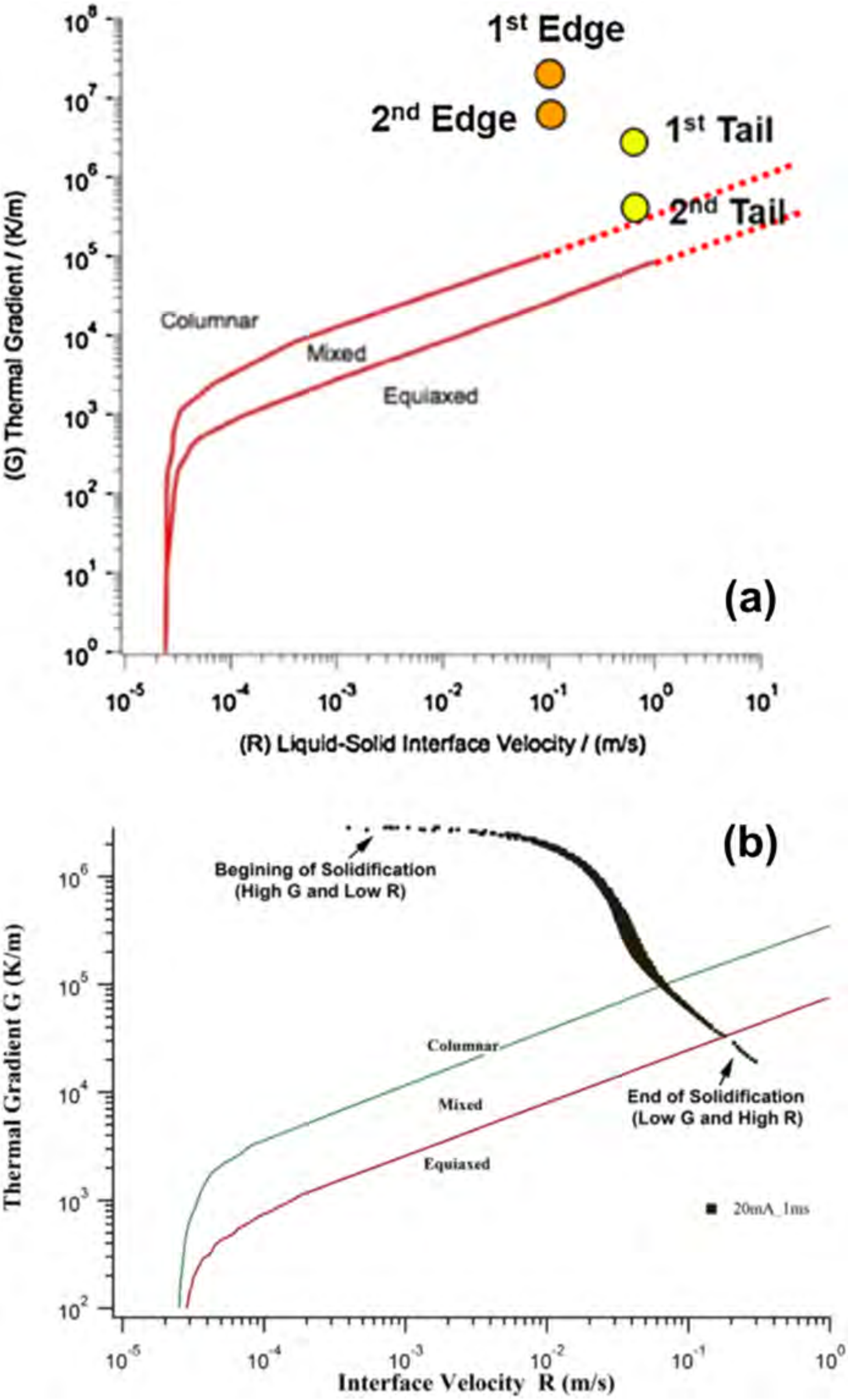

**Fig. 4.1.** Numerically calculated temperature gradient G and solidification rate R overlapped on the solidification map of IN718: (a) PBF-L with linear scanning strategy [22], (b) PBF-EB process with spot scanning strategy [204].

$G$ and $R$ can be calculated using mechanistic models of AM. Thus, methods capable of manipulating these three variables can be applied to control the solidification microstructure. For example, phase field method was used to predict CET considering the competition between grain growth and heterogeneous nucleation, the constitutional supercooling as well as thermal and curvature undercoolings in the melt pool [311]. Cellular Automata method was used to compute CET considering the maximum nuclei density and critical undercooling. The nuclei density, $N_d$, was calculated by [312,313]:

$$N_d = \int_0^{\Delta T_n} \frac{dN_d}{d(\Delta \mathrm{T})} d(\Delta \mathrm{T}) \tag{4.3}$$

where $\frac{dN_d}{d(\Delta \mathrm{T_n})}$ described the increase rate of nuclei density with undercooling. The nuclei distribution was expressed as a Gaussian distribution [313]:

$$\frac{dN_d}{d(\Delta T_n)} = \frac{N_0}{\Delta T_\sigma \sqrt{2\pi}} \exp(-\frac{\Delta T - \Delta T_c}{\sqrt{2}\ \Delta T_\sigma}) \tag{4.4}$$

where $N_0$ is the maximum nuclei density, $\Delta T_c$ is the critical undercooling, and $\Delta T_\sigma$ is the standard deviation at the critical undercooling. Nucleation occurred almost instantaneously and saturated all of the sites at a critical undercooling [312]. It was found that an increase of the nuclei density with decrease of critical undercooling encouraged the formation of equiaxed grains [312–314].

Formation of equiaxed grains can be promoted by process control and modification of feedstock materials. In the former case, process parameters such as heat source power, scanning speed, scanning strategy are manipulated to generate the desired solidification conditions, e.g., lower $G$ and higher $R$ for forming equiaxed grains [204,315]. Transport phenomena based mechanistic models can estimate the values of $G$ and $R$ for various processing conditions. In the latter case, additional materials are introduced to the feedstock to increase the heterogeneous nucleation sites and thus the probability to form equiaxed grains [308,309]. While these two approaches are extensively used in welding and casting, their effectiveness in the field of AM needs to be carefully examined.

*4.1.1.1. Columnar to equiaxed transition through process control.* Formation of equiaxed grains requires sufficient undercooling in the solidification front of the molten metal [310]. The value of the critical undercooling is a factor of several parameters, mainly those described in Eq. (4.2) - $G$, $R$ and $N_0$ at the solidification front. Fig. 4.1(a) shows an example of the numerically computed $G$ and $R$ on the solidification map of IN718 by PBF-L [22]. During PBF, $R$ is usually on the order of 1 m/s, which is significantly higher than that during DED, and thus appear to be favorable for the formation of equiaxed structure. However, $G$ is typically above $10^6$ K/m during the PBF process, and the high temperature gradient is favorable to columnar grain formation. Their combination $G/R$ varies over a range and the morphology depends on the specific values of $G/R$. In this case of PBF-L, the values of $G$ and $R$ produced columnar grains [22], however, Fig. 4.1(b) shows that PBF-EB of IN718 alloy creates values of $G$ and $R$ near the CET boundary [204]. Depending on the values of $G$ and $R$ at any given time during the solidification, certain microstructures may be favored at different locations or times during processing. The variations of $G$ and $R$ can result in initial columnar and final equiaxed solidification structure [205]. Because the magnitudes of $G$ and $R$ vary depending on the process and material used in a build, some alloys may have similar microstructural morphology over a wide range of processing condition while others may vary drastically. Notably, for common alloys including Ti-6Al-4V, SS316L and AlSi10Mg, columnar grains were extensively reported as dominant structure of the components built by linearly scanned PBF with a variety of process conditions [316–318].

In order to achieve equiaxed grains, the process parameters can be substantially adjusted so that $G$ gets reduced while $R$ is enhanced. Fig. 4.1(b) shows an example of PBF-EB process using specially designed spot scanning strategies, which are distinctive from regular linear scanning strategies used commonly during PBF-EB or PBF-L. A significantly broader range of values of $G$ and $R$ can be observed in the spot melting cases. During the latter solidification stage of the local molten pool, the combination of $G$ and $R$ brings the morphology of the solidification structure to the equiaxed region on the solidification map. In other words, columnar grains still occupy a considerable proportion of the microstructure even under such conditions [204].

There are other approaches promoting CET through control of the printing conditions. For instance, high-intensity ultrasound was integrated into the laser powder DED process for Ti-6Al-4V and IN625 to trigger significant acoustic cavitation in the molten pool during solidification, which generated a large number of nuclei for the formation of massive equiaxed grains [319]. Nevertheless, the applicable conditions for such method may be restricted considering the particular material compositions, printing processes, and equipment setups of the AM conditions.

In other scenarios, the application of mechanistic models during DED can aid to target a structure without stray grains for single crystal components [320]. Due to the complex nature of producing and maintaining the single crystal structure, it is practically impossible to quantitatively reveal the solidification conditions during DED-L without the assistance of the transport phenomena models. Location-dependence of $G$ and $R$ alters solidification conditions even within the same build. For example, in nearly all processes a relatively high $R$ and relatively low $G$ occur near the centerline of the molten pool, which favors the formation of equiaxed grains [315]. Thus, large modeling efforts have been made to compute the temporal and 3D spatial variation of critical solidification parameters such as $G$ and $R$ to predict spatial and transient variations in microstructure.

Combining a transport phenomena model with a crystal growth model, important features of microstructures including the orientation, morphology, and dimension of the local solidification structure can be effectively predicted [320–322]. Gäumann et al. developed a model to predict CET for solidification of single crystal alloy CMSX-4 during DED-L. Major influential factors including the $G$, $R$ and nucleation site density have been considered in their model [310]. Liu et al. developed a 3D transient transport phenomena model coupled with a crystal growth model to predict the variation of crystal growth and microstructure formation with substrate crystallographic orientation during the DED-L of a nickel-based SX superalloy Rene N5 as shown in Fig. 4.2 [323].

In brief, the temporal and spatial variations of *G* and *R* can be obtained through mechanistic models. Based on the data of *G* and *R*, the morphologies of solidification structure can be predicted from the solidification map of the deposit materials [284,306,307,315]. However, transition of columnar to equiaxed microstructure by adjusting processing variables can be a challenging task [324]. Some combinations of alloys and processing conditions may allow for the desired control over microstructure morphology, such as PBF-EB of IN718 alloy, though this may not be the case for all alloys. If hot tearing or other issues related to columnar grain formation are faced during the processing of AM alloys, a solidification map combined with *G* and *R* values from mechanistic modeling can yield insight into the feasibility of forming equiaxed grains through process control. If CET through changing the processing conditions is not feasible, then other options must be explored.

*4.1.1.2. Columnar to equiaxed transition through feed stock modification.* An effective approach for the formation of equiaxed structure is to reduce the critical undercooling by introducing low-energy-barrier heterogeneous nucleating agents under normal PBF process conditions [308]. For example, when the surfaces of Al 6061 and Al 7075 powder particles were decorated with lattice-matched nanoparticles to promote heterogeneous nucleation, massive equiaxed grains formed during solidification of the molten metal [308]. The feasibility of this approach is proved by the distinctive transition from columnar to equiaxed grains [308]. Mixture of columnar and equiaxed grains produced by PBF-L of Al-Mg-Sc-Zr [325] and Al-Mg-Zr alloys [326] as shown in Fig. 4.3(a) and (b). A similar successful example was PBF-L of AlSi10Mg reinforced with nano-$TiB_2$, in which case the microstructure was dominated by equiaxed grains as shown in Fig. 4.3(c) [309].

Scalmalloy® (Al-4.6 Mg-0.66Sc-0.42Zr-0.49Mn, wt.%) was developed via modifying the 5xxx aluminum alloy by adding scandium and zirconium [325,327,328]. $Al_3$(Sc,Zr), Al-Mg-oxides and mixed particles are generated during solidification, and subsequently act as nuclei promoting massive CET [327]. The microstructure of the as-built PBF-L component was featured by a bi-modal grain size distribution of fine equiaxed grains coexisting with coarse columnar grains [327]. Croteau et al. developed Al-Mg-Zr alloys, Al-3.60Mg-1.18Zr and Al-3.66Mg-1.57Zr (wt.%), which are free of the expensive Sc [326,329,330]. PBF-L component produced using these alloys also showed massive CET and bi-modal grain structure [329].

Silicon was added to Al 7075 with different content to examine its effect on grain refinement during PBF-L by Sistiaga et al. [331]. Fig. 4.3(d) and (e) shows the grain structure of 7075 aluminum alloy with addition of silicon of 2.0 wt% and 4.0 wt%, respectively [331]. It can be observed that the fraction of equiaxed grains is positively related to the silicon content. Yet fully equiaxed structure cannot be achieved even with silicon content as high as 4.0 wt%. A columnar structure or a combination of columnar and equiaxed structures is also widely observed in components deposited by DED [73,332,333]. Because the solidification is generally more favorable for equiaxed grains in DED than PBF (lower G due to higher energy inputs), the addition of grain refiners may be more effective in DED than PBF. However, this is speculative, as detailed studies relating the quantitative values of *G*, *R* and nuclei density of grain refiners have not been done for AM processes.

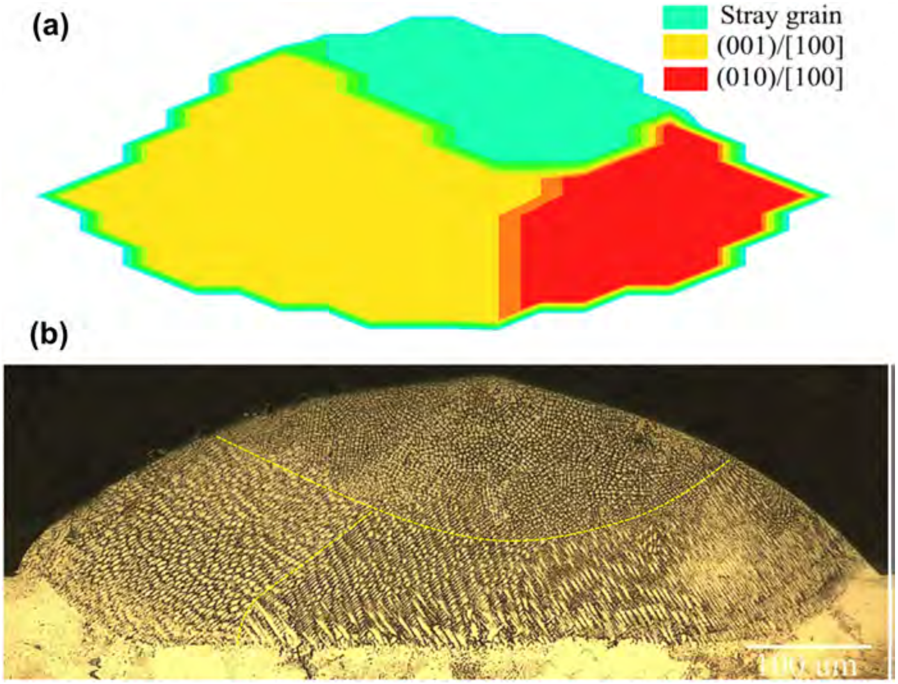

**Fig. 4.2.** Crystallographic orientation of the epitaxial columnar dendrites. (a) Simulated results, (b) Experimentally observed result [323].

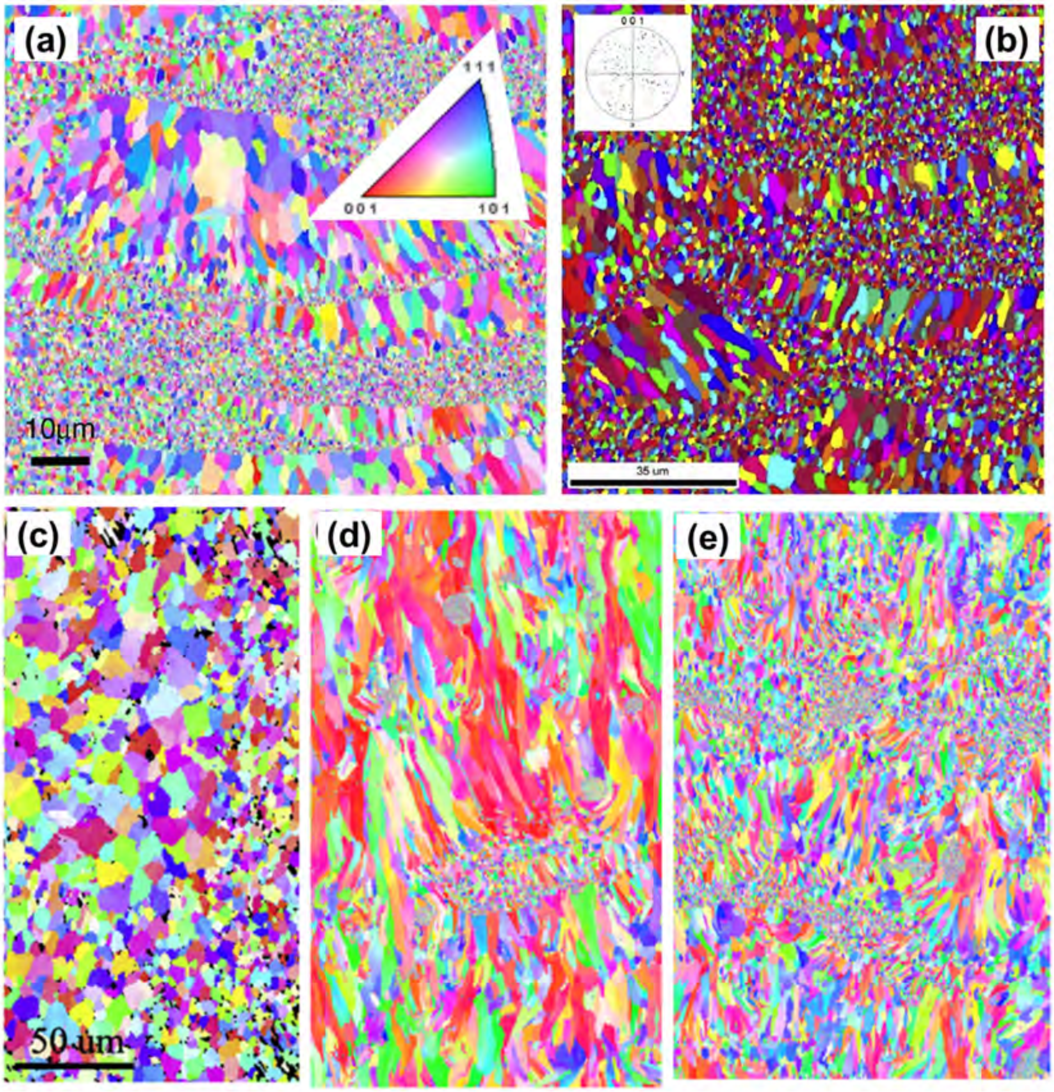

**Fig. 4.3.** (a) Mixture of columnar and equiaxed grains produced by PBF-L of an Al-Mg-Sc-Zr alloy [325]. (b) Mixture of columnar and equiaxed grains produced by PBF-L of an Al-Mg-Zr alloy [326]. (c) Equiaxed grains in nano-$TiB_2$ decorated AlSi10Mg alloy by PBF-L [309]. (d) Grain structure of 7075 aluminum alloy with 2.0 wt% Si added produced using PBF-L [331]. (e) Grain structure of 7075 aluminum alloy with 4.0 wt% Si added produced using PBF-L [331].

### 4.1.2. Scale of microstructure

The scale of the microstructure can be defined by the grain size, and the size of sub- grain structure for dendritic solidification, i.e., cellular, columnar and equiaxed. These dimensions depend on the local cooling rate (GR) during the AM process. The cooling rate can be calculated from either the slope of the temperature versus time curve or the product of $G$ and $R$. Numerical modeling of the heat transfer and fluid flow during AM processing provides the necessary data to calculate $GR$.

During dendritic solidification, the primary dendritic arm spacing (PDAS) depends on the solidification parameters of $G$ and $R$ [205]. A smaller PDAS appears near the bottom of the layer which has a higher $G$ and lower $R$ than the top of the layer. Heat generally accumulates in a build due to the high energy input and a relatively low amount of convective and radiative cooling. Thus, lower cooling rates near the end of a layer or a build can occur if adequate cooling of the part is not allowed. Several heat transfer and fluid flow models were used to simulate the AM process to quantitatively examine the cooling rates that result from the deposition of the multiple layers [17,18]. Additionally, the computed cooling rates can be further used to predict the scale of the microstructure. For example, the secondary dendrite arm spacing (SDAS), $\lambda_2$, of the solidification structure as a function of the cooling rate during multi-layer deposition was correlated in the literature [17,334,335]:

$$\lambda_2 = A\ (GR)^{-n} \tag{4.5}$$

where $\lambda_2$ is the SDAS in μm, $GR$ is cooling rate in K/s, and $A$ and $n$ are material specific constants. Notably, some experiments need to be conducted to find the constants for this type of empirical relationship. Once a relationship is generated for a particular alloy, the results can be used in mechanistic models of all AM processes capable of calculating cooling rates. Solidification models can further be used to explicitly reveal the dimensions of microstructural features. For example, Nie et al. [299] correlated the SDAS with cooling rates by use of a finite element numerical model combined with a stochastic solidification model.

When the experimental data for calibrating an empirical relationship between cooling rate and the scale of microstructure is not available, the trends of increasing cooling rates leading to finer microstructure can be used to get a qualitative understanding of relationships between processing parameters and microstructure. Heat transfer modeling by Song et al. [292] showed lower cooling rate near the surface than that in the lower region of the deposit during DED-L of IN718. In the actual builds, coarser grains were found near to the surface of the deposited single tracks whereas finer grains were observed near the boundary of the molten pool [292]. The qualitative understanding of the spatial variation of grain size is an important step for understanding microstructures.

### *4.1.3. Solid-state phase transformations*

Solid-state phase transformations occur in the solidified alloy during the cooling stage for heat treatable alloys, e.g. BCC β phase transforms to HCP α phase in Ti-6Al-4V. Furthermore, the low temperature phase transforms back to high temperature phase due to heating during the deposition of subsequent layers. Unlike transport phenomena models of AM, microstructure models that calculate phase fractions, grain and sub-grain structures are specific to each alloy. For example, the transport phenomena models for AM of Ti-6Al-4V and IN718 alloy would solve the same governing equations along with similar boundary conditions while taking into account different thermal-physical properties of the two different alloys [19]. In contrast, the microstructure models of Ti-6Al-4V may deal with the β grain growth at high temperatures and the transformation of β into different α variants (e.g., basket-weave, or martensite $\alpha'$ [336,337]) as a function of cooling rate. The models of IN718 alloy would consider the precipitation kinetics of $\gamma'$ and $\gamma''$ [338]. There is no common set of governing equations that can be solved to describe phenomenologically, both the β → α transformation in Ti-6Al-4V and the precipitation kinetics of $\gamma''$ in Alloy 718, making microstructure modeling highly alloy-specific. Here we review modeling solid-state phase transformations during AM of various commonly used alloys.

*4.1.3.1. Steels.* Modeling of microstructure evolution in steels during AM is just beginning, although there is a rich literature of modeling of phase transformations in steels [344–346]. Steels experience a series of phase transformations during the repetitive thermal cycles of AM. Possible phase transformations during heating and cooling of low alloy steels are α-ferrite → γ-austenite → δ-ferrite → liquid → δ-ferrite → γ-austenite → α-ferrite [339]. The microstructure of steel AM part was observed to present different phases along the build height direction due to variable cooling rates. For example, the as-deposited microstructure of 300M steel produced by DED-L showed tempered martensite at the bottom and a mixture of martensite and bainite at the top of the deposit [340]. Similarly, the amount of martensite was found increasingly higher from the 5th to the 20th layers for DED-GMA of 2Cr13 steel [341]. This is because that martensite is metastable and tends to decompose into stable ferrite when being heated. The extent of decomposition depends on the strength of the repeated heating and cooling cycles. The lower layers experience more thermal cycles than those for the upper layers and thus the decomposed martensite volume fractions are gradually smaller along the build height.

In order to predict the microstructure evolution in the solid steel deposit, phase transformation models have been developed based on thermodynamic and kinetic theories. Essential input data required by the model include the chemical composition, the prior austenite grain size, and the cooling curve. The volume fractions of allotriomorphic, Widmanstatten ferrite, acicular ferrite, and martensite can be computed as the output of these models [342,343]. During cooling allotriomorphic ferrite forms first by a diffusive mechanism and it nucleates heterogeneously at the boundaries of the columnar austenite grains. Widmanstatten ferrite plates form by a displacive mechanism at relatively low undercooling. Bainite nucleates and grows in the form of sheaves of small platelets at further undercooling. Acicular ferrite subsequently nucleates intragranularly around the inclusions inside the austenite. Martensite forms in a diffusionless manner if the cooling rate is higher than a critical cooling rate [343–346].

Isothermal time-temperature-transformation (TTT) and continuous-cooling-transformation (CCT) diagrams calculated by phase transformation models provide tools to calculate final phase fraction due to transient heating and cooling [344–346]. Work by Bhadeshia and colleagues provide a model that enables these types of calculations to be applied to steels. The TTT curves in the model were composed of two C curves, with one representing diffusive transformations at higher temperature, and the other representing displacive transformations at lower temperature. Russell's expression was used to calculate the incubation time for both diffusive and displacive transformations [347]:

$$\tau_i = T^{a_1} \times (\Delta G_{max})^{a_2} \times exp\left(\frac{a_3}{T}\right) \times a_4 \tag{4.6}$$

where $\tau_i$ is the incubation time for a transformation, $T$ is the temperature, $\Delta G_{max}$ is the maximum driving force for nucleation and $a_1$, $a_2$, $a_3$ and $a_4$ are constants. Aided by Scheil additive rule, the TTT diagram can be used to calculate the CCT diagram:

$$\int_0^t \frac{dt}{\tau_i(T)} = 1 \tag{4.7}$$

where $\tau_i(T)$ is the incubation time to a specified stage on a TTT diagram for isothermal reactions, $t$ is the time to that stage for the non-isothermal reactions, and $dt$ is the time interval at temperature $T$. For non-isothermal reactions the required time to reach a specified stage of transformation was obtained by accumulating the time fractions to reach this stage isothermally until the sum reaches unity.

*4.1.3.2. Modeling of phase transformations during cooling.* Allotriomorphic ferrite begins to form from the prior austenite grain boundary by diffusion when the solid metal cools below the A3 temperature. The start temperature is determined from the interception temperature of the cooling curve and upper C curve in the CCT diagram. The completion temperature is determined by the interception temperature of the cooling curve with the lower C curve [345]. Displacive transformations are kinetically favored below this temperature when the growth of allotriomorphic ferrite ceases. The growth rate of allotriomorphic ferrite is controlled by carbon diffusion at the interface of allotriomorphic ferrite/austenite. The thickness of the allotriomorphic ferrite layer can be calculated by the parabolic thickening relationship [339,345]:

$$q_a = \int_{T_l}^{T_h} 0.5\alpha_1 t^{-0.5} dt \tag{4.8}$$

where $q_a$ is the thickness of the allotriomorphic layer, $t$ is the time, $T_h$ and $T_l$ are the start and finish temperatures of the transformation, respectively, and $\alpha_1$ is the one-dimensional parabolic thickening rate constant. The volume fraction of allotriomorphic ferrite ($V_\alpha$) can be calculated based on the area that allotriomorphic ferrite occupies in the hexagonal cross section of austenite grain [339,345]:

$$V_a = \frac{[2q_a\tan(30°)(2a_A - 2q_a\tan(30°))]}{a_A^2} \tag{4.9}$$

where $V_a$ is the volume fraction of allotriomorphic ferrite, $q$ is the thickness of allotriomorphic ferrite, $a_A$ is the side length of austenite. The transformation of Widmanstatten ferrite from austenite is paraequilibrium displacive. The growth rate depends both on carbon diffusion and an invariant-plane strain change. The volume fraction of Widmanstatten ferrite ($V_w$) can be calculated based on the area that Widmanstatten ferrite occupied in the hexagonal cross section of austenite grain after the formation of the allotriomorphic ferrite [339,345]:

$$V_W = C_4 G_L \frac{2a_A - 4q_a\tan(30°)t^2}{(2a_A)^2} \tag{4.10}$$

where $C_4$ is a constant independent of alloy composition, $G_L$ is the lengthening rate of Widmanstatten ferrite, $a_A$ is the side length of austenite, $q_a$ is the thickness of the allotriomorphic ferrite layer and $t$ is the time available for the formation of Widmanstatten ferrite. The volume fraction of other phases including martensite, $V_o$, is calculated from the mass conservation equation [339,345]:

$$V_o = 1 - V_a - V_W \tag{4.11}$$

where $V_a$ and $V_w$ are volume fractions of allotriomorphic ferrite and Widmanstatten ferrite, respectively. Note that the formation of martensite is highly sensitive to the presence of carbon and alloying elements. A high carbon equivalent decreases the critical cooling rate, and thus results in a higher susceptibility for martensite transformation. Fig. 4.4 shows an example of the calculated CCT curves for a low alloy steel with various cooling curves superimposed [348]. For different cooling rates, grain boundary forms first upon the transformation from γ phase, followed by Widmanstatten $\alpha_W$ and acicular ferrite $\alpha_a$. Martensite forms if the cooling rate is higher than the critical cooling rate.

*4.1.3.3. Modeling of phase transformations during heating.* During heating γ-phase forms upon nucleation from the α-matrix. The growth of γ-phase is diffusive and can be described using the Johnson-Mehl-Avrami-Kolmogorov (JMAK) equation [339]:

$$f_e(t) = 1 - exp[-(RC\ t)^n] \tag{4.12}$$

where $f_e(t)$ is the extent of the transformation at a given time $t$, $n$ is the JMAK exponent, and $RC$ is a rate constant given as:

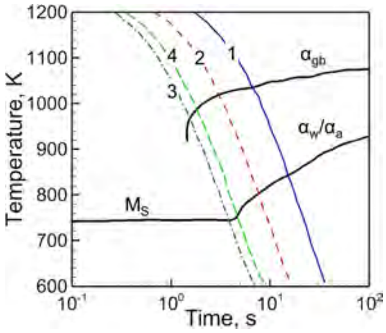

**Fig. 4.4.** Calculated CCT diagram for a low alloy steel with various cooling curves superimposed. The figure is plotted based on the data available in [348]. The cooling rates for curves 1 to 4 are 21.3, 48.4, 83.3 and 66.7 K/s, respectively. Grain boundary $\alpha_{gb}$ forms first upon the transformation from γ phase, followed by Widmanstatten $\alpha_W$ and acicular ferrite $\alpha_a$. Martensite forms if the cooling rate is higher than the critical cooling rate for martensite transformation.

$$RC = RC_0\ exp\left[-\left(\frac{Q}{R_g T}\right)\right] \tag{4.13}$$

where $RC_0$ is a pre-exponential constant, $Q$ is the activation energy of the transformation, including the driving forces for both nucleation and growth, $R_g$ is the gas constant, and $T$ is the absolute temperature in K.

The JMAK-based expression can be derived based on Eq. (4.12) to be applicable to non-isothermal phase transformations occurring in the ferrite and austenite two phase region. The calculated thermal profiles and the spatially resolved X-ray diffraction experimental data can be integrated to determine the JMAK parameters. The resulting kinetic parameters are useful in determining the transformation rates under various heating conditions.

In ferritic-martensitic steels, when martensite is reheated below the steel's A1 temperature, it can decompose into ferrite and cementite phases, a phenomenon called tempering. It reduces hardness but increases toughness and it is thus important for AM of highly-hardenable steels. The tempering kinetics and ensuing hardness drop of tempered martensite were described by the JMAK like equations for PBF-L of a high-strength low-alloy steel [349] and resistance spot welding of a fully martensitic steel [350]; the latter is relevant to AM due to a comparable heating rate.

### *4.1.4. Titanium alloys*

*4.1.4.1. Modeling of phase transformations during cooling.* The roadmap of β phase transformations for Ti-6Al-4V is shown in Fig. 4.5. Solid-state phase transformations occur as the deposit cools below the β-transus temperature for dual phase titanium alloys such as Ti-6Al-4V [351]. Grain boundary $\alpha_{gb}$ is the first phase to form on the boundaries of prior β grains during cooling at temperatures directly below β-transus. Subsequently, Widmanstatten $\alpha_W$ nucleates from the prior β grain boundary and grows into the prior β grains to form plate-like structure. Upon continuous cooling, the retained β phase may transform to massive $\alpha_m$ and martensite α′ phases. A small amount of β may retain with the α phases. During heating, massive α and martensitic α′ transforms to laminar α/β. All α phases transform to β phase at temperatures above the β-transus temperature.

Fig. 4.6 schematically shows the formation of grain boundary $\alpha_{gb}$, Widmanstatten $\alpha_W$, massive α phase $\alpha_m$, and Martensite α′ depending on different cooling rates for Ti-6Al-4V. For the case shown here, grain boundary $\alpha_{gb}$ and Widmanstatten $\alpha_W$ form if cooling rate is lower than 20 K/s, massive $\alpha_m$ plates form between 410 K/s and 20 K/s, whereas α′ forms at cooling rate higher than 410 K/s [352].

Widmanstatten $\alpha_W$ may orient coherently to form a colony within the β grain, and the size of the colony and individual plates decrease with higher cooling rate. Massive transformation in AM Ti-6Al-4V may lead to entirely new massive $\alpha_m$ grains. In contrast, martensite α′ forms in a pattern that martensite laths confine in the parent β grains without changing the parent β grain structure. Martensite is a supersaturated non-equilibrium hexagonal α phase formed by diffusionless transformation of the β phase [353]. The critical cooling rate for β → α′ transformation is somewhat uncertain [354], probably due to the deviations in the actual chemical compositions of the Ti-6Al-4V alloys used [351]. The presence of increasing β stabilizing elements such as V tends to reduce the critical cooling rates and results in more martensite α′ [351].

Phase field method was applied for PBF-EB of a Ti-6Al-4V component considering (α + β) microstructure features [336,355]. Empirical microstructure models were used for β → α transformation in Ti-6Al-4V by Makiewicz *et al.* [356] for DED-L and Lindgren *et al.* for PBF [357]. In any case, data about transformation kinetics, such as TTT diagrams are needed to provide inputs for the phase transformation models. The TTT diagrams for titanium alloys could be constructed through *in situ* measurements of the physical properties such as the electrical resistivity [358] and the hardness [359] under isothermal heat treatments. Alternatively, the TTT diagrams can be computed through thermodynamics and kinetics models such as JMatPro [360].

The diffusion-controlled phase transformations of β-phase to α-phase can be predicted using the JMAK equation. The grain

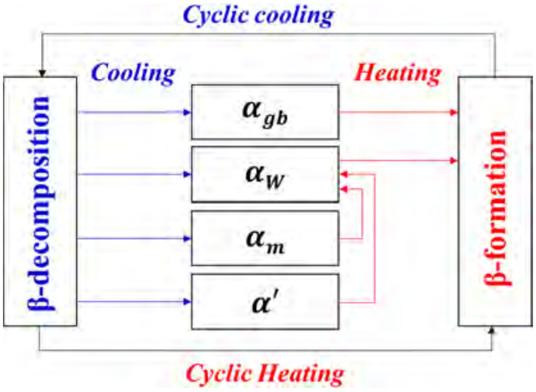

**Fig. 4.5.** Roadmap of β phase transformations for Ti-6Al-4V. At temperatures below the β-transus temperature during cooling, β phase may transform to grain boundary $\alpha_{gb}$, Widmanstatten $\alpha_W$, massive α, and martensitic α′ phases. A small amount of β may retain with the α phases. During heating, massive $\alpha_m$ and martensitic α′ transforms to laminar α/β. All α phases transform to β phase at temperatures above the β-transus temperature.

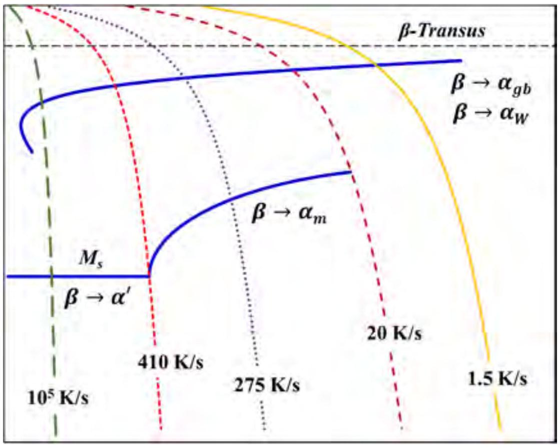

**Fig. 4.6.** Schematic CCT diagram for Ti–6Al–4V superimposed with various cooling curves. Grain boundary $\alpha_{gb}$ forms first upon the transformation from β phase, followed by Widmanstatten $\alpha_W$, at cooling rate lower than 1.5 K/s. Massive α plates form at cooling rate between 410 K/s and 20 K/s. Martensitic α′ forms at cooling rate higher than 410 K/s [186,352].

boundary $\alpha_{gb}$ is first formed since it has a high transformation rate at the highest temperatures [357,361]:

$$X_{\alpha_{gb}} = (1 - exp(-k_{gb}t^{N_{gb}}))X_\beta^0 X_{\alpha_{gb}}^{eq} \tag{4.14}$$

where $X_\beta{}^O$ is the initial amount of β-phase available for transformation, and $X_{\alpha_{gb}}$ denotes the Widmanstatten α-phase volume fraction. $X_{\alpha_{gb}}^{eq}$ can be obtained for equilibrium conditions at given temperatures. The parameters $k_{gb}$ and $N_{gb}$ can be determined from experimental TTT-diagrams. The original JMAK model describes a complete transformation of a phase to another. However, the transformation may be only partially completed during the thermal cycles of AM. Thus, the original JMAK equation needs to be modified. For example, the value of $X_\beta^0$ depends on the phase changes during the previous transformations. The fraction of Widmanstatten $X_{\alpha W}^{eq}$ can be extracted from the equilibrium phase diagrams of the alloys.

The volume fraction of $\alpha_W$ is calculated after the formation of $\alpha_{gb}$ through the same expression for that of $\alpha_{gb}$ but with different transformation properties [357,361]:

$$X_{\alpha_W} = (1 - exp(-k_W t^{N_W}))X_\beta^0 X_{\alpha W}^{eq} \tag{4.15}$$

where Widmanstatten $X_{\alpha W}^{eq}$ can be obtained experimentally for equilibrium conditions at given temperatures. The parameters $k_W$ and $N_W$ can be determined from TTT-diagrams. Certain amount of β-phase remains after the transformation to $\alpha_W$ and $\alpha_{gb}$, which is available for massive $\alpha_m$ and martensite $\alpha'$ formation as shown in Fig. 4.6.

For displacive or martensitic transformations, the kinetics of nucleation and growth are so fast that they are dependent only on temperature and not on time. The prediction of the volume fraction of martensite can be calculated using the Koistinen and Marburger equation [357,361]:

$$X_{\alpha_M} = (1 - exp(-b(M_s - T)^n))X_\beta^0 \tag{4.16}$$

$X_{\alpha_M}$denotes the volume fraction of both massive and martensitic α-phases, and $b$ and $n$ are materials dependent properties. The summation of volume fractions of all variants of the α-phase computed from the model is obtained as:

$$X_\alpha = X_{\alpha_{gb}} + X_{\alpha W} + X_{\alpha_m} + X_{\alpha'} \tag{4.17}$$

### 4.1.5. Modeling of phase transformations during heating

It was reported that significant gradient of microstructure was present along the build height of the PBF-L Ti-6Al-4V part, due to different thermal conditions for solid-state phase transformations [362]. The bottom region consisted of well-defined lamellar (α + β) structure, with finer lamellar (α + β) in the middle region, and α′ martensite in the last several layers [362]. The primary reason for such gradient microstructure was the different cyclic thermal treatment history along the build direction. The presence of martensite in the upper layers was because of the absence of *in situ* decomposition owing to the lack of successive depositions[362]. Note that significant *in situ* α′ martensite decomposition can occur only under proper PBF-L processing conditions to produce a series of ultrafine lamellar (α + β) microstructures causing high yield strength and ductility.

Martensite α′ and massive $\alpha_m$ are non-equilibrium phases and can transform to more stable laminar α/β structures at temperatures around 623–673 K during isothermal treatments. It was reported that for PBF-L such decomposition occurred in the solid deposit at temperatures around 873–1123 K when subsequent layers are being deposited [353,363]. Upon further heating the Widmanstatten $\alpha_W$ transforms to β-phase. The grain boundary $\alpha_{gb}$ is the last α-phase to transform to the β-phase after the $\alpha_W$ has been extinguished. The decomposition is diffusion-controlled and thus depends on the local temperature and residence time during the AM process. Similar to the phase transformations during cooling, the decomposition of metastable α′ and $\alpha_m$ phases can be described using the JMAK equation with the additivity rule.

### *4.1.6. Nickel base alloys*

*4.1.6.1. Modeling of phase transformations during cooling.* After solidification, various solid-state transformations take place upon continued cooling or subsequent reheating during AM. For example, Amato et al. [364] observed that the as-fabricated microstructure of Nickel Alloy 718 produced by PBF-L was composed of fine γ″ strengthening precipitates. For AM processes involving high pre-heating (e.g., PBF-EB) or significant heat build-up (e.g., DED-L), a portion or the entire build can experience high temperatures (e.g., 1200 K for preheated PBF-EB) over an extended period of time, resulting in a substantial amount of aging or grain growth. For instance, Tian et al. [365] observed a non-uniform distribution of hardness along the build height direction of a wall of Alloy 718 built by DED-L. Specifically, the hardness of the lower part of the wall was much higher than the upper part due to in-place aging and ensuing formation of strengthening precipitates in the lower part.

Considerable segregation of alloying elements occurs in the as-solidified microstructure for many nickel base alloys such as IN718, IN625, and CMSX-4. IN718 is a precipitation strengthened alloy with austenitic γ fcc matrix and precipitates such as γ′ and γ″ phases as well as various metallic carbides and nitrides [366]. IN625 is a solid-solution strengthened alloy, and is sensitive to precipitation of intermetallic phases such as γ″ phase, δ phase, Laves phase and carbides [367]. CMSX-4 is a single crystal alloy strengthened by the

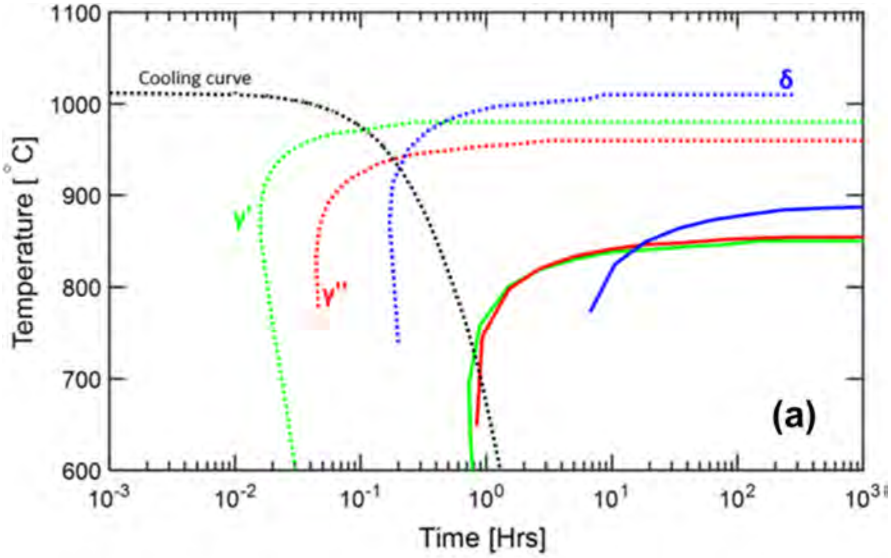

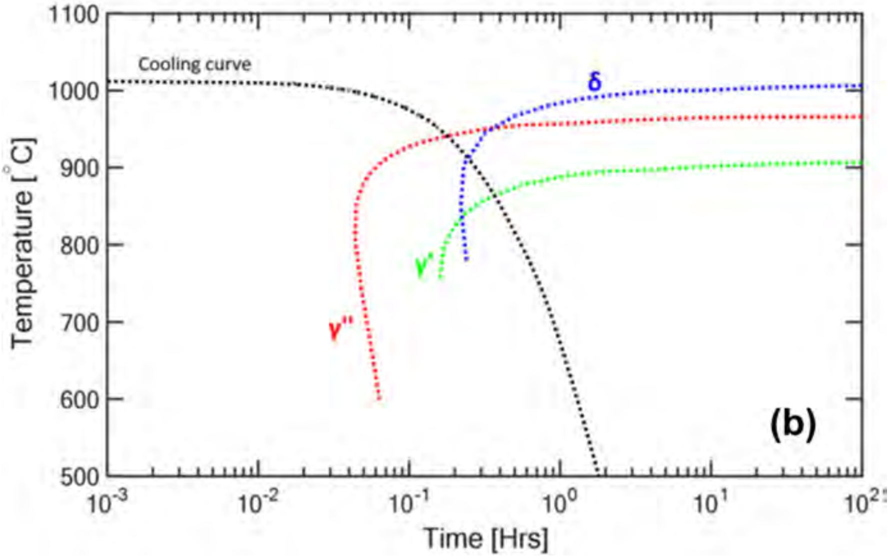

**Fig. 4.7.** CCT diagram created using a commercial software JMatPro for IN718 with cooling curves measured by thermocouples plotted. (a) Dotted lines represent the region close to Laves phase and solid lines represent the dendrite core for 0.5 pct transformation during PBF-EB. (b) The dotted line represents the 0.5 pct transformation related to the nominal composition of the Alloy [366].

γ′/γ″ precipitation as well as the alloying elements like Cr, W, Ta, and Re [368].

During PBF-EB of CMSX-4 alloy, alloying elements like Al, Ti, and Ta as γ′ stabilizers segregate within the interdendritic region, whereas γ stabilizers like W, Co, and Re segregate at dendrite cores [368]. Consequently, the local compositions of the microstructure differ significantly from their nominal composition values. The precipitation kinetics of the alloy are thus altered due to the large variations of the alloying elements distribution [368,369]. For PBF-EB of IN718, higher amount and larger sizes of γ′, γ″ and δ phases were found in the interdendritic regions than those in the dendritic cores [366,368]. Laves phase was found in the interdendritic region close to the γ′, γ″ and δ phases for DED-L of IN718 [370]. The density of the precipitates was found decreasing with greater distance from the Laves phase [366].

In order to reveal the mechanisms for the formation of the diverse precipitates, CCT diagrams can be generated using phase transformation programs such as JMatPro for compositions near the Laves phase and those in the dendrite core [366]. Fig. 4.7 shows that the precipitation kinetics were location dependent during PBF-EB of IN718 [366]. Note that the local chemical compositions of

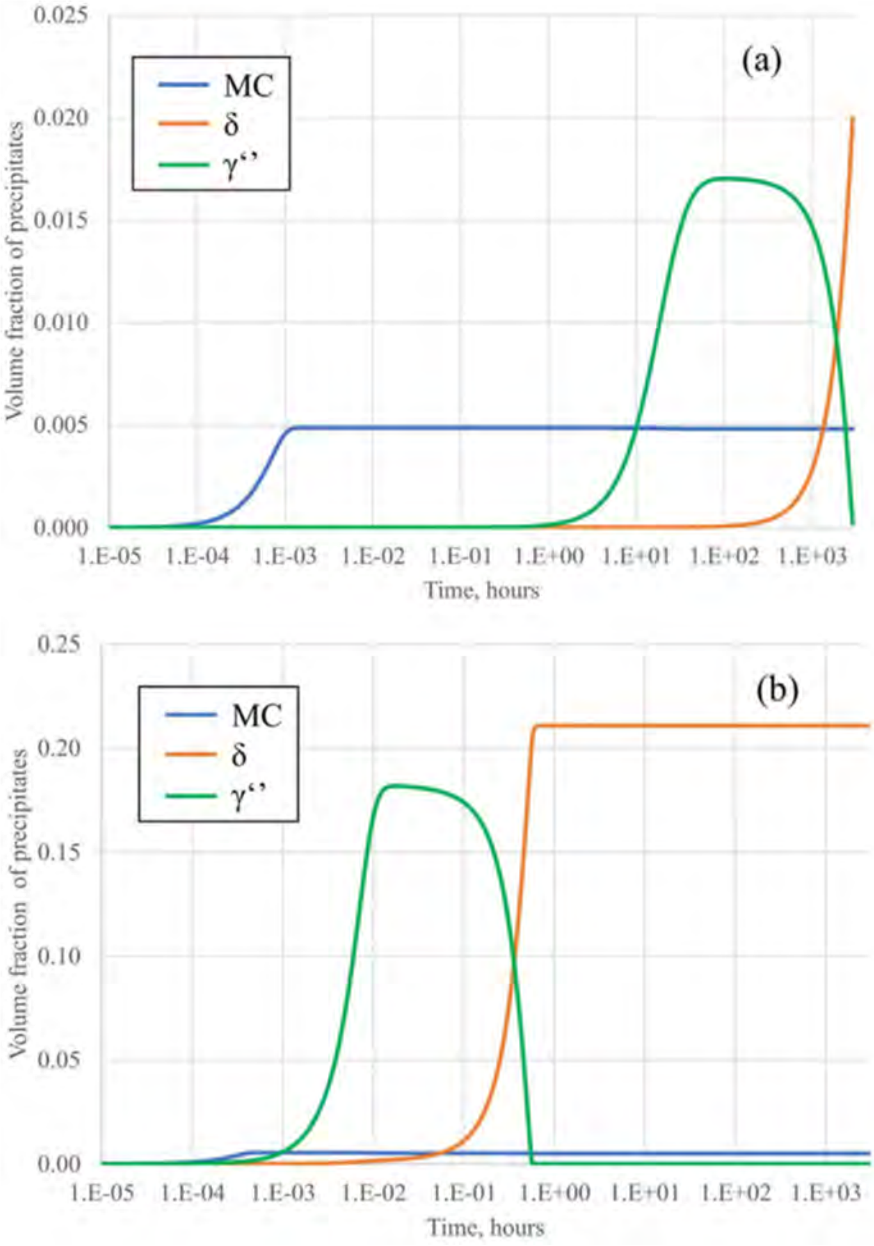

**Fig. 4.8.** Simulated precipitation kinetics of IN625 at 870 °C using a commercial software TC-PRISMA for (a) Nominal composition of the raw feedstock powder Ni-20.70Cr-9.00Mo-4.00Nb-0.72Fe-0.05C. (b) A typical composition in the segregated region of IN625 during PBF-L with Ni-20.20Nb-11.00Mo-8.70Nb-0.05C where Nb concentration exceeds the specified upper limit in IN625 [367].

the solidifying structure differ significantly from the nominal composition of IN718 because of the micro-segregation of alloying elements during solidification. Fig. 4.7(a) shows that γ′, γ″, and δ phases precipitated more than an order of magnitude faster in the region near the Laves phase compared with that at the dendrite core [366]. The precipitation time of γ′, γ″, and δ phases for the nominal composition of IN718 lies in between that for the interdendritic region and the dendrite core, comparing the CCT curves with the same cooling curve in Fig. 4.7(a) and (b) [366]. In brief, strikingly different precipitation kinetics of the constituent phases of nickel base alloys can be generated during the AM cooling process due to the highly non-equilibrium solidification conditions.

#### 4.1.7. *Modeling of phase transformations during heating*

As described above, nickel base superalloy AM builds retain considerable segregation of alloying elements in the as-solidified microstructure. Such non-uniform compositions significantly affect the precipitation behaviors of the constituent phases during heating. For example, Fig. 4.8 compares the precipitation behaviors of γ″, δ, and MC phases in IN625 with nominal and segregated chemical compositions at 870 °C [367]. Fig. 4.8(a) shows that δ phase started to form at the peak volume fraction of γ″ after over 100 h. However, Fig. 4.8(b) shows the peak volume fraction of γ″ phase and the formation of the δ phase occurred at a time scale of 1 min for the case with large amount of segregated alloying elements. Note that the transformed δ phase along the grain boundaries from the strengthening γ″ phase can significantly reduce the fracture toughness and ductility of nickel base alloy [367]. Thus, caution should be paid to the largely deviated local compositions that are outside the bounds of the allowable range of the initial alloys.

A great challenge in modeling solid-state transformations during AM involves repeated transformations (e.g., precipitation and dissolution) due to a large number of heating and cooling cycles. The multiple thermal cycles generated during the layerwise AM deposition process serve as *in situ* heat treatments. The precipitation rates of the phases depend on the strength of the thermal cycles characterized by the local temperature magnitude and residence time [368]. For instance, significant size gradient of the γ′ precipitates was observed along the build height for PBF-EB of CMSX-4. The precipitates at the bottom were coarser than those in regions near the top of the build. The coarsening rate of γ′ was described using a first-order approach for diffusion-controlled particle growth [368,371]:

$$\left(\frac{d_t}{2}\right)^3 - \left(\frac{d_0}{2}\right)^3 = At \tag{4.18}$$

where $d_0$ and $d_t$ denote the average diameter of the γ′ particles at time = 0 and time = $t$, respectively, and $A$ is a temperature-dependent constant which can be obtained through the evaluation of experimental results [368].

#### 4.1.8. *Grain growth*

For the modeling of grain growth, the methods established in materials processing literature, such as Monte Carlo simulations [372,373] and cellular automata [374], are directly applicable to AM. While demonstrated previously for a limited number of situations in AM [349,356,357] and welding [342], these models can be integrated with heat transfer calculations to simulate grain structure. For low heat input AM processes such as PBF-L, the typical as-built microstructure is very fine, and there are generally no significant recrystallization and coarsening during printing. This is attributed to the short period spent by the material at high temperatures due to rapid heating and cooling rates. Moreover, in nickel alloys, precipitates (e.g., Laves and delta phases in Alloy 718), formed in the inter-dendritic regions due to micro-segregation, can pin the grain boundaries [375]. On the other hand, for AM processes involving high pre-heating or heat build-up and in the absence of grain boundary pinning precipitates, grain growth (e.g., β in Ti-6Al-4V) during the build process can be substantial. Additionally, recrystallization and grain growth take place during post-fabrication heat treatment, and it is important to understand the kinetics of grain growth as a coarser grain structure improves the high-temperature creep property. Finally, a series of repeated phase transformations may occur over a large number of heating and cooling cycles during AM (for example in Ti-6Al-4V: α → β during heating, β grain growth and β → α during cooling, α → β during reheating, and so on). Modeling of grain growth in alloys processed with a moving heat source can provide important information about the evolution of grain structure [349,356,357].

In summary, modeling of microstructures of alloys commonly used in AM such as Ti-6Al-4V, IN718 and 300M steel are just beginning. The non-uniform spatial variation and convoluted temporal evolution of these phases were not revealed satisfactorily due to large technical and scientific difficulties and needs more work. The prediction of solid-state phase transformations during the layerwise AM process using verifiable mechanistic models is a promising approach and a challenging task which has not been undertaken adequately. For example, the prediction of the decomposition of martensite α′ phase during PBF-L of Ti-6Al-4V requires the integration of a phase transformation model and an AM process model which can provide reliable thermal cycles. Similarly, thermal cycles for the 3D build are required in the phase transformation model to compute the minor phase precipitation for nickel base alloys. However, such comprehensive integrated AM process and phase transformation models are needed.

### 4.2. *Defects*

Recent developments in mechanistic modeling allow for the prediction of various defects and provide a deeper understanding of why certain defects form. These modeling efforts can help to avoid the common defects in AM and eventually serve as a design tool. The main types of defects in AM are lack of fusion porosity, loss of alloying elements due to vaporization, cracking and the development of deformation and residual stresses within the part. This section will discuss the mechanistic modeling efforts made to predict these main types of defects. While it is also reasonable to consider microstructural inhomogeneity as a defect due to its effect on mechanical properties, details of modeling efforts for microstructural predictions are found in the previous section.

### 4.2.1. Vaporization of alloying elements

During AM, significant vaporization of alloying elements can occur in the molten pool due to high temperatures. This is especially the case when an electron beam is used as a heat source, because the combination of low chamber pressure and high temperatures promotes rapid vaporization of alloying elements. All elements do not vaporize at the same rate because of the difference in vapor pressures of elements, and such selective vaporization of alloying elements often results in a significant change in the composition of the alloy [25,99,376]. Composition change has been considered to be an important factor for evaluating printability of alloys [25].

Heat transfer and fluid flow calculations are required to estimate alloying element loss from pools of molten metal, because the temperature distribution of the molten surface is needed to calculate the rate of vaporization. Methods for calculating selective variation of alloying elements are already well-established in the fusion welding literature [20], and they can be applied in laser-based AM processing. Therefore, a critical assessment of the modeling of vaporization in laser welding is presented before examining the application of this knowledge to AM.

The loss of volatile alloying elements is known to occur during the processing of both steels and non-ferrous alloys. Laser welding of high manganese stainless steels is known to result in the depletion of manganese and chromium in the weld metal [377–381], and aluminum alloys are known to lose magnesium and zinc [382]. These losses often result in the degradation of mechanical properties due to changes in microstructure, as well as the deterioration of the corrosion resistance. Some aluminum alloys often experience an increase in hot cracking susceptibility. Fig. 4.9 shows the concentration profiles of manganese in the base plate and welding track during laser welding of three varieties of stainless steel [383]. Significant depletion of manganese in the weld metal is clearly observed in each case. Similarly, depletion of magnesium [382] in the weld zone in bead-on-plate autogenous conduction mode laser welding of thin aluminum alloy 5182 plates (4.2 wt% Mg, 0.2%Si, 0.35% Mn, 0.07% Zn, 0.15%Cu, 0.1% Ti and balance Al) can be observed in Fig. 4.10. These results indicate that relatively low boiling point elements, such as Al, Mg and Zn, selectively vaporize out of the molten pool more readily than other elements. The reason for this can be explained by a basic analysis of the factors that determine composition change.

A mass balance is a good starting point to understand the role of various factors that contribute to the alloying element loss and the resulting composition change. The decrease in the concentration of an element $i$, such as manganese or magnesium, can be expressed as follows [20]:

$$\Delta\%C_i = 100\sum (R_i\ dA_s)/(\rho\ V_m) \tag{4.19}$$

where $\%C_i$ is the decrease in the concentration of alloying elements, $R_i$ is the local vaporization rate of $i$ per unit surface area, $dA_s$ is the local surface area, ρ is the density of the weld metal, and $V_m$ is the volume of the weld metal melted per unit time. The term

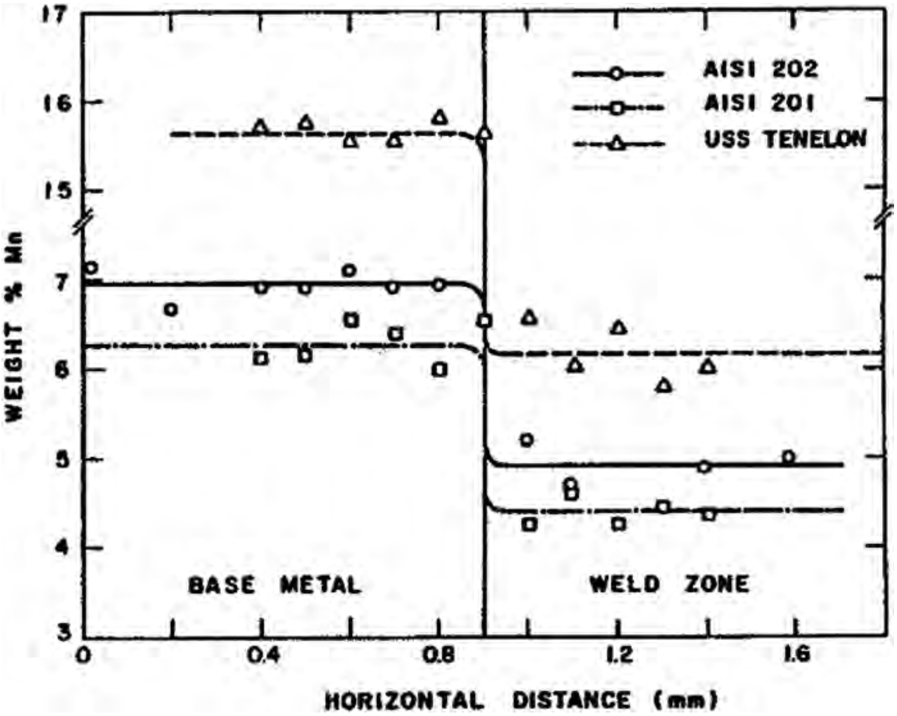

**Fig. 4.9.** Concentration profile of manganese in the weld zone and the base metal in a laser weld of stainless steel [383]. Laser power: 560 W, welding speed: 3.5 × $10^{-3}$ m/s, shielding gas flow rate: $10^{-4}$ $m^3/s$.

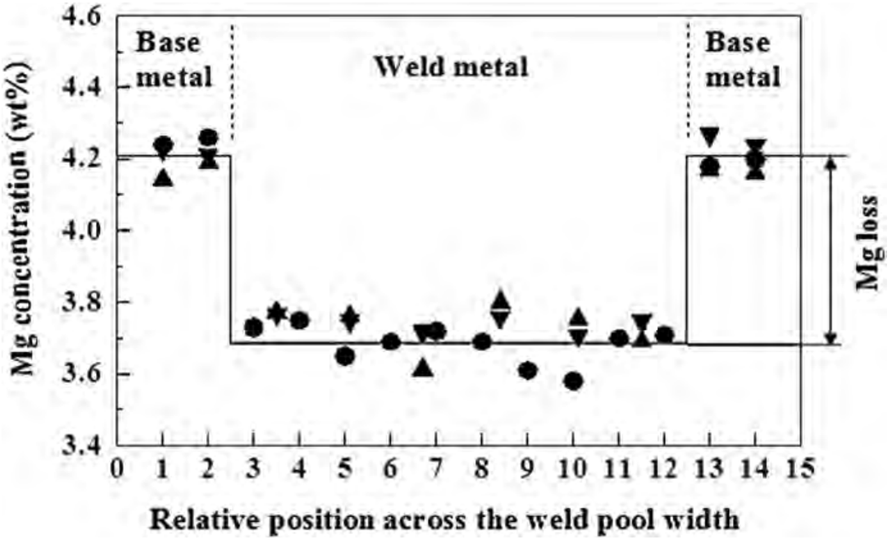

**Fig. 4.10.** . Typical magnesium concentration profile across the weld pool width [382]. The data were taken on three weld pool cross sections of the same welding condition: laser power 3.0 kW, welding speed 105.8 mm/s, and beam defocusing 1.5 mm.

$\sum (R_i \ dA_s)$ is the total rate of vaporization of element i per unit time from the top surface of the molten pool. Eq. (4.19) shows that the change in the concentration of an element depends on both the vaporization rate of the element and the volume of the molten pool. Since the vaporization rate depends on the top surface area and the elemental loss is distributed over the entire volume of the molten pool, the surface to volume ratio of the molten pool plays an important role in influencing the composition change, often being the more dominant factor than the pool size [20]. For the conditions of the experiments presented in Fig. 4.9, small molten pools were formed, and significant composition changes were observed in each case. For this reason, an increase in the power of the heat source does not always result in a more pronounced composition change. While this fact may appear counterintuitive at first, the higher power results in larger molten pools with a lower surface area to volume ratio. Consequently, in some cases a less pronounced composition change may be observed than at lower powers, despite higher vaporization flux at higher powers. In short, the composition change is most pronounced when the volume of the liquid pool is small and the surface area to volume ratio of the molten pool is high [20].

There are varying levels of complexity that can be used to calculate the vaporization flux, depending on the accuracy desired. However, most models are based on the fact that there is some relationship between the vapor pressure of an element above the molten pool and the vaporization rate of that element. A simple approach to calculate the vaporization flux of an element *i* in the alloy, $J_{i,}$ involves applying a modified form of Langmuir equation [25]:

$$J_i = \frac{\xi P_i}{\sqrt{2\pi M_i T}} \tag{4.20}$$

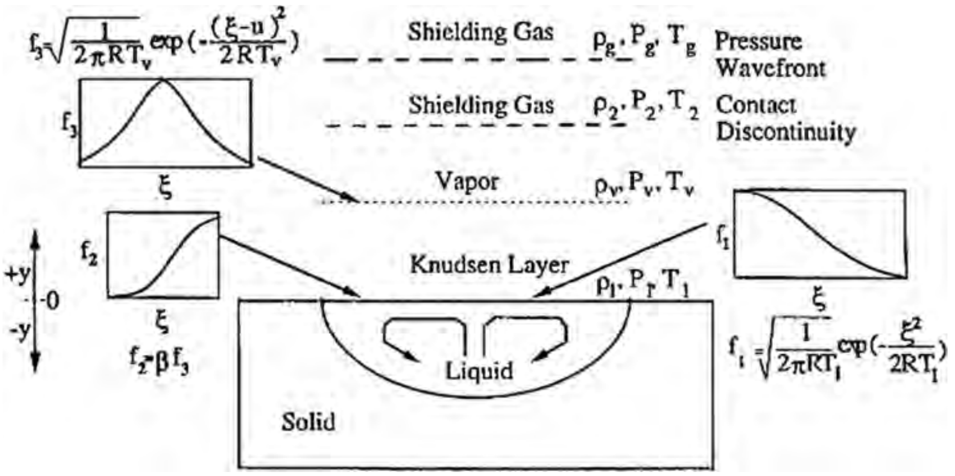

**Fig. 4.11.** Velocity distribution functions of vapor molecules at various locations, after references [382,385,386].

where $P_i$ is the partial pressure of element $i$ over the alloy, $M_i$ is the molecular weight, $T$ is the local temperature. The $P_i$ can be found from the product of activity of element $i$ and the equilibrium vapor pressure of $i$ at temperature $T$. The term $\xi$ is a positive fraction that represents an adjustment factor to account for the condensation of vaporized atoms on the surface. This variable is needed because the original Langmuir equation was derived for evaporation in vacuum where the condensation of the vaporized species could be safely ignored. Eq. (4.20) significantly overestimates the vaporization rate at ambient pressure when $\xi$ is taken as 1 [384]. However, the equation is useful for the calculation of relative rates of vaporization of various alloying elements from a liquid surface where the value of $\xi$ is considered to be a constant for all alloying elements. Temperatures of the molten pool can be calculated using a three-dimensional heat transfer and fluid flow model and using these values the equilibrium vapor pressures of all alloying elements at each location on the surface can be estimated.

A more accurate model for the calculation of vaporization rate that considers the effects of the ambient pressure was proposed by Anisimov and Rakhmatulina [385] and Knight [386]. Their model solves the equations of conservation of mass, momentum and energy in a thin layer adjacent to the liquid-vapor interface known as the Knudsen layer. Notably, they consider the possibility that some atoms that leave the molten pool as vapor will not escape into the atmosphere, and instead will condense on the molten pool surface. To account for this condensation, the model considers the velocity distribution functions of the metal vapor molecules close to the molten pool [385,386] shown in Fig. 4.11. At the liquid pool surface, the velocity distribution, $f_1$, is half-Maxwellian because the vapor molecules can only move away from the pool surface, i.e. the velocity is positive. A portion of the vaporized material, $f_2$, condenses on the liquid surface. The Knudsen layer which is a distance of several mean free paths length after which the velocity distribution, $f_3$, becomes fully Maxwellian and the velocity can vary between $-\infty$ to $+\infty$ as shown in Fig. 4.11. It can be shown that the temperature $T_v$, density $\rho_v$, pressure $p_v$ and the mean velocity $u_v$ of the vapor at the edge of the Knudsen layer can be related to temperature $T_L$, density $\rho_L$, and pressure $p_L$, of the vapor at the liquid surface by treating the Knudsen layer as a gas dynamic discontinuity. The derived relations across the Knudsen layer are given by:

$$\frac{T_v}{T_L} = \left[\sqrt{1 + \pi\left(\frac{\gamma_v - 1}{\gamma_v + 1}\frac{m}{2}\right)^2} - \sqrt{\pi}\frac{\gamma_v - 1}{\gamma_v + 1}\frac{m}{2}\right]^2 \tag{4.21}$$

$$\frac{\rho_v}{\rho_l} = \sqrt{\frac{T_L}{T_v}}\left[\left(m^2 + \frac{1}{2}\right) e^{m^2}\, erfc(m) - \frac{m}{\sqrt{\pi}}\right] + \frac{1}{2}\frac{T_L}{T_v}\left[1 - \sqrt{\pi}m\, e^{m^2}\, erfc(m)\right] \tag{4.22}$$

$$\beta = \left[(2m^2 + 1) - m\sqrt{\pi\frac{T_L}{T_v}}\right] e^{m^2}\frac{\rho_l}{\rho_v}\sqrt{\frac{T_L}{T_v}} \tag{4.23}$$

where $m = u_v/\sqrt{2\, R_v T_v/M_v}$, $R_v$ is the ratio of the universal gas constant ($R_g$) to the average molecular weight of the vapor ($M_v$), $\gamma_v$ is the ratio of specific heats of the vapor which is treated as a monatomic gas, and $\beta$ is the condensation factor. The equilibrium vapor pressure at the pool surface is obtained from the sum of the equilibrium vapor pressures of all alloying elements at the local temperature and $M_v$ is the average molecular weight of the vapor. In order to compute the four unknowns in Eqs. (4.21)–(4.23), namely, $T_v$, $\rho_v$, $\beta$, and $m$, another independent equation is necessary. This relation is obtained by applying the Rankine-Hugoniot relation [386] to relate the pressure at the edge of the Knudsen layer to the ambient pressure.

$$\frac{p_L}{p_g}\frac{p_2}{p_1} = 1 + \gamma_g M\Gamma\left[\frac{\gamma_g + 1}{4}M\Gamma + \sqrt{1 + \left(\frac{\gamma_g + 1}{4}M\Gamma\right)^2}\right] \tag{4.24}$$

where $p_1$ and $p_2$ are the pressures in front of and behind the wavefront, respectively, and $\Gamma = \sqrt{\gamma_v \mathrm{R_v T_v}}/\sqrt{\gamma_g \mathrm{R_g T_g}}$ and $M$ is the Mach number which is related to $m$ by the relation:

$$m = M\sqrt{\frac{\gamma_v}{2}} \tag{4.25}$$

The Mach number $M$ and the density $\rho_v$, obtained by solving Eqs. (4.21)–(4.24), can be used to calculate the vaporization flux due to convection from the liquid pool surface corresponding to a local surface temperature $T_L$ from:

$$J_P = \rho_v M S \tag{4.26}$$

where $S$ is the speed of sound in vapor at temperature $T_v$. The vaporization flux of an alloying element $i$, $J_i$, is given by the product of the total vapor flux and the mole fraction of $i$ in the gas.

$$J_i = a_i\frac{p_i^0}{p_L}\frac{M_i}{M_v}J_P \tag{4.27}$$

where $a_i$ is the activity of element $i$ and $p_i^0$ is the partial pressure of element $i$ over the pure liquid. Since the concentration of metal vapor at the molten pool surface differs from those of the gas atmosphere, an additional driving force exists for the diffusional flux of alloying elements. The flux of each element due to concentration gradients can be expressed as,

$$J_c = K_{g,i}\left(M_i\frac{a_i p_i^0}{RT} - C_i^b\right) \tag{4.28}$$

where $K_{g,i}$ is the mass transfer coefficient of element $i$, and $C_i^b$ is the concentration of element $i$ in the bulk gas. The total evaporative flux can be calculated by adding Eqs. (4.27) and (4.28).

Similar to Eq. (4.20), the temperature distribution on the molten pool surface is a prerequisite for the approach given by Eq. (4.21) through Eq. (4.28). Equilibrium vapor pressures at the temperatures of interest, typically up to 2500 K or higher, are also needed and can usually be obtained from literature data [387]. Mukherjee and DebRoy [283] used Knight's model to compute the change in the composition of alloying elements from SS316 in AM. The results are shown in Fig. 4.12 for a typical condition of deposition. Significant loss of manganese is clearly observed followed by less pronounced loss of chromium. Klassen et al. [101,201] applied this approach within a two-dimensional free-surface LBM. The temperature fields in the molten pool of Ti-6Al-4V was combined with the evaporation calculations, and the recoil pressure from evaporating material acted on the free-surface of the molten pool during EB-PBF. Vaporization of aluminum was shown to be strongly influenced by the electron beam current.

Many other experimental results of vaporization in AM have been published that display the trends predicted by vaporization models. Juechter et al. [376] confirm the considerable loss of Al for the PBF-EB of Ti-6Al-4V builds. Experimentally measured concentration of aluminum [376] for various speeds and powers is shown in Fig. 4.13. In all cases, the concentration of aluminum in the build was significantly lower than that in the powder. As shown in the figure, both the energy of the beam and the scanning speed were varied and, for a given linear energy density, higher scanning speed produced higher aluminum composition change. Because a faster scanning normally results in a shallower, longer molten pool with a larger surface area, the more pronounced composition change is consistent with the fact that a higher surface area to volume ratio will produce more vaporization.

Fig. 4.14 shows the average aluminum concentration [25,99,376] in builds of Ti-48Al-2Cr-2Nb. The experimental results and the simulations show the important effects of power and power density on the depletion of aluminum for a constant scanning speed. The builds were made using PBF-EB and the simulations were based on LBM that considered stochastic powder particle distribution. The considerable decrease in the aluminum concentration of up to about 1.4 wt% Al agrees with the results reported by several other Ti-Al alloys [388–392] considering the difference in the deposition conditions. For example, Biamino et al. [389] found a depletion of about 0.7 wt% Al for PBF-EB at a beam energy of 60 keV, scanning speed of 1000 mm/s and 0.1 mm spot diameter. Taminger [390] found that during PBF-EB of Ti-6Al-4V, the measured chemical composition along the build height showed a depletion in the Al concentration and an increase in the Ti concentration. Apart from the composition change, vaporization of alloying elements has also been attributed to other defects during AM. For example, PBF-EB of a high niobium-containing titanium aluminide alloy, Ti–45Al–7Nb–0.3 W at high scanning speed, resulted in the formation of banded structures which is a defect caused by the vaporization of aluminum [391].

Selective vaporization of magnesium has been reported during DED-EB of aluminum alloys [393,394]. Examination of the composition of the deposited material showed much lower Mg content compared with the wire feedstock. The magnesium concentration in the wire was 0.52 wt%, while the bottom of the deposit had 0.19 wt% Mg and the top had 0.11 wt% Mg. This loss is important since a critical amount of magnesium is necessary for the nucleation of precipitates that are responsible for strengthening in the aluminum alloy [395]. Dai and Gu [396] computed the velocity fields of the vaporized material above the molten pool and found that the velocity distribution was significantly affected by the type of surrounding gas, argon, helium or nitrogen. The surrounding gas affected the diffusion of the metal vapor. In addition, it influenced the surface morphology of the build. Some alloys such as Mg-4.2Zn-0.5Zr contain multiple volatile alloying elements such as Mg and Zn. Due to the difference between the vaporization rates of Mg and Zn, the final composition of the parts differed from the feedstock alloy [397]. A higher Mg to Zn ratio and a lower total content of Mg and Zn were obtained in the parts and losses of elements affect chemical composition, microstructure and properties of the parts [397].

With only a few exceptions, most models of AM do not consider vaporization and the resulting composition change of alloys. There is no significant barrier to the implementation of vaporization models, because the existing theory from laser welding literature provides computational methods that can be implemented into numerical calculations of AM. Though the trends predicted by these models are qualitatively observed in AM experiments, validation of these models for a quantitative prediction of composition change still needs to be undertaken. Furthermore, rapid vaporization of alloying elements from the molten pool exerts a recoil force on the liquid surface, which in extreme cases may lead to further defects, such as spattering.

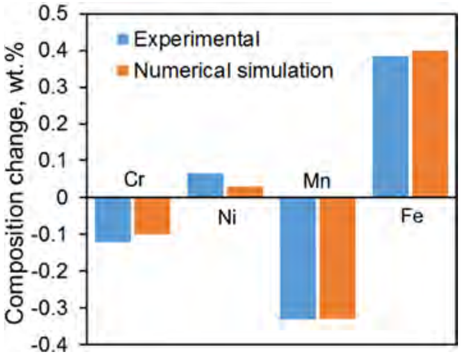

**Fig. 4.12.** Composition change in wt% of the most volatile elements due to vaporization for SS316 during DED-L [283].

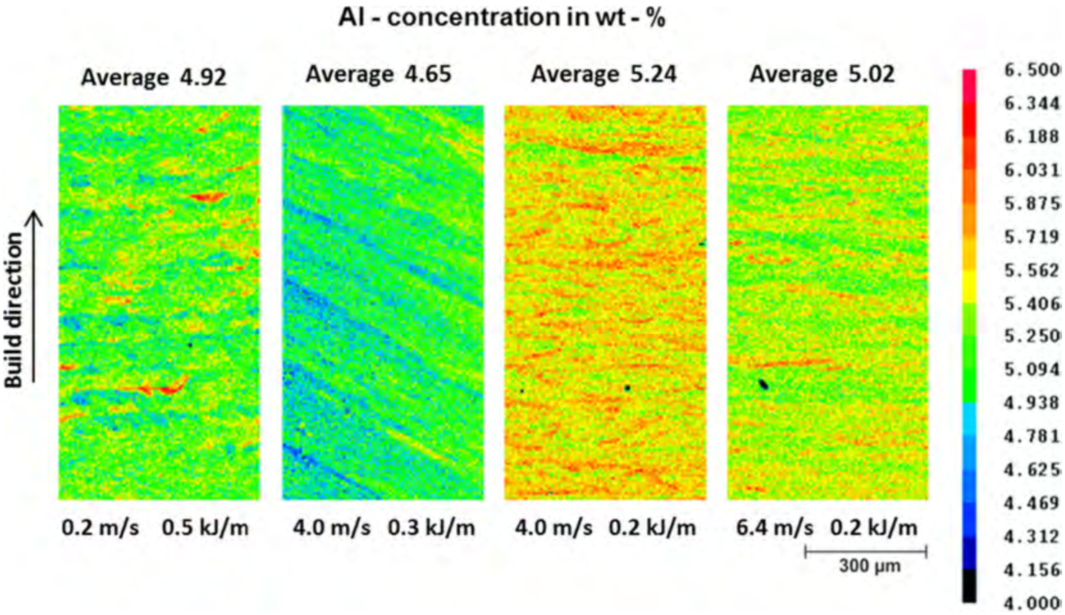

**Fig. 4.13.** Experimentally measured concentration of aluminum [376] for the deposition of Ti-6Al-4V by PBF-EB.

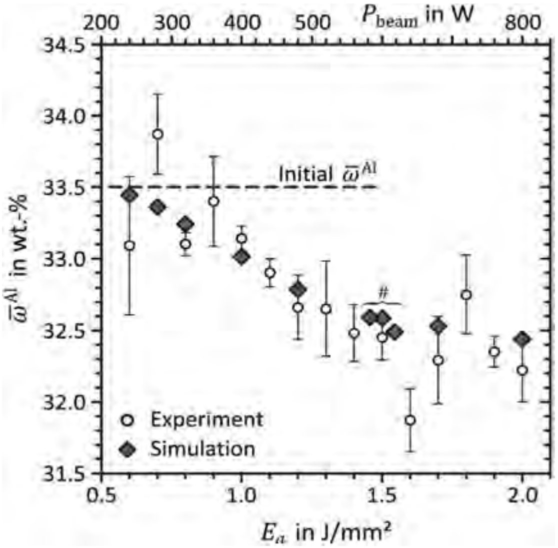

**Fig. 4.14.** Average concentration of aluminum [99] in builds of Ti-48Al-2Cr-2Nb samples produced by PBF-EB as a function of power density ($E_a$) showing higher power density results in more pronounced aluminum loss.

### 4.2.2. Spattering

There are two types of spatters common in AM. They include the ejection of liquid metal droplets from the molten pool [398,399] and the ejection of the powder particles near the molten pool [167,398]. Fig. 4.15 shows two types of spatters during PBF [398–400] and their origins are critically examined using transport phenomena-based models.

*4.2.2.1. Ejection of liquid metal droplets.* At very high temperatures, the vapor from the liquid pool exerts a large recoil force on the liquid pool surface which creates a driving force for liquid droplets to be torn off and ejected from the molten pool. Modeling of the ejection of molten metal droplets requires calculations of recoil and surface tension forces. For example, calculated results by Basu and DebRoy [401] showed that when the vapor recoil force exceeds the surface tension force of the liquid metal at the periphery of the molten pool, liquid expulsion takes place. The vapor recoil force $F_R$ and the surface tension force at the periphery of the liquid pool, $F_S$, can be expressed by:

$$F_R = \sum \Delta P dA_s \tag{4.29}$$

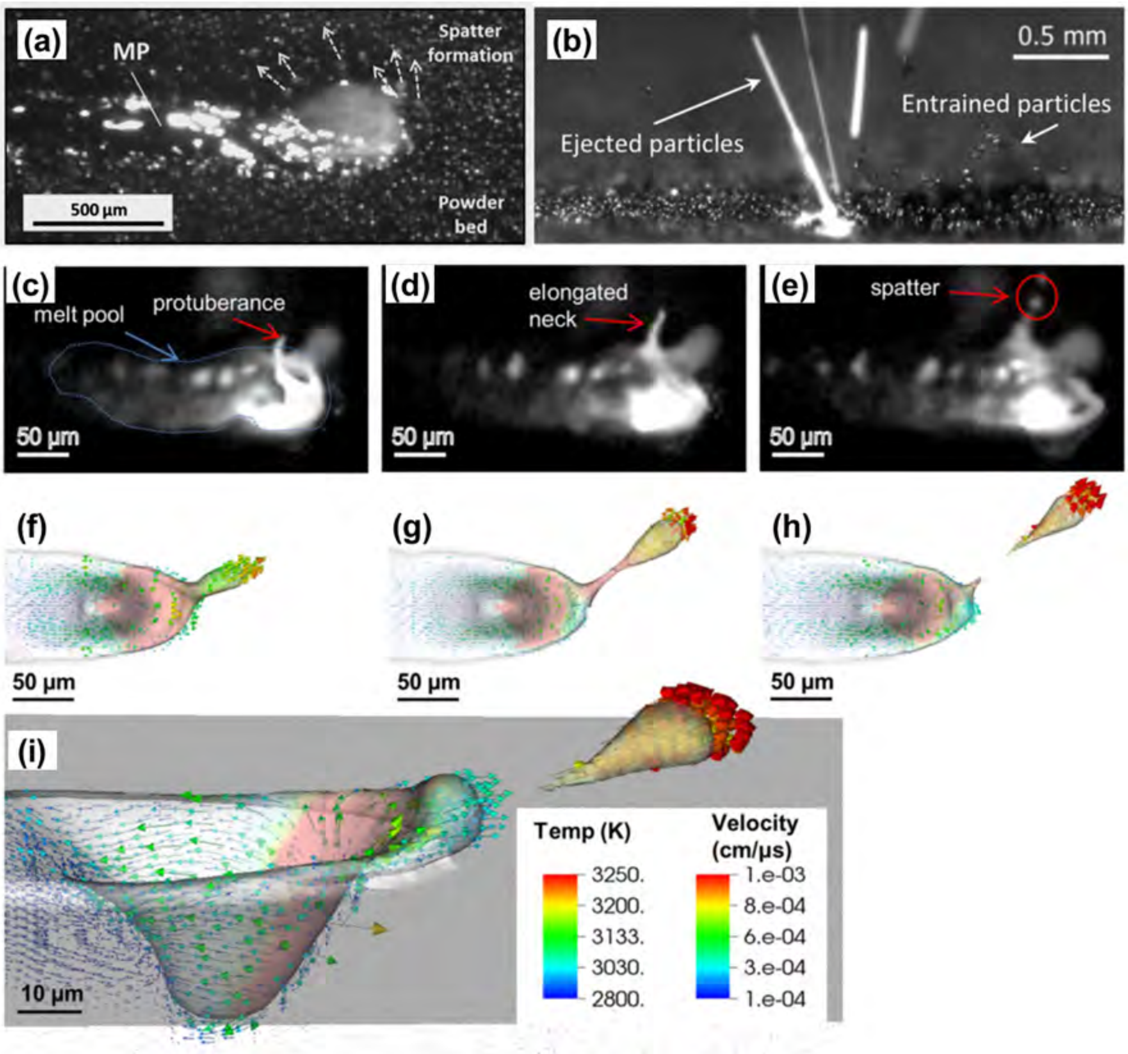

**Fig. 4.15.** Different types of spatters during PBF. (a) Ejection of liquid metal from the molten pool [400]. (b) Ejection of partially melted powder particles approaching the laser plume, and scattering of the moving solid powder particles beyond the molten pool [398]. (c)-(e) and (f)-(i) are for the comparison between experiment and simulation of the ejection of liquid metal from the molten pool for a bare SS316L plate [399].

$$F_S = l\ \gamma_M \tag{4.30}$$

where $dA_s$ is a local area on the surface of the liquid pool, $\Delta P$ is the difference between the local equilibrium vapor pressure and the atmosphere pressure, $l$ is the length of the boundary of the liquid pool top surface and $\gamma_M$ is the surface tension at the melting point. When the power density of the heat source is high, the recoil force may overpower the surface tension force which tries to contain the liquid metal within the pool [77,78] As a result, tiny metal droplets are expelled from the liquid pool. Chun and Rose [402] showed that as much as 90% of the material was lost from the molten pool as liquid when an aluminum specimen was treated with a laser pulse for more than 200 ms at a power density of $10^7$ W/cm$^2$. No significant expulsion occurred at lower power densities.

When irradiated with a single pulse, expulsion was observed only for long pulse durations for lead, titanium, and stainless steel. For multiple pulses, short pulses led to liquid metal expulsion only at high frequencies when the irradiated region could not cool sufficiently between pulses. The combinations of laser power and spot diameter [403] that led to expulsion of SS 304 droplets for pulse durations of 4.0 ms is shown by the dotted lines in Fig. 4.16(c). The points on a given curve have the same laser power density, i.e., laser power per unit area. The results show that the liquid metal expulsion can be prevented when the spot diameter is increased while keeping the power constant. In contrast, when the spot diameter is decreased, the laser power density increases and eventually expulsion occurs when the laser power density exceeds about 7.0 kW/mm$^2$ (or 0.7 MW/cm$^2$). The solid line shows the equality of recoil and surface tension forces. The computed spot diameter and laser power combination necessary to initiate liquid metal expulsion agreed well with experiments, indicating the accuracy of the mechanism of liquid metal expulsion. The size of the ejected droplets ranged from tens of micrometers to several hundred micrometers [403]. The increase in the power density resulted in larger droplets and greater size range of particles.

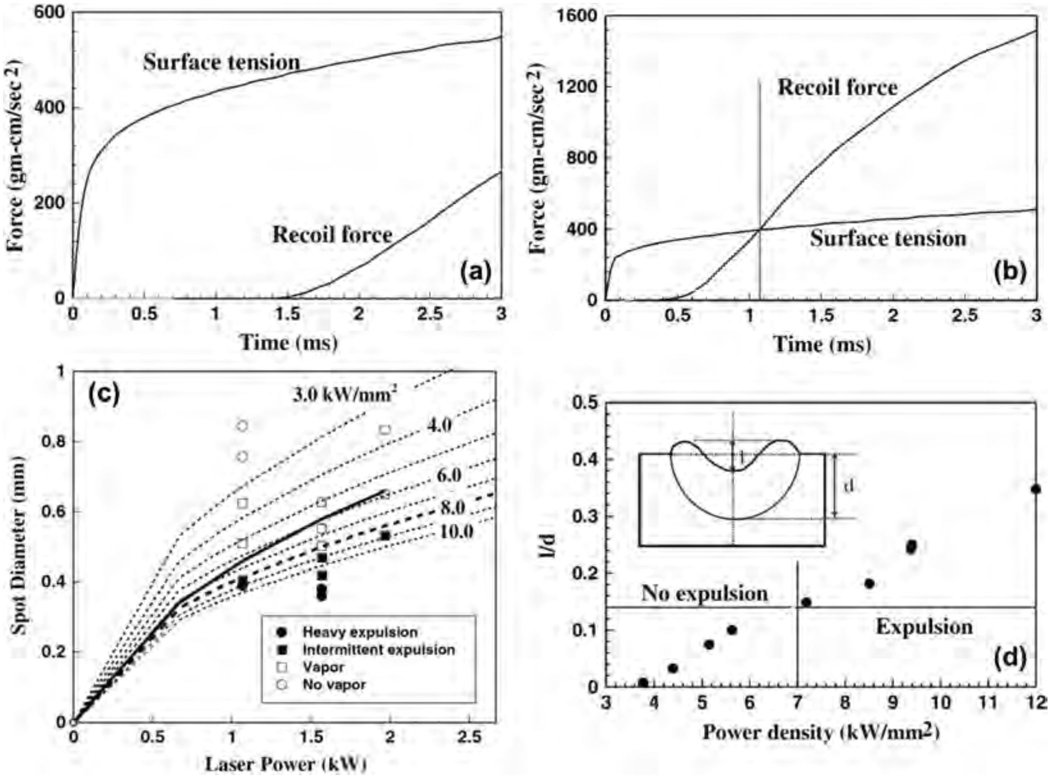

**Fig. 4.16.** Recoil pressure and surface tension force at the periphery of the molten pool as a function of time at laser power of 1967 W for spot diameter of the laser beam (a) 0.835 mm and (b) 0.533 mm [403]. (c) Liquid metal expulsion analysis data under different laser power densities for laser spot welding of SS 304 for 3.0 ms pulse duration [403]. (d) Variation of maximum depression to depth of the molten pool ($l/d$) with the laser power density [403].

Eqs. (4.28) and (4.29) indicate several fundamental aspects of spatter formation, i.e. generating strong vapor pressure from local boiling, acceleration and redirection of the local liquid metal, accumulation of vertical momentum, and eventually droplet ejection. Process parameters and material characteristics determine the boiling conditions and the local geometry of the fusion zone which in turn determine whether spatter occurs [404]. The energy input greatly influences spattering and higher energy leads to stronger spattering intensity [405]. The liquid metal expulsion was predicted by balancing the recoil pressure force with the surface tension force at the periphery of the liquid pool under various laser processing conditions [403].

Fig. 4.16(a) and (b) compares the recoil pressure and surface tension force at the periphery of the molten pool [403]. Smaller laser spot diameter results in higher energy density, which further causes higher recoil pressure. Ejection of a small portion of the liquid metal from the edge of the molten pool occurs when the recoil pressure exceeds the local surface tension force. Fig. 4.16(c) shows the trends of vapor and spatter generation for various power densities obtained from different laser powers and laser spot sizes [403]. No significant vaporization occurs under the conditions of low power and large laser spot diameter. In contrast, heavy expulsion occurs under conditions of high power and small laser spot diameter. Moreover, the increase in the power density resulted in larger droplets and greater size range of particles. The depression of the weld center under the recoil pressure could be used as an indicator of liquid metal expulsion which is shown in Fig. 4.16(d) [403].

Wang et al. [405] suggested that the recoil pressure, flow of liquid metal owing to Marangoni effect and the heat effect in the molten pool, all contributed to the spatter formation during PBF-L of CoCr. The morphologies of the spatter were affected by these three types of contributing factors. Spattered particles had an average size of approximately 162 μm compared with the original powder size of 32 μm. The particles were embedded into the surface and interior of the fabricated parts. Simonelli et al. [406] studied the spattering behavior during PBF-L of SS316L, Al-Si10-Mg and Ti-6Al-4V alloys. They found that the spatter was spherical in all cases and the size was significantly larger than the starting pre-alloyed powders. Oxides of several μm thickness formed on the surfaces of 316L and Al-Si10-Mg spatters. However, no oxide was formed on Ti-6Al-4V spatters. Note that the solubility of oxygen in Ti alloys is significantly higher than that in Fe and Al alloys. Thus, the Ti-6Al-Vspatters are contaminated with oxygen as well although oxide is not generated. It has been suggested [407] that sensing of spatters by a high-speed machine vision could be used as a part of a multi-sensor data collection for the detection of defects in builds.

Quantitative understanding of the spatter formation requires temperature field on the surface of the liquid pool, which requires heat and fluid flow calculations. Fig. 4.15(c)–(i) shows the experimental observation and numerical simulation results of the droplet ejected from the edge of the molten pool. The expulsion force is mainly the recoil pressure induced by the laser-material interaction.

At very high powers the peak temperature of the molten metal may reach the boiling temperature. Significant vaporization occurs, and thus strong recoil pressure is exerted on the surface of the molten pool. The resistant force exerted on the liquid metal is mainly surface tension.

*4.2.2.2. Ejection of powder particles.* During AM a vapor jet may be generated by the intense evaporation from the molten pool. A low-pressure zone is created near the vapor jet, which induces an inward gas flow due to the Bernoulli effect during common PBF conditions [182]. The induced gas flow can be sufficiently strong so that some powder particles are driven out as hot or cold ejections depending on the intersections of their trajectories with the laser beam [167]. The localized laser melting, generation of an intensive vapor jet, flow of the shielding gas, and the entrainment of the particles in the gas flow take place sequentially [408]. The orders of time duration are reported as microseconds for melting, tens of microseconds for vapor jet/plume formation, hundreds of microseconds for argon gas flow formation [408].

Utilizing the technique of high speed Schlieren imaging, the effect of refractive index gradients, associated with the laser plume and the heated atmosphere above the molten pool during PBF-L was visualized as shown in Fig. 4.17(a) [398]. The convection fronts originated from the surface of the molten pool propagates in the atmosphere above the deposit. Both heat and momentum are transferred from the vapor jet to the atmosphere, evidenced by the refractive index gradients observed around ejected particles. The dominant factors determining the movement of the entrained particles include the pressure and velocity of the induced gas flow, the local positions and traveling directions of the powder particles, and surrounding geometric restrictions on the powder particles.

Fig. 4.17(b) shows the numerically calculated velocity surface plot of a fast laser plume, with arrows showing the slower atmospheric gas flow that it induces [398]. The velocity is highest closer to the bed due to the maximum momentum being located near the surface of the molten pool. The velocity decelerates exponentially in the vertical direction and the variation of the velocity with height suggests that a swirl is imparted in the particles [398]. Upwards momentum carried by the plume is imparted to the surroundings, while a radial flow field is generated in the atmosphere induced via momentum conservation. Fig. 4.17(c) shows the numerically simulated results of the radial velocity component of the flow induced in the Ar atmosphere [398]. The radial flow of the gas near the laser beam is mainly inwards as indicated by the negative values. However, a short region of flow reversal exists further away from the center of the laser beam, approximately between the edge of the laser spot and the edge of the molten pool. The

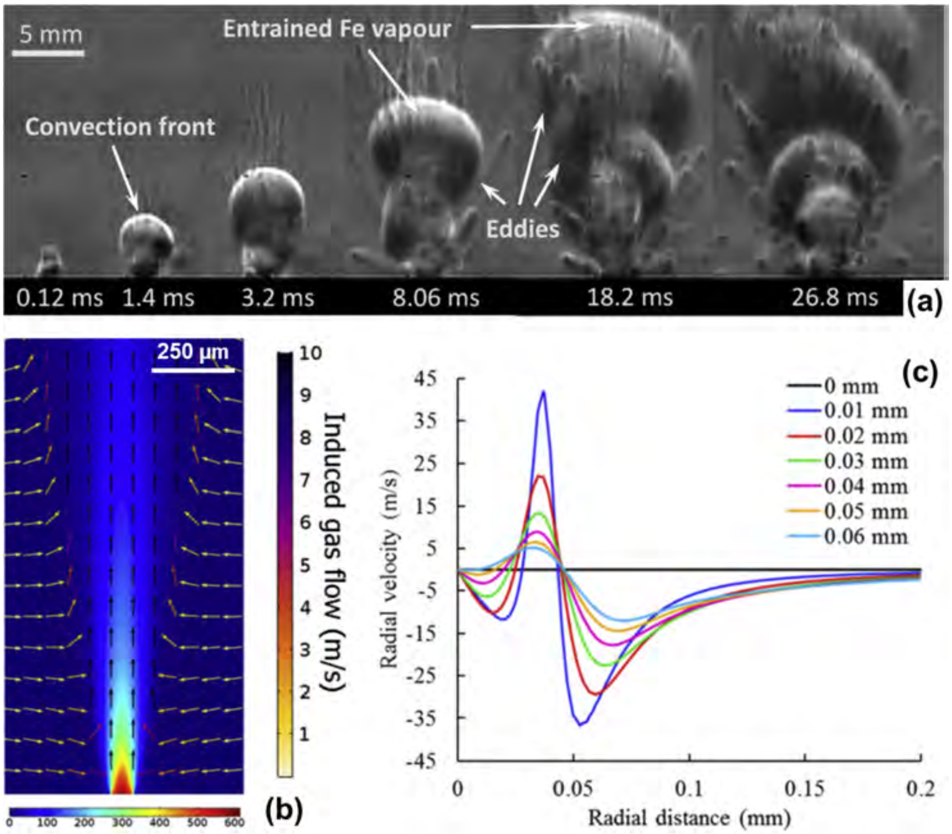

**Fig. 4.17.** (a) Composite schlieren image of the heated gas rising due to convection at the times indicated for laser power 100 W and scan speed 0.5 m/s towards the viewing direction. Radial momentum is imparted to the atmosphere by eddies trailing the convection fronts [398]. (b) Calculated velocity surface plot of fast laser plume, with arrows showing the slower atmospheric gas flow that it induces [398]. (c) Radial velocity component of the flow induced in the Ar atmosphere by the laser plume at different z-heights above the powder bed [398].

significant variations in the radial velocities indicate complex trajectories of the entrained powder particles in the induced gas flow. The reversal of the radial velocities shown in Fig. 4.17(c) indicates that a deceleration is experienced by entrained particles approaching the molten pool, promoting upwards ejection. Additionally, particles caught in the wake with no prior momentum are ejected upwards and outwards [398]. Drag force on the particles due to the shear flow slows down with decreasing gas density and at some pressure reverses the particle motion. At this pressure the width of the denudation zone is the minimum [182].

Fig. 4.18 shows schematically three trajectories of the entrained powder particles by the induced gas flow from the laser beam during PBF-L [399]. There are mainly three outcomes of the entrained powder particles depending on the interaction among the laser beam, deposited track and powder particles, i.e., (1) moving to the molten pool and being consolidated with the deposit, (2) flying to the vapor jet without being actually irradiated by the laser beam, and eventually scattered to the surroundings as cold particles, (3) approaching to the laser beam and getting irradiated non-uniformly, thus being ejected as hot particles [182]. It was reported that 60% of the total spatter generated was from hot ejections, 25% from cold ejections, and 15% from recoil pressure induced ejections in the power range of 200 to 300 W and scanning speeds of 1.5 to 2.0 m/s [399]. Powder spattering around the laser beam is mainly driven by the vapor pressure, while particles in the region behind and ahead of the laser beam are entrained by the argon gas flow. Particles driven by vapor pressure travel significantly faster than particles carried with the gas flow, and the acceleration and driving force of vapor driven particles are about one order of magnitude larger than argon gas flow-driven particles [408].

The ejection of partially melted powder particles which experience inhomogeneous irradiation of the laser beam is an important form of spatter during PBF-L. The powder particles are heated non-uniformly when they approach the laser beam. The laser beam energy can heat up a local position of the particle to the boiling temperature during a short time interval of several microseconds [182], which is significantly shorter than the thermal conduction time across a powder particle that is typically tens of microseconds [399]. Thus, only a portion of the particle may reach the boiling state which generates a strong temperature gradient in the particle. Therefore, a highly localized recoil force is created on the side of the particle, ejecting the particle as energetic spatters [399].

Collisions among multiple ejected hot powder particles may occur with transfer of momentum and energy. Upon colliding, weakly bonded agglomerates composed of sintered particles or strongly bonded clusters composed of fused particles may be generated [167,405]. This coalescence process and the resulting large particles reincorporated into the build can potentially lead to defects such as porosity and lack of fusion in subsequent depositing process.

### 4.2.3. *Porosity*

Formation of pores is one of the most commonly observed defects in the AM components. The origin of pores includes: (1) lack of fusion between neighboring tracks, (2) collapse of unstable keyhole, and (3) gas induced pores such as the residual pores in the feedstock powder materials resulting from the production process. The applications of mechanistic models for the understanding of porosity formation mechanisms are critically examine below.

*4.2.3.1. Lack of fusion.* Lack of fusion may result due to insufficient overlap between neighboring tracks of deposits. Inappropriately high scanning speed, low power of the heat source, large layer thickness or hatch spacing may result in this type of defects. Fig. 4.19 shows two examples of lack of fusion generated from excessively large hatch spacing and layer thicknesses [150,409]. The figure also shows that lack of fusion defects may have elongated and irregular shapes and sharp edges. Fig. 4.20 shows the variations of inter-track porosities during PBF-L of Ti-6Al-4V using hatch spacings of 80 μm and 100 μm [186]. Significant inter-track voids would be generated if excessively large hatch spacing is used, causing insufficient heating and melting of the powder feedstocks in the overlap region of adjacent tracks. Since the width and penetration depth of the molten pool often fluctuate due to process instability, considerable overlap between neighboring tracks and layers are necessary to ensure sufficient fusional bonding among the deposited tracks. In addition, inadequate supply of the feedstock materials due to faulty powder packing or localized powder ejection due to metal vaporization and gas flow may cause lack of fusion [182,398].

Models of varying levels of complexity have been applied to predict lack of fusion defects. For example, lack of fusion index which is the ratio of molten pool depth to the layer thickness was proposed to evaluate the susceptibility to lack of fusion defect [1,25]. The

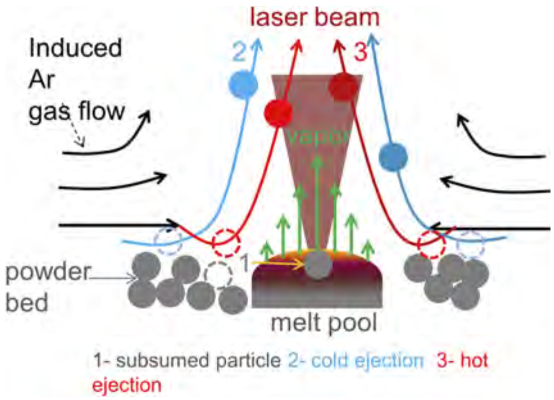

**Fig. 4.18.** Schematic depicting particle entrainment of the powder bed by an induced argon gas flow for a stationary laser beam [399].

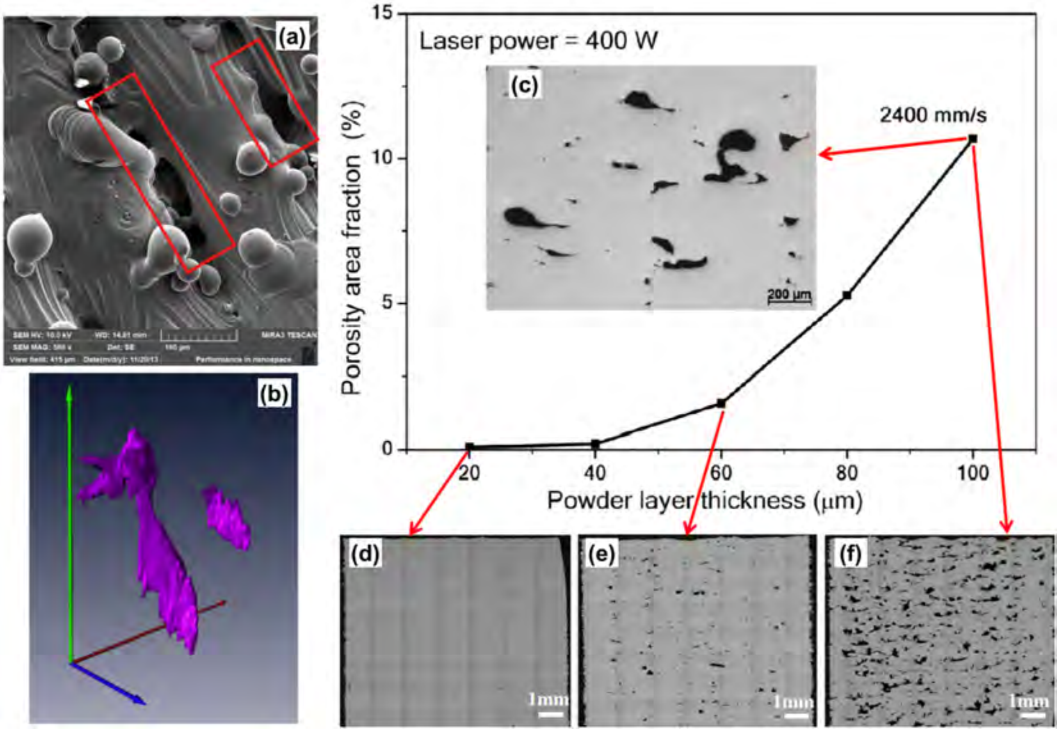

**Fig. 4.19.** Lack of fusion defects (a) Observed in SEM image, and (b) 3D reconstructed synchrotron radiation micro-CT images [409]. (c)-(f) Dependence of area fraction of porosity on powder layer thickness [150], PBF-L of Ti-6Al-4V, 400 W laser power and 2400 mm/s scanning speed.

volume percentage of lack of fusion porosity for Ti-6Al-4V, IN718, SS316, and carbon steel was correlated with the non-dimensional heat input [272]. Considerable overlap between adjacent molten pools was recommended to attain good deposit.

The dependence of lack of fusion defect on molten pool size is explained in Fig. 4.21. These results are obtained from a computationally efficient multi-layer and multi-hatch PBF model for heat, mass, and momentum transfer. The results [19,272] indicate that appropriate hatch spacing and layer thickness depend on feed stock material due to differences in the size of the fusion zone resulting from different thermophysical properties of alloys.

Pool dimensions calculated from numerical heat transfer and fluid flow models are useful to compute parameters that help to understand the lack of fusion defects. For example, Mukherjee and DebRoy [215] show that a lack of fusion index, $L_F$, can be related to materials properties, process parameters and pool shape by:

$$L_F = \rho(C_p \Delta T + \Delta H) \times \frac{\pi\ r_b^2\ V}{\eta_p\ P} \times Fo \times \frac{d_L}{d_P} \times \left(\frac{\delta}{w_P}\right)^2 \tag{4.31}$$

where $\rho$ is the density, $C_p$ is the specific heat, ΔH is the latent heat of fusion of the material, and $\eta_p$ is the absorptivity of the material. With regards to processing parameters, $P$ is the input power, $V$ is the scanning speed, $r_b$ is the beam radius, $d_L$ is the layer thickness, $\delta$ is the hatch spacing, $\Delta T$ is the difference between the peak temperature and the solidus temperature of the alloy, $Fo$ is the dimensionless Fourier number, $d_P$ is the molten pool depth, and $w_P$ is the molten pool width. Fig. 4.22 shows this parameter plotted against experimental data for a range of processing parameters, as well as the associated empirical relationship [215]. If accurate pool depth and width can be simulated from a mechanistic model, this simplified relationship provides a reliable way to predict the extent of lack of fusion voids based on mechanistic modeling.

Powder-based transport phenomena models can directly compute the shape and size of pores without the use of any empirical relations [186,187]. These simulations [67,151,152,175,195] and high-speed video of the process [76,408] both show the unstable nature of the interaction of a molten pool with the surrounding powders, vapor jets, and the gas flow. Xia et al. [191] used a 3-D powder-scale model to show that lack of fusion defects between two hatches may result from incomplete melting of powders, as shown in Fig. 4.20. Even with smart algorithms to reduce computational time, simulations are typically limited to only a few passes within a single layer [67,175,191,196,410]. However, multiple simulations are necessary to obtain reliable results because computational volumes need to be small since three-dimensional powder-scale models are computationally intensive. The need to simulate multiple hatches and layers required for an accurate estimation of lack of fusion porosity limits their applications.

For DED processes, lack of fusion porosity typically occurs due to unexpected variations in the geometry of the deposited bead. These defects in wire feeding processes also originate from temporal variations of deposit geometry. The process involves transport of metal droplets from the wire, through the arc, and into the molten pool. The mode of metal transfer between the wire and the

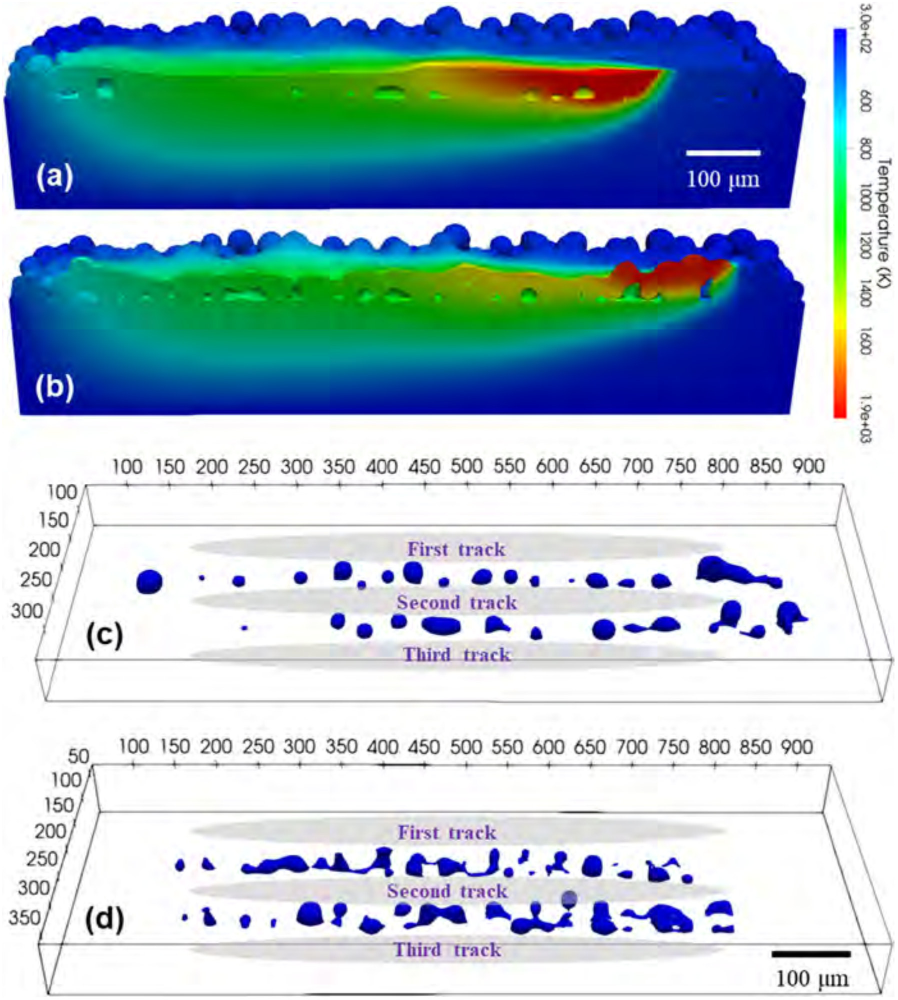

**Fig. 4.20.** Calculated variations of inter-track porosities during PBF-L of Ti-6Al-4V using different hatch spacings. (a) and (c) hatch spacing of 80 μm, (b) and (d) hatch spacing of 100 μm [186].

substrate can vary significantly depending on the selected wire feed rate and arc current, as well as effects due to the vaporization of elements from the molten pool [411]. For GMA welding, models for the droplet size, shape, temperature, and velocity have been studied [258,412–414]. Deflection of the droplets from the wire axis due to Lorentz force depends on the arc current [415,416] and any fluctuation of the arc current or the travel speed can affect the stability of the process. More work in AM is needed since temporal variations of arc current, wire feed rate or gas flow rate can result in spatial variations of track geometry resulting in porosity. Mechanistic modeling to examine the sensitivity of current and wire feed rate on track geometry would be a useful contribution to understand this difficulty.

*4.2.3.2. Keyhole induced pores.* Since AM is practiced at high speeds and powers, in many cases the lasers or electron beams form a keyhole that results in a high depth to width ratio of the fusion zone [75]. Previous experimental and modeling studies in keyhole mode welding has established that instability of the keyhole can result in the formation of large pores [417,418]. In addition, because of the high depth of the fusion zone, a portion of the underlying layer is often melted during AM. An interaction of the fusion zone with a preexisting pore in the underlying layer may result in the propagation of the void up above its original home.

In order to model the keyhole induced porosity, it is instructive to understand the experimental evidence of the formation of similar porosity in keyhole mode AM. For example, Fig. 4.23 shows the porosity formation at different energy densities [419]. At low energy density lack of fusion voids form due to incomplete melting as shown in Fig. 4.23(a). However, Fig. 4.23(c) shows that at a relatively high energy density where the keyhole is formed, keyhole induced porosity is observed. This phenomenon is also evident from Fig. 4.24(a) and (b) where variations in porosity volume fraction are represented as functions of scanning speed and laser power, respectively [419]. Fig. 4.24(c) and (d) also show that depending on the energy density different pore morphology and volume fractions are observed [187,420].

Powder scale models and models with free surface tracking such as VOF are commonly used to simulate the keyhole induced

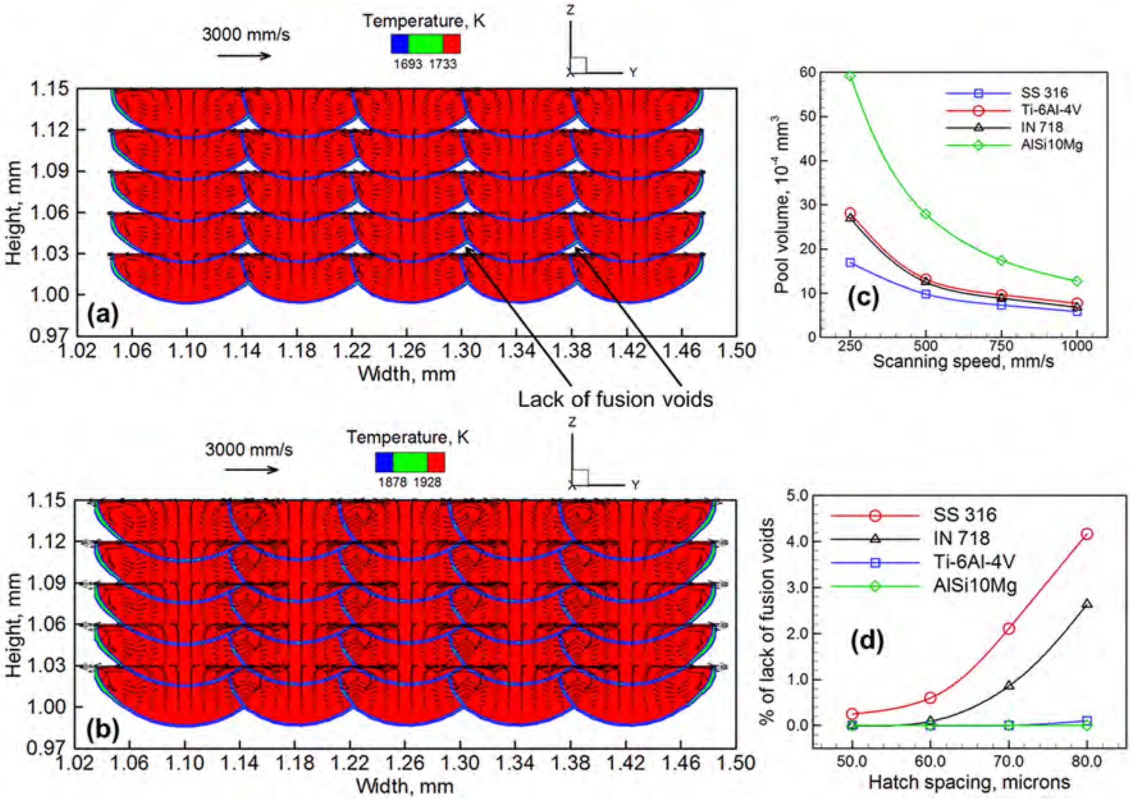

**Fig. 4.21.** Transverse sectional view of the molten pools for 5 layers 5 hatches build of (a) SS316, and (b) Ti-6Al-4V build using 1000 mm/s scanning speed and 80 µm hatch spacing. (c) Variation of lack of fusion ratio with hatch spacing for 5 layers 5 hatches build of four alloys using 1000 mm/s scanning speed. (d) Variation of volume percent of porosity with non-dimensional heat input [19].

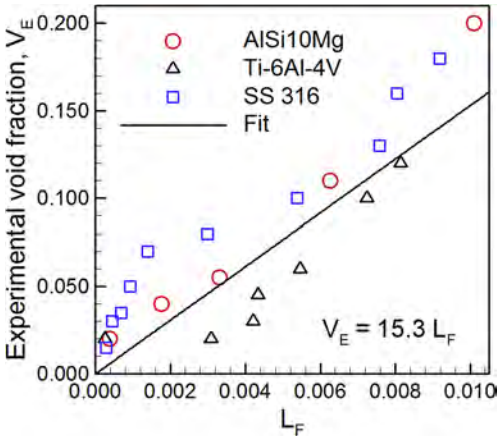

**Fig. 4.22.** Experimental data plotted against the simulated lack of fusion susceptibility index [215].

porosity formation in AM. For example, the collapse of the keyhole wall and the resultant formation of a pore calculated using VOF method [421]. The void near the bottom of the molten pool is more likely to be trapped due to the collapsing keyhole [421]. The gas bubbles experience floating processes driven by the buoyancy force and the flow of the liquid metal during the subsequent solidification process. Some of the bubbles escape the molten pool depending on their trajectories and the solidification rate of the molten pool, and some are trapped in the solidified deposit. Fig. 4.25(c) and (d) show the simulated process of a large ellipsoidal pore and two other small spherical pores getting trapped beneath the surface due to rapid solidification resulting from fast laser scanning [67].

Results from the powder scale models in Fig. 4.25(a) and (b) show that the keyhole depth often significantly exceeds the thickness of the depositing layer [184,421]. Thus, the keyhole may reach some the existing pores in the previously deposited layers and potentially release them during the deposition of the subsequent layers. Moreover, the morphology, size, and location of the present

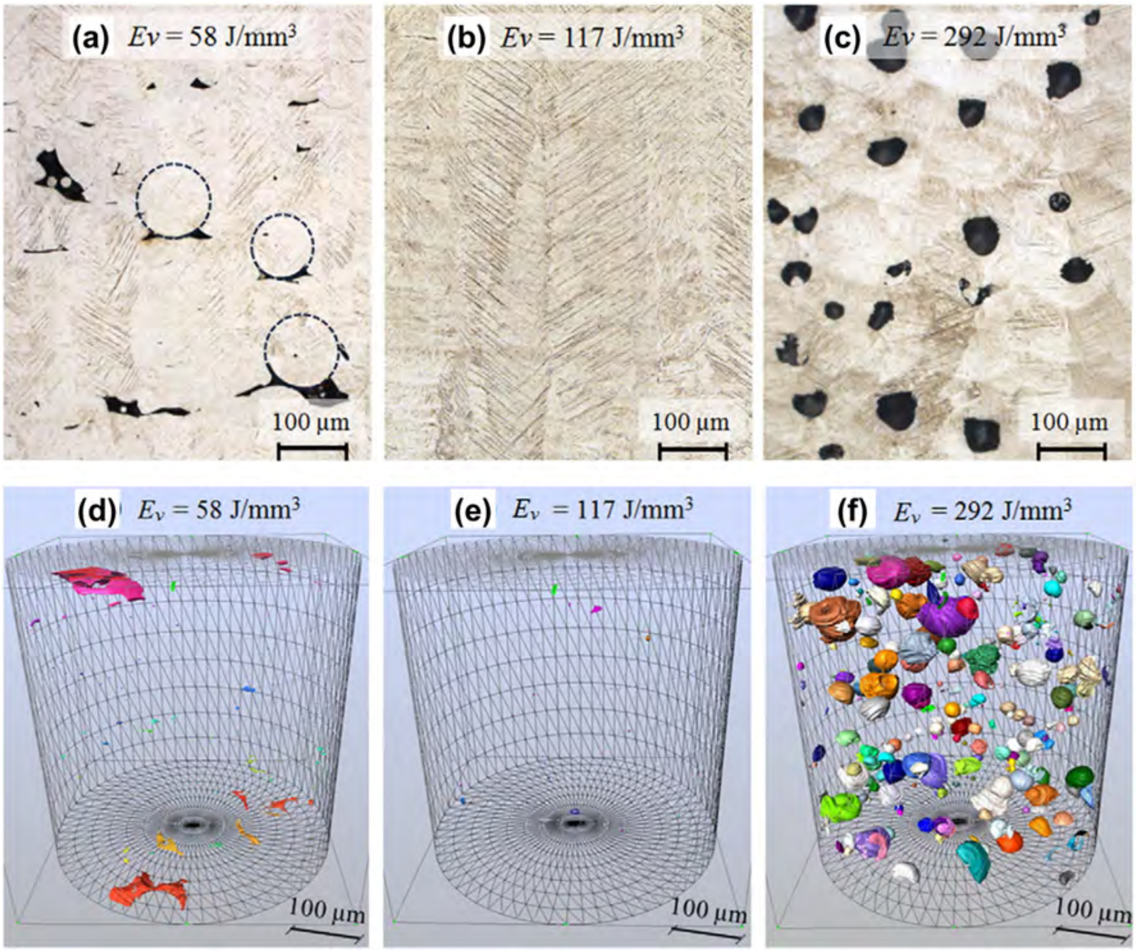

**Fig. 4.23.** Porosity as a function of energy density for PBF-L of Ti-6Al-4V: (a)–(c) Characterized by light optical microscopy, (d)–(f) Characterized by synchrotron tomography [419].

pores evolve and additional pores are generated during the deposition of subsequent layers [184,421].

Numerical heat and mass transfer models can be applied to simulate the evolution of the keyhole and molten pool depression [4,22] and provide useful starting point to examine on the effect of AM variables on the stability of keyhole and thus avoid keyhole induced porosity.

*4.2.3.3. Gas induced pores*. Different from the elongated lack of fusion void or the large spheroidal keyhole pores, the gas induced pores observed in the additive manufactured components are much smaller and spherical in shape. Fig. 4.26(a) shows an example of the many tiny pores in the deposit produced by PBF-L [422,423]. The origin of these pores includes residual pores in the feedstock powder materials [424], gases dissolved in liquid melt and released on solidification, and pores that previously contained entrapped metal vapors [419]. Fig. 4.26(b) and (c) shows the entrapped pores in the feedstock powder materials [422,423]. These small pores were generated during the powder atomization process. During AM, the small gas bubbles expand and coalesce into larger ones [420].

Models developed for the solidification of aluminium alloys showed that the formation of hydrogen diffusion induced pores was affected by the finite-rate diffusion of hydrogen in the melt, and the growth could be reduced by increasing cooling rate [425,426]. However, currently no comprehensive model for the evolution of gas induced pores during AM is available. Since the mechanistic models can simulate the molten pool dimensions, solidification rate, and cooling rate they can be useful for the understanding the coalescence and escape behavior of the gas induced pores.

Pores may be generated from the entrapment of gas during the deposition process due to the formation of other defects such as detrimental landing of spatters on the deposit. The accidental single layer defects form as gaps between adjacent laser melt tracks or track discontinuousness caused by inherent fluid instability under various disturbances [409]. If voids are formed due to the coverage of the spatter over small gaps, the voids then may serve as seeds for the propagation of large pores through multiple layers [427]. The pores may grow from the seeds and propagate through several or dozens of layer thicknesses. Fig. 4.27 shows the evolution of channel-like fault over 14 layers with beam parameters of 90 W and 800 mm/s obtained from a PBF model using Lattice Boltzmann

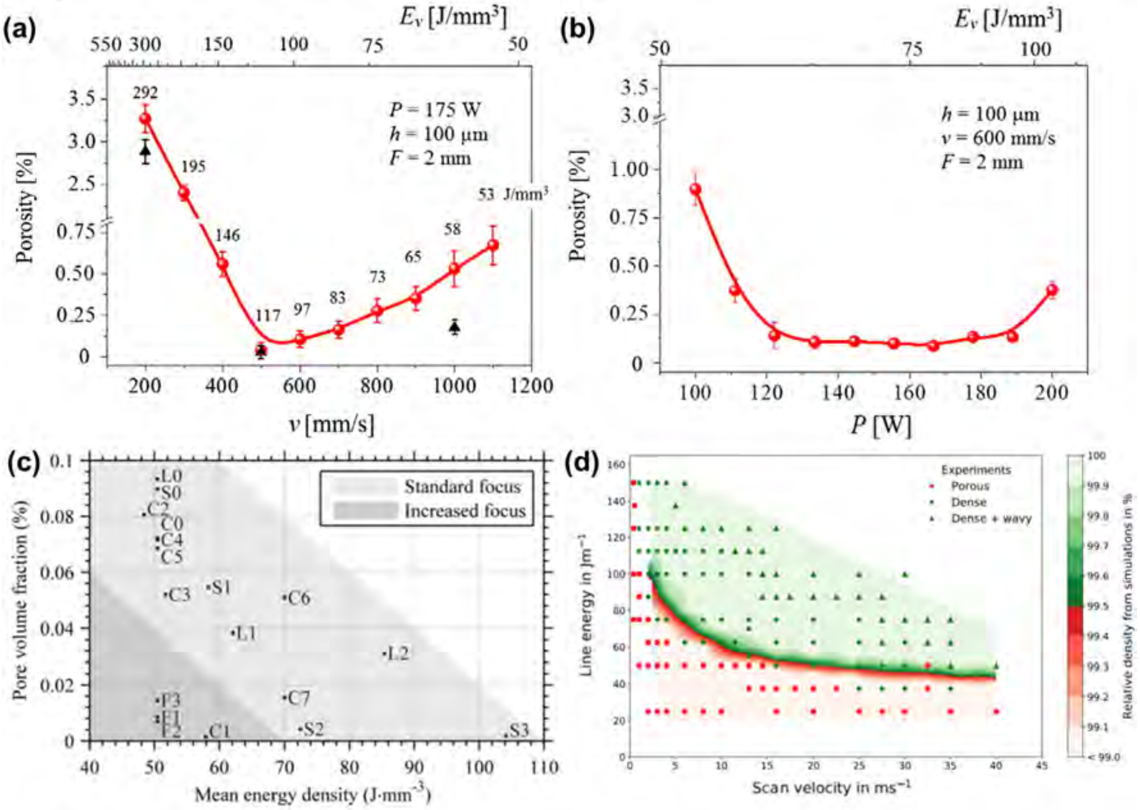

**Fig. 4.24.** Variation of porosity as functions (a) of scanning speed for PBF-L of Ti-6Al-4V [419], (b) laser power for PBF-L of Ti-6Al-4V [419], (c) energy density for PBF-EB of Ti-6Al-4V [420], and (d) scanning speed and energy density for PBF-EB of Ti-6Al-4V [187].

method [195]. Due to the narrow gap between the solid part, the molten pool metal may not be able to fully wet the void even with considerable remelting of the previous deposit. Upon continuous deposition, the void propagates with the build until it is covered at certain stage. Thus, an irregular local void may trigger the evolution of multi-layer binding faults ranging over several layers [187]. Moreover, the defect may appear as the combination of several different types of defects, e.g. partially melted or unmelted particles trapped within the lack of fusion voids.

### 4.2.4. *Cracking*

Cracking is one of the most detrimental defects hindering the application of many promising engineering materials for AM. Typically, metals and alloys with poor weldability display similar cracking susceptibilities during AM [308]. Thus, the fusion welding literature can provide a valuable starting point for understanding the cracking of AM components. The main types of cracking in the AM components include: (1) solidification cracking, (2) liquation cracking, and (3) ductility dip cracking [424,428]. The mechanisms of formation of these cracks are important for their prevention.

*4.2.4.1. Solidification cracking.* Solidification cracking, also known as hot cracking, has been observed in aluminum alloy, titanium alloy, steels, and nickel based alloys components processed by various AM methods [429–435], as shown in Fig. 4.28. Because the contraction rate of the solidifying metal is significantly higher than that of the surrounding solid metal, tensile stresses are exerted on the solidifying metal [86]. Solidification cracking occurs when the tensile stresses exceed the room temperature yield strength. Solidification cracking depends on the relationship of solid phase fraction with temperature and the morphology of the solidification structure. Dependence of solid phase fraction on temperature is examined using thermodynamic modeling whereas mechanistic models reveal the effects of solidification morphology on solid phase fraction.

Thermodynamic models based on the equilibrium phase diagram of an alloy provide a useful tool to calculate the correlation between temperature and solid fraction during solidification [436]. Fig. 4.29(a) shows the variation of temperature with solid fraction of AlSi10Mg and Al7075 which was calculated using the software package Thermo-Calc [308]. Compared with AlSi10Mg, Al7075 has a larger solidification range between the liquidus and solidus temperatures, which indicates higher susceptibility to solidification cracking. For a given temperature gradient, the alloy with a larger solidification range is more likely to form the long, liquid-filled channels shown in Fig. 4.29(c) [436]. During the last part of solidification, solid and liquid phases coexist with the liquid phase filling the areas between the dendrites [437]. Therefore, a larger solidification range causes long and thin liquid films residing

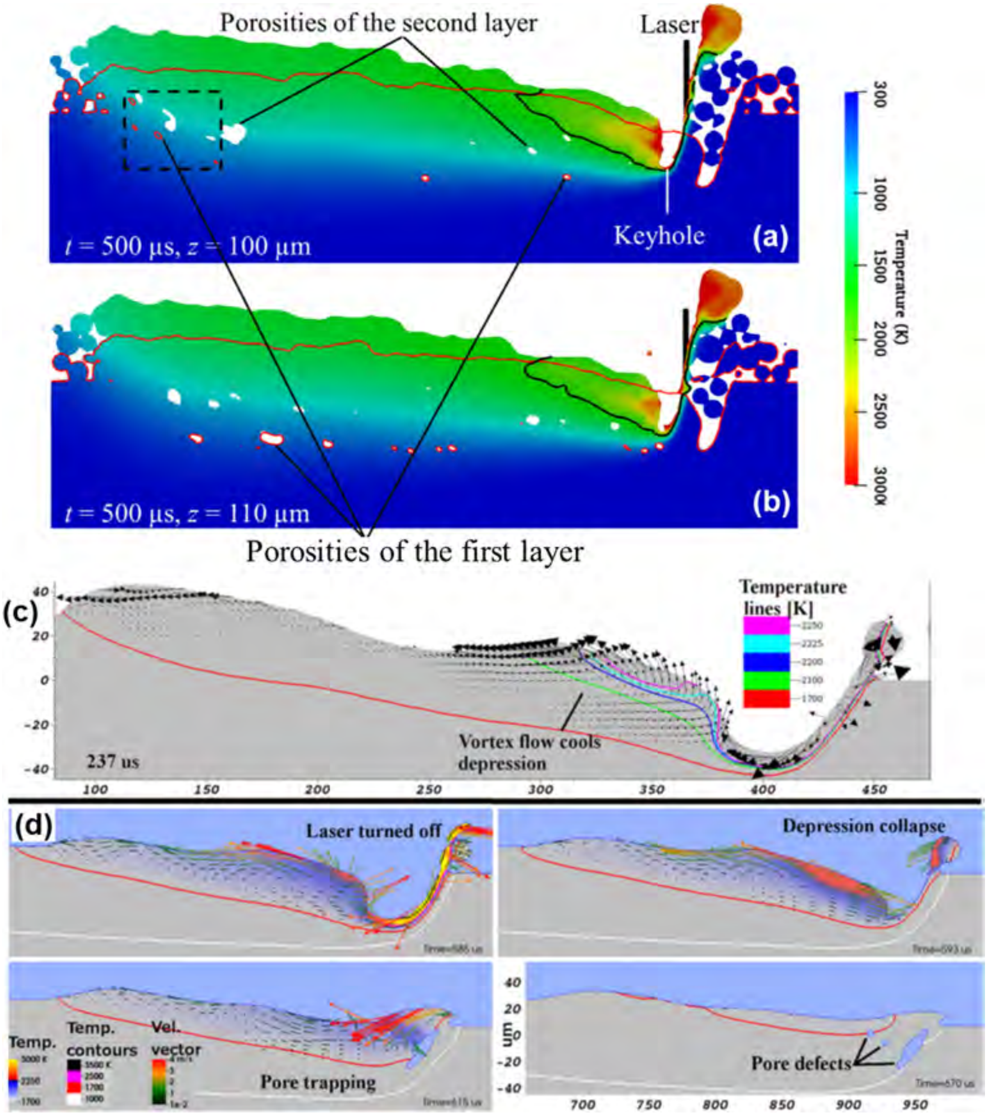

**Fig. 4.25.** (a) and (b) Longitudinal view of the molten pool during deposition of the second layer with pored generated from the first layer [184]. (c)-(d) Formation of pores upon the termination of the keyhole [67].

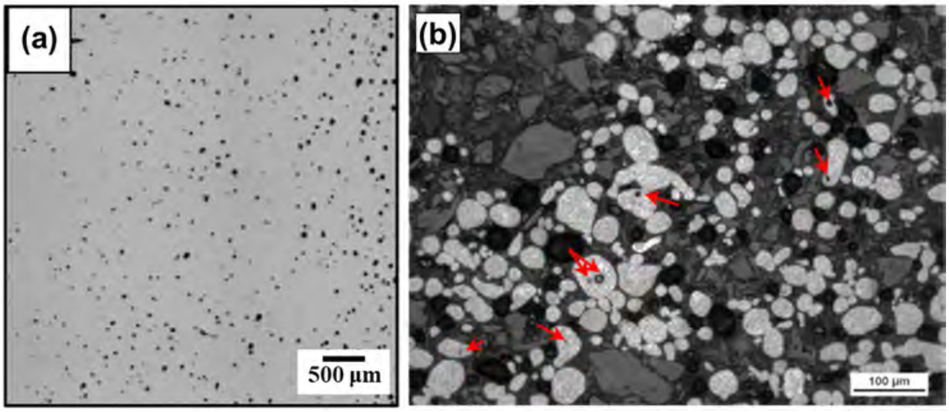

**Fig. 4.26.** (a) Metallurgical pores observed in the deposit [423]. Residual pores in the feedstock materials: (b) AlSi10Mg for PBF-L [423].

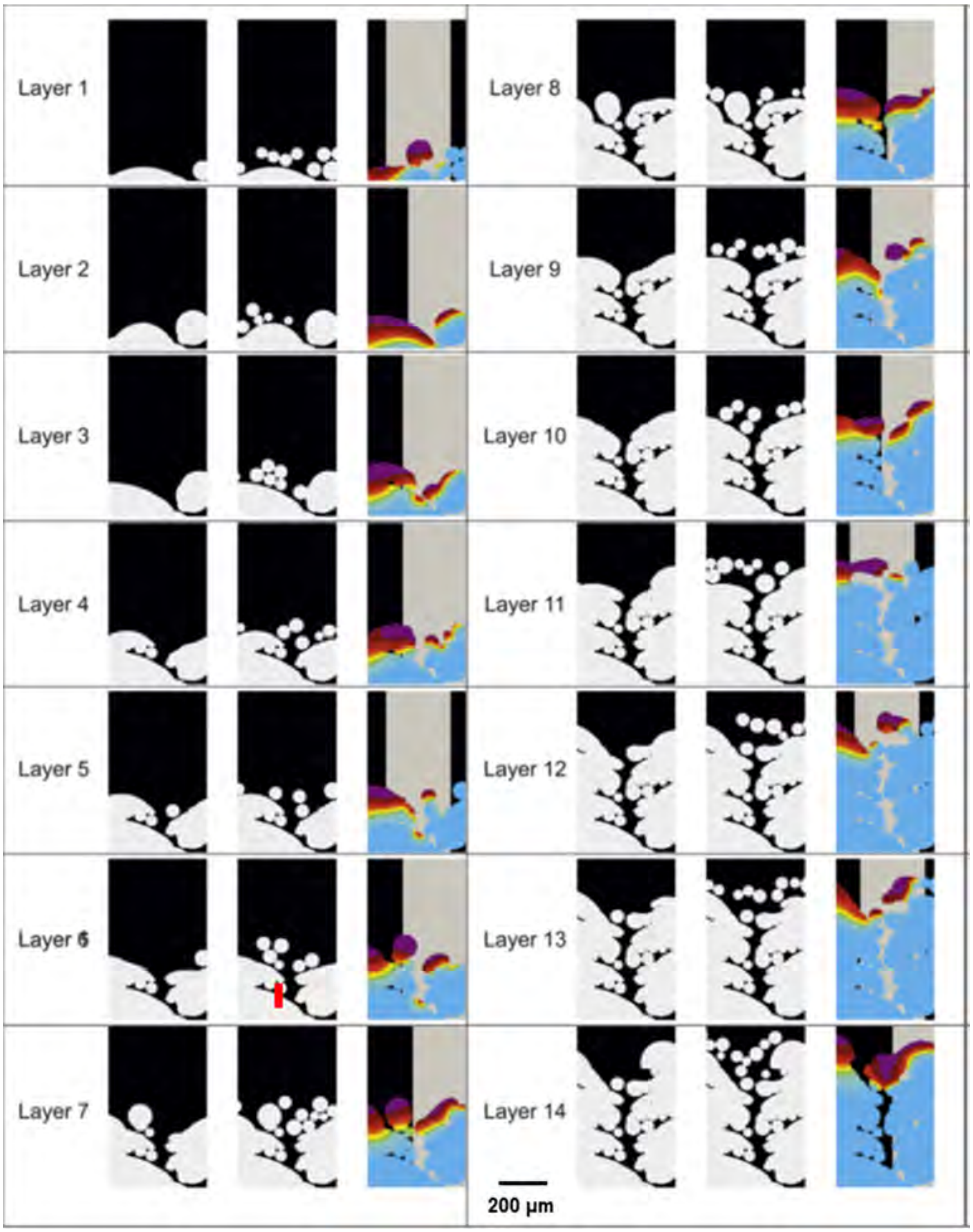

**Fig. 4.27.** Evolution of channel-like fault over 14 layers with beam parameters of 90 W and 800 mm/s. For each layer the first image shows the solidified deposit, the second shows the freshly added powders, and the third shows the temperature distributions during heating [195].

at the gaps between the columnar dendrites, which results in weak bonding between dendrites. This weak-bonding liquid film cannot resist stresses generated during solidification and cooling, and therefore creates a potential failure point that is susceptible to hot cracking. The same theory applies in other alloys, as seen for aluminum alloys A206 and A356 shown in Fig. 4.29(b) [436]. Thermodynamic modeling can help to compare the solidification cracking susceptibility of various alloys.

Mechanistic models are used to simulate sub-grain scale solidification phenomena that explain the effects of solidification structure on solidification cracking. Rappaz et al. developed a theoretical model of dendrite arm and grain coalescence for the last stage solidification of alloys [438]. The undercooling, $\Delta T_n$ needed for dendrite bridging or coalescence approaching planar liquid/solid interfaces is given by:

$$\Delta T_n = \frac{\Delta \Gamma_b}{t_{SL}} = \frac{\gamma_{gb} - 2\gamma_{SL}}{\Delta S_f} \frac{1}{t_{SL}} \tag{4.32}$$

where $\Delta\Gamma_b$ is the difference between the grain boundary energy $\gamma_{gb}$, and twice the solid/liquid interfacial energy $\gamma_{SL}$, $t_{SL}$ is the thickness

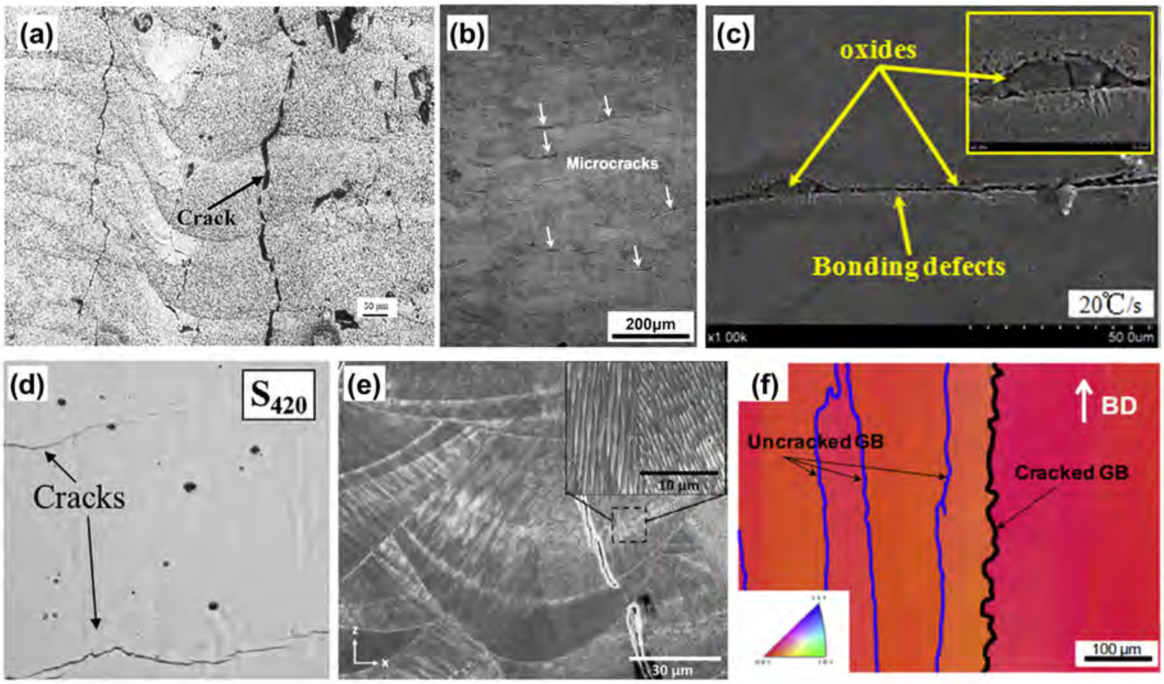

**Fig. 4.28.** Solidification cracking observed in the AM components: (a) Al 6061 processed by PBF-L [429], (b) Ti-6Al-4V processed by PBF-L [430], (c) AISI 4340 steel processed by DED-L [431], (d) A high-silicon steel (6.9%wt.Si) processed by PBF-L [432], (e) A nickel based alloy Hastelloy X processed by PBF-L [433], (f) A non-weldable nickel based alloy processed by PBF-EB [434].

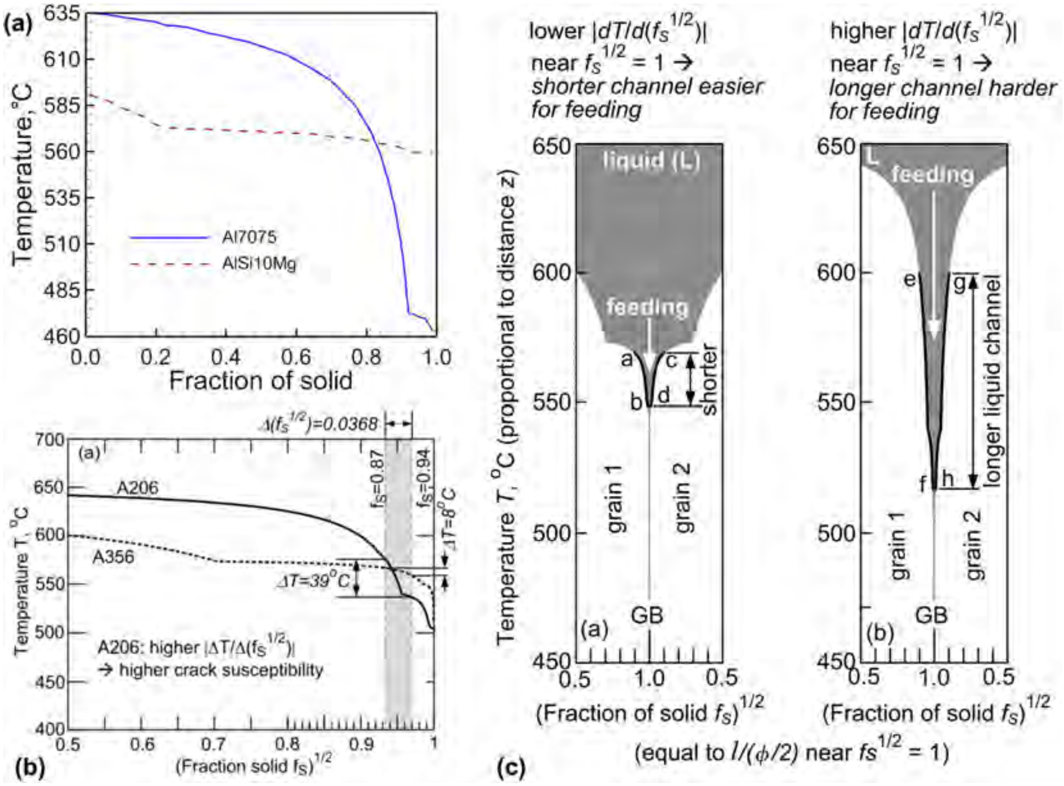

**Fig. 4.29.** (a) Solidification curves for aluminum alloy AlSi10Mg and Al7075, adapted from [308], (b) Correlation between temperature and solid fraction for aluminum alloy A206 and A356 [436], (c) Comparison of the spatial range of solidifying regions of aluminum alloys with different compositions [436].

of the isolated solid–liquid interface and $\Delta S_f$ is the fusion entropy. According to Eq. (4.32), $\Delta T_n$ is $< 0$ when $\gamma_{gb}$ is less than $2\gamma_{SL}$, indicating an unstable liquid film. Coalescence of the two interfaces occurs as soon as they get close enough, typically at a distance on the order of $t_{SL}$. Thus, an attractive condition forms where the dendrite arms often belong to the same grain. The situation is referred to as neutral when $\Delta\Gamma_b$ is equal to 0 and coalescence occurs at zero undercooling, whereas the liquid/solid interfaces are repulsive in the other situation with $\Delta\Gamma_b$ greater than 0. In such a scenario, the liquid film between adjacent dendrite arms will remain stable to a lower temperature until the undercooling exceeds $\Delta T_n$, which indicates a higher cracking susceptibility. This theoretical model has been applied to explain hot cracking in additive manufacturing [434]. While useful, this model requires knowledge of sub-grain features of the microstructure that are not readily attainable by most mechanistic models.

Other sub-grain features that influence hot cracking susceptibility are the grain boundary misorientation and the segregation of alloying elements [434,439]. As shown in Fig. 4.28(f), only high angle grain boundaries (HAGB, > 15°) were affected by cracking, while low angle grain boundaries (LAGB, 5°-15°) remained intact. Due to the increased misorientation of dendrites at the HAGB, the occurrence of dendrite bridging decreases and consequently the hot cracking susceptibility increases [440]. Grain boundary angles can be predicted from microstructural simulations of the AM process. Segregation of alloying elements during solidification can lead to formation of intermetallic phases that act as stress concentrators. Mechanistic modeling has shown how these intermetallic phases form as a function of solidification parameters in Nb-containing nickel-base superalloys [299,441]. Fig. 4.30 shows that for a fixed temperature gradient, lower cooling rates produce chains of Laves phase particles in the interdendritic region that are susceptible to hot cracking, while higher cooling rates create fewer, more distributed Laves phase regions. Mechanistic model of AM process was used to calculate temperature gradient and cooling rates in this investigation.

Overall, thermodynamic and sub-grain scale mechanistic modeling are useful in evaluating hot cracking susceptibility. While equilibrium thermodynamics can provide qualitative comparisons of various alloys' susceptibility, evaluation of hot cracking susceptibility of an alloy for different processing parameters are still needed.

*4.2.4.2. Liquation cracking.* Thermodynamic and kinetic modeling are used to predict the presence of the unwanted phases that may

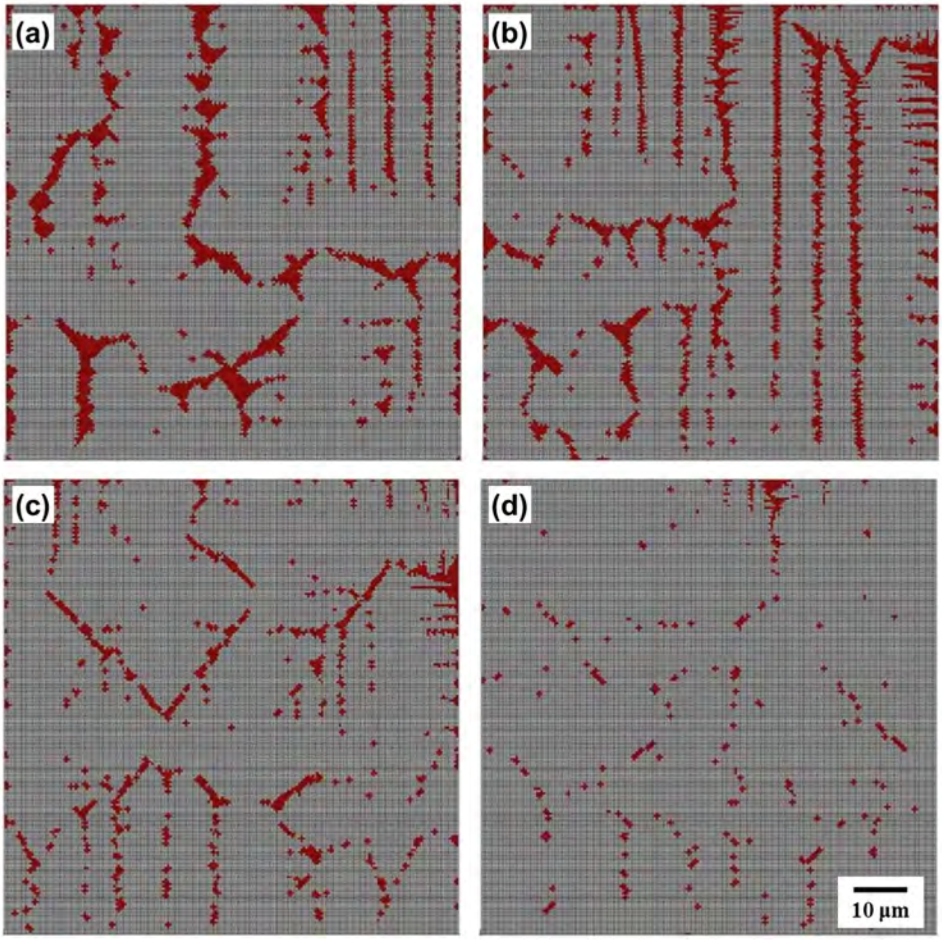

**Fig. 4.30.** Variation of morphology of Laves phase particles with cooling rate under fixed temperature gradient of $10^5$ K/m: (a) 500 K/s, (b) 1000 K/s, (c) 2000 K/s and (d) 4000 K/s [299].

cause liquation cracking. For example, thermodynamic modeling of IN 740 indicated that segregation of B, Nb, and Si during solidification resulted in the increase of low melting equilibrium phases such as MC and $MB_2$ and nonequilibrium phases such as Laves phase [442]. The solidus temperature of the system was depressed resulting in an increase of the solidification range from 169.7 K to 293.5 K, causing high susceptibility of liquation cracking of the partially melted zone [442]. The solute segregation of IN 738LC alloy during DED-L was analyzed using the Giovanola–Kurz and Scheil models [443]. A significant enrichment of γ-γ′ eutectic-forming elements was found in the residual liquid at the final stage of solidification with solid fraction of about 0.87 in the molten pool, which was the main cause of semicontinuous γ-γ′ eutectic phase along the grain boundary [443]. The susceptibility of liquation cracking depends also on the grain boundary misorientation, due to the better stability of the liquation films at high angle grain boundaries and the higher local stress concentration during the terminal stage of solidification [444,445].

Liquation cracking is prevalent during AM of aluminum alloys, nickel-based alloys, and austenitic stainless steels. If liquid films form at grain boundaries, they fail to accommodate the thermally and/or mechanically induced strain experienced during the cooling process [445]. In other words, the partially melted zone is weakened by grain boundary liquation, and it cracks when the solidifying metal contracts and drives out the low melting point liquid phases. Fig. 4.31 shows the liquation cracks in IN718 processed by DED-L [444,445]. Liquation cracking in AM is observed initiating from the weak site near the fusion line in the pre-deposited layers and propagating along the interdendritic region in the partially melted zone with subsequently deposited tracks and layers [444].

Influential factors in liquation cracking include the chemical compositions of the alloys, the temperature range of solidification, the solidification shrinkage, the thermal contraction during cooling and the presence of intermetallic compounds and precipitates [86,445]. For example, liquation cracking in IN718 processed by DED-L depends on the presence of Laves/γ eutectic particles [444]. As shown in Fig. 4.30, Laves phase exists as long chains of coarse particles at lower cooling rate and finer discrete forms at higher cooling rate. Such transition occurs because the secondary dendrite arm spacing is reduced under higher cooling rate and the solidification structure changes from columnar to equiaxed with higher solidification rate and thus lower G/R values [299]. Note that the size of the low melting point phases such as Laves phase is significantly reduced due to the high cooling rate during PBF. Therefore, liquation cracking is much less likely to be generated during PBF.

Kou and coworkers developed a criterion for predicting the susceptibility of liquation cracking for aluminum alloys during fusion welding [446–449]. According to their criterion, the heat affected zone surrounding the weld metal can become a partially melted zone that is susceptible to liquation cracking if the solid fraction of the solidifying liquid is greater than that of the partially melted zone [446–449]. The correlation of the solid fraction with temperature of the metal can be calculated using commercial software with Scheil model and corresponding databases, such as CompuTherm and ThermoCalc [447]. Fig. 4.32 shows an example comparing the crack susceptibilities of wrought Al alloy 2014 with composition alterations by adding a filler metal 4145 Al [436]. It implies that the temperature and solid fraction correlation and thus the cracking susceptibility depend on the chemical compositions of the alloys.

Though thermodynamic databases can provide the information to generate the Scheil solidification data, the high cooling rates of AM can affect the kinds of phases present and their amounts. Modeling and/or experimental results need to define the exact solidification conditions, specifically cooling rates, that occur if liquation cracking is to be predicted. Therefore, predicting liquation cracking in AM alloys requires both thermodynamic modeling and thermo-physical data.

*4.2.4.3. Ductility dip cracking.* Many face-centered cubic (FCC) alloys, e.g., nickel based alloys and stainless steels, experience a solid state cracking at elevated temperatures known as ductility dip cracking (DDC) [450]. Different from solidification cracking and liquation cracking where liquid films are present during the formation process of the cracks, DDC occurs without any liquid metal involved [451]. DDC occurs in the temperature range from one-half the absolute melting temperature up to the recrystallization or solidus temperature, accompanied with a ductility loss of the local structure [452].

Modeling of DDC is just beginning. One approach is to simulate the varestraint test through computational thermomechanical route. For example, Chen et al. developed a FEM polycrystalline model to simulate DDC initiation and propagation, and found that DDC tends to initiate and propagate on grain boundaries with 30–60° misorientation [453,454].

Fig. 4.33 shows a sample of nickel based alloy CM247LC, processed by PBF-L, with cracks distributed in the as-fabricated

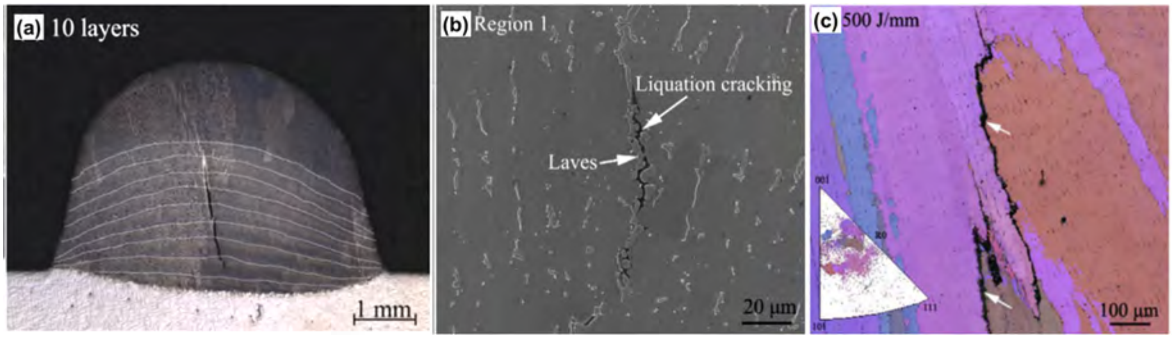

**Fig. 4.31.** (a) Macrograph showing the initiation and propagation details of liquation cracking of IN718 processed by DED-L [444], (b) Micrograph showing liquation cracking of IN718 processed by DED-L [445], (c) EBSD map with the liquation cracking observed in the as-deposited IN718 by DED-L [444].

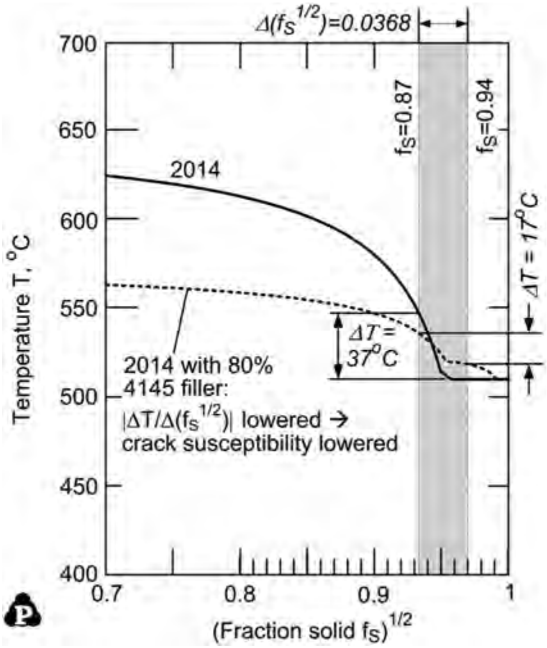

**Fig. 4.32.** Comparison of crack susceptibilities of wrought Al alloy 2014 with filler metal 4145 Al based on the correlations between fraction solid and temperature [436].

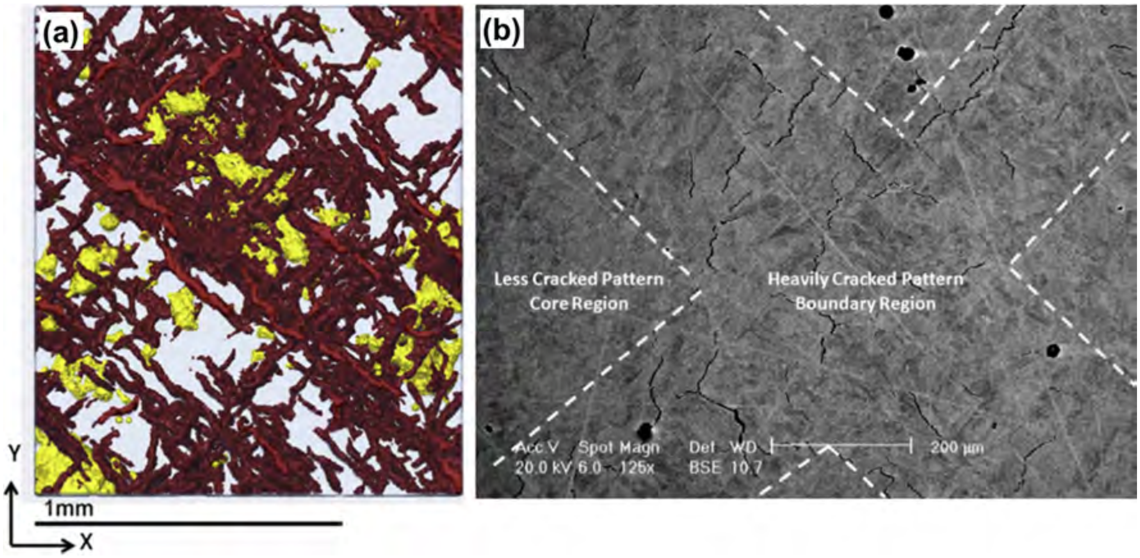

**Fig. 4.33.** A nickel based alloy CM247LC processed by PBF-L: (a) MicroCT data showing the cracks in red and voids in yellow, (b) SEM micrograph showing the heavy and less cracked regions due to a repeated scanning pattern [428].

components [428]. CM247LC is known to be susceptible to cracking in the as-fabricated state and DDC is one of the key mechanisms by which these cracks are formed [428]. DDC occurs if the imposed strain exhausts the available ductility within this temperature range during the high temperature processing of these alloys [450]. Liquation cracking and DDC can occur in the same component and may be distinguished by fractographic examination. Liquation cracking are often recognized by the evidence of liquid films along the fracture path while DDC show no evidence of liquation [455].

DDC is an intergranular form of cracking [451]. Several hypotheses have been proposed for the mechanisms for DDC including grain boundary sliding, intergranular impurity element embrittlement (P, S, and H), and intergranular second phase precipitation [451]. Thus, the grain boundary pinning precipitates, the grain boundary deformation factor, and the local stress near the grain boundary are influential factors [452]. Susceptibility of DDC was also found to positively correlate with grain size and the dimension of the components [452]. The addition of alloying elements can promote the precipitation of particles which further results in tortuous grain boundaries. The presence of grain boundary pinning precipitates can effectively lock the sliding of the boundaries. For example, the addition of C, Nb and Ti caused the eutectic formation of medium size (NbTi)C carbides during the welding of a nickel-base alloy [456]. Grain boundary sliding becomes much more difficult when strain is applied to these interlocked grains due to the various deformed geometries [456].

Both the macroscopic thermal and solidification stresses induced during intensive heating and cooling processes and the local stresses generated near the grain boundaries contribute to the formation of DDC. It was reported that the grain boundary precipitation of partially coherent $M_{23}C_6$ carbides induced considerable localized interfacial stresses [452,457]. Grain boundary sliding may be exacerbated by the highly localized stresses [457]. In contrast, alloys that form incoherent precipitates such as Ti(C,N), NbC and $M_7C_3$ do not exhibit such DDC susceptibility [457]. Thus, DDC can be mitigated through reducing the formation of partially coherent precipitates, decreasing the misfit between the matrix and these precipitates, and controlling the macroscopic stresses [452]. Chemical composition may have an adverse effect on DDC resistance, associated with resultant segregation of impurities to the grain boundaries. It was reported that S impaired DDC resistance and the observation of S rich films was one of the factors responsible for the low DDC resistance. Moreover, hydrogen migration to the grain boundaries and the intergranular precipitate/matrix interfaces also affects the DDC susceptibility [456].

Thermodynamic modeling of precipitates can provide one of the causative factors for DDC. However, currently there is no unified mechanistic model for DDC because of the possible involvement of many variables and lack of adequate mechanistic knowledge.

In summary, cracking is a common detrimental phenomenon related to the complex processes of heating, melting, solidification, and cooling during metal printing. As discussed in this section, cracking largely depends on the chemical compositions of the feedstock material, the microstructure, and the local stress conditions. Mechanistic models, which can provide an understanding of susceptibility to crack formation are emerging, considering some of the above factors. However, phenomenological models simulating the spatiotemporal variations of cracks in diverse conditions are still unavailable. Thus, it would be useful to develop comprehensive high-fidelity models to effectively eliminate or mitigate cracking in order to produce AM components with targeted properties.

### 4.2.5. Surface roughness

Surface roughness of the AM components is a major concern because it may affect the dimensions and geometric tolerances of the products. The causative factors include: (1) spatters landing on the deposit [150], (2) cavities and voids formed near the surface [191], (3) stair case effect due to uneven transitions between neighboring tracks and layers [409], (4) instabilities of the molten pool [189], and (5) partially melted powder particles attached to the surface and edges of the molten pool [67].

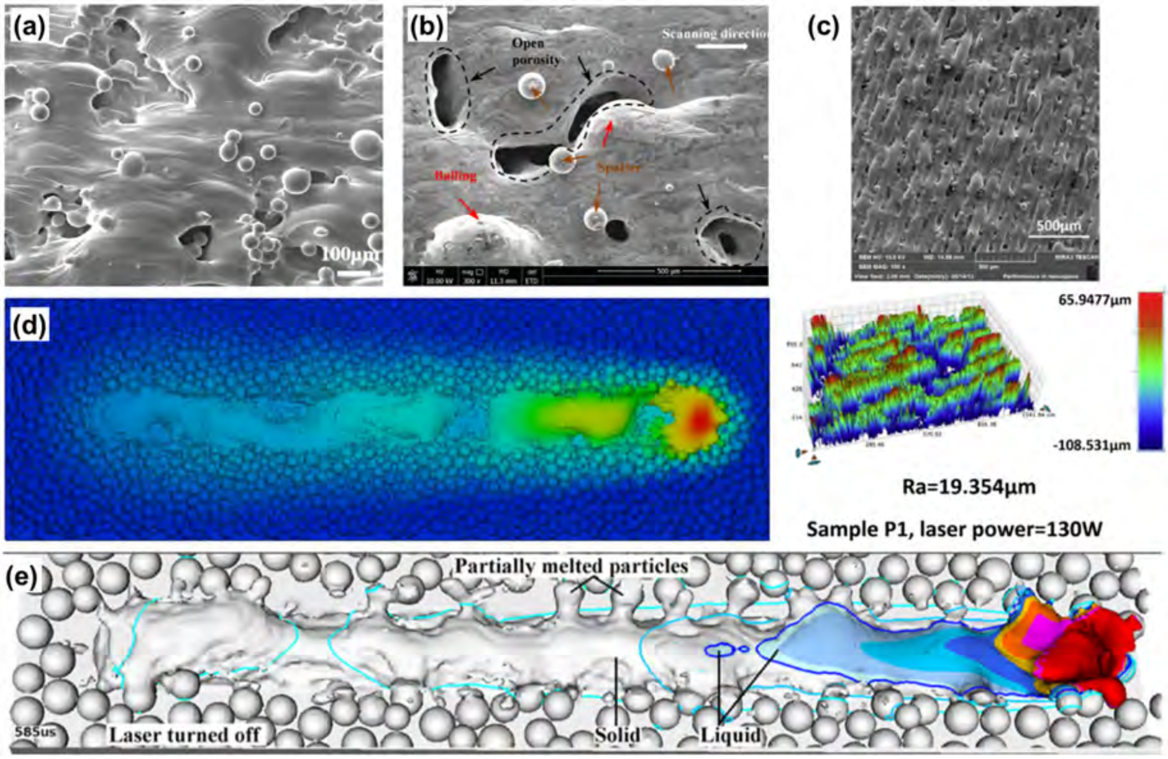

**Fig. 4.34.** Surface roughness due to various factors: (a) Spatters landing on the deposit surface [150], (b) Cavities and voids near the surface [191], (c) Unsmooth transitions between neighboring tracks [409], (d) Fluctuation of the molten pool [189], (e) Partially melted powder particles attached to the edges of the molten pool [67].

Fig. 4.34 explains the effects of the five causative factors on surface roughness. It is evident that the surface roughness is affected by spatters and pores as shown in Fig. 4.34(a) and (b). Denudation of metal powder particles during AM in the zone surrounding the solidified track results in irregularities in the part surface [182]. Formation mechanism of spatters and pores and applications of transport phenomena-based models to predict them have been discussed earlier in this paper.

Improper hatch spacing, layer thickness and build angle often result in sharp peaks and valleys between neighboring deposited tracks as shown in Fig. 4.34(c) [458]. Horizontal surfaces often exhibit undulations caused by large spacing between two successive tracks [459]. The vertical and inclined surfaces suffer from the stair case effect [1,459]. The average surface roughness ($R_a$) depends on the layer thickness ($d_L$) and the build angle ($\theta$) and can be represented by the following equation [460]:

$$R_a = 1000\ d_L\ sin\left(\frac{90-\theta}{4}\right)\ tan\ (90-\theta) \tag{4.33}$$

where $R_a$ is the arithmetic mean of the surface roughness of a region with a particular build angle. The stair case effect in the DED-GMA component are high due to the deposition of thick layers with high deposition rate [71].

Dynamic instabilities such as balling and humping of the molten pool occur under inappropriate conditions [1,461]. Balling appears due to the inadequate melting of the feedstock. As shown in Fig. 4.34(d), the melted particles prefer to cluster to minimize the surface area and surface energy rather than spread on the unmelted substrate [189]. Bertoli et al. reported that very high volumetric energy density (VOD) lead to a degradation of track shape [462] whereas insufficient melting occurs at low VOD. When the scanning speed is excessively high, balling effect of the molten pool occurs due to the Rayleigh-Plateau effect [189,463]. When the ratio between the length and the width of the molten pool is high, the pool becomes unstable and small humps form along the track. Humping of the deposit occurs when the scanning speed exceeds a critical value which can be explained by the Kelvin-Helmholtz hydrodynamic instability of the molten pool [1,464,465]. Formation of humping in AM is similar to that in welding. Therefore, the calculation methodology for humping in welding [466] can be applied to AM.

Fig. 4.34(e) shows the partially melted powder particles at the edge of the molten pool which are attached as satellites. Note that this is due to the nature of the powder feedstock based AM and cannot be completely avoided. The roughness caused by these satellites is in the order of the diameters of the particles. Thus, smaller powder particles tend to reduce the average roughness at the edges of the deposit. Powder scale models described earlier in this paper are often used to simulate the partially melted powder particles adjacent to the deposited track and thus can be used to estimate the surface roughness.

### *4.2.6. Simultaneous occurrence of multiple defects*

The formation and evolution of various defects described above may be interdependent. For example, the intense vaporization may occur simultaneously with severe spattering. The random landing of a large number of ejected liquid metal and solid powder particles leads to higher probabilities for the formation of voids. Lack of fusion void can propagate through multiple tracks and layers with the origin from earlier deposited tracks [409]. The spattering and the resultant attachment of materials to the deposit affect the surface roughness as well [405]. Moreover, the surface roughness deteriorates with more severe lack of fusion of neighboring layers and tracks [409]. Cracks may be initiated from other defects, e.g., solidification cracking is more easily generated near local voids due to the weaker bonding between neighboring grains [467]. Vaporization of alloying elements alters the chemical compositions of the alloys and thus may affect the cracking sensitivity.

Formation mechanisms of these defects are very complicated and often cannot be captured even with the advanced experiments. In contrast, numerical modeling can provide conditions for these defects to form simultaneously. However, the issue of physical processes occurring on small length and time scales hinders modeling efforts as well, because simulating larger, realistic parts

**Table 4.1**
Selected FEM thermomechanical models for various AM processes highlighting the important computational features.

| Process | Material | Method | Computational features | Ref. |
|---|---|---|---|---|
| DED-L | H13 steel | ABAQUS | ● Around 6 h for 2 × 2 × 3 mm solution domain<br>● 55,455 elements and 60,033 nodes<br>● Rectangular block with multiple layers and hatches | [572] |
| PBF-L | Ni-Ti shape memory alloy | ANSYS | ● Brick elements with size of 0.025 × 0.025 × 0.0125 mm<br>● Rectangular block with multiple layers and hatches | [197] |
| | Ti-6Al-4V | COMSOL | ● Total calculation time: 460 h for 2 s of actual manufacturing simulation<br>● Impeller with complex geometry | [476] |
| PBF-EB | IN718 | ABAQUS | ● Rectangular coupons with multiple layers and hatches<br>● Coupon dimensions are 80 × 18 × 20 mm | [573] |
| | Ti-6Al-4V | ABAQUS | ● Blocks with support structures and overhang<br>● Element size: 0.1 × 0.035 mm<br>● Calculation time: 20 h | [574] |
| DED-GMA | Low carbon steel | ANSYS | ● Rectangular block with single layer, multiple hatches<br>● 90,000 8-node brick elements | [575] |
| | Structural steel S355JR-AR | ABAQUS | ● Single pass multi-layer deposit<br>● 8-node brick elements with size 2 × 0.833 × 0.667 mm<br>● Total deposition length: 500 mm<br>● Total calculation time: 75 h 25 min | [260] |

requires prohibitive computational resources. Developing modeling tools that can predict the many kinds of defects that occur in AM on the part scale remains a challenge. Overcoming the difficulties of bridging multiple length and time scales will require the development of simplified models to predict the formation of various defects based on simple heat transfer and fluid flow predictions. Combining simplified models with verified heat transfer and fluid flow simulations could allow the computation of the evolution of various defects and provide quantitative understanding of defects for a range of processing parameters and materials.

### *4.3. Calculations of residual stresses and distortion*

In all AM processes, the cyclic heating and prolonged build time lead to complex stresses and strains within the solidified part. They originate from thermal expansion and contraction [468,469] while the part is constrained by the build plate. Consequently, their magnitude depends on the part geometry, deposition strategy, material properties, and process parameters [26–28]. If the strain is large, part deformation may lead to rejection. Furthermore, residual stresses may lead to delamination between layers or cracking in areas of high stress [1]. Heat transfer and fluid flow modeling can provide the changes of temperature field with time needed for finite element analysis of the stress-strain fields within the material. Additionally, simulation of the maximum temperature variation within a part allows for analysis of the susceptibility of a material to deform under various processing conditions.

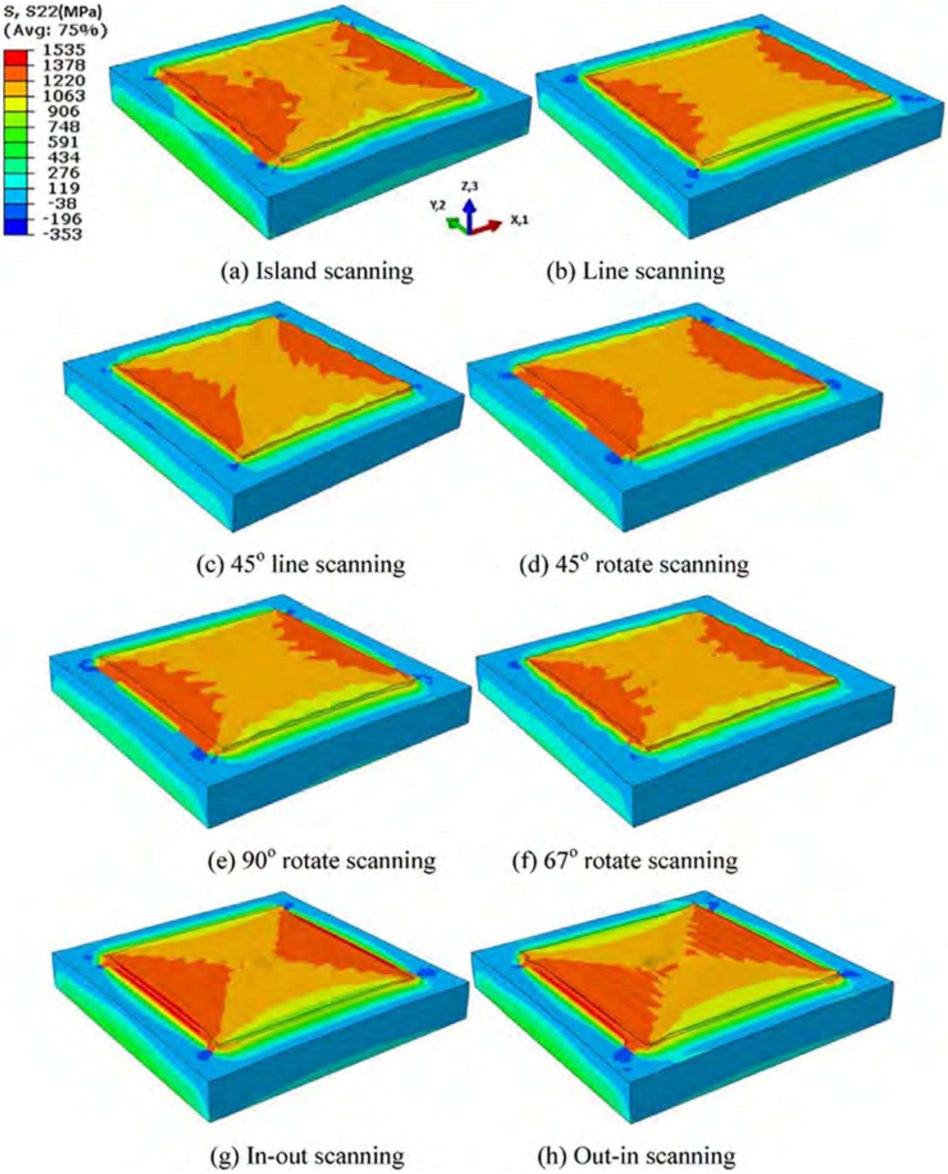

(a) Island scanning (b) Line scanning

(c) 45° line scanning (d) 45° rotate scanning

(e) 90° rotate scanning (f) 67° rotate scanning

(g) In-out scanning (h) Out-in scanning

**Fig. 4.35.** Residual stresses in the Y-direction for a variety of different scanning patterns during PBF-L processing of IN718 alloy. Reproduced from [470].

### *4.3.1. Residual stresses and distortion for single alloy components*

Prediction of build failures due to deformation and residual stresses has been demonstrated using methods of varying complexity. A selection of thermomechanical models for various AM processes are shown in Table 4.1. Coupled thermo-mechanical models are common, linking transient temperature fields to thermal strains. These models require temperature dependent mechanical properties of alloys that are difficult to obtain and are often estimated using commercial software packages. For PBF-L and PBF-EB, rapid scanning of a small beam makes a myriad of complex scanning strategies and part geometries feasible, leading to differences in the heating and cooling of the material both spatially and temporally. Fig. 4.35 shows how different scanning strategies lead to different residual stress states for the same material and processing parameters [211,470]. Similar models have been developed for DED-L processes [27,111,260,471–475], an example of which is shown in Fig. 4.36. Notably, most of the models show that the edges of the material where the part joins the base plate are subject to the highest residual stresses. If these stresses surpass the yield strength of the material, it is possible that delamination or cracking would cause a build failure during AM process. Fig. 4.37 shows that the highest accumulation of residual stresses occurs near the top of the deposit for DED-GMA due to the cooling of bulk deposition [260]. However, these stresses are partially alleviated when the component and the substrate are released from the clamps resulting in high compressive stresses in the substrate [260]. In addition, releasing of the clamps also may cause longitudinal buckling and in extreme cases, part rejection.

Table 4.1 shows that FEM has been successfully implemented for AM of very complex geometries such as impeller, triangular prisms, parts with overhang and compressor blade. However, for large components, FEM is computationally expensive and requires

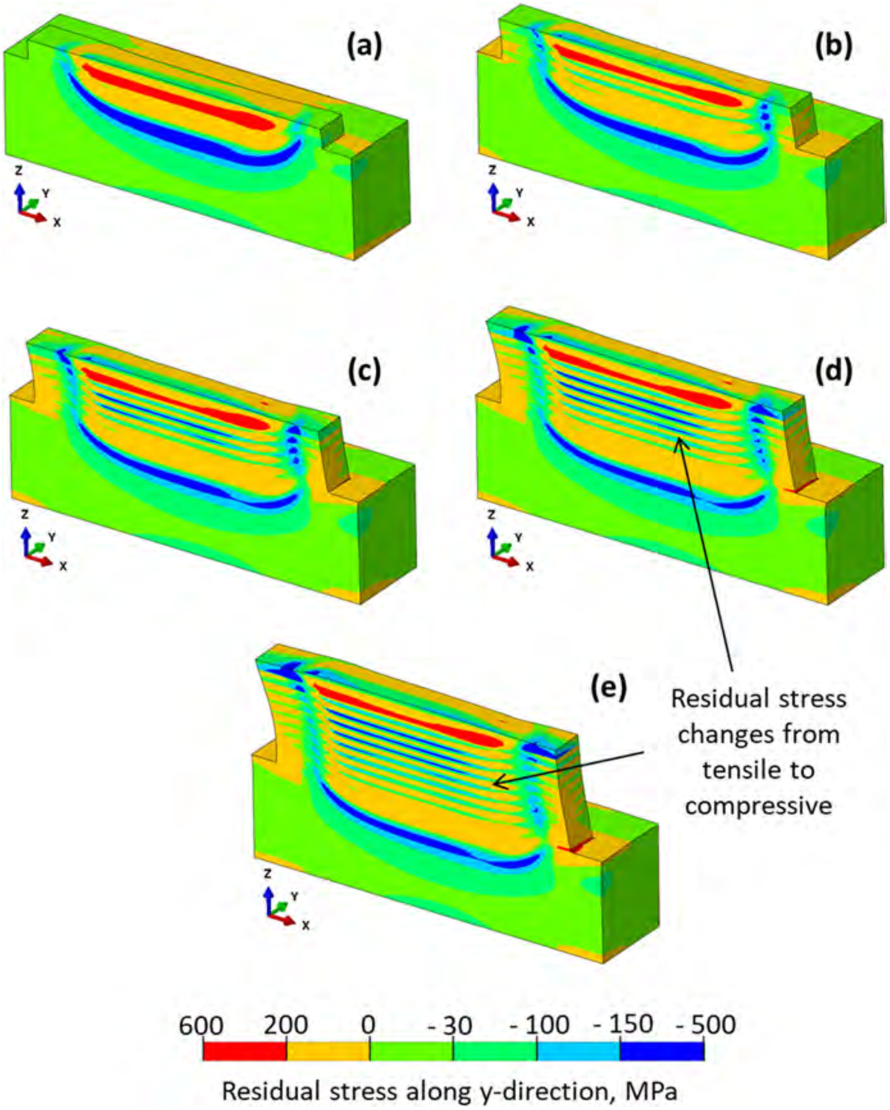

**Fig. 4.36.** Residual stress during the (a) 2nd, (b) 4th, (c) 6th, (d) 8th, and (e) 10th layers during the DED-L processing of an IN718 thin-wall part. Simulation is for 300 W laser power at 11 mm/s scanning speed. Reproduced from [27].

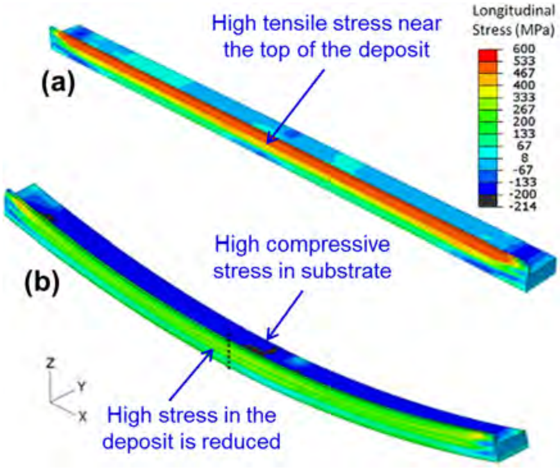

**Fig. 4.37.** Residual stress 4 layers structural steel deposit fabricated using DED-GMA (a) as-fabricated and (b) after releasing the clamps. Reproduced from [260].

large computational memory. For example, residual stresses and distortion calculations for actual process of 2 s can take up to 460 h [476]. The required calculation time may vary depending on the efficiency and capability of the computing facility. However, there are several ways to reduce computational burden in FEM of large scale systems [87,477]. Jayanath et al. [477] proposed a dynamic grid system where the grids are updated with the progress of the building process. After the completion of each layer the fine grid region moves up and is applied for the depositing layer. Already deposited layers are discretized with coarser grids. This process reduces the total number of nodes and elements for large components. It is reported that the total calculation time was reduced from 45 h to 27 h by using this technique for a cylindrical geometry fabricated using 32 layers. Ding et al. [87] separates the elastically and plastically deformed zone in their thermo-mechanical calculations. In AM, the plastically deformed zone is very small in size but the simulation of this region requires a large amount of computational resources because of the non-linear relation between stress and strain. Confining the plastic deformation calculation in a small region where material yields because of very high temperature, the total calculation time for a 500 mm long four layers deposit is reduced from 75 h to 42 min [87]. Therefore, the selection of a useful numerical model depends not only on the part geometry and types of the calculation, but also computational facilities and availability of the smart algorithms to enhance computational efficiency.

High computational time and memory requirements in the calculations of residual stresses and distortion in AM parts allows for development of semi-analytical models for predicting the susceptibility to these defects for a given alloy and process condition combination. Mukherjee et al. presented a formula for a thermal strain parameter, $\varepsilon^*$, which relates to the maximum thermal strain expected within the part [27]:

$$\varepsilon^* = \frac{\beta_L T}{EI}\frac{t}{Fo\sqrt{\rho}}H^{3/2} \tag{4.34}$$

The material and geometry are considered by the elastic modulus $E$, the moment of inertia of the baseplate $I$, the coefficient of thermal expansion of the alloy $\beta_L$, and the alloy's density $\rho$. Process-dependent parameters that are extracted from heat transfer and

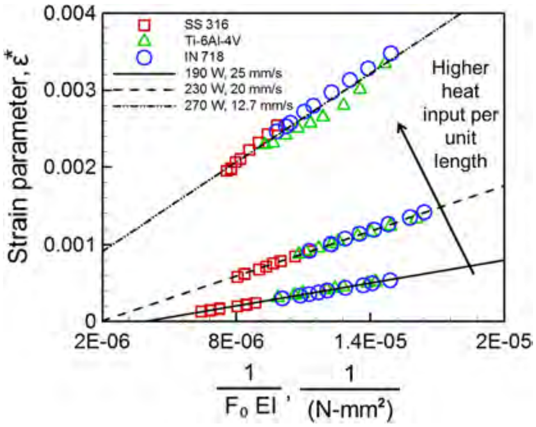

**Fig. 4.38.** Variation of strain parameter with processing conditions and alloy selection for a directed energy deposition process [27].

fluid flow simulations are considered by the peak temperature rise above the solidus temperature $T$, the heat input per unit length $H$, the characteristic time $t$, and the resultant dimensionless Fourier number ($Fo$) from the process. This approach provides a means to compare multiple alloys and processing conditions for their susceptibility to thermal deformation with only a heat transfer and fluid flow model, as shown in Fig. 4.38. The magnitude of thermal strain increases with heat input if everything else is held constant, which is important to consider when selecting process parameters. If a proper reference point for acceptable thermal strain is established, values of the thermal strain parameter may be compared to the reference for a prediction of the severity of thermal strain. An analytical model that calculates the spatial distribution of residual stresses along the height of a part during PBF-L was developed [478], and the trends of residual stress distributions for different materials it predicted were validated by experiments. However, if quantitative values of plastic deformation or the location of possible failures need to be determined, then thermo-mechanical simulations are more appropriate than simplified models.

Besides thermal strain, there are several other contributors to the final residual stresses in an AM part. In many materials, at least one solid-state phase transformation occurs during the cooling of the part from solidus to room temperature. The volumetric change of the crystal structure during a phase transformation leads to the development of “transformation plasticity,” or the deformation due to the expansion or contraction of the material. For the welding of steels, modeling has shown transformation plasticity to have a significant effect on the final residual stresses [479]. Nonetheless, the effect of solid-state phase transformations varies between alloys, which has not been explored in great depth within the AM literature. One of the few examples of thermo-mechanical models that consider this form of residual stress is the model for DED-L developed by Bailey et al. for AISI H13 tool steel [471]. Because the modeling foundations exist for investigating the effects of phase transformations on the final residual stresses, there is potential for exploring the impact of this phenomenon on additive manufacturing for various materials.

Another factor contributing to the final residual stresses is the stress relaxation that can occur due to layer-by-layer mass deposition and heating. As materials are heated above a certain temperature, annealing can occur that relieves some of the existing stresses. Consideration of stress relaxation was shown to be necessary for simulations to match experimental measurements of distortion [480]. However, the time-dependent effects were ignored in those simulations, using instead an instantaneous transition temperature where the material went from stressed to fully stress-free. This simplification is computationally efficient, though requires fitting to experimental data and often not practical. For this reason, further work on creating physics-based models that do not rely on experiments is desirable.

### *4.3.2. Residual stresses and distortion in functionally graded alloys*

The variations in thermo-physical and mechanical properties present two challenges for controlling residual stresses and distortion in functionally graded alloys. Residual stresses evolve during the cooling of a component because the alloy contracts as it cools but is restrained by neighboring material or mechanical clamps attached to the build plate. In a single alloy the extent and rate of contraction is largely governed by the spatial variation cooling rates and temperature gradients during the cooling process. In a functionally graded part, differences in thermal expansion coefficients can lead to the development of unique residual stresses and distortion patterns. Variations in thermo-physical properties can also lead to different cooling rates and temperature gradients during cooling, further influencing the development of residual stresses. Finally, the yield strength varies spatially in many graded components, so two regions with the same magnitude of residual stresses can have different susceptibilities to delamination, buckling and warping.

The dependence of residual stresses on the difference in the thermo-physical properties of the two terminal alloys is shown in

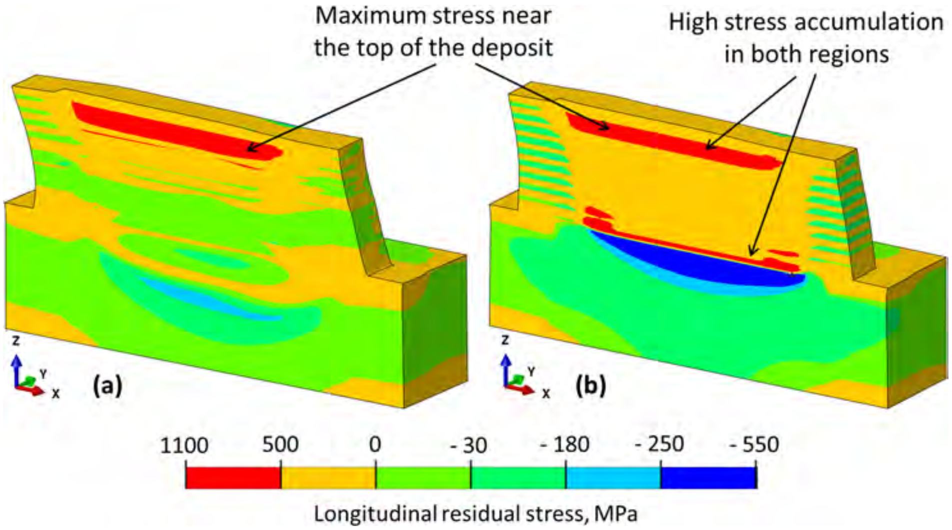

**Fig. 4.39.** Longitudinal residual stress distribution for (a) 2.25Cr-1Mo steel to 800H, and (b) Ti-6Al-4V to 800H graded components. Scanning direction is along the positive x-axis [28].

Fig. 4.39 [28]. The figure shows the simulated longitudinal residual stress distribution of graded parts made with a gradient to Alloy 800H from substrates of 2.25Cr-1Mo steel (Fig. 4.39 a) and Ti-6Al-4V (Fig. 4.39 b). Both the parts are fabricated by depositing 10 layers on the substrate of 2.25Cr-1Mo steel and Ti-6Al-4V, respectively. The amount of Alloy 800H increases by 10 wt% in each layer. Longitudinal stress is the component of the residual stresses along the scanning direction. The positive and the negative values of the stresses correspond to the tensile and the compressive stresses, respectively. For both graded components, the maximum value of the longitudinal stress is near the top of the deposit. However, in Ti-6Al-4V to Alloy 800H joint, high tensile residual stresses accumulates near the substrate-deposit interface. This is attributed to significantly higher room temperature yield strength of Ti-6Al-4V substrate than that of Alloy 800H. The accumulation of tensile residual stresses are absent in the 2.25Cr-1Mo steel to Alloy 800H joint because the room temperature yield strength of the steel is comparable to that of Alloy 800H. [28].

Furthermore, Fig. 4.40 explains the benefits of fabricating compositionally graded alloys over dissimilar joints in order to minimize the sharp change in residual stresses and distortion. Fig. 4.40(a)–(c) and Fig. 4.40(d)–(f) represent longitudinal and

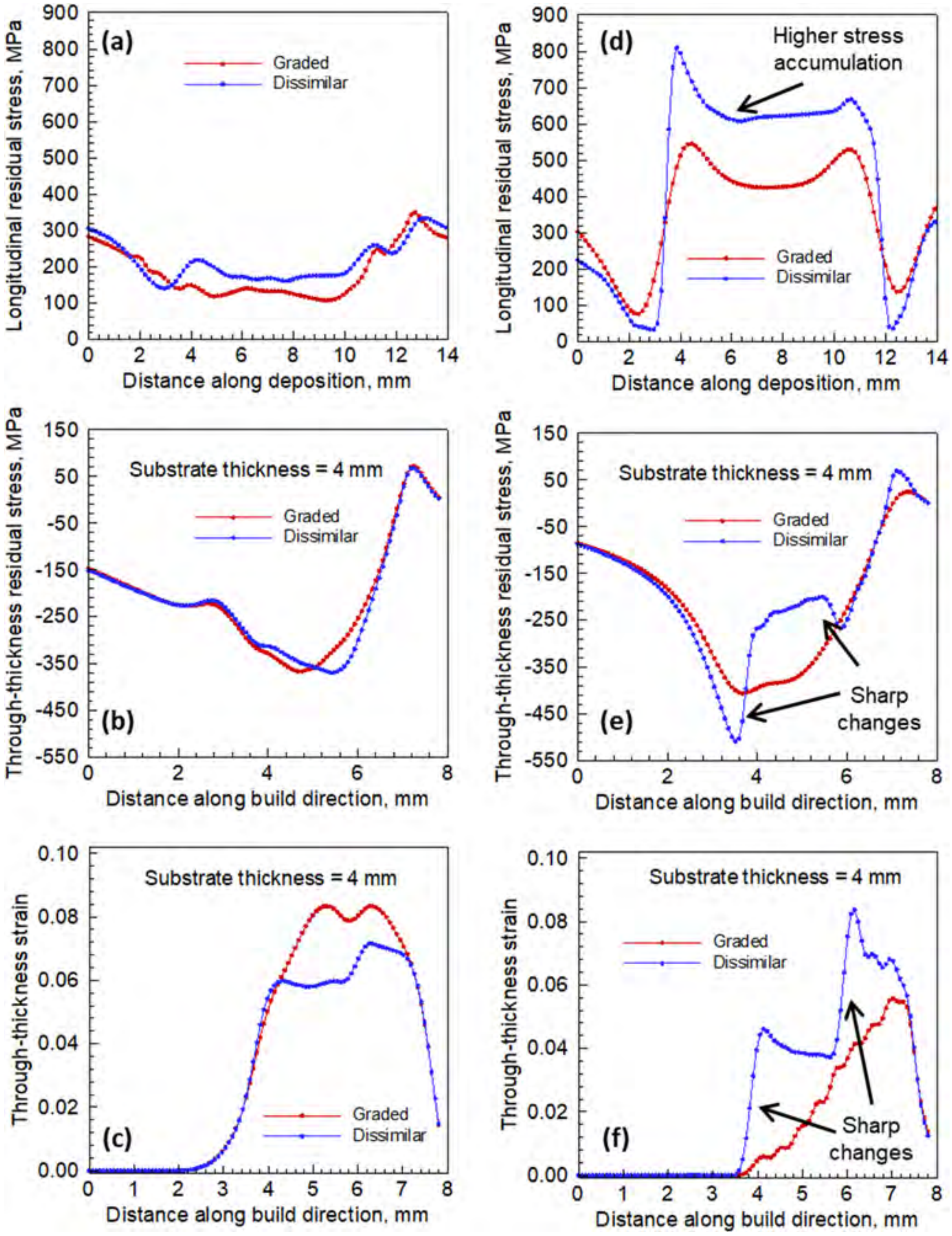

**Fig. 4.40.** (a) Longitudinal residual stress, through-thickness (b) stress and (c) strain for 2.25Cr-1Mo steel to 800H joint, (d) Longitudinal residual stress, through-thickness (e) stress and (f) strain Ti-6Al-4V to 800H joints [28].

through-thickness components of residual stresses and strains for 2.25Cr-1Mo to Alloy 800H joint and Ti-6Al-4V to Alloy 800H joint, respectively [28]. Longitudinal and through-thickness components are along the scanning and building directions, respectively. Since the mechanical properties of 2.25Cr-1Mo steel and Alloy 800H are similar, no sharp changes in residual stresses and strain at the dissimilar joint interface are observed. Therefore, compositional grading between these two alloys provides marginal benefit over the dissimilar joint [28]. However, mechanical properties of Ti-6Al-4V are significantly different from those of Alloy 800H. Therefore, sharp changes in residual stresses and strain in the dissimilar joints between these two alloys can be minimized by fabricating graded joints between them [28], as shown in Fig. 4.40(d)–(f).

The previous example illustrates the importance of understanding the differences in thermo-physical properties of the two materials and the utility of modeling to understand where potentially detrimental stresses would develop. Numerical modeling can be used to design a graded part that minimizes residual stresses at the interface of a dissimilar friction weld between 304L steel and IN 625 [481]. Using numerical modeling efforts to calculate transient temperature fields and the resultant residual stresses and distortion could allow for a larger number of graded joint geometries to be evaluated than that could be feasible with experiments.

### 4.4. *Calculation of printability of metallic materials*

Printability is the ability to convert feedstock materials to defect free, structurally sound reliable components. This concept is similar to weldability where the process-material combination is evaluated for its susceptibility to common defects. The determination of weldability involves preparation of welds and their subsequent characterization and evaluation to determine fitness for service. Although such an experimental approach has been successful in welding, a similar method by conducting a matrix of experiments is not viable to determine printability. First, printing metals is a much slower process than welding because many thin layers have to be deposited to make a three-dimensional component. It sometimes takes a day or more to print a component. In addition, both the equipment and the feed stock are expensive. These are compelling reasons why it is impractical to evaluate printability by experiments alone. A practical alternative is to use well-tested mechanistic models for the evaluation of printing process-alloy combination to determine printability. Since the mechanistic models can determine the susceptibilities of formation of various types of defects for a given alloy-process parameter combination, the parameter space for conducting experiments may be significantly reduced, thus saving both time and expense.

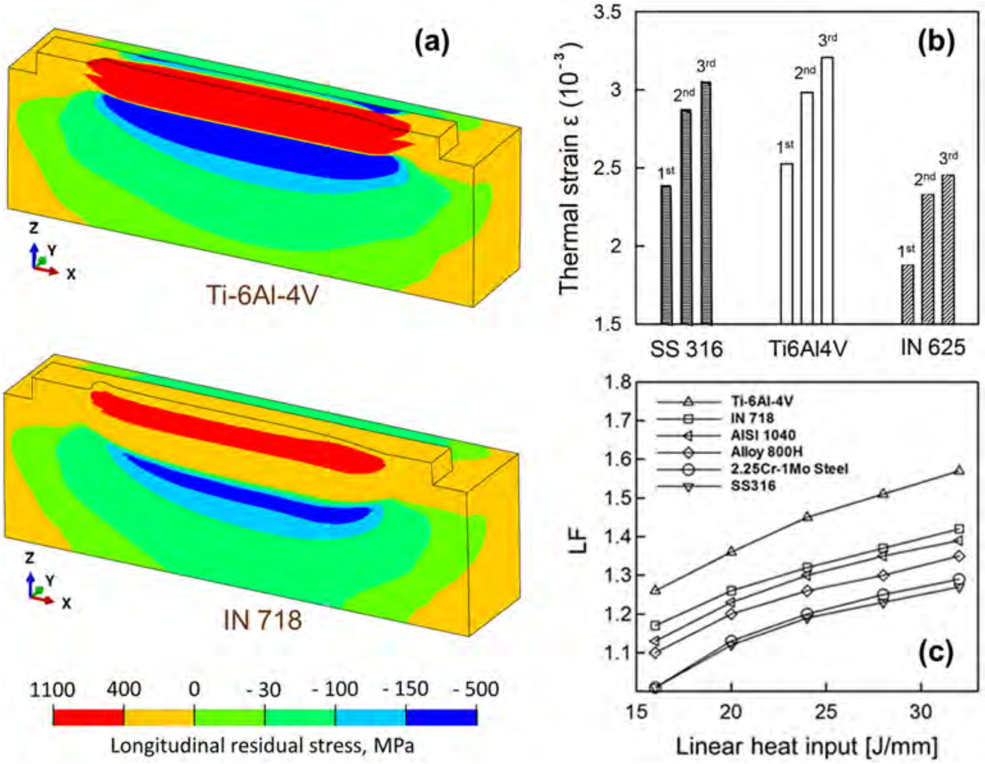

**Fig. 4.41.** (a) Comparison between longitudinal residual stress developed in Ti-6Al-4V and IN718 components printed using DED-L under the same processing conditions [27]. (b) Values of maximum thermal strain ε (an indicator of thermal distortion) in DED-L of a single-track three-layer deposition of SS316, Ti-6Al-4V and IN 625 powder materials [25]. (c) Correlation between LF (pool depth to layer thickness ratio) and linear heat input for six different alloys during DED-L [25].

### 4.4.1. *Calculation of printability of different alloys*

Printability of alloys is defined as the relative susceptibilities to common printing defects such as residual stresses, distortion, composition change and lack of fusion defect. These defects depend on transient temperature field and fusion zone geometry that can be calculated using mechanistic models [25]. Therefore, mechanistic models can provide a ranking of alloys for a specific AM process with respect to their susceptibility to forming common printing defects. For example, Fig. 4.41(a) shows that the Ti-6Al-4V component printed using DED-L is more susceptible to residual stresses than IN718 due to higher yield strength of Ti-6Al-4V. In addition, Fig. 4.41(b) shows that the Ti-6Al-4V component printed using DED-L is the most susceptible to thermal distortion compared to stainless steel and Inconel components. Ti-6Al-4V exhibits a larger molten pool due to its low density. Larger pools shrink more during solidification and makes the Ti-6Al-4V component more susceptible to distortion.

AM alloys contain volatile elements that can vaporize during the process causing changes in chemical composition. Mechanistic models are capable of predicting composition change for different AM alloys as described earlier in this review. For example, under identical DED-L processing conditions, calculations by Mukherjee et al. [25] showed that Ti-6Al-4V is the most susceptible to composition change among the common engineering alloys. Similarly, aluminum alloys are also highly susceptible to vaporization during AM due to the high equilibrium vapor pressures at relatively low temperatures. Aluminum alloys 5xxx and 7xxx containing volatile elements such as Mg and Zn are also susceptible to selective vaporization of alloying elements which can result in chemical composition change.

Mechanistic models are also used to predict lack of fusion defect as explained earlier in this review. For example, Mukherjee et al. used the ratio (LF) of molten pool depth to layer thickness to examine the susceptibility of different alloys to lack of fusion defect. The molten pool depth was calculated using a mechanistic model. Fig. 4.41(c) shows that Ti-6Al-4V components printed using DED-L exhibit the deepest molten pool among the common AM alloys and are thus the least susceptible to lack of fusion defects.

In addition, mechanistic models can also assess defects specific to individual alloys to evaluate their printability. For example, Nie et al. [299] used a FEM model and stochastic analysis to show how processing parameters could be adjusted to reduce Laves phase and increase crack resistance for the DED-L of IN718. An inspection of the Ellingham diagram indicates that compared to other alloys, aluminum alloys exhibit a higher susceptibility to form oxide particles or films that can be detrimental to mechanical properties and increase the susceptibility to defects. For example, Tang et al. [482] found that presence of oxide particles were associated with the lack of fusion defects during the PBF-L of AlSi10Mg. In addition, calculation of printability of carbon steels can be performed based on carbon equivalent (CE) which considers the role of each alloying elements in crack formation.

**Table 4.2**

A summary of reported formation of defects such as cracks, gas porosity, lack of fusion (LOF), and vaporization of alloying elements in aluminum alloys of diverse chemical compositions fabricated by different AM processes [308,327,331,393,482-493].

| Alloy | Cu | Fe | Mg | Mn | Si | Zn | Others | Process | Defects | Ref |
|---|---|---|---|---|---|---|---|---|---|---|
| **2xxx Series** | | | | | | | | | | |
| AA2024 | 4.24 | – | 1.97 | 0.56 | – | – | – | PBF-L | Cracks, gas porosity, LOF | [492] |
| AA2024 + Zr | 4.24 | – | 1.97 | 0.56 | – | – | 2.0Zr | PBF-L | Gas porosity, LOF | [491] |
| Al2139 | 4.7 | 0.06 | 0.52 | 0.36 | 0.01 | 0 | 0.38Ag-0.051Ti | DED-EB | Mg loss | [393] |
| AlCuMgSi | 3.56 | – | 1.45 | 0.62 | 1.12 | – | – | PBF-L | Cracks, gas porosity, LOF | [489] |
| **4xxx Series** | | | | | | | | | | |
| Al4047 | 0.03 | 0.18 | < 0.01 | < 0.01 | 11.28 | < 0.01 | – | DED-L | Gas porosity | [493] |
| A357 | < 0.01 | 0.15 | 0.7 | – | 7.37 | < 0.01 | 0.01O-0.01Ti | PBF-L | Gas porosity, keyhole porosity | [487] |
| AlSi10Mg | – | 0.14 | 0.291 | 0.004 | 9.92 | 0.01 | 0.01(Pb + Sn + Ti) | PBF-L | Oxide film cracks, gas porosity | [488] |
| A356 | 0.01 | 0.16 | 0.29 | – | 7.12 | 0.03 | – | PBF-L | Gas porosity | [484] |
| AlSi10Mg | – | 0.15 | 0.38 | – | 10.6 | – | – | PBF-L | Oxide inclusions, LOF, gas porosity | [482] |
| **5xxx Series** | | | | | | | | | | |
| Scalmalloy | – | 0.07 | 4.6 | 0.49 | – | – | 0.66Sc-0.42Zr | PBF-L | Minor porosity | [327] |
| Al-Mg | – | – | 6.2 | – | – | – | 0.36Sc-0.09Zr | PBF-L | Mg loss | [486] |
| Addaloy® | – | – | 3.6 | – | – | – | 1.18Zr | PBF-L | Gas porosity | [326] |
| **6xxx Series** | | | | | | | | | | |
| Al6061 | 0.23 | 0.25 | 0.83 | 0.04 | 0.62 | 0.04 | 0.08Cr-0.02Ti | PBF-L | Cracking | [308] |
| Al6061 + Zr | | | | | | | – | PBF-L | None | |
| Al5Si1CuMg | 1.19 | 0.09 | 0.46 | – | 5.32 | – | – | DED-L | Small porosity | [485] |
| **7xxx Series** | | | | | | | | | | |
| Al7075 | 1.54 | 0.17 | 2.25 | 0.02 | 0.13 | 5.4 | 0.19Cr | PBF-L | Cracking | [308] |
| Al7075 + Zr | | | | | | | – | PBF-L | Loss of Mg and Zn | |
| Al7075 | 1.64 | 0.19 | 2.48 | 0.053 | 0.73 | 6.52 | 0.26Cr-0.01Ti | PBF-L | Cracking, Gas porosity | [331] |
| Al7075 + 1Si | 1.64 | 0.19 | 2.48 | 0.05 | 1.73 | 6.52 | 0.26Cr-0.01Ti | PBF-L | Cracking, Gas porosity | |
| Al7075 + 2Si | 1.64 | 0.19 | 2.48 | 0.05 | 2.73 | 6.52 | 0.26Cr-0.01Ti | PBF-L | Cracking, Gas porosity | |
| Al7075 + 3Si | 1.64 | 0.19 | 2.48 | 0.05 | 3.73 | 6.52 | 0.26Cr-0.01Ti | PBF-L | Gas porosity | |
| Al7075 + 4Si | 1.64 | 0.19 | 2.48 | 0.05 | 4.73 | 6.52 | 0.26Cr-0.01Ti | PBF-L | Gas porosity | |
| AlZnMgCu | 1.41 | – | 2.72 | – | – | 11.9 | – | PBF-L | Loss of Mg and Zn, | [490] |
| Al7075 | 1.3 | 0.12 | 2.2 | – | 0.07 | 5.2 | 0.2Cr-0.08O | PBF-L | Cracking, Porosity, Zn loss | [483] |

$$CE = \%C + \left(\frac{\%Mn + \%Si}{6}\right) + \left(\frac{\%Cr + \%Mo + \%V}{5}\right) + \left(\frac{\%Cu + \%Ni}{15}\right) \tag{4.35}$$

where each element is expressed in wt%. Carbon steels with high values of CE are more susceptible to cracking compared to steels with lower values.

### *4.4.2. Calculation of printability for different processes*

Susceptibilities to the printing defects of a particular alloy vary significantly depending on the printing process used. For example, Table 4.2 summarizes the reported [308,327,331,393,482–493] defect formation for aluminum alloys fabricated by different AM processes. Therefore, an alloy is not equally printable by all printing processes. Mechanistic models of different printing processes useful to evaluate the formation of various defects for a particular alloy. For example, Szost et al. [494] found that titanium alloy parts accumulate higher residual stresses when printed by the DED-GMA process compared with the DED-L process. Fig. 4.42 shows that the computed longitudinal stress in the DED-GMA component is the highest among three processes because the component is printed using the thickest layers. In contrast, because of the small molten pool and thin layers in PBF-L, the component printed using this process accumulates the least residual stresses.

The effects of composition change are more pronounced during PBF processes compared to DED [20] since the small beam sizes of the heat source and rapid scanning speeds in PBF result in larger surface area to volume ratio, as shown in Fig. 4.43(a). Martin et al.

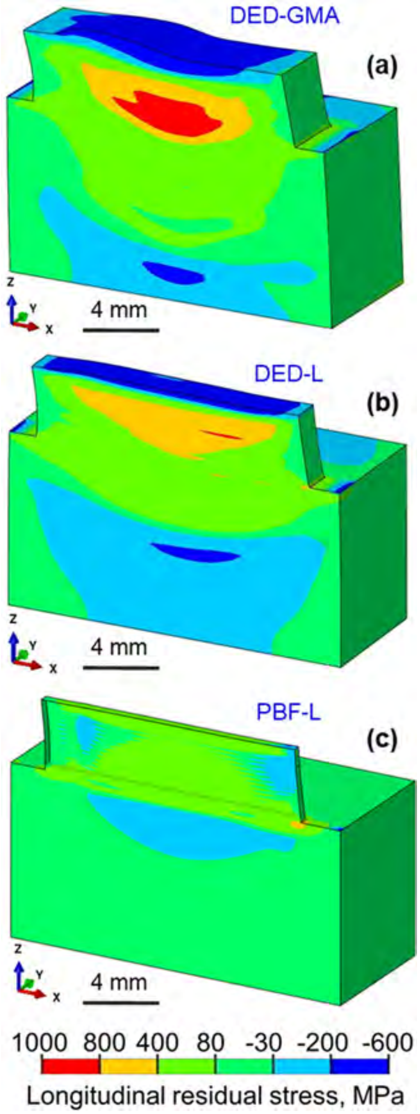

**Fig. 4.42.** Longitudinal residual stress distributions in a SS316 deposit printed using (a) DED-GMA. (b) DED-L and (c) PBF-L. The scanning direction is along the positive x-axis. Half of the solution domain is shown because of the symmetry with respect to XZ plane [283].

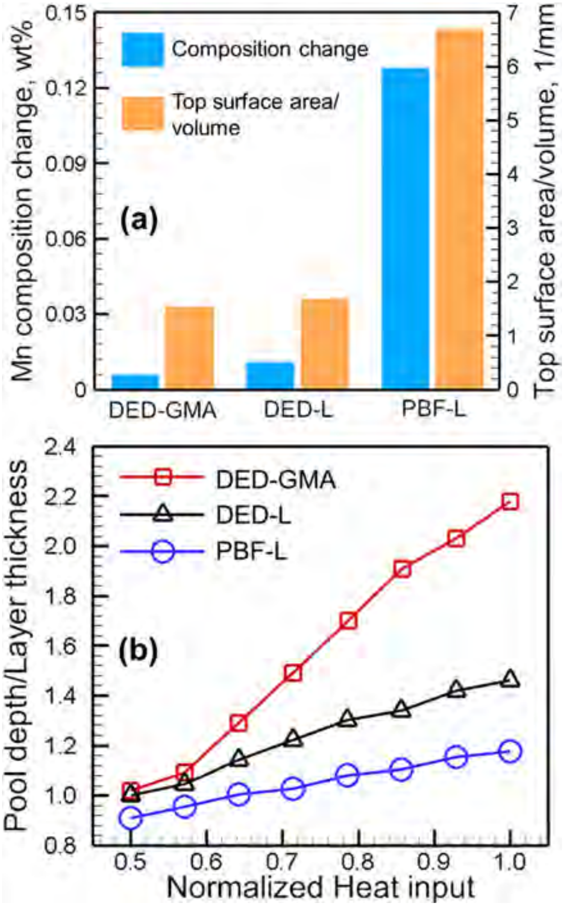

**Fig. 4.43.** (a) Change in manganese composition and the ratio of the top surface area to volume of the fusion zone for a single track SS316 component printed using three printing techniques. Composition change refers to reduction in its concentration[283]. (b) Variations in pool depth to layer thickness ratio (an indicator of lack of fusion defect) of SS316 builds printed using three techniques. The normalized heat input refers to the ratio of heat input to the maximum heat input for the printing process [283].

[308] reported a 1.35 wt% loss of Zn and a 0.72 wt% loss of Mg compared to the initial chemical composition of the powder feedstock during the PBF-L of Al7075 modified with Zr. Similarly, Li et al. [486] reported a 1.1 wt% loss of Mg of a modified Al-Mg alloy during PBF-L.

The ratio of molten pool depth to layer thickness is used to evaluate the susceptibility to lack of fusion defect of SS316 components fabricated using DED-GMA, DED-L and PBF-L components as shown in Fig. 4.43(b). The pool depth required to calculate the ratio is estimated using a mechanistic model. For all three processes, pool depth increases with the heat input and ensures proper fusional bonding among neighboring tracks. However, deep penetration of the molten pool in the DED-GMA due to the impingement of molten droplets makes this process the least susceptible to this defect among the three processes.

In summary, the printability of an alloy-process combination depends on the sensitivity of the alloy to changes in the processing conditions. Certain alloys can be printed over a large range of processing parameters without forming defects. Other alloys require careful selection of process parameters in order to produce acceptable components. Mechanistic models can predict many common defects, such as lack of fusion or vaporization of alloying elements, and serve as a useful tool for reducing the number of experiments needed to determine appropriate process parameters for the printing of an alloy.

### *4.5. Research needs*

The printability of an alloy-process combination depends on the sensitivity of the microstructure and properties to changes in the processing conditions. Certain alloys can be printed over a large range of processing parameters without forming defects. Other alloys require careful selection of process parameters in order to produce acceptable components. Mechanistic models can predict the microstructures of components, as well as many common defects, such as lack of fusion or and vaporization of alloying elements. Therefore, they serve as a useful tool for reducing the number of experiments needed to determine appropriate process parameters for the printing of an alloy. However, much work is still needed in order to integrate mechanistic models for the various aspects of printability. There are also many opportunities for researching the fundamentals of microstructural development and defect formation in AM. In addition, a printability database needs to be constructed for different possible combinations of alloy and printing processes.

## 5. Models for rapid qualification of products

The diversity of cooling rates, solidification growth rates, liquid pool shape and size and many other variables affect the microstructure and properties of the components [23]. The optimization of structure and properties and mitigation of defects are now undertaken by trial and error testing of many process variables. This empirical qualification technique works for welding and other manufacturing processes where the equipment and feedstocks are inexpensive. However, the high price of feedstock material and printing equipment makes this brute force method of qualifying parts by experiments alone intractable. To address these difficulties, the trial and error testing needs to be replaced by an advanced tool that takes advantage of our growing knowledge base of 3D printing and reduces the parameter space that needs to be investigated to qualify parts. Here we explain how verifiable mechanistic models will reduce the number of trial and error tests to obtain desired product attributes and reduce the time required for part qualification to make the printed components cost effective.

As has been discussed in details in previous sections, mechanistic models [19,31,272] can estimate the metallurgical attributes such as the transient temperature field, solidification morphology, grain structure, phases present, and susceptibilities to defect formation [272] based on well-established theories of engineering, science, and metallurgy. These models rely on the interaction between moving heat sources such as a laser beam, electron beam and electric arc with metallic materials that have been studied to understand fusion welding [495] and more recently 3D printing [18,248,272]. Starting with the calculations of transient temperature fields, calculations of simple features of microstructures [248], defects and properties [18] have been demonstrated.

### *5.1. Scale models*

As indicated before, significant progress has been made in understanding the process and the products by using comprehensive numerical mechanistic models of heat transfer, fluid flow and microstructural features. These models are accurate but often computationally intensive and therefore often cannot be used in real time. In contrast, scale models provide the effects of selected groups of parameters to reveal important trends, often qualitatively. They are widely used since they can compute important variables for multi-track components and insightful.

#### *5.1.1. Dimensionless numbers*

In a multi-variable process like AM, groups of variables often simultaneously affect the heat transfer and fluid flow behavior and the structure and properties of the components. Therefore, combinations of variables in dimensionless forms are often used to understand the evolution of structure and properties of the components made by AM [1,272,496]. These groups of variables reduce the number of parameters that need to be investigated in a multi-variable and complex system such as AM. In addition, these dimensionless numbers are formed with important physical meanings that cannot be expressed by any single variable. Furthermore, important insights can be missed when one variable is varied at a time, because such results rarely provide any indication of the interdependence of multiple variables that affect physical processes. Because of these unique advantages, dimensionless numbers are often used to evaluate the feasibility of a set of AM techniques, process conditions and alloy system to print a sound part. Utilization of these numbers can reduce the parameter window for testing and thus accelerates the product qualification process.

Table 5.1 defines the most commonly used dimensionless numbers in AM and their physical significance. In AM, dimensionless numbers are used for two main purposes. First, they are used to compare common AM processes applied to a particular alloy to provide better understanding of the processes. Second, they are also used to understand the behavior of different alloys and their susceptibilities to various AM defects under the same processing conditions. These purposes of dimensionless numbers are explained below.

*5.1.1.1. Comparison of AM processes using dimensionless numbers.* Fig. 5.1(a)–(d) show the roles of four important dimensionless numbers for the fabrication of SS316 components using DED-L, PBF-L and DED-GMA processes. Data related to these plots are taken from the literature [17,19,31,55,67,208]. The linear heat input (power/travel speed) is the highest for DED-GMA because of very high arc current and voltage associated with it. The lowest linear heat input for PBF-L is attributed to its rapid scanning speed. Rapid

**Table 5.1**
Important non-dimensional numbers and their significance [1,272,496].

| Non-dimensional number | Mathematical formulation | Significance |
|---|---|---|
| Marangoni number ($Ma$) | $Ma = -\frac{d\gamma}{dT}\ \frac{wP\ \ \Delta \mathrm{T}}{\mu\ \ D}$ | Signifies the strength of convective flow of the molten metal inside the pool driven by surface tension gradient |
| Peclet number ($Pe$) | $Pe = \frac{U\ \ l}{D}$ | Indicates the relative importance of the convective heat transfer over the heat transfer by conduction. |
| Fourier number ($F_o$) | $F_o = \frac{D}{V\ \ l}$ | Represents the ratio of heat dissipation rate to heat storage rate |
| Strain parameter ($\varepsilon^*$) | $\varepsilon^* = \frac{\beta_L T}{EI}\frac{t}{Fo\sqrt{\rho}}H^{3/2}$ | Embodies all important process parameters and alloy properties which affect the thermal strain and distortion |

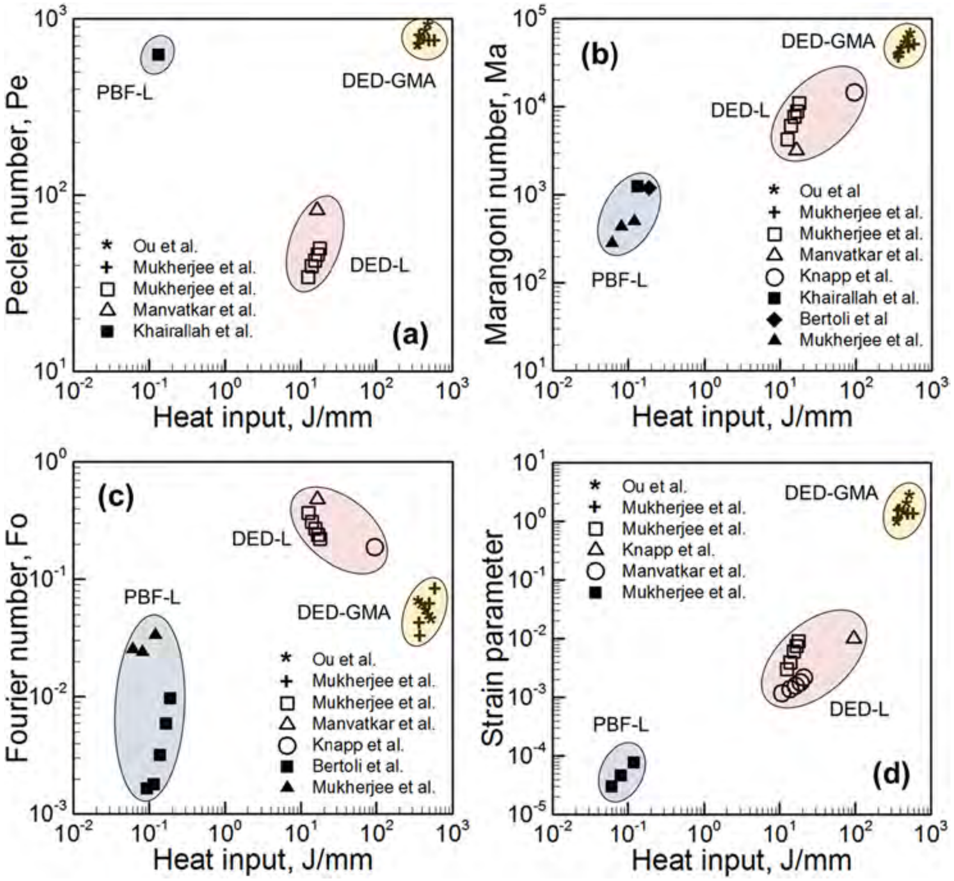

**Fig. 5.1.** Peclet number (Pe), Marangoni number (Ma), Fourier number (Fo), and strain parameter for DED-L, PBF-L and DED-GMA processes of SS316. Values of non-dimensional numbers are either provided or calculated based on the given parameters. The values are taken from Ou et al. [23], Manvatkar et al. [17], Mukherjee et al. [19], Knapp et al. [31], Khairallah et al. [67] and Bertoli et al. [208].

scanning in PBF-L elongates the molten pool that accumulates more heat per unit time. Faster scanning also reduces the heat dissipation rate along the width and depth directions. Both of these attributes are reflected by the lowest value of the Fourier number for PBF-L. High heat input in DED-GMA results in large molten pool that allows vigorous convective flow of liquid metal indicated by the highest Marangoni number for that process. However, for all three processes typical Peclet numbers are significantly higher than one. It signifies that the convective heat transfer is the dominant mechanism of heat flow in the molten pool in all the three processes. DED-GMA exhibits the largest volume of molten pool that shrinks considerably during solidification. Therefore, thermal distortion is most pronounced during DED-GMA among the three processes considered.

*5.1.1.2. Comparison among AM alloys using dimensionless numbers.* Fig. 5.2(a)–(d) compare the pool dimensions, cooling rates and susceptibility to thermal distortion of the three commonly used alloys during DED-L process. Higher Marangoni number indicates more efficient convective heat transfer that results in larger length and width of the liquid metal pool. Both the length and the aspect ratio (length/depth) of the molten pool are enhanced because of higher Marangoni number as shown in Fig. 5.2(a) and (b), respectively. Because of its lowest density, Ti-6Al-4V exhibits the largest volume of molten pool as observed in the figures. In addition, high temperature gradient in the pool results in vigorous convective flow of molten metal for Ti-6Al-4V. Therefore, Ti-6Al-4V exhibits the highest Marangoni number among the three alloys. Cooling rates during solidification can be directly correlated with Fourier number as shown in Fig. 5.2(c). Faster rate of heat dissipation enhances cooling rate and Fourier number. Among the three alloys, Ti-6Al-4V has the highest thermal diffusivity that results in the fastest rate of heat dissipation. Therefore, the Fourier number for Ti-6Al-4V is the highest, as shown in Fig. 5.2(c). For a particular Fourier number, IN718 exhibits the fastest cooling rate during solidification attributed to its lowest latent heat of fusion. Fig. 5.2(d) shows the effects of Fourier number on the thermal strain parameter which is a quantitative representation of the thermal distortion during deposition. It is evident that maintaining a high Fourier number by lowering heat input is always an effective way to minimize thermal distortion during AM. Among the three alloys, Ti-6Al-4V exhibits the largest volume of molten pool that shrinks more during solidification and makes the builds susceptible to distortion.

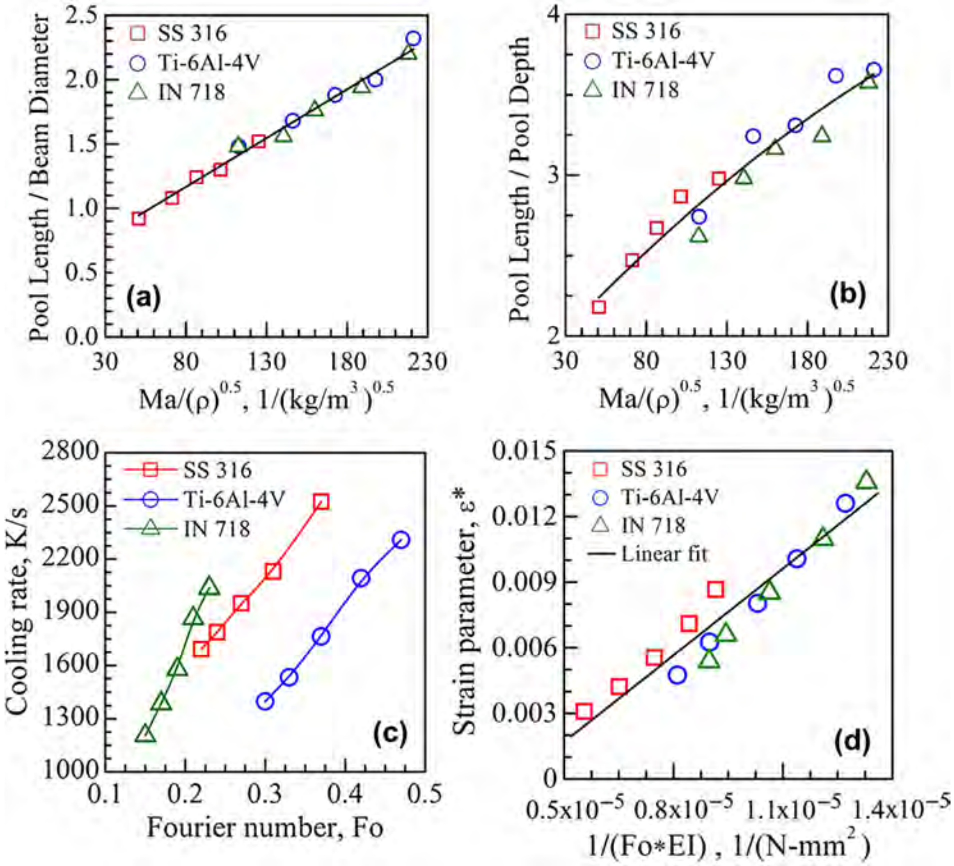

**Fig. 5.2.** Effects of Marangoni number on (a) pool length and (b) pool aspect ratio (length/depth). Effects of Fourier number on (c) cooling rate during solidification and (d) thermal strain during deposition [272]. All results are for DED-L process.

### 5.1.2. Reduced-order models

Comprehensive mechanistic models are rigorous and accurate but computationally intensive. Therefore, these models are often not appropriate for real time applications to simulate large components printed using multiple layers and hatches. Reduced order models simplify the complex multi-dimensional calculations by starting with a simple one-dimensional algorithm of heat flow and other physical processes and extrapolating the algorithm to fit a complex geometry using various simplifications. For example, a 3D heat conduction problem is reduced to a 1D problem where the Fourier's law of heat conduction is discretized [497]. The calculated results in 1D is expanded to obtain an approximate temperature field in 3D by considering the movement of the heat source and deposition pattern [497]. Since these models can capture the transient variation of the temperature field for a particular location, they can be used to calculate the fusion zone geometry, cooling rate, temperature gradient and other important variables [415,416]. These models have already been applied for large computational domains with complex geometry [498–500].

Accuracy of these models depends on the number of variables to be calculated, convergence criteria and the algorithm used [497]. Therefore, reduced order models achieve efficiency of calculations economically by accepting a lower accuracy [497,498]. For example, Peng et al. [501] reported that their reduced order model predicted the temperature history during powder bed fusion with more than two orders of magnitude faster computational speed than the existing finite element models while sacrificing less than 15% accuracy. Since AM deals with complex and intricate geometry, reduced order models are beneficial for real-time parameter identification and control of AM process [502]. These models are often used to predict transient temperature field, residual stresses and distortion in AM [503]. Element sizes may be taken larger than the heat source to accommodate larger geometry [497]. However, these models are unable to consider complicated physics such as convective flow of liquid metal inside the molten pool. In addition, temperature dependent thermophysical properties of alloys are not commonly used [497]. Since these models exclude several underlying physical phenomena, rigorous experimental validation is a prerequisite for their application. These models often need to be rebuilt for different sets of parameters [497] and their applicability is limited to a narrow window of parameter space. Therefore, these models can only be used for approximate calculations of a few variables and do not provide insights about the process and product that can be achieved using comprehensive mechanistic models.

**Table 5.2**

Bi-directional models for AM and welding.

| Process | Forward model | Optimization algorithm | Focus | References. |
|---|---|---|---|---|
| DED AM | Analytical heat conduction | Use of a weighted diffusivity function | Fitting of a weighted diffusivity function by tallying estimated and measured temperatures | [515,516] |
| DED-GMA | Heat conduction analysis using FEM | Multivariate pattern search using ANN and Fibonacci search method | Values of arc efficiency & source parameters were found by comparing computed & measured temperatures on deposit side wall using ANN. Convective heat transfer coefficient was estimated from cooling rates. | [263] |
| GTAW | FEM based 2D conduction heat transfer analysis | Newton-Raphson interpolation | Shape of molten pool was reconstructed by minimizing error between computed & measured thermal cycles. | [576] |
| PAW | FEM based 3D conduction heat transfer analysis | Multidimensional simplex minimization | Similar to reference [576]; thermocouple data was used improve accuracy. | [577] |
| GTAW | 3D analytical heat conduction model | Simulated annealing & golden section method | Arc efficiency, melting efficiency and radius of molten pool were determined from thermal cycles. | [578] |
| GTAW | FDM based 3D conduction heat transfer analysis | Golden section method | Heat input and pool shape were corrected by minimizing error between estimated & measured thermal cycles at multiple locations. | [579] |
| EBW | FDM based 2D conduction heat transfer analysis | Unconstrained conjugate gradient method | The difference between the computed and measured surface temperatures was minimized to reconstruct the Gaussian heat source. | [580] |
| Laser heating | FDM based 3D conduction heat transfer analysis | Conjugate gradient method | The difference between the computed and measured surface temperatures was minimized to reconstruct the Gaussian heat source. | [581] |
| RSW | FDM based 3D conduction heat transfer analysis | Fletcher-Reeves conjugate gradient method | Computed sheet-sheet interface temperature was corrected from surface temperature measured by IR camera. | [581] |
| GTAW | 3D FDM based heat and fluid flow analysis | Levenberg-Marquardt method | Values of effective conductivity and viscosity in molten pool & three variables for arc energy were found by minimizing the error between computed and measured weld dimensions | [510] |
| LBW | 3D FDM based heat and fluid flow analysis | Levenberg-Marquardt method | By minimizing errors in computed weld shapes, the nature of values of effective conductivity and viscosity in molten pool were examined. | [511,512,576] |
| FSW | 3D FDM based heat & material flow analysis | Differential evolution based genetic algorithm | Estimated frictional heat generation rate were corrected by minimizing error between computed & measured thermal cycles and tool torque | [508,513] |
| GMAW | 3D FDM based heat conduction analysis | Levenberg-Marquardt and conjugate gradient | First, values of a set of uncertain parameters were identified. Next, permissible welding conditions were designed for a target weld geometry. | [514] |
| GTAW | 3D FDM based heat and fluid flow analysis | Parent centric recombination (PCX) based genetic algorithm | First, values of a set of uncertain parameters were identified. Next, permissible welding conditions were designed for a target weld pool shape in a bi-directional manner. | [504,506,507] |

ANN: Artificial neural network; FEM: Finite element method; FDM: Finite difference method; PAW: Plasma arc welding; GTAW: Gas tungsten arc welding; GMAW: Gas metal arc welding; RSW: Resistance spot welding; EBW: Electron beam welding; FSW: Friction stir welding.

### 5.2. Bidirectional models

Most of the mechanistic models of PBF and DED take process parameters as input and calculate fusion zone geometry, temperature fields, cooling rates, temperature gradients and other important parameters as output. However, their utility for shop floor applications has so far been limited. Apart from the accessibility and inherent complexity of these models, they are also structured as forward models. In other words, they restrict process variables and materials properties as input and pre-determined attributes of the process and the product as output. For example, it is possible to specify the power, speed and the thermophysical properties of the alloy being deposited and other variables as input parameters to calculate fusion zone dimensions and cooling rates at monitoring locations. However, very often the real need is to know what values of laser power, speed and other variables will result in a given cooling rate or a given fusion zone geometry. The available forward models are incapable of determining these sets of process variables without multiple trial and error runs. In other words, the models cannot switch between the input and output variables [495]. Furthermore, there are often several combinations of speed, power and other process variables that can generate a given target attribute [504]. The available forward models are incapable to determining multiple sets of process variable that can result in a given target attribute such as the fusion zone geometry. In other words, what is needed and not available are mechanistic models that can compute a target attribute such as fusion zone geometry or the cooling rate as an input based on phenomenological consideration multiple sets of process variable to achieve the specified attribute. The utility of the mechanistic models can be greatly enhanced by the construction of bi-directions models that are capable of providing a choice of alternate process variable sets to attain desired product and process attributes.

One way to transform the available well-tested forward models to bi-directional models is by combining the available models with an optimization algorithm. The algorithm seeks to search one or more set of process variables that minimizes the difference between the user specified desired attribute and the model predicted attribute. This methodology has been used successfully in welding. However, since the process requires many forward runs of the comprehensive mechanistic model, the method is computationally intensive. A recourse is to develop, validate and test a neural network (NN) trained with the results of a phenomenological forward model that provide an instantaneous output for any set of process variables [495]. The resulting NN embodies the power of a large well-tested mechanistic model that can be executed instantly.

The construction of bi-directional models of AM are just beginning. However, in the allied field of fusion welding, examples of the success of these models are well documented [505–508]. The recent work on AM and welding are documented in Table 5.2 that includes different forward models and the accompanying optimization or search algorithms. They have been applied and tested for calculating multiple sets of welding variables that can result in target weld attributes such as weld geometry, cooling rate, peak temperature and other variables. Different optimization algorithms such as Levenberg-Marquardt [509–512], differential evolution [508,513], conjugate gradient [514] and genetic algorithm [504,506,507] were used. For arc and laser welding, the calculated welding parameters include heat input, arc radius and energy distribution coefficient and effective thermal conductivity and viscosity of the molten material [509–512]. A similar approach was also applied to friction stir welding that predicted the sets of welding variables to achieve the desired temperature and material flow, tool torque and force [508,513]. The correctness of the suggested welding conditions for a target weld pool shape and size was checked extensively by conducting experiments to test the appropriateness of the predicted values.

Both PBF and DED based AM process use similar heat sources and feedstock or filler alloys and thus, the volume of uncertain modeling parameters are of similar nature. The inverse models for AM [263,515,516] are scarce. The well-tested bi-directional models consisting of a forward model and a suitable optimization algorithm can be useful to identify suitable combinations of AM process variables to achieve a target attribute of AM parts and greatly expand the usefulness of the models for practical applications.

### 5.3. Big data in AM

Big data is the set of voluminous and complex data that cannot be processed using traditional data-processing techniques [517] and cannot be stored in commonly used storage devices [518–520]. The total volume of big data is in the order of petabytes ($10^6$ gigabytes). Currently, there is a total storage of 3500 petabytes of data in the North America alone [521]. However, according to the Reuters, the global volume of big data is expected to reach 35 zettabytes ($10^{12}$ gigabytes) by 2020 if the data are appropriately preserved [521]. Although the source of big data includes the government agencies, media, health care, information technology, science and education sectors, manufacturing sector generates more data than any other sectors which is around 2 exabytes ($10^9$ gigabytes) per year now [521–523]. AM being a rapidly developing manufacturing process largely contributes to the generation of this voluminous data [524].

There are four main sources of big data in AM, such as, (1) in-situ monitored variables such as temperature, distortion and bead shape, (2) post-process characterization data, such as, microstructural features, residual stresses, composition and surface roughness, properties and service performance, (3) theoretical results calculated using numerical models of AM and (4) published articles, proceedings, technical reports and patents. While fabricating a typical single layer single hatch build consisting of about 2.3 trillion voxels, in-situ monitoring and post processing generate about 0.5 TB of data [524]. Most of these data are unstructured and require careful acquisition methods. However, data generated by numerical models of AM and published literature are structured data. On 22nd April 2020, there are total 29,478 articles, proceedings and books on AM or 3D printing in Web of Science. They occupy several hundred gigabytes of storage.

In the traditional manufacturing processes, such as, casting, welding and forming, standardization is done by fabrication, characterization and testing. However, for a time consuming and expensive process like AM a more efficient method is desirable to reduce the time between design and qualification of parts. Therefore, methodical acquisition, storage, analysis and interpretation of the big data generated in AM industries and research organizations with the help of the advanced tools of the digital age can contribute to time-efficient standardization and qualification of the AM processes and products [29,525,526].

### *5.3.1. Management of big data in AM*

Fig. 5.3 summarizes different steps of management of the big data generated by the AM models. Handling of these big data is typically done in several stages as explained below:

Source: Transport phenomena models generate different process related data such as temperature and velocity distributions, build geometry, cooling rates and solidification parameters. There are other auxiliary models that generate data on microstructure, properties and defect formation. All of these data contribute to the big data of AM. Control models used to analyze the sensing data captured during the process also generate a large volume of data.

Collection: Collection of big data is typically done in two steps. First, the data is recorded using a suitable recording device. Next, the unnecessary data are cleaned from the data sample. Uncertainty in AM data is the first challenge during the data collection process. The second challenge is to automatically generate the right metadata that describes what data is recorded and how it is recorded and measured. Properly assigned metadata [520,527] helps users to easily access the data.

Storage: Traditional data storage systems such as hard drive in PC are capable of storing data in the order of terabytes ($10^3$ gigabytes). Therefore, this devices are not suitable for storing big data of AM. Typically, the storage devices used for big data are in the order of petabytes ($10^6$ gigabytes) to exabytes ($10^3$ petabytes). Commonly used storage devices are cluster storage [527], cloud storage [527], redundant array of independent disks (RAID) system [521,527], Hadoop [522] and Google file system [527]. To store big data, all national labs in the United States have assembled High Performance Storage System (HPSS) with parallel storage connectivity that can facilitate a storage in the order of several exabytes [528]. Storage of the data from the numerical models can be done more efficiently by generating the data in binary format instead of ASCII format.

Access: All big data generated and collected are assigned metadata [520,527] that includes all the necessary information about the data that helps user to easily access them. Different internet based search engines are also used for accessing different data. For example, search engines like Google Scholar, Web of Science, Scopus and Baidu Scholar are used to find published AM literature. In recent days, Internet of Things (IoT) and cyber manufacturing system are used for easy access of big data [529]. The Internet of Things is an information technology based network of AM machines, sensors, controllers, computers, storage devices and other items that allows interaction and access of these facilities to reach common research goals [529]. Cyber manufacturing system facilitate information technology based management of AM data to provide accessibility and configurability of the data for maintaining productivity [530–533].

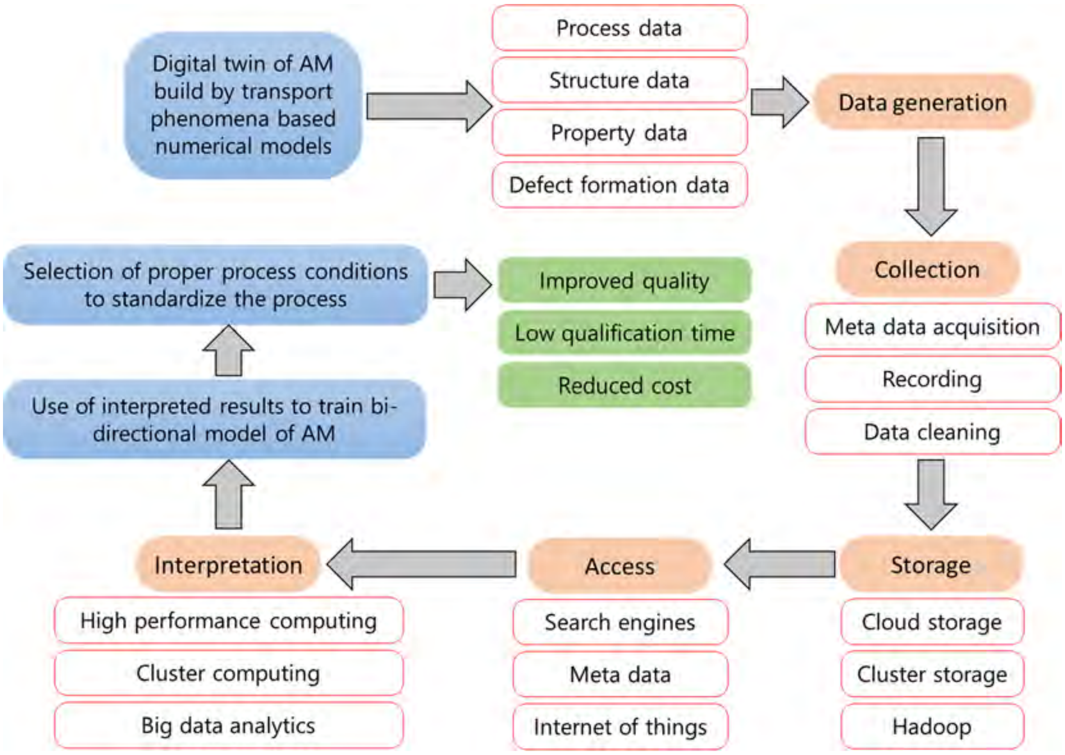

**Fig. 5.3.** Schematic representation of the contributions of transport phenomena models and digital twins in the management and use of big data in additive manufacturing.

Analysis and interpretation: For analyzing the big data in AM, high performance computing (HPC) clusters [522] and cloud computing [533] are used. HPC clusters with multiple core CPUs and GPUs have been utilized to accelerate solid modeling, slicing, control system support generation, heat and mass transfer calculations [522]. Big Data Analytics [534] is used in design and development of cyber-manufacturing systems where proper data handling and processing are done using artificial intelligence and predictive analytics. Although there are well-established algorithms [535] to handle big voluminous data, analysis and interpretation of such data remains a major challenge.

### 5.3.2. Challenges and path forward

Since, AM is a multi-variable process, theoretical investigations of effects of different process variables on important metallurgical variables and defect formation generate heterogeneous data. It is challenging to analyze such a heterogeneous data to provide better understanding of the process. Voluminous real time data needs big storage and high performance computing facilities to analyze and interpret. Therefore, the timeliness of these data depends on the storage capability and computational efficiency of the facility [520]. Many theoretical models are not open for public use. The data generated by different private organizations and national labs are often not disclosed because of safety, security, intellectual rights and market competition. That hinders the accessibility of important information that can otherwise be very insightful. Published literature are mostly not open access and are owned by the publishers. Universities and other research organizations need to buy them from the publishers. That largely deprives the user to access all available published documents.

Fig. 5.3 explains that the interpreted and classified big data are useful to train reverse models [536] based on search algorithms such as neural network and genetic algorithm to restrict the limit of the process variables. That will reduce the heterogeneity and inconsistency of the AM data set. These proper process conditions are beneficial for quick standardization of the AM process. Scaling, dimensional analysis and back-of-the-envelope calculations [496] can be useful to extract important insights from the big data set in a time efficient manner. When distributed AM resources are collected, shared, and applied in a cloud platform, this will be a promising globalized and time-efficient environment for customized production [524]. Coherently connected big data in AM will allow to select the appropriate printable alloys, the right AM process and process variables, improve the quality of the AM components, reduce qualification time and cost [29]. However, how to intelligently and effectively manage the wide variety of AM data with dynamic evaluation, intelligent matching, planning, and scheduling in a cloud platform requires in-depth study.

## 5.4. Machine learning in AM

The transport phenomena-based models in AM, although powerful and deterministic, often fail to consider all the complexities of physical phenomena in AM. As a result, mechanistic models are not widely used in the design of parts. AM is still a developing field and the detailed mechanisms to explain various part attributes are yet to be discovered. In contrast, machine learning can discover hidden relations among variables within a set of available data and use it to make useful predictions without any phenomenological understanding. There are several important problems in AM where a database of results can be used to train machine learning algorithms to help analyze results and serve as predictive tools. Several reviews [537–539] are available on the theory, applications, and algorithms used in machine learning.

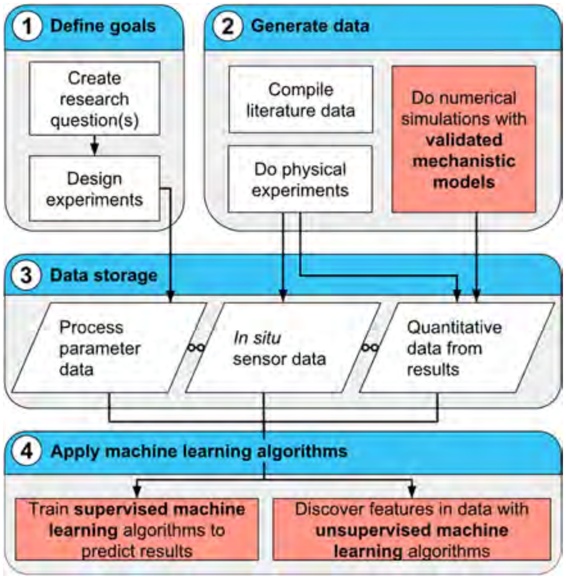

**Fig. 5.4.** A diagram showing the data needed to apply machine learning algorithms in AM. Flow of information is indicated by arrows. Mechanistic models and machine learning are in the red, highlighted panels.

### 5.4.1. *Benefits of machine learning in AM*

Fig. 5.4 summarizes the ways that machine learning can be used as a tool for AM. Datasets for most current machine learning approaches used in the AM community stem from numerical simulations, experimental measurements, or a combination of both. Machine learning often requires some prior knowledge of the influential factors (e.g., process parameters) that affect a property (e.g., pool geometry), and the goal is to establish a quantitative relationship that can accurately predict a property for any set of input data. For example, both experiments and simulations in AM have shown that higher laser powers increase molten pool volume and fast scanning speeds yield long and narrow deposits, yet the quantitative descriptions of these phenomena are often unknown for a given set of parameters. It was indicated in an earlier section that insufficient overlap of fusion zones between tracks contributes to lack of fusion defects. Because these defects can also originate from other mechanisms that are poorly understood, mechanistic models can only quantitatively predict some lack of fusion defects. Likewise, there is an absence of unified phenomenological predictions for surface roughness and geometric accuracy of AM parts, because both are caused by many complex processes that are incompletely understood. Lack of fusion defects, surface roughness, and geometrical accuracy are all examples of problems where a database of results can be used to train machine learning algorithms to serve as predictive tools. In addition, the availability of the open-source, well-tested, easy to use commercial codes for machine learning also provides an opportunity for rapid prediction of part attributes.

### 5.4.2. *Machine learning examples in AM*

The two main categories of machine learning algorithms, supervised and unsupervised, are used in AM. In supervised learning, causative factors are mathematically mapped to a material response or property. To implement supervised machine learning algorithms, a training dataset with both input data and the corresponding output data determines the hidden relationship through the use of an appropriate algorithm. Once trained, the algorithm can predict the outputs for specified input data. Supervised machine learning has been used in AM for part design, controlling powder spreading, defect formation, process monitoring, and process-structure relations. In general, supervised machine learning is applied for the problems where experimental characterization or measurements are difficult or mechanistic models need development. The commonly used supervised machine learning algorithms for AM include neural networks [540–542], decision tree [543], Bayesian Networks [544], K-nearest neighbor [543] and support vector machines [499]. There are several examples of neural networks being trained to predict various aspects of the AM build quality. Zhang et al. [540] utilized neural networks to develop a powder spreading process map that relates powder spreading parameters, i.e. translational and rotational speed of the roller, to the overall quality of the powder bed and surface roughness. Powder rheology measurements and spreading simulations based on the discrete element method were used to produce a large dataset, and the neural network was employed to relate the spreading parameters to powder bed quality. Yuan et al. [541] used in-situ high speed images captured during PBF-L to train, validate, and test a neural network for controlling the deposit geometry. Scime and Beuth [542] used neural networks to control the defect formation during PBF-L by correlating the defects with the interactions between the powder spreading blade and powder particles.

There are also several examples of other supervised machine learning algorithms being applied to AM. Popova et al. [499] used support vector machines trained on data generated by mechanistic models to correlate molten pool dimensions and temperature with grain structure. Kamath [545] used multiple thermal models to generate training data for a decision tree algorithm that predicted molten pool depth in PBF-L. A visual data analysis technique was used to determine important variables in the process, shown in

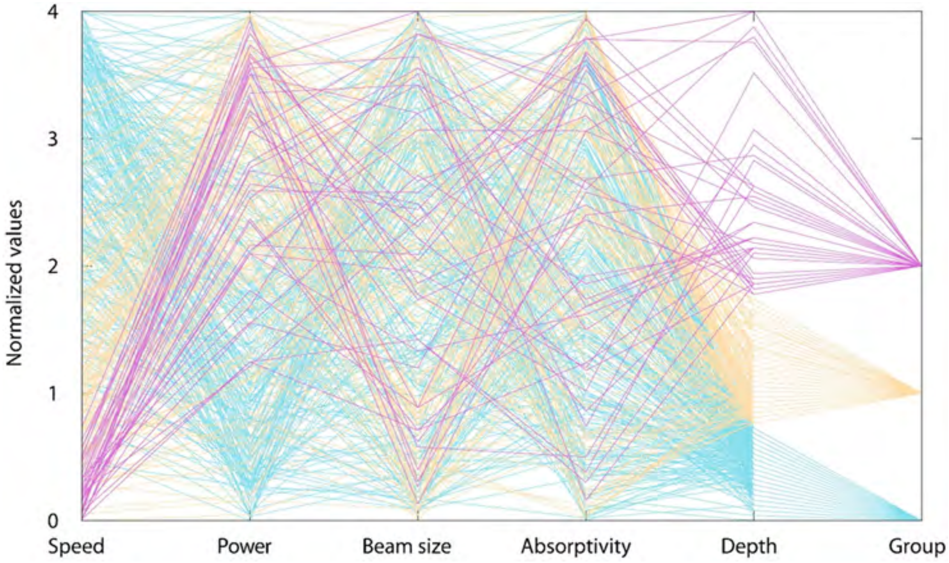

**Fig. 5.5.** A visual data analysis approach to categorize the correlation between molten pool depth and magnitude of input parameters where the polyline color refers to the classification of the molten pool determined from simulations (cyan = shallow, orange = moderate, purple = deep). All process variables were scaled to values between zero and four so they could be plotted on the same ordinate axis. This figure is adapted from [545].

Fig. 5.5, where each line represents a simulation and its process parameters, and the colors represent different magnitudes of the molten pool depth classified as shallow (cyan), moderate (orange), or deep (purple). High concentrations of lines of a single color indicate a strong correlation of the depth with a specific input parameter. For example, high normalized powers and low scanning speeds led to deep molten pools as indicated by the high concentration of purple polylines at these values. Interestingly, the molten pool depth did not show a strong dependence on either beam size or absorptivity. The results of this visual analysis were used to narrow the number of experiments needed for training the machine learning algorithms and optimizing process parameters to achieve fully-dense AM parts. Khanzadeh et al. [543] evaluated the effectiveness of decision tree, K-nearest neighbor, and support vector machines algorithms in predicting porosity during DED-L using molten pool morphology extracted *in situ* thermal imaging data to train the algorithms. Using *in situ* imaging data for supervised machine learning relies heavily on image processing and computer vision techniques to extract meaningful quantitative data. Computer vision algorithms have also been used to quantify powder characteristics, which generated data used to train a supervised support vector machine [546]. In addition, in-situ data from acoustic signals have been used in machine learning to control part quality [547] and detect defects [548]. As can be seen through the variety of supervised machine learning examples, the type of data being used to train the algorithm, and the desired output are key factors for choosing an effective machine learning method.

Unlike supervised machine learning, unsupervised machine learning identifies features or relationships within the data fed into the algorithm. This is useful in situations where causative factors are unknown but there is still a need to find order among sets of data. These features/relationships are useful for obtaining important correlations that are often qualitative. A common application of unsupervised machine learning is the classification of features or objects within a digital image or output signal from a sensor. This could be used to identify unique features from the output of *in situ* sensors, such as classifying various features of a powder bed surface. Unsupervised machine learning has been used for the classification and detection of defects and anomalies during AM of metallic materials [549,550]. Specific types of unsupervised algorithms include self-organizing mapping and hierarchical clustering. There are fewer examples of AM-specific unsupervised machine learning because its application to AM is fewer than supervised algorithms. Scime and Beuth [549] used automated image analysis to detect anomalies during the spreading of layers in PBF, where anomalies were classified in terms of recoater hopping or streaking, debris in powder, part warpage or failure, and incomplete spreading. Individual images were taken after the recoating of each layer and a machine learning algorithm was trained to identify and classify these anomalies based on visual appearance. Khanzadeh et al. [550] used an unsupervised self-organizing map algorithm to classify thermal imaging of the molten pool temperature distribution during DED-L as “normal” or “abnormal.” Abnormal molten pool temperature distributions were shown to correlate well with the location of porosity in the build. In both examples, the goal of the unsupervised learning algorithm is to classify data into meaningful categories that can be correlated with the occurrence of defects. As *in situ* sensing techniques are further developed for AM, there will be an increased potential for unsupervised machine learning applications that can classify vast amounts of *in situ* data to enable rapid qualification techniques.

### *5.4.3. Challenges and path forward*

Machine learning offers a way to effectively use existing data because data analysis can reveal trends and the most important variables even if there is no phenomenological understanding. Of course, there is an inherent risk of making decisions based on this knowledge without fully understanding the inherent biases or limitations of the machine learning methods. Nevertheless, the proper

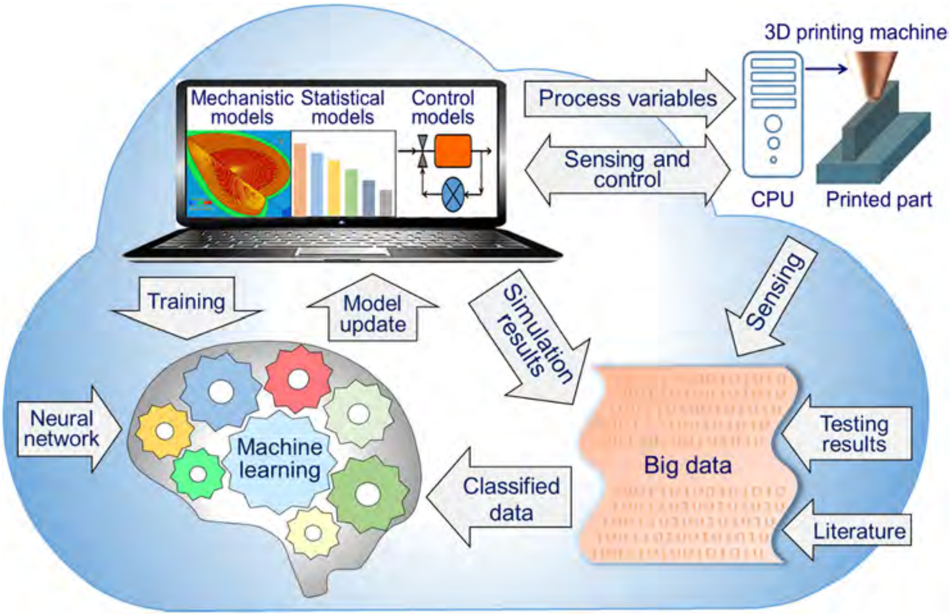

**Fig. 5.6.** Schematic representation of a digital twin of additive manufacturing [23].

use of modern machine learning technology will advance the understanding and improve the utility of AM processes. Supervised and unsupervised machine learning algorithms serve different but complementary purposes, but to implement them requires sufficient data tailored to answer a specific research question or solve a particular problem. As described by Ramprasad et al. [538], the quantification and classification of input data is perhaps the most important step in machine learning. To enable machine learning methods to provide insight into the physical parameters, care should be taken to digitally capture and store detailed data about experimental parameters, output *in situ* sensors, and quantitative results obtained from physical experiments and validated mechanistic models.

When rigorously tested and validated, mechanistic models can be used to meet data generation requirements in a cost-effective and timely manner and thus the rate of discovery through machine learning techniques can be accelerated. In addition, a bridge between the mechanistic models and machine learning models can lead to efficient predictive tools that can significantly accelerate the prediction of important variables [551,552]. An adequately tested machine learning algorithm can be a critical component of a digital twin of AM, as explained subsequently.

### *5.5. Digital twins of AM*

A digital twin is a virtual replica of a hardware that has been successfully tested to replicate behavior of the hardware through computer simulations [553,554]. A digital twin can reduce the number of trial and error tests to obtain a desired set of product attributes and reduce the time required for part qualification [31]. General Electric currently uses over 550,000 digital twins for a wide variety of applications ranging from jet engines to power turbines [555]. In addition, NASA and the U.S. Air Force have also utilized digital twins to increase reliability and safety of vehicle designs [556]. However, currently digital twins of AM are not generally available. AM is a developing technology and only a few components of the digital twin have so far been developed [30,31]. Here, we discuss the most important building blocks of a digital twin of AM and their functions.

#### *5.5.1. Components of a digital twin*

Various components of a digital twin and the interconnections among them are shown in Fig. 5.6. It consists of mechanistic and statistical models, machine learning, big data analytics and sensing and control [31]. A mechanistic model can estimate the metallurgical attributes such as the transient temperature field, fusion zone geometry, cooling rates and solidification parameters as described in Section 3 as well as microstructures and defects discussed in Section 4. This model needs to be bi-directional, so that it can switch between inputs and outputs as described in Section 5.2. Another important component of the digital twin is a sensing and control model. This model can interface with multiple sensors and monitoring systems for in-situ measurements of temperature [162,557–561], deposit geometry and surface features [562], detection of defects [563] and deviations of component dimensions from its design [165,564]. Both the mechanistic and control models can have errors due to uncertainties in input parameters, thermophysical data and the simplifying assumptions. Statistical models correct these errors and improve the accuracies of the model predictions without considering any physical processes. In addition, machine learning is an effective tool to model highly complex attributes of AM that are not well understood phenomenologically. This machine learning algorithm is first trained using a data set classified from the big data of AM as discussed in Section 5.4. The algorithm is validated and tested using a suitable data set independent of the data used for training. Although the aforementioned components of a digital twin have been reported in the literature [30,31], currently there is no generally available digital twin of AM.

Since, AM is a developing field, many of the aforementioned building blocks are required to be developed or modified. For example, computationally efficient mechanistic models applicable for a wide variety of alloy-AM process combinations need to be developed. Since, control models depend on sensing data, predictions of such models can be improved by enhancing the resolution, accuracy and precision of the sensors. New algorithms, computational facilities and storage devices are needed to store, analyze and interpret the continuously expanding big data set of AM. The machine learning algorithms tested for welding should be modified and verified for different AM conditions. Finally, all of these components are required to bring under one framework that can consider many alloy-AM process combinations to predict the structure, properties and performance of AM components [31].

#### *5.5.2. Digital twins for rapid qualification*

Digital twins can reshape the way researchers approach problems in AM. Mechanistic models involving heat transfer and fluid flow serve as an engine for the calculation of the most important variables, such as cooling rates and fusion zone geometry that affect part quality and performance. When adequately tested, digital twins will provide multiple avenues for obtaining structurally sound and reliable parts. While digital twins are not intended to replace experimental studies, they can help to narrow the window of process parameter space and reduce trial and error testing. Thus, the digital twins will have the ability to transform the brute force qualification and certification of parts into a way that will significantly shorten the lead time between design and certification.

Connecting the physical and virtual world of printing by creating a set of verifiable models and ultimately a digital twin will accelerate the qualification process and thus reduce cost and increase market share of AM components. The advanced software and hardware capabilities and a rich knowledge base of metallurgy are crucial factors that will make building and utilization of digital twin in AM a realistic venture.

### *5.6. Research needs*

Data-driven approaches have great potential to expedite the process development and part design for AM components. Initial examples that use machine learning to improve build quality show the benefits of this approach, and more research should be done to expand the useful applications of machine learning and big data in AM. Verified mechanistic models can help expand existing datasets and reduce the amount of necessary experiments. Furthermore, mixing data-driven approaches with the underlying physical understanding developed through mechanistic modeling offers a unique chance to create digital twins of the AM process. While examples of these modern approaches to predict critical aspects of AM are sparse, there are great opportunities for research and development in this area.

## 6. Concluding remarks

A critical review of the recent progress in the mechanistic models of AM, particularly numerical modeling of heat transfer, fluid flow and mass transfer establishes the central role of the models in understanding the most important parameters such as temperature and velocity fields, cooling rates, solidification morphology and the scale of microstructure, all of which affect the product quality. These parameters are difficult to obtain by any other technique including real-time monitoring. This review provides many examples to show that when numerical simulations of transport processes are conducted concurrently with experiments, they can uncover the underlying scientific basis for understanding why certain microstructure and properties are observed. In addition, these models can provide an understanding of the formation of many of the common defects in AM. Apart from providing a better understanding of the structure, properties and serviceability of the AM components, these models can be a powerful tool to optimize production variables, reduce defects, improve product quality and reduce the time lag between the component design and certification.

This review also uncovers many opportunities in expanding the reach of AM to newer alloys and products. For example, out of the 5500 available commercial alloys, only a handful are now used for AM. The current path of empirical, trial and error testing for the qualification of new alloys and components is expensive and does not always provide the optimized solution. Use of a heat transfer and fluid flow model, on the other hand shrinks the process parameter space to tractable combinations of AM variables, thus saving time and efforts. A combination of mechanistic modeling of heat and fluid flow and appropriately selected experiments within a narrow range of AM parameters would help make the generation of printability data more efficient. A practical way of expanding the reach of AM to newer alloys and to expedite the deployment of new components is to further develop a printability data base that can help in selecting alloy-process combinations as described in this review. Printability of alloys is an important area where the numerical simulation of heat transfer and fluid flow can provide a cost effective and useful solution.

Well-tested mechanistic models of AM are computationally intensive because they simulate many simultaneously occurring complex physical processes. As a result, these models are not suitable for real time shop floor use. A practical way to bridge the gaps between the attributes of the phenomenological models and the needs of the shop floor is the development of simpler, real-time models that are useful for selecting process variables and avoiding common defects in parts. In the welding literature, back of the envelop analytical calculations of important parameters have been used to address this need [565,566]. Furthermore, the outputs from the comprehensive models have been used to create neural network models that can be run in real time [567–570]. A similar approach can be useful for AM. The resulting models will have the predictive power of comprehensive mechanistic models, but capable of operating at a much higher speed, enabling their real time use.

The generally available transport phenomena-based models of AM are forward models, i.e., they are structured to predict attributes of the products such as the geometry, cooling rate and solidification parameters from process variables and thermophysical properties. While these models can reveal detailed insight about the AM process that cannot be obtained otherwise, they are not designed to provide guidance to practicing engineers to select appropriate AM process parameters to achieve a selected attribute of a component. In other words, the practicing engineers need reverse/bi-directional models while all the generally available models are forward models. This gap between the needs and the capabilities can be bridged by coupling the forward models with appropriate global search algorithms such as a genetic algorithm. Building bi-directional models of AM is within the reach of AM community because a similar goal has already been achieved in fusion welding [506,514,569,571].

When experiments are conducted or models are run, a large volume of data are generated. This review outlines a methodology to combine a large volume of classifiable data with verifiable mechanistic models for the construction of digital twins of AM machines [30,31]. Such integrated frameworks, when adequately tested, can predict the geometry, composition, structure and other attributes of metallic components and reduce defects. Although the construction of digital twins is just beginning, their impact cannot be overestimated because of the potential cost savings by shrinking the large parameter space for trial and error testing.

The printing of metallic components is the fastest growing section in AM. However, production of nearly defect free, structurally sound, reproducible parts and reducing the time lag between the design and certification in a cost-effective manner remain important goals. This review shows that the transport phenomena-based mechanistic models can play an important role in pursuing these goals.

## Declaration of Competing Interest

The authors declare that they have no known competing financial interests or personal relationships that could have appeared to influence the work reported in this paper.

## References

[1] DebRoy T, Wei HL, Zuback JS, Mukherjee T, Elmer JW, Milewski JO, et al. Additive manufacturing of metallic components - process, structure and properties. Prog Mater Sci 2018;92:112–224.

[2] DebRoy T, Mukherjee T, Milewski JO, Elmer JW, Ribic B, Blecher JJ, et al. Scientific, technological and economic issues in metal printing and their solutions. Nat Mater 2019;18:1026–32.

[3] Thompson SM, Bian L, Shamsaei N, Yadollahi A. An overview of Direct Laser Deposition for additive manufacturing; Part I: Transport phenomena, modeling and diagnostics. Addit Manuf 2015;8:36–62.

[4] King WE, Anderson AT, Ferencz RM, Hodge NE, Kamath C, Khairallah SA, et al. Laser powder bed fusion additive manufacturing of metals; physics, computational, and materials challenges. Appl Phys Rev 2015;2:041304.

[5] Markl M, Körner C. Multiscale modeling of powder bed-based additive manufacturing. Ann Rev Mater Res 2016;46:93–123.

[6] Schoinochoritis B, Chantzis D, Salonitis K. Simulation of metallic powder bed additive manufacturing processes with the finite element method: a critical review. Proc Inst Mech Eng B J Eng Manuf 2017;231:96–117.

[7] Francois MM, Sun A, King WE, Henson NJ, Tourret D, Bronkhorst CA, et al. Modeling of additive manufacturing processes for metals: Challenges and opportunities. Curr Opin Solid St M 2017;21:198–206.

[8] Galati M, Iuliano L. A literature review of powder-based electron beam melting focusing on numerical simulations. Addit Manuf 2018;19:1–20.

[9] Teng C, Pal D, Gong H, Zeng K, Briggs K, Patil N, et al. A review of defect modeling in laser material processing. Addit Manuf 2017;14:137–47.

[10] Ghosh S. Predictive modeling of solidification during laser additive manufacturing of nickel superalloys: recent developments, future directions. Mater Res Exp 2018;5:012001.

[11] Yan Z, Liu W, Tang Z, Liu X, Zhang N, Li M, et al. Review on thermal analysis in laser-based additive manufacturing. Opt Laser Technol 2018;106:427–41.

[12] Stavropoulos P, Foteinopoulos P. Modelling of additive manufacturing processes: a review and classification. Manuf Rev 2018;5:2.

[13] Luo Z, Zhao Y. A survey of finite element analysis of temperature and thermal stress fields in powder bed fusion additive manufacturing. Addit Manuf 2018;21:318–32.

[14] Yan W, Lin S, Kafka OL, Yu C, Liu Z, Lian Y, et al. Modeling process-structure-property relationships for additive manufacturing. Front Mech Eng 2018;13:482–92.

[15] Zhang Y, Chen Q, Guillemot G, Gandin C-A, Bellet M. Numerical modelling of fluid and solid thermomechanics in additive manufacturing by powder-bed fusion: continuum and level set formulation applied to track-and part-scale simulations. Comptes Rendus Mécanique 2018;346:1055–71.

[16] Liu J, Jalalahmadi B, Guo Y, Sealy MP, Bolander N. A review of computational modeling in powder-based additive manufacturing for metallic part qualification. Rapid Prototyp J 2018;24:1245–64.

[17] Manvatkar V, De A, DebRoy T. Heat transfer and material flow during laser assisted multi-layer additive manufacturing. J Appl Phys 2014;116:124905.

[18] Manvatkar V, De A, DebRoy T. Spatial variation of melt pool geometry, peak temperature and solidification parameters during laser assisted additive manufacturing process. Mater Sci Tech 2015;31:924–30.

[19] Mukherjee T, Wei HL, De A, DebRoy T. Heat and fluid flow in additive manufacturing - Part II: Powder bed fusion of stainless steel, and titanium, nickel and aluminum base alloys. Comp Mater Sci 2018;150:369–80.

[20] DebRoy T, David SA. Physical processes in fusion welding. Rev Mod Phys 1995;67:85–112.

[21] Khairallah SA, Anderson A. Mesoscopic simulation model of selective laser melting of stainless steel powder. J Mater Process Tech 2014;214:2627–36.

[22] Lee YS, Zhang W. Modeling of heat transfer, fluid flow and solidification microstructure of nickel-base superalloy fabricated by laser powder bed fusion. Addit Manuf 2016;12:178–88.

[23] Mukherjee T, DebRoy T. A digital twin for rapid qualification of 3D printed metallic components. Appl Mater Today 2019;14:59–65.

[24] Sames WJ, List F, Pannala S, Dehoff RR, Babu SS. The metallurgy and processing science of metal additive manufacturing. Int Mater Rev 2016;61:315–60.

[25] Mukherjee T, Zuback JS, De A, DebRoy T. Printability of alloys for additive manufacturing. Sci Rep 2016;6:Article No. 19717.

[26] Mukherjee T, Manvatkar V, De A, DebRoy T. Mitigation of thermal distortion during additive manufacturing. Scripta Mater 2017;127:79–83.

[27] Mukherjee T, Zhang W, DebRoy T. An improved prediction of residual stresses and distortion in additive manufacturing. Comp Mater Sci 2017;126:360–72.

[28] Mukherjee T, Zuback J, Zhang W, DebRoy T. Residual stresses and distortion in additively manufactured compositionally graded and dissimilar joints. Comp Mater Sci 2018;143:325–37.

[29] Nassar A, Reutzel E. A proposed digital thread for additive manufacturing. In: International solid freeform fabrication symposium, Austin, Texas; 2013.

[30] DebRoy T, Zhang W, Turner J, Babu S. Building digital twins of 3D printing machines. Scripta Mater 2017;135:119–24.

[31] Knapp GL, Mukherjee T, Zuback JS, Wei HL, Palmer TA, De A, et al. Building blocks for a digital twin of additive manufacturing. Acta Mater 2017;135:390–9.

[32] Technologies ACFoAM, Terminology ACFoAMTSFo. Standard terminology for additive manufacturing technologies: ASTM International; 2012.

[33] Zeng K, Pal D, Stucker B. A review of thermal analysis methods in laser sintering and selective laser melting. In: Proceedings of solid freeform fabrication symposium, Austin, TX; 2012. p. 796–814.

[34] Yang Y, Ayas C. Point, surface and volumetric heat sources in the thermal modelling of selective laser melting. In: AIP conference proceedings; 2017. p. 040006.

[35] Li J, Wang Q, Michaleris PP. An analytical computation of temperature field evolved in directed energy deposition. J Manuf Sci Eng 2018;140:101004.

[36] de La Batut B, Fergani O, Brotan V, Bambach M, El Mansouri M. Analytical and numerical temperature prediction in direct metal deposition of Ti6Al4V. J Manuf Mater Proc 2017;1:3.

[37] Promoppatum P, Yao S-C, Pistorius PC, Rollett AD. A Comprehensive comparison of the analytical and numerical prediction of the thermal history and solidification microstructure of Inconel 718 products made by laser powder-bed fusion. Engineering 2017;3:685–94.

[38] Grong O. Metallurgical modelling of welding: materials modelling series. The Institute of Materials; 1994.

[39] Svensson L, Gretoft B, Bhadeshia H. An analysis of cooling curves from the fusion zone of steel weld deposits. Scand J Metall 1986;15:e103.

[40] Sahoo P, DebRoy T, McNallan M. Surface tension of binary metal—surface active solute systems under conditions relevant to welding metallurgy. Metall Trans B 1988;19:483–91.

[41] Pitscheneder W, DebRoy T, Mundra K, Ebner R. Role of sulfur and processing variables on the temporal evolution of weld pool geometry during multi-kilowatt laser welding of steels. Weld J 1996;75:71s–80s.

[42] Steen W, Dowden J, Davis M, Kapadia P. A point and line source model of laser keyhole welding. J Phys D Appl Phys 1988;21:1255.

[43] Short A, McCartney D, Webb P, Preston E. Parametric envelopes for keyhole plasma arc welding of a titanium alloys. Proceedings of the 8th international conference on trends in welding research. 2009. p. 690–6.

[44] Mackwood A, Crafer R. Thermal modelling of laser welding and related processes: a literature review. Opt Laser Technol 2005;37:99–115.

[45] Burgardt P, Heiple C. Weld penetration sensitivity to welding variables when near full joint penetration. Weld J 1993;72.

[46] Brown R. Keyhole welding studies with a moderate-power, high-brightness fiber laser. J Laser Appl 2008;20:201–8.

[47] Javid Y, Ghoreishi M, Shamsaei S. A three-dimensional heat transfer simulation of laser full penetration welding of rene-80 super alloy. Lasers Eng (Old City Publishing) 2012;22.

[48] Kiyoshima S, Deng D, Ogawa K, Yanagida N, Saito K. Influences of heat source model on welding residual stress and distortion in a multi-pass J-groove joint. Comp Mater Sci 2009;46:987–95.

[49] Dehoff RR, Kirka MM, Sames WJ, Bilheux H, Tremsin AS, Lowe LE, et al. Site specific control of crystallographic grain orientation through electron beam additive manufacturing. Mater Sci Tech 2015;31:931–8.

[50] Farahmand P, Kovacevic R. An experimental–numerical investigation of heat distribution and stress field in single-and multi-track laser cladding by a high-power direct diode laser. Opt Laser Technol 2014;63:154–68.

[51] Wang X, Laoui T, Bonse J, Kruth J-P, Lauwers B, Froyen L. Direct selective laser sintering of hard metal powders: experimental study and simulation. Int J Adv Manuf Tech 2002;19:351–7.

[52] Schiller S, Heisig U, Panzer S. Electron beam technology. John Wiley & Sons; 1982.

[53] Gajapathi S, Mitra S, Mendez P. Part I: Development of new heat source model applicable to micro electron beam welding. Sci Technol Weld Join 2012;17:429–34.

[54] Galati M, Iuliano L, Salmi A, Atzeni E. Modelling energy source and powder properties for the development of a thermal FE model of the EBM additive

manufacturing process. Addit Manuf 2017;14:49–59.
[55] Ou W, Mukherjee T, Knapp G, Wei Y, DebRoy T. Fusion zone geometries, cooling rates and solidification parameters during wire arc additive manufacturing. Int J Heat Mass Tran 2018;127:1084–94.
[56] Kumar S, Bhaduri S. Theoretical investigation of penetration characteristics in gas metal-arc welding using finite element method. Metall Mater Trans B 1995;26:611–24.
[57] Yang Z, DebRoy T. Modeling macro-and microstructures of gas-metal-arc welded HSLA-100 steel. Metall Mater Trans B 1999;30:483–93.
[58] Goldak J, Chakravarti A, Bibby M. A new finite element model for welding heat sources. Metall Trans B 1984;15:299–305.
[59] Pinkerton AJ, Li L. An analytical model of energy distribution in laser direct metal deposition. Proc Inst Mech Eng B J Eng Manuf 2004;218:363–74.
[60] Andrew JP, Lin L. Modelling the geometry of a moving laser melt pool and deposition track via energy and mass balances. J Phys D Appl Phys 2004;37:1885.
[61] Bergström. The absorption of laser light by rough metal surfaces. Sweden: Luleå University of Technology; 2008.
[62] Rubenchik AM, Wu SSQ, Kanz VK, LeBlanc MM, Lowdermilk WH, Rotter MD, et al. Temperature-dependent 780-nm laser absorption by engineering grade aluminum, titanium, and steel alloy surfaces. Opt Eng 2014;53.
[63] Boley CD, Mitchell SC, Rubenchik AM, Wu SSQ. Metal powder absorptivity: modeling and experiment. Appl Optics 2016;55:6496–500.
[64] Boley CD, Khairallah SA, Rubenchik AM. Calculation of laser absorption by metal powders in additive manufacturing. Appl Optics 2015;54:2477–82.
[65] Cho J-H, Na S-J. Implementation of real-time multiple reflection and Fresnel absorption of laser beam in keyhole. J Phys D Appl Phys 2006;39:5372.
[66] Tan W, Bailey NS, Shin YC. Investigation of keyhole plume and molten pool based on a three-dimensional dynamic model with sharp interface formulation. J Phys D Appl Phys 2013;46:055501.
[67] Khairallah SA, Anderson AT, Rubenchik A, King WE. Laser powder-bed fusion additive manufacturing: physics of complex melt flow and formation mechanisms of pores, spatter, and denudation zones. Acta Mater 2016;108:36–45.
[68] Khan K, De A. Modelling of selective laser melting process with adaptive remeshing. Sci Technol Weld Join 2019:1–10.
[69] Tolochko Nikolay K, Khlopkov Yurii V, Mozzharov Sergei E, Ignatiev Michail B, Laoui T, Titov Victor I. Absorptance of powder materials suitable for laser sintering. Rapid Prototyp J 2000;6:155–61.
[70] Ding D, Pan Z, Cuiuri D, Li H. Wire-feed additive manufacturing of metal components: technologies, developments and future interests. Int J Adv Manuf Tech 2015;81:465–81.
[71] Williams SW, Martina F, Addison AC, Ding J, Pardal G, Colegrove P. Wire + arc additive manufacturing. Mater Sci Tech 2016;32:641–7.
[72] Xu X, Mi G, Luo Y, Jiang P, Shao X, Wang C. Morphologies, microstructures, and mechanical properties of samples produced using laser metal deposition with 316 L stainless steel wire. Opt Laser Eng 2017;94:1–11.
[73] Wang T, Zhu Y, Zhang S, Tang H, Wang H. Grain morphology evolution behavior of titanium alloy components during laser melting deposition additive manufacturing. J Alloy Comp 2015;632:505–13.
[74] Buvanashekaran G, Shanmugam SN, Sankaranarayanasamy K, Sabarikanth R. A study of laser welding modes with varying beam energy levels. Proc Inst Mech Eng, Part C: J Mech Eng Sci 2009;223:1141–56.
[75] Cunningham R, Zhao C, Parab N, Kantzos C, Pauza J, Fezzaa K, et al. Keyhole threshold and morphology in laser melting revealed by ultrahigh-speed x-ray imaging. Science 2019;363:849–52.
[76] King WE, Barth HD, Castillo VM, Gallegos GF, Gibbs JW, Hahn DE, et al. Observation of keyhole-mode laser melting in laser powder-bed fusion additive manufacturing. J Mater Process Tech 2014;214:2915–25.
[77] Kawahito Y, Matsumoto N, Abe Y, Katayama S. Relationship of laser absorption to keyhole behavior in high power fiber laser welding of stainless steel and aluminum alloy. J Mater Process Tech 2011;211:1563–8.
[78] Rai R, Elmer JW, Palmer TA, DebRoy T. Heat transfer and fluid flow during keyhole mode laser welding of tantalum, Ti-6Al-4V, 304L stainless steel and vanadium. J Phys D Appl Phys 2007;40:5753–66.
[79] Murr LE, Gaytan SM, Ramirez DA, Martinez E, Hernandez J, Amato KN, et al. Metal fabrication by additive manufacturing using laser and electron beam melting technologies. J Mater Sci Technol 2012;28:1–14.
[80] Körner C. Additive manufacturing of metallic components by selective electron beam melting - a review. Int Mater Rev 2016;61:361–77.
[81] Liu YJ, Li SJ, Wang HL, Hou WT, Hao YL, Yang R, et al. Microstructure, defects and mechanical behavior of beta-type titanium porous structures manufactured by electron beam melting and selective laser melting. Acta Mater 2016;113:56–67.
[82] Knapp GL, Raghavan N, Plotkowski A, DebRoy T. Experiments and simulations on solidification microstructure for Inconel 718 in powder bed fusion electron beam additive manufacturing. Addit Manuf 2019;25:511–21.
[83] Hu R, Chen X, Yang G, Gong S, Pang S. Metal transfer in wire feeding-based electron beam 3D printing: Modes, dynamics, and transition criterion. Int J Heat Mass Tran 2018;126:877–87.
[84] Lancaster JF. The physics of welding. Phys Technol 1984;15:73.
[85] Ribic B, Palmer TA, DebRoy T. Problems and issues in laser-arc hybrid welding. Int Mater Rev 2009;54:223–44.
[86] Kou S. Welding metallurgy. 2nd ed. Hoboken, NJ: John Wiley & Sons; 2003.
[87] Ding J, Colegrove P, Mehnen J, Williams S, Wang F, Almeida PS. A computationally efficient finite element model of wire and arc additive manufacture. Int J Adv Manuf Tech 2014;70:227–36.
[88] Bai X, Colegrove P, Ding J, Zhou X, Diao C, Bridgeman P, et al. Numerical analysis of heat transfer and fluid flow in multilayer deposition of PAW-based wire and arc additive manufacturing. Int J Heat Mass Tran 2018;124:504–16.
[89] Mundra K, DebRoy T, Kelkar KM. Numerical prediction of fluid flow and heat transfer in welding with a moving heat source. Numer Heat Tr A - Appl 1996;29:115–29.
[90] Brackbill J, Kothe DB, Zemach C. A continuum method for modeling surface tension. J Comput Phys 1992;100:335–54.
[91] Keene B. Review of data for the surface tension of pure metals. Int Mater Rev 1993;38:157–92.
[92] Kou S, Sun D. Fluid flow and weld penetration in stationary arc welds. Metall Trans A 1985;16:203–13.
[93] Kumar A, DebRoy T. Calculation of three-dimensional electromagnetic force field during arc welding. J Appl Phys 2003;94:1267–77.
[94] Hu J, Tsai HL. Heat and mass transfer in gas metal arc welding. Part II: The metal. Int J Heat Mass Tran 2007;50:808–20.
[95] Ushio M, Wu CS. Mathematical modeling of three-dimensional heat and fluid flow in a moving gas metal arc weld pool. Metall Mater Trans B 1997;28:509–16.
[96] Katinas C, Shang W, Shin YC, Chen J. Modeling particle spray and capture efficiency for direct laser deposition using a four nozzle powder injection system. J Manuf Sci Eng 2018;140:041014.
[97] Gan Z, Liu H, Li S, He X, Yu G. Modeling of thermal behavior and mass transport in multi-layer laser additive manufacturing of Ni-based alloy on cast iron. Int J Heat Mass Tran 2017;111:709–22.
[98] Turner JS. Buoyancy effects in fluids. Cambridge University Press; 1979.
[99] Klassen A, Forster VE, Juechter V, Körner C. Numerical simulation of multi-component evaporation during selective electron beam melting of TiAl. J Mater Process Tech 2017;247:280–8.
[100] Semak V, Matsunawa A. The role of recoil pressure in energy balance during laser materials processing. J Phys D Appl Phys 1997;30:2541.
[101] Klassen A, Scharowsky T, Körner C. Evaporation model for beam based additive manufacturing using free surface lattice Boltzmann methods. J Phys D Appl Phys 2014;47:275303.
[102] Shyy W, Thakur S, Ouyang H, Liu J, Blosch E. Computational techniques for complex transport phenomena. Cambridge University Press; 1997.
[103] Zhang W, Kim C-H, DebRoy T. Heat and fluid flow in complex joints during gas metal arc welding—part I: numerical model of fillet welding. J Appl Phys 2004;95:5210–9.
[104] Hirt CW, Nichols BD. Volume of fluid (VOF) method for the dynamics of free boundaries. J Comput Phys 1981;39:201–25.
[105] Youngs DL. Time-dependent multi-material flow with large fluid distortion. Numerical methods for fluid dynamics; 1982.
[106] Adalsteinsson D, Sethian JA. A fast level set method for propagating interfaces. J Comput Phys 1995;118:269–77.

[107] Gibou F, Fedkiw R, Osher S. A review of level-set methods and some recent applications. J Comput Phys 2018;353:82–109.
[108] Chen Q, Guillemot G, Gandin C-A, Bellet M. Three-dimensional finite element thermomechanical modeling of additive manufacturing by selective laser melting for ceramic materials. Addit Manuf 2017;16:124–37.
[109] Qi H, Mazumder J, Ki H. Numerical simulation of heat transfer and fluid flow in coaxial laser cladding process for direct metal deposition. J Appl Phys 2006;100:024903.
[110] Shen B, Li H, Liu S, Zou J, Shen S, Wang Y, et al. Influence of laser post-processing on pore evolution of Ti–6Al–4V alloy by laser powder bed fusion. J Alloy Comp 2020;818:152845.
[111] Shin YC, Bailey N, Katinas C, Tan W. Predictive modeling capabilities from incident powder and laser to mechanical properties for laser directed energy deposition. Comput Mech 2018;61:617–36.
[112] Olsson E, Kreiss G, Zahedi S. A conservative level set method for two phase flow II. J Comput Phys 2007;225:785–807.
[113] Cao ZN, Dong P. Modeling of GMA weld pools with consideration of droplet impact. J Eng Mater Technol 1998;120:313–20.
[114] Mundra K, DebRoy T. Toward understanding alloying element vaporization during laser beam welding of stainless steel. Weld J 1993;72:1–9.
[115] Mills K. Recommended values of thermophysical properties for selected commercial alloys. England: Woodhead Publishing Limited; 2002.
[116] Rombouts M, Froyen L, Gusarov A, Bentefour EH, Glorieux C. Photopyroelectric measurement of thermal conductivity of metallic powders. J Appl Phys 2005;97:024905.
[117] Mukherjee T, DebRoy T. Control of asymmetric track geometry in printed parts of stainless steels, nickel, titanium and aluminum alloys. Comp Mater Sci 2020;182:109791.
[118] Giauque W, Clayton J. The heat capacity and entropy of nitrogen. heat of vaporization. Vapor pressures of solid and liquid. The reaction 1/2 N2 + 1/2 O2 = NO from spectroscopic data. J Am Chem Soc 1933;55:4875–89.
[119] Hoshino T, Mito K, Nagashima A, Miyata M. Determination of the thermal conductivity of argon and nitrogen over a wide temperature range through data evaluation and shock-tube experiments. Int J Thermophys 1986;7:647–62.
[120] Tsilingiris P. Thermophysical and transport properties of humid air at temperature range between 0 and 100 C. Energ Convers Manage 2008;49:1098–110.
[121] Zhang Y, Faghri A. Melting and resolidification of a subcooled mixed powder bed with moving Gaussian heat source. J Heat Transf-Trans ASME 1998;120:883–91.
[122] Hussein A, Hao L, Yan C, Everson R. Finite element simulation of the temperature and stress fields in single layers built without-support in selective laser melting. Mater Des 2013;52:638–47.
[123] Zareie Rajani HR, Phillion AB. A mesoscale solidification simulation of fusion welding in aluminum–magnesium–silicon alloys. Acta Mater 2014;77:162–72.
[124] Cook PS, Murphy AB. Simulation of melt pool behaviour during additive manufacturing: underlying physics and progress. Addit Manuf 2020;31:100909.
[125] Sih SS, Barlow JW. The prediction of the emissivity and thermal conductivity of powder beds. Particul Sci Technol 2004;22:427–40.
[126] Li Z, Liu C, Xu T, Ji L, Wang D, Lu J, et al. Reducing arc heat input and obtaining equiaxed grains by hot-wire method during arc additive manufacturing titanium alloy. Mater Sci Eng A 2019;742:287–94.
[127] Mukherjee T, Wei HL, De A, DebRoy T. Heat and fluid flow in additive manufacturing - part I: modeling of powder bed fusion. Comp Mater Sci 2018;150:304–13.
[128] Wang P, Lao CS, Chen ZW, Liu YK, Wang H, Wendrock H, et al. Microstructure and mechanical properties of Al-12Si and Al-3.5Cu-1.5Mg-1Si bimetal fabricated by selective laser melting. J Mater Sci Technol 2020;36:18–26.
[129] Tey CF, Tan X, Sing SL, Yeong WY. Additive manufacturing of multiple materials by selective laser melting: Ti-alloy to stainless steel via a Cu-alloy interlayer. Addit Manuf 2020;31:100970.
[130] Chen J, Yang Y, Song C, Zhang M, Wu S, Wang D. Interfacial microstructure and mechanical properties of 316L/CuSn10 multi-material bimetallic structure fabricated by selective laser melting. Mater Sci Eng A 2019;752:75–85.
[131] Nguyen D-S, Park H-S, Lee C-M. Applying selective laser melting to join Al and Fe: an investigation of dissimilar materials. Appl Sci 2019;9:3031.
[132] Wei K, Zeng X, Li F, Liu M, Deng J. Microstructure and mechanical property of Ti-5Al-2.5Sn/Ti-6Al-4V dissimilar titanium alloys integrally fabricated by selective laser melting. JOM 2020;72:1031–8.
[133] Zuback JS, Palmer TA, DebRoy T. Additive manufacturing of functionally graded transition joints between ferritic and austenitic alloys. J Alloy Comp 2019;770:995–1003.
[134] Ge W, Lin F, Guo C. Functional gradient material of Ti-6Al-4V and γ-TiAl fabricated by electron beam selective melting. Proceedings: 26th annual international solid freeform fabrication symposium - an additive manufacturing conference. 2015. p. 10–2.
[135] Wang F, Mei J, Jiang H, Wu XH. Production of functionally-graded samples using simultaneous powder and wire-feed. Mater Sci Forum 2007:3631–6.
[136] Gupta A, Talha M. Recent development in modeling and analysis of functionally graded materials and structures. Prog Aerosp Sci 2015;79:1–14.
[137] Miettinen J. Calculation of solidification-related thermophysical properties for steels. Metall Mater Trans B 1997;28:281–97.
[138] Gan Z, Yu G, He X, Li S. Numerical simulation of thermal behavior and multicomponent mass transfer in direct laser deposition of Co-base alloy on steel. Int J Heat Mass Tran 2017;104:28–38.
[139] Saunders N, Guo U, Li X, Miodownik A, Schillé J-P. Using JMatPro to model materials properties and behavior. JOM 2003;55:60–5.
[140] Saunders N, Miodownik AP. CALPHAD: a comprehensive guide. Elsevier; 1998.
[141] Saunders N, Guo Z, Li X, Miodownik A, Schille J-P. Modelling the material properties and behaviour of Ni-based superalloys. Superalloys 2004;2004:849–58.
[142] Fan Z, Tsakiropoulos P, Miodownik A. A generalized law of mixtures. J Mater Sci 1994;29:141–50.
[143] Carroll BE, Otis RA, Borgonia JP, Suh JO, Dillon RP, Shapiro AA, et al. Functionally graded material of 304L stainless steel and inconel 625 fabricated by directed energy deposition: characterization and thermodynamic modeling. Acta Mater 2016;108:46–54.
[144] Bobbio LD, Otis RA, Borgonia JP, Dillon RP, Shapiro AA, Liu Z-K, et al. Additive manufacturing of a functionally graded material from Ti-6Al-4V to Invar: experimental characterization and thermodynamic calculations. Acta Mater 2017;127:133–42.
[145] Shuai C, He C, Feng P, Guo W, Gao C, Wu P, et al. Biodegradation mechanisms of selective laser-melted Mg–xAl–Zn alloy: grain size and intermetallic phase. Virt Phys Prototyp 2018;13:59–69.
[146] Wang P, Deng L, Prashanth KG, Pauly S, Eckert J, Scudino S. Microstructure and mechanical properties of Al-Cu alloys fabricated by selective laser melting of powder mixtures. J Alloy Comp 2018;735:2263–6.
[147] Martinez R, Todd I, Mumtaz K. In situ alloying of elemental Al-Cu12 feedstock using selective laser melting. Virt Phys Prototyp 2019;14:242–52.
[148] Wang JC, Liu YJ, Qin P, Liang SX, Sercombe TB, Zhang LC. Selective laser melting of Ti–35Nb composite from elemental powder mixture: Microstructure, mechanical behavior and corrosion behavior. Mater Sci Eng A 2019;760:214–24.
[149] Vrancken B, Dadbakhsh S, Mertens R, Vanmeensel K, Vleugels J, Yang S, et al. Selective Laser Melting process optimization of Ti–Mo–TiC metal matrix composites. CIRP Ann 2019;68:221–4.
[150] Qiu C, Panwisawas C, Ward M, Basoalto HC, Brooks JW, Attallah MM. On the role of melt flow into the surface structure and porosity development during selective laser melting. Acta Mater 2015;96:72–9.
[151] Körner C, Attar E, Heinl P. Mesoscopic simulation of selective beam melting processes. J Mater Process Tech 2011;211:978–87.
[152] Körner C, Bauereiß A, Attar E. Fundamental consolidation mechanisms during selective beam melting of powders. Model Simul Mater Sci Eng 2013;21:085011.
[153] Steuben JC, Iliopoulos AP, Michopoulos JG. Discrete element modeling of particle-based additive manufacturing processes. Comput Method Appl M 2016;305:537–61.
[154] Russell M, Souto-Iglesias A, Zohdi T. Numerical simulation of Laser Fusion Additive Manufacturing processes using the SPH method. Comput Method Appl M 2018;341:163–87.
[155] Patankar S. Numerical heat transfer and fluid flow. New York: Hemisphere Publishing; 1982.
[156] Kumar A, Zhang W, DebRoy T. Improving reliability of modelling heat and fluid flow in complex gas metal arc fillet welds—part I: an engineering physics model. J Phys D Appl Phys 2004;38:119.

[157] Hillston J. Model validation and verification. Edinburgh: University of Edinburgh; 2003.
[158] Bandyopadhyay A, Traxel KD. Invited review article: Metal-additive manufacturing-Modeling strategies for application-optimized designs. Addit Manuf 2018;22:758–74.
[159] du Plessis A, Sperling P, Beerlink A, Tshabalala L, Hoosain S, Mathe N, et al. Standard method for microCT-based additive manufacturing quality control 2: density measurement. MethodsX 2018:1117–23.
[160] du Plessis A. Effects of process parameters on porosity in laser powder bed fusion revealed by X-ray tomography. Addit Manuf 2019;30:100871.
[161] Lia F, Park JZ, Keist JS, Joshi S, Martukanitz RP. Thermal and microstructural analysis of laser-based directed energy deposition for Ti-6Al-4V and Inconel 625 deposits. Mater Sci Eng A 2018;717:1–10.
[162] Rodriguez E, Mireles J, Terrazas CA, Espalin D, Perez MA, Wicker RB. Approximation of absolute surface temperature measurements of powder bed fusion additive manufacturing technology using in situ infrared thermography. Addit Manuf 2015;5:31–9.
[163] Bartlett JL, Heim FM, Murty YV, Li X. In situ defect detection in selective laser melting via full-field infrared thermography. Addit Manuf 2018;24:595–605.
[164] Lu Y, Sun G, Xiao X, Mazumder J. Online stress measurement during laser-aided metallic additive manufacturing. Sci Rep 2019:7630.
[165] Heigel J, Michaleris P, Reutzel E. Thermo-mechanical model development and validation of directed energy deposition additive manufacturing of Ti–6Al–4V. Addit Manuf 2015;5:9–19.
[166] Elmer J, Palmer T, Zhang W, DebRoy T. Time resolved X-ray diffraction observations of phase transformations in transient arc welds. Sci Technol Weld Join 2008;13:265–77.
[167] Leung CLA, Marussi S, Atwood RC, Towrie M, Withers PJ, Lee PD. In situ X-ray imaging of defect and molten pool dynamics in laser additive manufacturing. Nat Commun 2018;9:1355.
[168] Hocine Samy, Van Swygenhoven Helena, Van Petegem Steven, Chang Cynthia Sin Ting, Maimaitiyili Tuerdi, Tinti Gemma, Ferreira Sanchez Dario, Grolimund Daniel, Casati Nicola. Operando X-ray diffraction during laser 3D printing. Mater Today 2020;34:30–40. https://doi.org/10.1016/j.mattod.2019.10.001.
[169] Kenel C, Grolimund D, Li X, Panepucci E, Samson VA, Sanchez DF, et al. In situ investigation of phase transformations in Ti-6Al-4V under additive manufacturing conditions combining laser melting and high-speed micro-X-ray diffraction. Sci Rep 2017;7:16358.
[170] Simonds BJ, Sowards J, Hadler J, Pfeif E, Wilthan B, Tanner J, et al. Time-resolved absorptance and melt pool dynamics during intense laser irradiation of a metal. Phys Rev Appl 2018;10:044061.
[171] Levine L, Stoudt M, Lane B. A preview of the NIST/TMS additive manufacturing benchmark test and conference series. JOM 2018;70:259–60.
[172] Zhou J, Zhang Y, Chen J. Numerical simulation of random packing of spherical particles for powder-based additive manufacturing. J Manuf Sci Eng 2009;131:031004.
[173] Kovaleva I, Kovalev O, Smurov I. Model of heat and mass transfer in random packing layer of powder particles in selective laser melting. Phys Proc 2014;56:400–10.
[174] Mindt HW, Megahed M, Lavery NP, Holmes MA, Brown SGR. Powder bed layer characteristics: the overseen first-order process input. Metall Mater Trans A 2016;47:3811–22.
[175] Lee YS, Nandwana P, Zhang W. Dynamic simulation of powder packing structure for powder bed additive manufacturing. Int J Adv Manuf Tech 2018;96:1507–20.
[176] Gu D, Xia M, Dai D. On the role of powder flow behavior in fluid thermodynamics and laser processability of Ni-based composites by selective laser melting. Int J Mach Tools Manuf 2019;137:67–78.
[177] Yan W, Qian Y, Ge W, Lin S, Liu WK, Lin F, et al. Meso-scale modeling of multiple-layer fabrication process in Selective Electron Beam Melting: Inter-layer/track voids formation. Mater Des 2018;141:210–9.
[178] Parteli EJR, Pöschel T. Particle-based simulation of powder application in additive manufacturing. Powder Technol 2016;288:96–102.
[179] Haeri S, Wang Y, Ghita O, Sun J. Discrete element simulation and experimental study of powder spreading process in additive manufacturing. Powder Technol 2017;306:45–54.
[180] Cundall PA, Strack OD. A discrete numerical model for granular assemblies. Geotechnique 1979;29:47–65.
[181] Kozicki J, Donzé F. A new open-source software developed for numerical simulations using discrete modeling methods. Comput Method Appl M 2008;197:4429–43.
[182] Matthews MJ, Guss G, Khairallah SA, Rubenchik AM, Depond PJ, King WE. Denudation of metal powder layers in laser powder bed fusion processes. Acta Mater 2016;114:33–42.
[183] Gürtler FJ, Karg M, Leitz KH, Schmidt M. Simulation of laser beam melting of steel powders using the three-dimensional volume of fluid method. Phys Proc 2013;41:881–6.
[184] Tang C, Tan JL, Wong CH. A numerical investigation on the physical mechanisms of single track defects in selective laser melting. Int J Heat Mass Tran 2018;126:957–68.
[185] Wang Z, Yan W, Liu WK, Liu M. Powder-scale multi-physics modeling of multi-layer multi-track selective laser melting with sharp interface capturing method. Comput Mech 2019;63:649–61.
[186] Wei HL, Cao Y, Liao WH, Liu TT. Mechanisms on inter-track void formation and phase transformation during laser powder bed fusion of Ti-6Al-4V. Addit Manuf 2020;34:101221.
[187] Rausch AM, Küng VE, Pobel C, Markl M, Körner C. Predictive simulation of process windows for powder bed fusion additive manufacturing: influence of the powder bulk density. Materials 2017;10:1117.
[188] Ammer R, Markl M, Ljungblad U, Körner C, Rüde U. Simulating fast electron beam melting with a parallel thermal free surface lattice Boltzmann method. Comput Math Appl 2014;67:318–30.
[189] Yan W, Ge W, Qian Y, Lin S, Zhou B, Liu WK, et al. Multi-physics modeling of single/multiple-track defect mechanisms in electron beam selective melting. Acta Mater 2017;134:324–33.
[190] Wei P, Wei Z, Chen Z, He Y, Du J. Thermal behavior in single track during selective laser melting of AlSi10Mg powder. Appl Phys A 2017;123.
[191] Xia M, Gu D, Yu G, Dai D, Chen H, Shi Q. Porosity evolution and its thermodynamic mechanism of randomly packed powder-bed during selective laser melting of Inconel 718 alloy. Int J Mach Tools Manuf 2017;116:96–106.
[192] Shrestha S, Chou K. Mesoscopic multilayer simulation of selective laser melting process. In: Annual international solid freeform fabrication symposium; 2017.
[193] Zhang T, Li H, Liu S, Shen S, Xie H, Shi W, et al. Evolution of molten pool during selective laser melting of Ti–6Al–4V. J Phys D Appl Phys 2019;52:055302.
[194] Panwisawas C, Qiu C, Anderson MJ, Sovani Y, Turner RP, Attallah MM, et al. Mesoscale modelling of selective laser melting: thermal fluid dynamics and microstructural evolution. Comp Mater Sci 2017;126:479–90.
[195] Bauereiß A, Scharowsky T, Körner C. Defect generation and propagation mechanism during additive manufacturing by selective beam melting. J Mater Process Tech 2014;214:2522–8.
[196] Xia M, Gu D, Yu G, Dai D, Chen H, Shi Q. Influence of hatch spacing on heat and mass transfer, thermodynamics and laser processability during additive manufacturing of Inconel 718 alloy. Int J Mach Tools Manuf 2016;109:147–57.
[197] Yu G, Gu D, Dai D, Xia M, Ma C, Shi Q. On the role of processing parameters in thermal behavior, surface morphology and accuracy during laser 3D printing of aluminum alloy. J Phys D Appl Phys 2016;49:135501.
[198] Konrad C, Zhang Y, Shi Y. Melting and resolidification of a subcooled metal powder particle subjected to nanosecond laser heating. Int J Heat Mass Tran 2007;50:2236–45.
[199] Konrad C, Zhang Y, Xiao B. Analysis of melting and resolidification in a two-component metal powder bed subjected to temporal Gaussian heat flux. Int J Heat Mass Tran 2005;48:3932–44.
[200] Xiao B, Zhang Y. Analysis of partial melting in metal powder bed with constant heat flux. Heat Transfer Eng 2007;28:472–83.
[201] Xiao B, Zhang Y. Analysis of melting of alloy powder bed with constant heat flux. Int J Heat Mass Tran 2007;50:2161–9.
[202] Zhang Y, Faghri A. Melting of a subcooled mixed powder bed with constant heat flux heating. Int J Heat Mass Tran 1999;42:775–88.

[203] Korzekwa DA. Truchas – a multi-physics tool for casting simulation. Int J Cast Metal Res 2009;22:187–91.
[204] Raghavan N, Dehoff R, Pannala S, Simunovic S, Kirka M, Turner J, et al. Numerical modeling of heat-transfer and the influence of process parameters on tailoring the grain morphology of IN718 in electron beam additive manufacturing. Acta Mater 2016;112:303–14.
[205] Raghavan N, Simunovic S, Dehoff R, Plotkowski A, Turner J, Kirka M, et al. Localized melt-scan strategy for site specific control of grain size and primary dendrite arm spacing in electron beam additive manufacturing. Acta Mater 2017;140:375–87.
[206] Gu D, Dai D. Role of melt behavior in modifying oxidation distribution using an interface incorporated model in selective laser melting of aluminum-based material. J Appl Phys 2016;120:083104.
[207] Dai D, Gu D. Tailoring surface quality through mass and momentum transfer modeling using a volume of fluid method in selective laser melting of TiC/AlSi10Mg powder. Int J Mach Tools Manuf 2015;88:95–107.
[208] Bertoli US, Guss G, Wu S, Matthews MJ, Schoenung JM. In-situ characterization of laser-powder interaction and cooling rates through high-speed imaging of powder bed fusion additive manufacturing. Mater Des 2017;135:385–96.
[209] Loh L-E, Chua C-K, Yeong W-Y, Song J, Mapar M, Sing S-L, et al. Numerical investigation and an effective modelling on the Selective Laser Melting (SLM) process with aluminium alloy 6061. Int J Heat Mass Tran 2015;80:288–300.
[210] Masoomi M, Pegues JW, Thompson SM, Shamsaei N. A numerical and experimental investigation of convective heat transfer during laser-powder bed fusion. Addit Manuf 2018;22:729–45.
[211] Parry L, Ashcroft I, Wildman RD. Understanding the effect of laser scan strategy on residual stress in selective laser melting through thermo-mechanical simulation. Addit Manuf 2016;12:1–15.
[212] Li Y, Gu D. Parametric analysis of thermal behavior during selective laser melting additive manufacturing of aluminum alloy powder. Mater Des 2014;63:856–67.
[213] Gu D, He B. Finite element simulation and experimental investigation of residual stresses in selective laser melted Ti–Ni shape memory alloy. Comp Mater Sci 2016;117:221–32.
[214] Cheng B, Price S, Lydon J, Cooper K, Chou K. On process temperature in powder-bed electron beam additive manufacturing: model development and validation. J Manuf Sci Eng 2014;136:061018.
[215] Mukherjee T, DebRoy T. Mitigation of lack of fusion defects in powder bed fusion additive manufacturing. J Manuf Process 2018;36:442–9.
[216] Jamshidinia M, Kong F, Kovacevic R. Numerical modeling of heat distribution in the electron beam melting® of Ti-6Al-4V. J Manuf Sci Eng 2013;135:061010.
[217] Wu J, Zhao P, Wei H, Lin Q, Zhang Y. Development of powder distribution model of discontinuous coaxial powder stream in laser direct metal deposition. Powder Technol 2018;340:449–58.
[218] Wen SY, Shin YC, Murthy JY, Sojka PE. Modeling of coaxial powder flow for the laser direct deposition process. Int J Heat Mass Tran 2009;52:5867–77.
[219] Haley JC, Schoenung JM, Lavernia EJ. Observations of particle-melt pool impact events in directed energy deposition. Addit Manuf 2018;22:368–74.
[220] Wirth F, Wegener K. A physical modeling and predictive simulation of the laser cladding process. Addit Manuf 2018;22:307–19.
[221] Nie P, Ojo OA, Li Z. Modeling analysis of laser cladding of a nickel-based superalloy. Surf Coat Technol 2014;258:1048–59.
[222] Zekovic S, Dwivedi R, Kovacevic R. Numerical simulation and experimental investigation of gas–powder flow from radially symmetrical nozzles in laser-based direct metal deposition. Int J Mach Tools Manuf 2007;47:112–23.
[223] Bedenko DV, Kovalev OB, Smurov I, Zaitsev AV. Numerical simulation of transport phenomena, formation the bead and thermal behavior in application to industrial DMD technology. Int J Heat Mass Tran 2016;95:902–12.
[224] Tabernero I, Lamikiz A, Ukar E, López de Lacalle LN, Angulo C, Urbikain G. Numerical simulation and experimental validation of powder flux distribution in coaxial laser cladding. J Mater Process Tech 2010;210:2125–34.
[225] Pinkerton AJ, Li L. Modelling powder concentration distribution from a coaxial deposition nozzle for laser-based rapid tooling. J Manuf Sci Eng 2004;126:33–41.
[226] Pinkerton AJ. An analytical model of beam attenuation and powder heating during coaxial laser direct metal deposition. J Phys D Appl Phys 2007;40:7323–34.
[227] Liu Z, Qi H, Jiang L. Control of crystal orientation and continuous growth through inclination of coaxial nozzle in laser powder deposition of single-crystal superalloy. J Mater Process Tech 2016;230:177–86.
[228] Wen S, Shin YC. Modeling of transport phenomena during the coaxial laser direct deposition process. J Appl Phys 2010;108:044908.
[229] Balu P, Leggett P, Kovacevic R. Parametric study on a coaxial multi-material powder flow in laser-based powder deposition process. J Mater Process Tech 2012;212:1598–610.
[230] Ibarra-Medina J, Pinkerton AJ. Numerical investigation of powder heating in coaxial laser metal deposition. Surf Eng 2013;27:754–61.
[231] Katinas C, Liu S, Shin YC. Self-sufficient modeling of single track deposition of Ti–6Al–4V with the prediction of capture efficiency. J Manuf Sci Eng 2019;141:011001.
[232] Kovalev OB, Zaitsev AV, Novichenko D, Smurov I. Theoretical and experimental investigation of gas flows, powder transport and heating in coaxial laser direct metal deposition (DMD) process. J Therm Spray Techn 2010;20:465–78.
[233] Wirth F, Arpagaus S, Wegener K. Analysis of melt pool dynamics in laser cladding and direct metal deposition by automated high-speed camera image evaluation. Addit Manuf 2018;21:369–82.
[234] Zhang A, Li D, Zhou Z, Zhu G, Lu B. Numerical simulation of powder flow field on coaxial powder nozzle in laser metal direct manufacturing. Int J Adv Manuf Tech 2010;49:853–9.
[235] Tan H, Shang W, Zhang F, Clare AT, Lin X, Chen J, et al. Process mechanisms based on powder flow spatial distribution in direct metal deposition. J Mater Process Tech 2018;254:361–72.
[236] Huang Y, Khamesee MB, Toyserkani E. A comprehensive analytical model for laser powder-fed additive manufacturing. Addit Manuf 2016;12:90–9.
[237] Yang N. Concentration model based on movement model of powder flow in coaxial laser cladding. Opt Laser Technol 2009;41:94–8.
[238] Ibarra-Medina J, Pinkerton AJ, Vogel M, N'Dri N. Transient modelling of laser deposited coatings. 26th international conference on surface modification technologies. 2012.
[239] Ibarra-Medina J, Vogel M, Pinkerton AJ. A CFD model of laser cladding: from deposition head to melt pool dynamics; 2011. p. 378–86.
[240] Wen S, Shin YC. Comprehensive predictive modeling and parametric analysis of multitrack direct laser deposition processes. J Laser Appl 2011;23:022003.
[241] Pinkerton AJ. Advances in the modeling of laser direct metal deposition. J Laser Appl 2015;27:S15001.
[242] Han L, Phatak KM, Liou FW. Modeling of laser cladding with powder injection. Metall Mater Trans B 2004;35:1139–50.
[243] Wen S, Shin YC. Modeling of transport phenomena in direct laser deposition of metal matrix composite. Int J Heat Mass Tran 2011;54:5319–26.
[244] Peyre P, Aubry P, Fabbro R, Neveu R, Longuet A. Analytical and numerical modelling of the direct metal deposition laser process. J Phys D Appl Phys 2008;41:025403.
[245] Jouvard JM, Grevey DF, Lemoine F, Vannes AB. Continuous wave Nd:YAG laser cladding modeling: a physical study of track creation during low power processing. J Laser Appl 1997;9:43–50.
[246] Tan H, Zhang F, Fu X, Meng J, Hu G, Fan W, et al. Development of powder flow model of laser solid forming by analysis method. Int J Adv Manuf Tech 2015;82:1421–31.
[247] Gan Z, Yu G, He X, Li S. Surface-active element transport and its effect on liquid metal flow in laser-assisted additive manufacturing. Int Commun Heat Mass 2017;86:206–14.
[248] Wei HL, Mazumder J, DebRoy T. Evolution of solidification texture during additive manufacturing. Sci Rep 2015;5.
[249] Wei HL, Liu FQ, Liao WH, Liu TT. Prediction of spatiotemporal variations of deposit profiles and inter-track voids during laser directed energy deposition. Addit Manuf 2020;34:101219.
[250] Netfabb®. AutoDesk Inc.; 2018.
[251] Virfac®. GeonX; 2018.
[252] Lee Y, Farson DF. Simulation of transport phenomena and melt pool shape for multiple layer additive manufacturing. J Laser Appl 2016;28:012006.

[253] He X, Mazumder J. Transport phenomena during direct metal deposition. J Appl Phys 2007;101:053113.
[254] Tan W, Wen S, Bailey N, Shin YC. Multiscale modeling of transport phenomena and dendritic growth in laser cladding processes. Metall Mater Trans B 2011;42:1306–18.
[255] Morville S, Carin M, Peyre P, Gharbi M, Carron D, Le Masson P, et al. 2D longitudinal modeling of heat transfer and fluid flow during multilayered direct laser metal deposition process. J Laser Appl 2012;24:032008.
[256] Yang Z, Elmer J, Wong J, DebRoy T. Evolution of titanium arc weldment macro and microstructures-modeling and real time mapping of phases. Weld J 2000;79:97s–111s.
[257] Wei S, Wang G, Shin YC, Rong Y. Comprehensive modeling of transport phenomena in laser hot-wire deposition process. Int J Heat Mass Tran 2018;125:1356–68.
[258] Fan HG, Kovacevic R. Dynamic analysis of globular metal transfer in gas metal arc welding - a comparison of numerical and experimental results. J Phys D Appl Phys 1998;31:2929.
[259] Fan HG, Kovacevic R. A unified model of transport phenomena in gas metal arc welding including electrode, arc plasma and molten pool. J Phys D Appl Phys 2004;37:2531.
[260] Ding J, Colegrove P, Mehnen J, Ganguly S, Sequeira Almeida PM, Wang F, et al. Thermo-mechanical analysis of Wire and Arc Additive Layer Manufacturing process on large multi-layer parts. Comp Mater Sci 2011;50:3315–22.
[261] Ding D, Pan Z, Cuiuri D, Li H. A multi-bead overlapping model for robotic wire and arc additive manufacturing (WAAM). Robot Cim-int Manuf 2015;31:101–10.
[262] Tang Q, Pang S, Chen B, Suo H, Zhou J. A three dimensional transient model for heat transfer and fluid flow of weld pool during electron beam freeform fabrication of Ti-6-Al-4-V alloy. Int J Heat Mass Tran 2014;78:203–15.
[263] Bai X, Zhang H, Wang G. Improving prediction accuracy of thermal analysis for weld-based additive manufacturing by calibrating input parameters using IR imaging. Int J Adv Manuf Tech 2013;69:1087–95.
[264] Zhou X, Zhang H, Wang G, Bai X. Three-dimensional numerical simulation of arc and metal transport in arc welding based additive manufacturing. Int J Heat Mass Tran 2016;103:521–37.
[265] Graf M, Pradjadhiana K, Hälsig A, Manurung YHP, Awiszus B. Numerical simulation of metallic wire arc additive manufacturing (WAAM). In: AIP conference proceedings; 2018. p. 140010.
[266] Neela V, De A. Three-dimensional heat transfer analysis of LENSTM process using finite element method. Int J Adv Manuf Tech 2009;45:935–43.
[267] Brown D, Li C, Liu Z, Fang X, Guo Y. Surface integrity of Inconel 718 by hybrid selective laser melting and milling. Virt Phys Prototyp 2018;13:26–31.
[268] Zhang S, Zhang Y, Gao M, Wang F, Li Q, Zeng X. Effects of milling thickness on wire deposition accuracy of hybrid additive/subtractive manufacturing. Sci Technol Weld Join 2019;24:375–81.
[269] Ambrogio G, Gagliardi F, Muzzupappa M, Filice L. Additive-incremental forming hybrid manufacturing technique to improve customised part performance. J Manuf Process 2019;37:386–91.
[270] Eisenbarth D, Soffel F, Wegener K. Effects of direct metal deposition combined with intermediate and final milling on part distortion. Virt Phys Prototyp 2019;14:130–4.
[271] Ma M, Wang Z, Zeng X. A comparison on metallurgical behaviors of 316L stainless steel by selective laser melting and laser cladding deposition. Mater Sci Eng A 2017;685:265–73.
[272] Mukherjee T, Manvatkar V, De A, DebRoy T. Dimensionless numbers in additive manufacturing. J Appl Phys 2017;121:064904.
[273] Zhang K, Wang S, Liu W, Shang X. Characterization of stainless steel parts by laser metal deposition shaping. Mater Des 2014;55:104–19.
[274] Bennett JL, Wolff SJ, Hyatt G, Ehmann K, Cao J. Thermal effect on clad dimension for laser deposited Inconel 718. J Manuf Process 2017;28:550–7.
[275] Wolff SJ, Lin S, Faierson EJ, Liu WK, Wagner GJ, Cao J. A framework to link localized cooling and properties of directed energy deposition (DED)-processed Ti-6Al-4V. Acta Mater 2017;132:106–17.
[276] Chen X, Li J, Cheng X, He B, Wang H, Huang Z. Microstructure and mechanical properties of the austenitic stainless steel 316L fabricated by gas metal arc additive manufacturing. Mater Sci Eng A 2017;703:567–77.
[277] Yadollahi A, Shamsaei N, Thompson SM, Seely DW. Effects of process time interval and heat treatment on the mechanical and microstructural properties of direct laser deposited 316L stainless steel. Mater Sci Eng A 2015;644:171–83.
[278] Gray GT, Livescu V, Rigg PA, Trujillo CP, Cady CM, Chen SR, et al. Structure/property (constitutive and spallation response) of additively manufactured 316L stainless steel. Acta Mater 2017;138:140–9.
[279] Kruth J-P, Badrossamay M, Yasa E, Deckers J, Thijs L, Van Humbeeck J. Part and material properties in selective laser melting of metals. Proceedings of the 16th international symposium on electromachining. 2010.
[280] Wang X, Deng D, Yi H, Xu H, Yang S, Zhang H. Influences of pulse laser parameters on properties of AISI316L stainless steel thin-walled part by laser material deposition. Opt Laser Technol 2017;92:5–14.
[281] Rodriguez N, Vázquez L, Huarte I, Arruti E, Tabernero I, Alvarez P. Wire and arc additive manufacturing: a comparison between CMT and TopTIG processes applied to stainless steel. Weld World 2018;62:1083–96.
[282] Caiazzo F, Alfieri V. Laser-aided directed energy deposition of steel powder over flat surfaces and edges. Materials 2018;11:15.
[283] Mukherjee T, DebRoy T. Printability of 316 stainless steel. Sci Technol Weld Join 2019:1–8.
[284] Wei HL, Knapp GL, Mukherjee T, DebRoy T. Three-dimensional grain growth during multi-layer printing of a nickel-based alloy Inconel 718. Addit Manuf 2019;25:448–59.
[285] Zhao L, Tsukamoto S, Arakane G, Sugino T, DebRoy T. Influence of oxygen on weld geometry in fibre laser and fibre laser–GMA hybrid welding. Sci Technol Weld Join 2011;16:166–73.
[286] Mishra S, Lienert T, Johnson M, DebRoy T. An experimental and theoretical study of gas tungsten arc welding of stainless steel plates with different sulfur concentrations. Acta Mater 2008;56:2133–46.
[287] Wei HL, Pal S, Manvatkar V, Lienert TJ, DebRoy T. Asymmetry in steel welds with dissimilar amounts of sulfur. Scripta Mater 2015;108:88–91.
[288] Arora A, Roy GG, DebRoy T. Unusual wavy weld pool boundary from dimensional analysis. Scripta Mater 2009;60:68–71.
[289] Aucott L, Dong H, Mirihanage W, Atwood R, Kidess A, Gao S, et al. Revealing internal flow behaviour in arc welding and additive manufacturing of metals. Nat Commun 2018;9:5414.
[290] Arrizubieta JI, Lamikiz A, Klocke F, Martínez S, Arntz K, Ukar E. Evaluation of the relevance of melt pool dynamics in Laser Material Deposition process modeling. Int J Heat Mass Tran 2017;115:80–91.
[291] Plotkowski A, Kirka MM, Babu SS. Verification and validation of a rapid heat transfer calculation methodology for transient melt pool solidification conditions in powder bed metal additive manufacturing. Addit Manuf 2017;18:256–68.
[292] Song J, Chew Y, Bi G, Yao X, Zhang B, Bai J, et al. Numerical and experimental study of laser aided additive manufacturing for melt-pool profile and grain orientation analysis. Mater Des 2018;137:286–97.
[293] Lin X, Yue T, Yang H, Huang W. Solidification behavior and the evolution of phase in laser rapid forming of graded Ti6Al4V-Rene88DT alloy. Metall Mater Trans A 2007;38:127–37.
[294] Bobbio LD, Bocklund B, Otis R, Borgonia JP, Dillon RP, Shapiro AA, et al. Experimental analysis and thermodynamic calculations of an additively manufactured functionally graded material of V to Invar 36. J Mater Res 2018;33:1642–9.
[295] Bobbio LD, Bocklund B, Otis R, Borgonia JP, Dillon RP, Shapiro AA, et al. Characterization of a functionally graded material of Ti-6Al-4V to 304L stainless steel with an intermediate V section. J Alloy Comp 2018;742:1031–6.
[296] Kirk T, Galvan E, Malak R, Arroyave R. Computational design of gradient paths in additively manufactured functionally graded materials. J Mech Des 2018;140:111410.
[297] Tan C, Zhou K, Kuang T. Selective laser melting of tungsten-copper functionally graded material. Mater Lett 2019;237:328–31.

[298] Acharya R, Sharon JA, Staroselsky A. Prediction of microstructure in laser powder bed fusion process. Acta Mater 2017;124:360–71.
[299] Nie P, Ojo OA, Li Z. Numerical modeling of microstructure evolution during laser additive manufacturing of a nickel-based superalloy. Acta Mater 2014;77:85–95.
[300] Hu X, Nycz A, Lee Y, Shassere B, Simunovic S, Noakes M, et al. Towards an integrated experimental and computational framework for large-scale metal additive manufacturing. Mater Sci Eng A 2019;761:138057.
[301] Zhang Z, Tan ZJ, Yao XX, Hu CP, Ge P, Wan ZY, et al. Numerical methods for microstructural evolutions in laser additive manufacturing. Comput Math Appl 2019;78:2296–307.
[302] Yang YP, Jamshidinia M, Boulware P, Kelly SM. Prediction of microstructure, residual stress, and deformation in laser powder bed fusion process. Comput Mech 2018;61:599–615.
[303] Shi R, Khairallah S, Heo TW, Rolchigo M, McKeown JT, Matthews MJ. Integrated simulation framework for additively manufactured Ti-6Al-4V: melt pool dynamics, microstructure, solid-state phase transformation, and microelastic response. JOM 2019;71:3640–55.
[304] Sahoo S, Chou K. Phase-field simulation of microstructure evolution of Ti–6Al–4V in electron beam additive manufacturing process. Addit Manuf 2016;9:14–24.
[305] Koepf JA, Gotterbarm MR, Markl M, Körner C. 3D multi-layer grain structure simulation of powder bed fusion additive manufacturing. Acta Mater 2018;152:119–26.
[306] Wei HL, Elmer JW, DebRoy T. Crystal growth during keyhole mode laser welding. Acta Mater 2017;133:10–20.
[307] Wei HL, Elmer JW, DebRoy T. Three-dimensional modeling of grain structure evolution during welding of an aluminum alloy. Acta Mater 2017;126:413–25.
[308] Martin JH, Yahata BD, Hundley JM, Mayer JA, Schaedler TA, Pollock TM. 3D printing of high-strength aluminium alloys. Nature 2017;549:365–9.
[309] Li XP, Ji G, Chen Z, Addad A, Wu Y, Wang HW, et al. Selective laser melting of nano-TiB2 decorated AlSi10Mg alloy with high fracture strength and ductility. Acta Mater 2017;129:183–93.
[310] Gaumann M, Bezencon C, Canalis P, Kurz W. Single-crystal laser deposition of superalloys: processing-microstructure maps. Acta Mater 2001;49:1051–62.
[311] Liu P, Wang Z, Xiao Y, Horstemeyer MF, Cui X, Chen L. Insight into the mechanisms of columnar to equiaxed grain transition during metallic additive manufacturing. Addit Manuf 2019;26:22–9.
[312] Rappaz M, Gandin CA. Probabilistic modeling of microstructure formation in solidification processes. Acta Metall Mater 1993;41:345–60.
[313] Li X, Tan W. Numerical investigation of effects of nucleation mechanisms on grain structure in metal additive manufacturing. Comp Mater Sci 2018;153:159–69.
[314] Rappaz M, Gandin CA, Desbiolles JL, Thevoz P. Prediction of grain structures in various solidification processes. Metall Mater Trans A 1996;27:695–705.
[315] Wei HL, Elmer JW, DebRoy T. Origin of grain orientation during solidification of an aluminum alloy. Acta Mater 2016;115:123–31.
[316] Antonysamy AA, Meyer J, Prangnell PB. Effect of build geometry on the β-grain structure and texture in additive manufacture of Ti6Al4V by selective electron beam melting. Mater Charact 2013;84:153–68.
[317] Wang D, Song C, Yang Y, Bai Y. Investigation of crystal growth mechanism during selective laser melting and mechanical property characterization of 316L stainless steel parts. Mater Des 2016;100:291–9.
[318] Thijs L, Kempen K, Kruth J-P, Van Humbeeck J. Fine-structured aluminium products with controllable texture by selective laser melting of pre-alloyed AlSi10Mg powder. Acta Mater 2013;61:1809–19.
[319] Todaro CJ, Easton MA, Qiu D, Zhang D, Bermingham MJ, Lui EW, et al. Grain structure control during metal 3D printing by high-intensity ultrasound. Nat Commun 2020;11:142.
[320] Anderson TD, DuPont JN, DebRoy T. Origin of stray grain formation in single-crystal superalloy weld pools from heat transfer and fluid flow modeling. Acta Mater 2010;58:1441–54.
[321] Acharya R, Bansal R, Gambone JJ, Das S. A coupled thermal, fluid flow, and solidification model for the processing of single-crystal alloy CMSX-4 through scanning laser epitaxy for turbine engine hot-section component repair (Part I). Metall Mater Trans B 2014;45:2247–61.
[322] Wang L, Wang N, Yao WJ, Zheng YP. Effect of substrate orientation on the columnar-to-equiaxed transition in laser surface remelted single crystal superalloys. Acta Mater 2015;88:283–92.
[323] Liu Z, Qi H. Effects of substrate crystallographic orientations on crystal growth and microstructure formation in laser powder deposition of nickel-based superalloy. Acta Mater 2015;87:248–58.
[324] Helmer H, Bauereiß A, Singer RF, Körner C. Grain structure evolution in Inconel 718 during selective electron beam melting. Mater Sci Eng A 2016;668:180–7.
[325] Spierings AB, Dawson K, Heeling T, Uggowitzer PJ, Schäublin R, Palm F, et al. Microstructural features of Sc- and Zr-modified Al-Mg alloys processed by selective laser melting. Mater Des 2017;115:52–63.
[326] Croteau JR, Griffiths S, Rossell MD, Leinenbach C, Kenel C, Jansen V, et al. Microstructure and mechanical properties of Al-Mg-Zr alloys processed by selective laser melting. Acta Mater 2018;153:35–44.
[327] Spierings AB, Dawson K, Voegtlin M, Palm F, Uggowitzer PJ. Microstructure and mechanical properties of as-processed scandium-modified aluminium using selective laser melting. CIRP Ann 2016;65:213–6.
[328] Spierings AB, Dawson K, Dumitraschkewitz P, Pogatscher S, Wegener K. Microstructure characterization of SLM-processed Al-Mg-Sc-Zr alloy in the heat treated and HIPed condition. Addit Manuf 2018;20:173–81.
[329] Griffiths S, Rossell MD, Croteau J, Vo NQ, Dunand DC, Leinenbach C. Effect of laser rescanning on the grain microstructure of a selective laser melted Al-Mg-Zr alloy. Mater Charact 2018;143:34–42.
[330] Griffiths S, Croteau JR, Rossell MD, Erni R, De Luca A, Vo NQ, et al. Coarsening- and creep resistance of precipitation-strengthened Al–Mg–Zr alloys processed by selective laser melting. Acta Mater 2020;188:192–202.
[331] Montero Sistiaga ML, Mertens R, Vrancken B, Wang X, Van Hooreweder B, Kruth J-P, et al. Changing the alloy composition of Al7075 for better processability by selective laser melting. J Mater Process Tech 2016;238:437–45.
[332] Parimi LL, A RG, Clark D, Attallah MM. Microstructural and texture development in direct laser fabricated IN718. Mater Charact 2014;89:102–11.
[333] Ren YM, Lin X, Fu X, Tan H, Chen J, Huang WD. Microstructure and deformation behavior of Ti-6Al-4V alloy by high-power laser solid forming. Acta Mater 2017;132:82–95.
[334] Manvatkar VD, Gokhale AA, Jagan Reddy G, Venkataramana A, De A. Estimation of melt pool dimensions, thermal cycle, and hardness distribution in the laser-engineered net shaping process of austenitic stainless steel. Metall Mater Trans A 2011;42:4080–7.
[335] Zheng B, Zhou Y, Smugeresky J, Schoenung J, Lavernia E. Thermal behavior and microstructure evolution during laser deposition with laser-engineered net shaping: part II. Experimental investigation and discussion. Metall Mater Trans A 2008;39:2237–45.
[336] Radhakrishnan B, Gorti SB, Babu SS. Large scale phase field simulations of microstructure evolution during thermal cycling of Ti-6Al-4V. Oak Ridge National Lab, Joint Institute for Computational Sciences; 2015.
[337] Prabhu A, Vincent T, Chaudhary A, Zhang W, Babu S. Effect of microstructure and defects on fatigue behaviour of directed energy deposited Ti–6Al–4V. Sci Technol Weld Join 2015;20:659–69.
[338] Zhou N, Lv D, Zhang H, McAllister D, Zhang F, Mills M, et al. Computer simulation of phase transformation and plastic deformation in IN718 superalloy: microstructural evolution during precipitation. Acta Mater 2014;65:270–86.
[339] Zhang W, Elmer JW, DebRoy T. Modeling and real time mapping of phases during GTA welding of 1005 steel. Mater Sci Eng A 2002;333:320–35.
[340] Liu F, Lin X, Song M, Yang H, Zhang Y, Wang L, et al. Microstructure and mechanical properties of laser solid formed 300M steel. J Alloy Comp 2015;621:35–41.
[341] Ge J, Lin J, Lei Y, Fu H. Location-related thermal history, microstructure, and mechanical properties of arc additively manufactured 2Cr13 steel using cold metal transfer welding. Mater Sci Eng A 2018;715:144–53.
[342] Zhang W, Elmer J, DebRoy T. Integrated modelling of thermal cycles, austenite formation, grain growth and decomposition in the heat affected zone of carbon steel. Sci Technol Weld Join 2005;10:574–82.
[343] Yan C, Hao L, Hussein A, Young P, Huang J, Zhu W. Microstructure and mechanical properties of aluminium alloy cellular lattice structures manufactured by

direct metal laser sintering. Mater Sci Eng A 2015;628:238–46.

[344] Bhadeshia H. Thermodynamic analysis of isothermal transformation diagrams. Metal Sci 1982;16:159–66.

[345] Bhadeshia H, Svensson L-E, Gretoft B. A model for the development of microstructure in low-alloy steel (Fe-Mn-Si-C) weld deposits. Acta Metall 1985;33:1271–83.

[346] Bhadeshia H, Svensson L. Modelling the evolution of microstructure in steel weld metal. Math Model Weld Phenomena 1993;1(109):82.

[347] Russell K. Linked flux analysis of nucleation in condensed phases. Acta Metall 1968;16:761–9.

[348] Wei HL, Blecher JJ, Palmer TA, Debroy T. Fusion zone microstructure and geometry in complete-joint-penetration laser-arc hybrid welding of low-alloy steel. Weld J 2015;94:135s–44s.

[349] Yang Y, Jamshidinia M, Boulware P, Kelly S. Prediction of microstructure, residual stress, and deformation in laser powder bed fusion process. Comput Mech 2018:1–17.

[350] Lu Y, Peer A, Abke T, Kimchi M, Zhang W. Subcritical heat affected zone softening in hot-stamped boron steel during resistance spot welding. Mater Des 2018;155:170–84.

[351] Short A. Gas tungsten arc welding of $\alpha+\beta$ titanium alloys: a review. Mater Sci Tech 2009;25:309–24.

[352] Ahmed T, Rack H. Phase transformations during cooling in $\alpha+\beta$ titanium alloys. Mater Sci Eng A 1998;243:206–11.

[353] Qian M, Xu W, Brandt M, Tang HP. Additive manufacturing and postprocessing of Ti-6Al-4V for superior mechanical properties. MRS Bull 2016;41:775–84.

[354] Baykasoglu C, Akyildiz O, Candemir D, Yang Q, To AC. Predicting microstructure evolution during directed energy deposition additive manufacturing of Ti-6Al-4V. J Manuf Sci Eng 2018;140:051003.

[355] Ji Y, Chen L, Chen L-Q. Understanding microstructure evolution during additive manufacturing of metallic alloys using phase-field modeling. Thermo - Mechanical Modeling of Additive Manufacturing: Butterworth-Heinemann; 2018. p. 93–116.

[356] Makiewicz KT. Development of simultaneous transformation kinetics microstructure model with application to laser metal deposited Ti-6Al-4V and alloy 718. The Ohio: State University; 2013.

[357] Lindgren L-E, Lundbäck A, Fisk M, Pederson R, Andersson J. Simulation of additive manufacturing using coupled constitutive and microstructure models. Addit Manuf 2016;12:144–58.

[358] Malinov S, Markovsky P, Sha W. Resistivity study and computer modelling of the isothermal transformation kinetics of Ti–8Al–1Mo–1V alloy. J Alloy Comp 2002;333:122–32.

[359] Mur FG, Rodriguez D, Planell J. Influence of tempering temperature and time on the $\alpha'$-Ti-6Al-4V martensite. J Alloy Comp 1996;234:287–9.

[360] Kelly SM. Thermal and microstructure modeling of metal deposition processes with application to Ti-6Al-4V: Virginia Tech; 2004.

[361] Murgau CC, Pederson R, Lindgren LE. A model for Ti–6Al–4V microstructure evolution for arbitrary temperature changes. Model Simul Mater Sci Eng 2012;20:055006.

[362] Xu W, Brandt M, Sun S, Elambasseril J, Liu Q, Latham K, et al. Additive manufacturing of strong and ductile Ti–6Al–4V by selective laser melting via in situ martensite decomposition. Acta Mater 2015;85:74–84.

[363] Xu W, Lui EW, Pateras A, Qian M, Brandt M. In situ tailoring microstructure in additively manufactured Ti-6Al-4V for superior mechanical performance. Acta Mater 2017;125:390–400.

[364] Amato K, Gaytan S, Murr L, Martinez E, Shindo P, Hernandez J, et al. Microstructures and mechanical behavior of Inconel 718 fabricated by selective laser melting. Acta Mater 2012;60:2229–39.

[365] Tian Y, McAllister D, Colijn H, Mills M, Farson D, Nordin M, et al. Rationalization of microstructure heterogeneity in Inconel 718 builds made by the direct laser additive manufacturing process. Metall Mater Trans A 2014;45:4470–83.

[366] Kumara C, Deng D, Hanning F, Raanes M, Moverare J, Nylén P. Predicting the microstructural evolution of electron beam melting of alloy 718 with phase-field modeling. Metall Mater Trans A 2019;50:2527–37.

[367] Zhang F, Levine LE, Allen AJ, Stoudt MR, Lindwall G, Lass EA, et al. Effect of heat treatment on the microstructural evolution of a nickel-based superalloy additive-manufactured by laser powder bed fusion. Acta Mater 2018;152:200–14.

[368] Ramsperger M, Singer RF, Körner C. Microstructure of the nickel-base superalloy CMSX-4 fabricated by selective electron beam melting. Metall Mater Trans A 2016;47:1469–80.

[369] Murr LE, Martinez E, Pan XM, Gaytan SM, Castro JA, Terrazas CA, et al. Microstructures of Rene 142 nickel-based superalloy fabricated by electron beam melting. Acta Mater 2013;61:4289–96.

[370] Sui S, Tan H, Chen J, Zhong C, Li Z, Fan W, et al. The influence of Laves phases on the room temperature tensile properties of Inconel 718 fabricated by powder feeding laser additive manufacturing. Acta Mater 2019;164:413–27.

[371] Lifshitz IM, Slyozov VV. The kinetics of precipitation from supersaturated solid solutions. J Phys Chem Solids 1961;19:35–50.

[372] Mishra S, DebRoy T. Non-isothermal grain growth in metals and alloys. Mater Sci Tech 2006;22:253–78.

[373] Rodgers TM, Madison JD, Tikare V. Simulation of metal additive manufacturing microstructures using kinetic Monte Carlo. Comp Mater Sci 2017;135:78–89.

[374] Raabe D. Cellular automata in materials science with particular reference to recrystallization simulation. Ann Rev Mater Res 2002;32:53–76.

[375] Donachie MJ, Donachie SJ. Superalloys: a technical guide. 2nd ed. United States of America: ASM International; 2002.

[376] Juechter V, Scharowsky T, Singer RF, Körner C. Processing window and evaporation phenomena for Ti–6Al–4V produced by selective electron beam melting. Acta Mater 2014;76:252–8.

[377] Liu T, Yang LJ, Wei HL, Qiu WC, DebRoy T. Composition change of stainless steels during keyhole mode laser welding. Weld J 2017;96:258s–70s.

[378] Khan P, DebRoy T. Alloying element vaporization and weld pool temperature during laser welding of AlSl 202 stainless steel. Metall Trans B 1984;15:641–4.

[379] Collur M, Debroy T. Emission spectroscopy of plasma during laser welding of AISI 201 stainless steel. Metall Mater Trans B 1989;20:277–86.

[380] He X, DebRoy T, Fuerschbach P. Alloying element vaporization during laser spot welding of stainless steel. J Phys D Appl Phys 2003;36:3079.

[381] He X, DebRoy T, Fuerschbach PW. Probing temperature during laser spot welding from vapor composition and modeling. J Appl Phys 2003;94:6949.

[382] Zhao H, Debroy T. Weld metal composition change during conduction mode laser welding of aluminum alloy 5182. Metall Mater Trans B 2001;32:163–72.

[383] Collur M, Paul A, DebRoy T. Mechanism of alloying element vaporization during laser welding. Metall Trans B 1987;18:733–40.

[384] DebRoy T, Basu S, Mundra K. Probing laser induced metal vaporization by gas dynamics and liquid pool transport phenomena. J Appl Phys 1991;70:1313–9.

[385] Anisimov S, Rakhmatulina AK. The dynamics of the expansion of a vapor when evaporated into a vacuum. Soviet J ExpTheor Phys 1973;37:441–4.

[386] Knight CJ. Theoretical modeling of rapid surface vaporization with back pressure. AIAA J 1979;17:519–23.

[387] Yaws CL, Nijhawan S, Bu L. Appendix C - Coefficients for Vapor Pressure Equation. In: Yaws CL, editor. Handbook of Vapor Pressure: Gulf Professional Publishing; 1995. p. 352–7.

[388] Brice CA, Rosenberger BT, Sankaran SN, Taminger KM, Woods B, Nasserrafi R. Chemistry control in electron beam deposited titanium alloys. Mater Sci Forum 2009:155–8.

[389] Biamino S, Penna A, Ackelid U, Sabbadini S, Tassa O, Fino P, et al. Electron beam melting of Ti–48Al–2Cr–2Nb alloy: microstructure and mechanical properties investigation. Intermetallics 2011;19:776–81.

[390] Taminger K. Electron beam additive manufacturing: state-of-the-technology, challenges & opportunities. Direct digital manufacturing workshop; 2010.

[391] Tang H, Yang G, Jia W, He W, Lu S, Qian M. Additive manufacturing of a high niobium-containing titanium aluminide alloy by selective electron beam melting. Mater Sci Eng A 2015;636:103–7.

[392] Gaytan S, Murr L, Medina F, Martinez E, Lopez M, Wicker R. Advanced metal powder based manufacturing of complex components by electron beam melting. Mater Technol 2009;24:180–90.

[393] Brice C, Shenoy R, Kral M, Buchannan K. Precipitation behavior of aluminum alloy 2139 fabricated using additive manufacturing. Mater Sci Eng A 2015;648:9–14.

[394] Brice CA. Compositional sensitivity in additively manufactured aluminum alloy 2139. University of Canterbury; 2018.

[395] Bai Y, Wagner G, Williams CB. Effect of particle size distribution on powder packing and sintering in binder jetting additive manufacturing of metals. J Manuf

Sci Eng 2017;139:081019.
[396] Dai D, Gu D. Effect of metal vaporization behavior on keyhole-mode surface morphology of selective laser melted composites using different protective atmospheres. Appl Surf Sci 2015;355:310–9.
[397] Wei K, Wang Z, Zeng X. Influence of element vaporization on formability, composition, microstructure, and mechanical performance of the selective laser melted Mg–Zn–Zr components. Mater Lett 2015;156:187–90.
[398] Bidare P, Bitharas I, Ward RM, Attallah MM, Moore AJ. Fluid and particle dynamics in laser powder bed fusion. Acta Mater 2018;142:107–20.
[399] Ly S, Rubenchik AM, Khairallah SA, Guss G, Matthews MJ. Metal vapor micro-jet controls material redistribution in laser powder bed fusion additive manufacturing. Sci Rep 2017;7:4085.
[400] Gunenthiram V, Peyre P, Schneider M, Dal M, Coste F, Koutiri I, et al. Experimental analysis of spatter generation and melt-pool behavior during the powder bed laser beam melting process. J Mater Process Tech 2018;251:376–86.
[401] Basu S, DebRoy T. Liquid metal expulsion during laser irradiation. J Appl Phys 1992;72:3317–22.
[402] Chun M, Rose K. Interaction of high-intensity laser beams with metals. J Appl Phys 1970;41:614–20.
[403] He X, Norris JT, Fuerschbach PW, DebRoy T. Liquid metal expulsion during laser spot welding of 304 stainless steel. J Phys D Appl Phys 2006;39:525–34.
[404] Kaplan AFH, Powell J. Spatter in laser welding. J Laser Appl 2011;23.
[405] Wang D, Wu S, Fu F, Mai S, Yang Y, Liu Y, et al. Mechanisms and characteristics of spatter generation in SLM processing and its effect on the properties. Mater Des 2017;117:121–30.
[406] Simonelli M, Tuck C, Aboulkhair NT, Maskery I, Ashcroft I, Wildman RD, et al. A study on the laser spatter and the oxidation reactions during selective laser melting of 316L stainless steel, Al-Si10-Mg, and Ti-6Al-4V. Metall Mater Trans A 2015;46:3842–51.
[407] Repossini G, Laguzza V, Grasso M, Colosimo BM. On the use of spatter signature for in-situ monitoring of Laser Powder Bed Fusion. Addit Manuf 2017;16:35–48.
[408] Guo Q, Zhao C, Escano LI, Young Z, Xiong L, Fezzaa K, et al. Transient dynamics of powder spattering in laser powder bed fusion additive manufacturing process revealed by in-situ high-speed high-energy x-ray imaging. Acta Mater 2018;151:169–80.
[409] Zhou X, Wang DZ, Liu XH, Zhang DD, Qu SL, Ma J, et al. 3D-imaging of selective laser melting defects in a Co-Cr-Mo alloy by synchrotron radiation micro-CT. Acta Mater 2015;98:1–16.
[410] Ganeriwala R, Zohdi TI. A coupled discrete element-finite difference model of selective laser sintering. Granular Matter 2016;18:21.
[411] Zhao J, Zhang B, Li X, Li R. Effects of metal-vapor jet force on the physical behavior of melting wire transfer in electron beam additive manufacturing. J Mater Process Tech 2015;220:243–50.
[412] Wang F, Hou WK, Hu SJ, Kannatey-Asibu E, Schultz WW, Wang PC. Modelling and analysis of metal transfer in gas metal arc welding. J Phys D Appl Phys 2003;36:1143.
[413] Hertel M, Spille-Kohoff A, Füssel U, Schnick M. Numerical simulation of droplet detachment in pulsed gas–metal arc welding including the influence of metal vapour. J Phys D Appl Phys 2013;46:224003.
[414] Rao ZH, Hu J, Liao SM, Tsai HL. Modeling of the transport phenomena in GMAW using argon–helium mixtures. Part I - The arc. Int J Heat Mass Tran 2010;53:5707–21.
[415] Xu G, Hu J, Tsai HL. Three-dimensional modeling of arc plasma and metal transfer in gas metal arc welding. Int J Heat Mass Tran 2009;52:1709–24.
[416] Hu J, Tsai H-L. Effects of current on droplet generation and arc plasma in gas metal arc welding. J Appl Phys 2006;100:053304.
[417] Zhao H, DebRoy T. Macroporosity free aluminum alloy weldments through numerical simulation of keyhole mode laser welding. J Appl Phys 2003;93:10089–96.
[418] Blecher JJ, Palmer TA, Debroy T. Porosity in thick section alloy 690 welds - experiments, modeling, mechanism, and remedy. Weld J 2016;95:17s–26s.
[419] Kasperovich G, Haubrich J, Gussone J, Requena G. Correlation between porosity and processing parameters in TiAl6V4 produced by selective laser melting. Mater Des 2016;105:160–70.
[420] Tammas-Williams S, Zhao H, Léonard F, Derguti F, Todd I, Prangnell PB. XCT analysis of the influence of melt strategies on defect population in Ti–6Al–4V components manufactured by Selective Electron Beam Melting. Mater Charact 2015;102:47–61.
[421] Tan JL, Tang C, Wong CH. A computational study on porosity evolution in parts produced by selective laser melting. Metall Mater Trans A 2018;49:3663–73.
[422] Cunningham R, Narra SP, Ozturk T, Beuth J, Rollett AD. Evaluating the effect of processing parameters on porosity in electron beam melted Ti-6Al-4V via synchrotron X-ray microtomography. JOM 2016;68:765–71.
[423] Aboulkhair NT, Everitt NM, Ashcroft I, Tuck C. Reducing porosity in AlSi10Mg parts processed by selective laser melting. Addit Manuf 2014;1–4:77–86.
[424] Attallah MM, Jennings R, Wang X, Carter LN. Additive manufacturing of Ni-based superalloys: the outstanding issues. MRS Bull 2016;41:758–64.
[425] Carlson KD, Lin Z, Beckermann C. Modeling the effect of finite-rate hydrogen diffusion on porosity formation in aluminum alloys. Metall Mater Trans B 2007;38:541–55.
[426] Rappaz M. Modeling and characterization of grain structures and defects in solidification. Curr Opin Solid St M 2016;20:37–45.
[427] Gong H, Rafi K, Gu H, Starr T, Stucker B. Analysis of defect generation in Ti–6Al–4V parts made using powder bed fusion additive manufacturing processes. Addit Manuf 2014;1–4:87–98.
[428] Carter LN, Martin C, Withers PJ, Attallah MM. The influence of the laser scan strategy on grain structure and cracking behaviour in SLM powder-bed fabricated nickel superalloy. J Alloy Comp 2014;615:338–47.
[429] Uddin SZ, Murr LE, Terrazas CA, Morton P, Roberson DA, Wicker RB. Processing and characterization of crack-free aluminum 6061 using high-temperature heating in laser powder bed fusion additive manufacturing. Addit Manuf 2018;22:405–15.
[430] Gu D, Hagedorn Y-C, Meiners W, Meng G, Batista RJS, Wissenbach K, et al. Densification behavior, microstructure evolution, and wear performance of selective laser melting processed commercially pure titanium. Acta Mater 2012;60:3849–60.
[431] Sun GF, Zhou R, Lu JZ, Mazumder J. Evaluation of defect density, microstructure, residual stress, elastic modulus, hardness and strength of laser-deposited AISI 4340 steel. Acta Mater 2015;84:172–89.
[432] Garibaldi M, Ashcroft I, Simonelli M, Hague R. Metallurgy of high-silicon steel parts produced using Selective Laser Melting. Acta Mater 2016;110:207–16.
[433] Harrison NJ, Todd I, Mumtaz K. Reduction of micro-cracking in nickel superalloys processed by Selective Laser Melting: a fundamental alloy design approach. Acta Mater 2015;94:59–68.
[434] Chauvet E, Kontis P, Jägle EA, Gault B, Raabe D, Tassin C, et al. Hot cracking mechanism affecting a non-weldable Ni-based superalloy produced by selective electron beam melting. Acta Mater 2018;142:82–94.
[435] Qiu C, Adkins NJE, Attallah MM. Selective laser melting of Invar 36: microstructure and properties. Acta Mater 2016;103:382–95.
[436] Kou S. A criterion for cracking during solidification. Acta Mater 2015;88:366–74.
[437] Todd I. Metallurgy: no more tears for metal 3D printing. Nature 2017;549:342.
[438] Rappaz M, Jacot A, Boettinger WJ. Last-stage solidification of alloys: theoretical model of dendrite-arm and grain coalescence. Metall Mater Trans A 2003;34:467–79.
[439] Cloots M, Uggowitzer PJ, Wegener K. Investigations on the microstructure and crack formation of IN738LC samples processed by selective laser melting using Gaussian and doughnut profiles. Mater Des 2016;89:770–84.
[440] Zhou Y, Volek A, Singer RF. Effect of grain boundary characteristics on hot tearing in directional solidification of superalloys. J Mater Res 2006;21:2361–70.
[441] Keller T, Lindwall G, Ghosh S, Ma L, Lane BM, Zhang F, et al. Application of finite element, phase-field, and CALPHAD-based methods to additive manufacturing of Ni-based superalloys. Acta Mater 2017;139:244–53.
[442] Ramirez J. Susceptibility of IN740 to HAZ liquation cracking and ductility-dip cracking. Weld J 2012;91:122–31.
[443] Xu J, Lin X, Zhao Y, Guo P, Wen X, Li Q, et al. HAZ liquation cracking mechanism of IN-738LC superalloy prepared by laser solid forming. Metall Mater Trans A 2018;49:5118–36.
[444] Chen Y, Zhang K, Huang J, Hosseini SRE, Li Z. Characterization of heat affected zone liquation cracking in laser additive manufacturing of Inconel 718. Mater

Des 2016;90:586–94.

[445] Chen Y, Lu F, Zhang K, Nie P, Elmi Hosseini SR, Feng K, et al. Dendritic microstructure and hot cracking of laser additive manufactured Inconel 718 under improved base cooling. J Alloy Comp 2016;670:312–21.

[446] Cao G, Kou S. Liquation cracking in full-penetration Al-Si welds. Weld J 2005;84:63s–71s.

[447] Kou S. Fluid flow and solidification in welding: three decades of fundamental research at the University of Wisconsin. Weld J 2012;91:287s–302s.

[448] Cao G, Kou S. Predicting and reducing liquation-cracking susceptibility based on temperature vs. fraction solid. Weld J 2006;85:9.

[449] Huang C, Kou S. Liquation cracking in full-penetration AI-Mg-Si welds. Weld J 2004;84:111s–22s.

[450] Ramirez AJ, Lippold JC. High temperature behavior of Ni-base weld metal - Part I - ductility and microstructural characterization. Mater Sci Eng A 2004;380:259–71.

[451] Noecker FF, DuPont JN. Metallurgical investigation into ductility dip cracking in Ni-based alloys: Part I. Weld J 2009;88:7s–20s.

[452] Young GA, Capobianco TE, Penik MA, Morris BW, McGee JJ. The mechanism of ductility dip cracking in nickel-chromium alloys. Weld J 2008;87:31s–43s.

[453] Chen JQ, Lu H, Yu C, Chen JM, Zhang ML. Ductility dip cracking mechanism of Ni–Cr–Fe alloy based on grain boundary energy. Sci Technol Weld Join 2013;18:346–53.

[454] Chen JQ, Yu C, Chen JM, Lu H, Zhang ML. Assessment of ductility dip cracking susceptibility on Ni based alloy by FEM simulation. Sci Technol Weld Join 2013;17:656–64.

[455] Nissley NE, Lippold JC. Ductility-dip cracking susceptibility of nickel-based weld metals Part 1: Strain-to-fracture testing. Weld J 2008;87:257s–64s.

[456] Ramirez AJ, Lippold JC. High temperature behavior of Ni-base weld metal - Part II - Insight into the mechanism for ductility dip cracking. Mater Sci Eng A 2004;380:245–58.

[457] Noecker FF, DuPont JN. Metallurgical investigation into ductility dip cracking in Ni-based alloys: Part II. Weld J 2009;88:62s–77s.

[458] Shrestha S, Chou K. A build surface study of Powder-Bed Electron Beam Additive Manufacturing by 3D thermo-fluid simulation and white-light interferometry. Int J Mach Tools Manuf 2017;121:37–49.

[459] Boschetto A, Bottini L, Veniali F. Roughness modeling of AlSi10Mg parts fabricated by selective laser melting. J Mater Process Tech 2017;241:154–63.

[460] Rahmati S, Vahabli E. Evaluation of analytical modeling for improvement of surface roughness of FDM test part using measurement results. Int J Adv Manuf Tech 2015;79:823–9.

[461] Gunenthiram V, Peyre P, Schneider M, Dal M, Coste F, Fabbro R. Analysis of laser–melt pool–powder bed interaction during the selective laser melting of a stainless steel. J Laser Appl 2017;29.

[462] Scipioni Bertoli U, Wolfer AJ, Matthews MJ, Delplanque J-PR, Schoenung JM. On the limitations of volumetric energy density as a design parameter for selective laser melting. Mater Des 2017;113:331–40.

[463] Gusarov A, Smurov I. Modeling the interaction of laser radiation with powder bed at selective laser melting. Phys Proc 2010;5:381–94.

[464] Soderstrom E, Mendez P. Humping mechanisms present in high speed welding. Sci Technol Weld Join 2006;11:572–9.

[465] Lopes G, Miranda R, Quintino L, Rodrigues J. Additive manufacturing of Ti-6Al-4V based components with high power fiber lasers. Virtual Rapid Manuf 2007:369–74.

[466] Kumar A, DebRoy T. Toward a unified model to prevent humping defects in gas tungsten arc welding. Weld J 2006;85:292s–304s.

[467] Coniglio N, Cross CE. Initiation and growth mechanisms for weld solidification cracking. Int Mater Rev 2013;58:375–97.

[468] Messler Jr RW. Principles of welding: processes, physics, chemistry, and metallurgy. John Wiley & Sons; 2008.

[469] Bhadeshia HKDH. Residual stress. Part 2 – Nature and origins AU - Withers, P.J. Mater Sci Tech 2001;17:366–75.

[470] Cheng B, Shrestha S, Chou K. Stress and deformation evaluations of scanning strategy effect in selective laser melting. Addit Manuf 2016;12:240–51.

[471] Bailey NS, Katinas C, Shin YC. Laser direct deposition of AISI H13 tool steel powder with numerical modeling of solid phase transformation, hardness, and residual stresses. J Mater Process Tech 2017;247:223–33.

[472] Alimardani M, Toyserkani E, Huissoon JP, Paul CP. On the delamination and crack formation in a thin wall fabricated using laser solid freeform fabrication process: an experimental–numerical investigation. Opt Laser Eng 2009;47:1160–8.

[473] Kamara AM, Marimuthu S, Li L. A numerical investigation into residual stress characteristics in laser deposited multiple layer waspaloy parts. J Manuf Sci Eng 2011;133:031013–31019.

[474] Labudovic M, Hu D, Kovacevic R. A three dimensional model for direct laser metal powder deposition and rapid prototyping. J Mater Sci 2003;38:35–49.

[475] Alimardani M, Toyserkani E, Huissoon JP. A 3D dynamic numerical approach for temperature and thermal stress distributions in multilayer laser solid freeform fabrication process. Opt Laser Eng 2007;45:1115–30.

[476] Kundakcioglu E, Lazoglu I, Rawal S. Transient thermal modeling of laser-based additive manufacturing for 3D freeform structures. Int J Adv Manuf Tech 2016;85:493–501.

[477] Jayanath S, Achuthan A. A computationally efficient finite element framework to simulate additive manufacturing processes. J Manuf Sci Eng 2018;140:041009.

[478] Mercelis P, Kruth JP. Residual stresses in selective laser sintering and selective laser melting. Rapid Prototyp J 2006;12:254–65.

[479] Ferro P, Porzner H, Tiziani A, Bonollo F. The influence of phase transformations on residual stresses induced by the welding process—3D and 2D numerical models. Model Simul Mater Sci Eng 2006;14:117–36.

[480] Denlinger ER, Heigel JC, Michaleris P. Residual stress and distortion modeling of electron beam direct manufacturing Ti-6Al-4V. Proc Inst Mech Eng B J Eng Manuf 2015;229:1803–13.

[481] Hofmann DC, Kolodziejska J, Roberts S, Otis R, Dillon RP, Suh J-O, et al. Compositionally graded metals: a new frontier of additive manufacturing. J Mater Res 2014;29:1899–910.

[482] Tang M, Pistorius PC. Oxides, porosity and fatigue performance of AlSi10Mg parts produced by selective laser melting. Int J Fatigue 2017;94:192–201.

[483] Kaufmann N, Imran M, Wischeropp T, Emmelmann C, Siddique S, Walther F. Influence of process parameters on the quality of aluminium alloy EN AW 7075 using selective laser melting (SLM). Phys Proc 2016;83:918–26.

[484] Kimura T, Nakamoto T. Microstructures and mechanical properties of A356 (AlSi7Mg0.3) aluminum alloy fabricated by selective laser melting. Mater Des 2016;89:1294–301.

[485] Li J, Cheng X, Liu D, Zhang S-Q, Li Z, He B, et al. Phase evolution of a heat-treatable aluminum alloy during laser additive manufacturing. Mater Lett 2018;214:56–9.

[486] Li R, Wang M, Yuan T, Song B, Chen C, Zhou K, et al. Selective laser melting of a novel Sc and Zr modified Al-6.2Mg alloy: processing, microstructure, and properties. Powder Technol 2017;319:117–28.

[487] Rao H, Giet S, Yang K, Wu X, Davies CHJ. The influence of processing parameters on aluminium alloy A357 manufactured by Selective Laser Melting. Mater Des 2016;109:334–46.

[488] Read N, Wang W, Essa K, Attallah MM. Selective laser melting of AlSi10Mg alloy: Process optimisation and mechanical properties development. Mater Des 2015;65:417–24.

[489] Wang P, Gammer C, Brenne F, Prashanth KG, Mendes RG, Rümmeli MH, et al. Microstructure and mechanical properties of a heat-treatable Al-3.5Cu-1.5Mg-1Si alloy produced by selective laser melting. Mater Sci Eng A 2018;711:562–70.

[490] Wang P, Li HC, Prashanth KG, Eckert J, Scudino S. Selective laser melting of Al-Zn-Mg-Cu: Heat treatment, microstructure and mechanical properties. J Alloy Comp 2017;707:287–90.

[491] Zhang H, Zhu H, Nie X, Yin J, Hu Z, Zeng X. Effect of Zirconium addition on crack, microstructure and mechanical behavior of selective laser melted Al-Cu-Mg alloy. Scripta Mater 2017;134:6–10.

[492] Zhang H, Zhu H, Qi T, Hu Z, Zeng X. Selective laser melting of high strength Al–Cu–Mg alloys: processing, microstructure and mechanical properties. Mater Sci Eng A 2016;656:47–54.

[493] Dinda GP, Dasgupta AK, Bhattacharya S, Natu H, Dutta B, Mazumder J. Microstructural characterization of laser-deposited Al 4047 alloy. Metall Mater Trans A

2013;44:2233–42.
[494] Szost BA, Terzi S, Martina F, Boisselier D, Prytuliak A, Pirling T, et al. A comparative study of additive manufacturing techniques: Residual stress and microstructural analysis of CLAD and WAAM printed Ti–6Al–4V components. Mater Des 2016;89:559–67.
[495] Mishra S, DebRoy T. Tailoring gas tungsten arc weld geometry using a genetic algorithm and a neural network trained with convective heat flow calculations. Mater Sci Eng A 2007;454:477–86.
[496] Van Elsen M, Al-Bender F, Kruth J-P. Application of dimensional analysis to selective laser melting. Rapid Prototyp J 2008;14:15–22.
[497] McMillan M, Leary M, Brandt M. Computationally efficient finite difference method for metal additive manufacturing: a reduced-order DFAM tool applied to SLM. Mater Des 2017;132:226–43.
[498] Lucia DJ, Beran PS, Silva WA. Reduced-order modeling: new approaches for computational physics. Prog Aerosp Sci 2004;40:51–117.
[499] Popova E, Rodgers TM, Gong X, Cecen A, Madison JD, Kalidindi SR. Process-structure linkages using a data science approach: application to simulated additive manufacturing data. Integrating Mater Manuf Innov 2017;6:54–68.
[500] Wang Q, Li J, Gouge M, Nassar AR, Michaleris P, Reutzel EW. Reduced-order multivariable modeling and nonlinear control of melt-pool geometry and temperature in directed energy deposition. In: American Control Conference (ACC), 2016; 2016. p. 845–51.
[501] Peng H, Ghasri-Khouzani M, Gong S, Attardo R, Ostiguy P, Gatrell BA, et al. Shankar MR. Fast prediction of thermal distortion in metal powder bed fusion additive manufacturing: Part 1, a thermal circuit network model. Addit Manuf 2018.
[502] Huang Y, Leu MC, Mazumder J, Donmez A. Additive manufacturing: current state, future potential, gaps and needs, and recommendations. J Manuf Sci Eng 2015;137:014001.
[503] Patil N, Pal D, Stucker B. A new finite element solver using numerical eigen modes for fast simulation of additive manufacturing processes. In: Proceedings of the solid freeform fabrication symposium, Austin, TX; Aug 2013.p. 12–4.
[504] Bag S, De A, DebRoy T. A genetic algorithm-assisted inverse convective heat transfer model for tailoring weld geometry. Mater Manuf Process 2009;24:384–97.
[505] Kumar A, Mishra S, Elmer JW, Debroy T. Optimization of the Johnson-Mehl-Avarami equation parameters for alpha-ferrite to gamma-austenite transformation in steel welds using a genetic algorithm. Metall Mater Trans A 2005;36A:15–22.
[506] Mishra S, DebRoy T. A heat-transfer and fluid-flow-based model to obtain a specific weld geometry using various combinations of welding variables. J Appl Phys 2005;98:044902.
[507] Mishra S, DebRoy T. A computational procedure for finding multiple solutions of convective heat transfer equations. J Phys D Appl Phys 2005;38:2977.
[508] Nandan R, Lienert T, DebRoy T. Toward reliable calculations of heat and plastic flow during friction stir welding of Ti-6Al-4V alloy. Int J Mater Res 2008;99:434–44.
[509] De A, DebRoy T. Probing unknown welding parameters from convective heat transfer calculation and multivariable optimization. J Phys D Appl Phys 2003;37:140.
[510] De A, DebRoy T. A smart model to estimate effective thermal conductivity and viscosity in the weld pool. J Appl Phys 2004;95:5230–40.
[511] De A, DebRoy T. Reliable calculations of heat and fluid flow during conduction mode laser welding through optimization of uncertain parameters. Weld J 2005;84:101–12.
[512] De A, DebRoy T. Improving reliability of heat and fluid flow calculation during conduction mode laser spot welding by multivariable optimisation. Sci Technol Weld Join 2006;11:143–53.
[513] Nandan R, Prabu B, De A, Debroy T. Improving reliability of heat transfer and materials flow calculations during friction stir welding of dissimilar aluminum alloys. Weld J 2007;86:313.
[514] Kumar A, DebRoy T. Guaranteed fillet weld geometry from heat transfer model and multivariable optimization. Int J Heat Mass Tran 2004;47:5793–806.
[515] Cooper KP, Lambrakos SG. Thermal modeling of direct digital melt-deposition processes. J Mater Eng Perform 2011;20:48–56.
[516] Lambrakos S, Shabaev A, Bernstein N, Cooper K. Overview of inverse thermal analysis of drop-by-drop liquid-metal deposition using green's functions. J Mater Eng Perform 2012;21:1598–610.
[517] Pandya R, Sawant V, Mendjoge N, D'silva M. Big Data vs Traditional Data; 2015.
[518] Chen M, Mao S, Liu Y. Big data: a survey. Mobile Networks Appl 2014;19:171–209.
[519] Sagiroglu S, Sinanc D. Big data: a review. In: International conference on collaboration technologies and systems (CTS), 2013; 2013. p. 42–7.
[520] Jagadish H, Gehrke J, Labrinidis A, Papakonstantinou Y, Patel JM, Ramakrishnan R, et al. Big data and its technical challenges. Commun ACM 2014;57:86–94.
[521] Nedelcu B. About big data and its challenges and benefits in manufacturing. Database Sys J 2013;4:10–9.
[522] Wang L, Alexander CA. Big data in design and manufacturing engineering. Am J Eng Appl Sci 2015;8:223.
[523] Zhong RY, Newman ST, Huang GQ, Lan S. Big Data for supply chain management in the service and manufacturing sectors: challenges, opportunities, and future perspectives. Comput Ind Eng 2016;101:572–91.
[524] Wang L, Alexander CA. Additive manufacturing and big data. Int J Math Eng Manag Sci 2016;1:107–21.
[525] Seifi M, Salem A, Beuth J, Harrysson O, Lewandowski JJ. Overview of materials qualification needs for metal additive manufacturing. JOM 2016;68:747–64.
[526] Waller MA, Fawcett SE. Click here for a data scientist: Big data, predictive analytics, and theory development in the era of a maker movement supply chain. J Bus Logist 2013;34:249–52.
[527] Kalidindi SR, De Graef M. Materials data science: current status and future outlook. Ann Rev Mater Res 2015;45:171–93.
[528] Cahoon RM. High performance storage system at Sandia National Labs. Albuquerque, NM (United States): Sandia National Labs; 1996.
[529] Jeschke S, Brecher C, Meisen T, Özdemir D, Eschert T. Industrial internet of things and cyber manufacturing systems. Industrial Internet of Things. Springer; 2017. p. 3–19.
[530] Babiceanu RF, Seker R. Big Data and virtualization for manufacturing cyber-physical systems: a survey of the current status and future outlook. Comput Ind 2016;81:128–37.
[531] Chan SL, Lu Y, Wang Y. Data-driven cost estimation for additive manufacturing in cybermanufacturing. J Manuf Syst 2018;46:115–26.
[532] Lee J, Lapira E, Yang S, Kao A. Predictive manufacturing system-Trends of next-generation production systems. IFAC Proc 2013;46:150–6.
[533] Mai J, Zhang L, Tao F, Ren L. Customized production based on distributed 3D printing services in cloud manufacturing. Int J Adv Manuf Tech 2016;84:71–83.
[534] Elgendy N, Elragal A. Big data analytics: a literature review paper. In: Industrial conference on data mining; 2014. p. 214–27.
[535] Gandomi A, Haider M. Beyond the hype: Big data concepts, methods, and analytics. Int J Inform Manag 2015;35:137–44.
[536] Saqib S, Urbanic R, Aggarwal K. Analysis of laser cladding bead morphology for developing additive manufacturing travel paths. Procedia CIRP 2014;17:824–9.
[537] Jordan MI, Mitchell TM. Machine learning: trends, perspectives, and prospects. Science 2015;349:255.
[538] Ramprasad R, Batra R, Pilania G, Mannodi-Kanakkithodi A, Kim C. Machine learning in materials informatics: recent applications and prospects. npj Comp Mater 2017;3..
[539] Baker RE, Pena J-M, Jayamohan J, Jerusalem A. Mechanistic models versus machine learning, a fight worth fighting for the biological community? Biol Lett 2018;14.
[540] Zhang W, Mehta A, Desai PS, Higgs C. Machine learning enabled powder spreading process map for metal additive manufacturing (AM). In: Int Solid Free Form Fabr Symp Austin, TX; 2017. p. 1235–49.
[541] Yuan B, Guss GM, Wilson AC, Hau-Riege SP, DePond PJ, McMains S, et al. Machine-learning-based monitoring of laser powder bed fusion. Adv Mater Technol 2018;3:1800136.
[542] Scime L, Beuth J. A multi-scale convolutional neural network for autonomous anomaly detection and classification in a laser powder bed fusion additive manufacturing process. Addit Manuf 2018;24:273–86.
[543] Khanzadeh M, Chowdhury S, Marufuzzaman M, Tschopp MA, Bian L. Porosity prediction: supervised-learning of thermal history for direct laser deposition. J Manuf Syst 2018;47:69–82.
[544] Bacha A, Sabry AH, Benhra J. Fault diagnosis in the field of additive manufacturing (3D Printing) using Bayesian networks. Int J Online Eng 2019;15.
[545] Kamath C. Data mining and statistical inference in selective laser melting. Int J Adv Manuf Tech 2016;86:1659–77.

[546] Decost BL, Jain H, Rollett AD, Holm EA. Computer vision and machine learning for autonomous characterization of AM powder feedstocks. JOM 2017;69:456–65.
[547] Shevchik SA, Kenel C, Leinenbach C, Wasmer K. Acoustic emission for in situ quality monitoring in additive manufacturing using spectral convolutional neural networks. Addit Manuf 2018;21:598–604.
[548] Ye D, Hong GS, Zhang Y, Zhu K, Fuh JYH. Defect detection in selective laser melting technology by acoustic signals with deep belief networks. Int J Adv Manuf Tech 2018;96:2791–801.
[549] Scime L, Beuth J. Anomaly detection and classification in a laser powder bed additive manufacturing process using a trained computer vision algorithm. Addit Manuf 2018;19:114–26.
[550] Khanzadeh M, Chowdhury S, Tschopp MA, Doude HR, Marufuzzaman M, Bian L. In-situ monitoring of melt pool images for porosity prediction in directed energy deposition processes. IISE Trans 2018:1–19.
[551] Du Y, Mukherjee T, DebRoy T. Conditions for void formation in friction stir welding from machine learning. npj Comp Mater 2019;5:1–8.
[552] Du Y, Mukherjee T, Mitra P, DebRoy T. Machine learning based hierarchy of causative variables for tool failure in friction stir welding. Acta Mater 2020;192:67–77.
[553] Qi Q, Tao F. Digital Twin and Big Data Towards Smart Manufacturing and Industry 4.0: 360 Degree Comparison. IEEE Access 2018;6:3585–93.
[554] Tao F, Cheng JF, Qi QL, Zhang M, Zhang H, Sui FY. Digital twin-driven product design, manufacturing and service with big data. Int J Adv Manuf Tech 2018;94:3563–76.
[555] General Electric Digital Twin at Work: The Technology That's Changing Industry; 2017.
[556] Glaessgen E, Stargel D. The digital twin paradigm for future NASA and US Air Force vehicles. 53rd AIAA/ASME/ASCE/AHS/ASC Structures, Structural Dynamics and Materials Conference 20th AIAA/ASME/AHS Adaptive Structures Conference 14th AIAA 2012 1818.
[557] Mani M, Lane B, Donmez A, Feng S, Moylan S, Fesperman R. Measurement science needs for real-time control of additive manufacturing powder bed fusion processes. National Institute of Standards and Technology, Gaithersburg, MD, Standard No NISTIR 2015;8036.
[558] Salehi D, Brandt M. Melt pool temperature control using LabVIEW in Nd : YAG laser blown powder cladding process. Int J Adv Manuf Tech 2006;29:273–8.
[559] Islam M, Purtonen T, Piili H, Salminen A, Nyrhilä O. Temperature profile and imaging analysis of laser additive manufacturing of stainless steel. Phys Proc 2013;41:835–42.
[560] Tang L, Landers RG. Melt pool temperature control for laser metal deposition processes-Part I: Online temperature control. J Manuf Sci Eng 2010;132:9.
[561] Tang L, Landers RG. Melt pool temperature control for laser metal deposition processes-Part II: Layer-to-layer temperature control. J Manuf Sci Eng 2010;132:9.
[562] Fathi A, Khajepour A, Durali M, Toyserkani E. Geometry control of the deposited layer in a nonplanar laser cladding process using a variable structure controller. J Manuf Sci Eng 2008;130:11.
[563] Barua S, Liou F, Newkirk J, Sparks T. Vision-based defect detection in laser metal deposition process. Rapid Prototyp J 2014;20:77–85.
[564] Denlinger ER, Heigel JC, Michaleris P, Palmer TA. Effect of inter-layer dwell time on distortion and residual stress in additive manufacturing of titanium and nickel alloys. J Mater Process Tech 2015;215:123–31.
[565] Arora A, DebRoy T, Bhadeshia H. Back-of-the-envelope calculations in friction stir welding–velocities, peak temperature, torque, and hardness. Acta Mater 2011;59:2020–8.
[566] Roy G, Nandan R, DebRoy T. Dimensionless correlation to estimate peak temperature during friction stir welding. Sci Technol Weld Join 2006;11:606–8.
[567] DebRoy T, De A, Bhadeshia H, Manvatkar V, Arora A. Tool durability maps for friction stir welding of an aluminium alloy. Proc R Soc A 2012;468:3552–70.
[568] Kumar A, DebRoy T. Neural network model of heat and fluid flow in gas metal arc fillet welding based on genetic algorithm and conjugate gradient optimisation. Sci Technol Weld Join 2006;11:106–19.
[569] Kumar A, DebRoy T. Tailoring fillet weld geometry using a genetic algorithm and a neural network trained with convective heat flow calculations. Weld J 2007;86:26.
[570] Manvatkar V, Arora A, De A, DebRoy T. Neural network models of peak temperature, torque, traverse force, bending stress and maximum shear stress during friction stir welding. Sci Technol Weld Join 2012;17:460–6.
[571] Rai R, DebRoy T. Tailoring weld geometry during keyhole mode laser welding using a genetic algorithm and a heat transfer model. J Phys D Appl Phys 2006;39:1257.
[572] Nie Z, Wang G, McGuffin-Cawley JD, Narayanan B, Zhang S, Schwam D, et al. Experimental study and modeling of H13 steel deposition using laser hot-wire additive manufacturing. J Mater Process Tech 2016;235:171–86.
[573] Prabhakar P, Sames WJ, Dehoff R, Babu SS. Computational modeling of residual stress formation during the electron beam melting process for Inconel 718. Addit Manuf 2015;7:83–91.
[574] Cheng B, Chou K. Geometric consideration of support structures in part overhang fabrications by electron beam additive manufacturing. Comput Aided Des 2015;69:102–11.
[575] Hodge N, Ferencz R, Vignes R. Experimental comparison of residual stresses for a thermomechanical model for the simulation of selective laser melting. Addit Manuf 2016;12:159–68.
[576] Hsu Y, Rubinsky B, Mahin K. An inverse finite element method for the analysis of stationary arc welding processes. J Heat Transf-Trans ASME 1986;108:734–41.
[577] Keanini RG, Rubinsky B. An inverse finite element minimization-based method for solution of multi-dimensional phase-change and material boundary shapes. Int J Numer Meth Eng 1994;37:1125–41.
[578] Goncalves C, Vilarinho L, Scotti A, Guimaraes G. Estimation of heat source and thermal efficiency in GTAW process by using inverse techniques. J Mater Process Tech 2006;172:42–51.
[579] Gonçalves CV, Carvalho SR, Guimarães G. Application of optimization techniques and the enthalpy method to solve a 3D-inverse problem during a TIG welding process. Appl Therm Eng 2010;30:2396–402.
[580] Guo J-L, Le Masson P, Artioukhine E, Loulou T, Rogeon P, Carin M, et al. Estimation of a source term in a quasi steady two-dimensional heat transfer problem: application to an electron beam welding. Front Mater Sci 2011;5:126.
[581] Zhou J, Zhang Y, Chen J, Feng Z. Inverse estimation of front surface temperature of a plate with laser heating and convection–radiation cooling. Int J Therm Sci 2012;52:22–30.